



<https://theses.gla.ac.uk/>

Theses Digitisation:

<https://www.gla.ac.uk/myglasgow/research/enlighten/theses/digitisation/>

This is a digitised version of the original print thesis.

Copyright and moral rights for this work are retained by the author

A copy can be downloaded for personal non-commercial research or study, without prior permission or charge

This work cannot be reproduced or quoted extensively from without first obtaining permission in writing from the author

The content must not be changed in any way or sold commercially in any format or medium without the formal permission of the author

When referring to this work, full bibliographic details including the author, title, awarding institution and date of the thesis must be given

Enlighten: Theses

<https://theses.gla.ac.uk/>
research-enlighten@glasgow.ac.uk

FABRICATION AND OPTICAL SPECTROSCOPY OF SEMICONDUCTOR QUANTUM STRUCTURES

thesis by

Hazel Elisabeth Gillian Arnot

**Submitted for the degree of Doctor of Philosophy to the
Electrical and Electronics Engineering Department of
Glasgow University**

July 1990

© Hazel Arnot, 1990

ProQuest Number: 11007353

All rights reserved

INFORMATION TO ALL USERS

The quality of this reproduction is dependent upon the quality of the copy submitted.

In the unlikely event that the author did not send a complete manuscript and there are missing pages, these will be noted. Also, if material had to be removed, a note will indicate the deletion.



ProQuest 11007353

Published by ProQuest LLC (2018). Copyright of the Dissertation is held by the Author.

All rights reserved.

This work is protected against unauthorized copying under Title 17, United States Code
Microform Edition © ProQuest LLC.

ProQuest LLC.
789 East Eisenhower Parkway
P.O. Box 1346
Ann Arbor, MI 48106 – 1346

Acknowledgements

I now have the opportunity to thank those people that have helped, supported and encouraged me throughout this PhD.

One of the great strengths of the Electronics department is the superb standard of support that is provided by the technical staff. I would therefore like to thank Andy "I can do ten things at once" Stark and Dave "Hitachi Man" Gourlay for their help in mask fabrication, Vic Law, Ray Darkin, Jimmy Young and Dave Clifton for dry etching and Doug "Fix it" Irons for his excellent support in cryogenics. Without their contribution this work would not have been possible. Thank you Lois "Been there, seen that, done that" Hobbs for all your words of wisdom on matters technical or otherwise. Your support was often needed and greatly appreciated.

It is also the camaraderie of my fellow PhD students and post doctorate colleagues which make life bearable in Basement 3. Therefore I would like to thank all the students who work in the Nanoelectronics and Low Temperature lab for all their patience in listening to me complaining, and especially Kim Lee and Stephen Thoms for their advice on fabrication. Bill Leitch, Rory McLeod, Alistair Kean and I spent many hours working together in the Spectroscopy Lab and again their support was invaluable. However Morag Watt must deserve the biggest thank you of all for teaching me so much about optical spectroscopy.

Naturally no acknowledgement would be complete without thanking my supervisors - Steve Beaumont in Glasgow and Steve Andrews from GEC Hirst Research Centre. Despite the distance between Glasgow and London I had plenty of input from Steve Andrews and I learned much from his excellent experimental technique. It is safe to say that without his input I could not have completed this work. I don't know who will be more relieved when I finish - Steve Beaumont or me. Thank you Steve for supporting me throughout. Though it may not show I really appreciate the time and guidance you gave me. Thank you also to Rick Glew, my collaborator from STC Technology for his superb support right up to the end and for always returning samples to me so promptly. That alone was a wonderful help. I must also thank Clivia Sotomayor Torres for the impetus she provided in the overgrowth work and for the use of the equipment in her lab. I also wish to express my gratitude to Professor J Lamb for the provision of the departmental laboratory and computing facilities and to Chris Wilkinson and Gordon Doughty for their invaluable advice on dry etching.

I would also like to thank the Central College of Commerce in Glasgow for providing me with part-time employment and hence much needed income for the last three and a half years. Without it I would have spent the next three and a half years paying for my PhD.

Finally my heart felt thanks must go to those that have provided so much emotional support - to my Mum and Sandy Fraser. How you stood it, I don't know.

Table of Contents

Acknowledgements	ii
Table of Contents	iii
List of Figures	viii
List of Tables	xii
Publications	xiii
Summary	xv

Chapter 1 - Theory and Literature Review

1.1	Introduction	1
1.2	Background	2
1.2.1	Exciton Formation	2
1.2.2	Heterojunctions	3
1.2.3	Quantum Wells	3
1.2.4	Quantum Wires and Dots	7
1.2.5	Discussion	11
1.3	Optical Characterization of 2D and 3D Structures	11
1.4	Literature Review	13
1.4.1	GaAs/AlGaAs Quantum Structures	
1.4.1.1	Confinement achieved using a combination of electron beam lithography and dry etching.	13
1.4.1.2	Confinement achieved using ion implantation.	16
1.4.2	InP/InGaAs Quantum Structures	17
1.4.3	Quantum Dot or Wires Lasers	17
1.4.4	Electrical behaviour of Quantum Structures	21
1.4.5	Summary	22
	References	22

Chapter 2 - Mask Fabrication

2.1	Introduction	24
2.2	Electron Beam Lithography	24
2.3	The Proximity Effect	26

2.4	Electron Beam Resists	26
2.4.1	Positive Resist Process for Mask Fabrication	27
2.4.2	Positive Resist Process Steps	28
2.4.3	Negative Resist Process for Mask Fabrication	30
2.4.4	Negative Resist Process Steps	30
2.4.5	Comparison of the Positive and Negative Resist Processes	32
2.5	Exposure of Dot Patterns	32
2.5.1	Pattern Design and Exposure Data	32
2.5.2	Results	38
2.6	Exposure of Wire Patterns	38
2.6.1	Exposure of Negative Resist Wire Masks	38
2.6.2	Exposure of Positive Resist Wire Masks	38
2.7	Sample Design for Optical Spectroscopy	42
2.7.1	Design and Fabrication of Alignment Marks	42
2.7.2	Alignment and Exposure of Pattern Areas	47
2.8	Quantum Dot Mask Fabrication using Laser Holography	47
2.8.1	Background	47
2.8.2	Quantum Dot Fabrication on GaAs	48
2.9	Summary	51
	References	52
 Chapter 3 - Etching		
3.1	Introduction	53
3.2	Wet Chemical Etching	54
3.3	Plasma Etching	54
3.3.1	Self-Sustained Glow Discharges	56
3.3.2	Physical and Chemical Phenomena in Gas Discharges	57
3.3.3	Method of Plasma Production	58
3.3.4	Plasma Etching and Reactive Ion Etching	59
3.3.5	Reactive Ion Etch Parameters	60

3.4	SiCl ₄ Reactive Ion Etching	61
3.4.1	The Etch Mechanism in SiCl ₄ RIE	61
3.4.2	Results	61
3.5	SiCl ₄ /H ₂ Reactive Ion Etching	66
3.5.1	The Etch Mechanism in SiCl ₄ /H ₂ RIE	68
3.5.2	Results	72
3.6	CH ₄ /H ₂ RIE	74
3.6.1	The Etch Mechanism in CH ₄ /H ₂ RIE	74
3.6.2	Results	76
3.7	Ion Beam Milling	78
3.7.1	Comparison of Ion Beam Milling and Reactive Ion Etching	78
3.7.2	The Etch Mechanism in Ion Beam Milling using Argon	79
3.7.3	Results	79
3.8	Oxygen Plasma Etching	82
3.9	Reactive Ion Etch Induced Damage	82
3.9.1	Damage assessment by current carrying devices	82
3.9.2	Damage assessment by photoluminescence measurements	83
3.9.3	Damage assessment by cathodoluminescence measurements and transmission electron microscopy	84
3.9.4	Damage assessment by Raman Scattering	86
3.10	Summary	90
	References	91

Chapter 4 - Experimental and Material growth methods

4.1	Introduction	93
4.2	Experimental Apparatus	93
4.2.1	Lasers	93
4.2.2	Focussing and Collecting Optics	94
4.2.2.1	Nearly Backscattering Geometry	94
4.2.2.2	90° Scattering Geometry	94
4.2.3	The Spectrometer	96
4.2.4	Photon Counting Techniques	96
4.2.5	The Spectral Response of the System	96

4.2.6	Computerisation and Software	99
4.2.6	Cryostats	99
4.2.6.1	Large Bore Optical Cryostat	99
4.2.6.2	Continuous Flow Cryostat and Flow Controller	99
4.3	The MOCVD and MBE Growth Processes	103
4.3.1	MBE	103
4.3.2	MOCVD	104
4.4	Comparison of the MBE and MOCVD growth processes	104
4.4.1	Interface Quality	105
	References	108
 Chapter 5 - Photoluminescence Studies of Free Standing MBE Quantum Dots		
5.1	Introduction	109
5.2	Surface Recombination Velocity	109
5.3	Experimental Details	110
5.4	Experimental Results	112
4.4.1	GaAs/AlGaAs Quantum Dots	112
4.4.2	InGaAs/GaAs Quantum Dots	122
4.4.3	Broad Etched Areas	122
5.5	Discussion	124
5.6	Summary	127
	References	128
 Chapter 6 - Photoluminescence Studies of Overgrown GaAs/AlGaAs Quantum Dots		
6.1	Introduction	129
6.2	Experimental Details	129
6.3	Comparison of MOCVD QDs etched using SiCl₄ and CH₄/H₂ before and after regrowth	130
6.3.1	Sample Details	130
6.3.2	Results and Discussion	132

6.3.3	Summary	135
6.4	Overgrown MBE Quantum Dots	135
6.4.1	Sample Details	135
6.4.2	Results and Discussion	135
6.5	Comparison of MOCVD and MBE QDs	137
6.6	Experiments to answer questions raised in Sections 6.3 and 6.4	137
6.7	Photoluminescence obtained from MOCVD QDs and QWWs before and after overgrowth	140
6.7.1	Material Design	140
6.7.2	Quality of MOCVD quantum well material	140
6.8	Sample Design	144
6.9	Photoluminescence of SiCl ₄ etched dots and wires from 5 to 200K	145
6.9.1	Experimental results before regrowth	145
6.9.2	Experimental results after regrowth	157
6.9.3	Discussion	180
6.10	Photoluminescence of CH ₄ /H ₂ etched dots from 5 to 200K	183
6.10.1	Experimental results before regrowth	183
6.10.2	Experimental results after regrowth	185
6.10.3	Discussion	190
6.11	Temperature Cycling on SiCl ₄ etched dots and mesas	190
6.11.1	Experimental results and discussion	190
6.12	Summary	194
	References	195
	Chapter 7 - Conclusions and Future Work	197

List of Figures

Chapter 1

1.1	The band diagram of a semiconductor heterojunction	4
1.2	Energy levels in a quantum well	5
1.3	Variation of density-of-states of electrons with increasing quantization in QW structures	8
1.4	Energies of excitons confined in a square box	9
1.5	Excitation and Luminescence spectra of GaAs/AlGaAs quantum well	12
1.6	PL intensity versus width of GaAs/AlGaAs and InP/InGaAs quantum well wires	15
1.7	A quantum box laser in GaAs/AlGaAs system	18
1.8	Gain spectra of InP/InGaAs and GaAs/AlGaAs quantum box, wire, well and bulk lasers	20

Chapter 2

2.1	The Glasgow Electron-beam Lithographic System	25
2.2	Positive and negative mask fabrication process	29
2.3	Exposure response curves for PMMA and HRN resists	31
2.4	Quantum dot Nichrome etch masks	35
2.5	Quantum dot 250nm thick HRN etch masks	36
2.6	Quantum wire 250nm thick HRN etch masks	39
2.7	Quantum wire PMMA etch mask	41
2.8	Alignment mark design for optical experiments	43
2.9	Window alignment marks and exposed dot arrays and mesa	45
2.10	Window frame alignment marks and exposed dot arrays and mesa	46
2.11	Wet etched alignment marks and exposed dot arrays and mesa	46
2.12	Laser interferometer arrangements for generating holographic gratings	49
2.13	Crossed gratings in photoresist	50
2.14	Photoresist dot etch mask after oxygen plasma etching	50
2.15	Quantum dots obtained after reactive ion etching of photoresist dot etch mask	50

Chapter 3

3.1	Wet etch of quantum dots after reactive ion etching	55
3.2	Quantum dots etched in SiCl_4	64
3.3	Quantum wires etched by SiCl_4	64
3.4	20nm quantum dots etched by SiCl_4	65
3.5	Anisotropic SiCl_4 etch followed by 3min plasma etch	67
3.6	Anisotropic SiCl_4 etch followed by 5min plasma etch	67
3.7	SiCl_4 reactive ion etching at high pressure	67
3.8	Low pressure anisotropic followed by high pressure reactive ion etch	67
3.9	Effect on etch rate of Si and SiO_2 on addition of O_2 to CF_4	70

3.10	Effect on etch rate of Si and SiO ₂ on addition of H ₂ to CF ₄	70
3.11	Etch rate versus percentage of H ₂ in SiCl ₄	71
3.12	RGA analysis as the percentage of H ₂ in SiCl ₄ is increased	71
3.13	Etch depth versus power density for SiCl ₄ /H ₂	71
3.14	Etch of GaAs dots using 1:5 SiCl ₄ /H ₂	73
3.15	Etch of GaAs dots using 1:1 SiCl ₄ /H ₂	73
3.16	Etch of GaAs dots using 1:3 SiCl ₄ /H ₂ a power density of 0.22W/cm ²	75
3.17	Etch of GaAs dots using 1:3 SiCl ₄ /H ₂ a power density of 0.43W/cm ²	75
3.18	Etch of GaAs dots using 1:3 SiCl ₄ /H ₂ a power density of 0.65W/cm ²	75
3.19	CH ₄ /H ₂ etched GaAs quantum dots	77
3.20	CH ₄ /H ₂ etched InP/InGaAs quantum dots	77
3.21	Argon ion milled GaAs/AlGaAs quantum dots	81
3.22	Cathodoluminescence micrograph of GaAs/AlGaAs quantum dots	85
3.23	Raman scattering spectra from two etched samples	87
3.24	Raman spectra of two quantum dot samples	89
3.25	Plot of the experimental data points for the additional Raman feature	90

Chapter 4

4.1	Schematic of the 90° scattering geometry Photoluminescence apparatus	95
4.2	Schematic representation of the light path within a double spectrometer	97
4.3	The Spectral Response of the System	98
4.4a	Schematic of the continuous gas flow system	101
4.4b	CF 1204 Cryostat and Insert	102
4.5	Effects on PL linewidth due to interface roughness	107

Chapter 5

5.1	Material structure of GaAs/AlGaAs and GaAs/InGaAs quantum well samples grown by MBE	111
5.2	Representative Photoluminescence spectra of mesa and dots at 5K	113
5.3	Integrated PL intensity at 5K v diameter for SiCl ₄ etched GaAs/AlGaAs quantum dots	116
5.4	Integrated PL intensity at 5K v diameter for CH ₄ /H ₂ etched GaAs/AlGaAs quantum dots	117
5.5	Integrated PL intensity at 5K versus diameter for Argon ion milled GaAs/AlGaAs quantum dots showing incident angle dependence	119
5.6	Excitation power dependence of integrated PL intensity of dots and mesa in GaAs/AlGaAs	120
5.7	Temperature dependence of integrated PL intensity of CH ₄ /H ₂ etched GaAs/AlGaAs dots and mesa	121
5.8	PL spectra of InGaAs/GaAs 500nm dots and mesa at 5K	123
5.9	Temperature dependence of ratio of PL intensity of GaAs epilayer with top surface bombarded by AlGaAs relative to oxygen exposed surface revealed by SiCl ₄ RIE.	125

Chapter 6

6.1	SEMs of 350nm diameter QDs after RIE with SiCl_4 or CH_4/H_2 .	131
6.2	SEMs of 350nm diameter QDs after regrowth with a layer of $0.2\mu\text{m}$ of $\text{Al}_{0.4}\text{Ga}_{0.6}\text{As}$.	131
6.3	QW PL emission from SiCl_4 etched mesa (A) before and (B) after regrowth.	133
6.4	QW PL emission from SiCl_4 etched patterns.	134
6.5	SEMs of MBE 300nm diameter dots a) after RIE b) after regrowth.	136
6.6	QW emission from the MBE mesa (A) and 300nm dots (B) before regrowth (solid line) and after regrowth (dashed line).	138
6.7	PL spectra excited at 2.54eV at 5K from the 4, 7 and 10nm QWs and GaAs substrate.	141
6.8	15K PL peak emission wavelength plotted against well width of the GaAs QW for $\text{Al}_{0.3}\text{Ga}_{0.7}\text{As}$.	143
6.9	FWHM of the PL spectrum from GaAs/AlGaAs QWs as a function of well width.	143
6.10	Representative PL spectra from a) $200\mu\text{m}^2$ mesa and b) 75nm dots excited at 2.54eV at 5K.	146
6.11	Representative PL spectra from 80nm wide wires excited at 2.54eV at 5K.	146
6.12	Linewidth broadening compared to a corresponding mesa of the PL spectra excited at 2.54eV at 5K from the 4 and 7nm QW in both dots and wires.	147
6.13	Relative integrated PL intensity excited at 2.54eV from GaAs/AlGaAs quantum dots and wires etched using SiCl_4 from the 4 and 7nm QW.	149
6.14	Temperature dependence of the integrated PL intensity relative to that at 5K from the 4nm QW in a mesa and the 75, 100, 300 and 550nm dots.	150
6.15	Temperature dependence of the integrated PL intensity relative to that at 5K from the 4nm QW in a mesa and the 80, 150, 250 and 500nm wires.	151
6.16	Temperature dependence of the integrated PL intensity relative to that at 5K from the 7nm QW in a mesa and the 75, 100, 300 and 550nm dots.	152
6.17	Temperature dependence of the integrated PL intensity relative to that at 5K from the 7nm QW in a mesa and the 80, 150, 250 and 500nm wires.	153
6.18	Wavelength shift in exciton emission relative to the 5K position in all dot sizes and a mesa.	154
6.19	Wavelength shift in exciton emission relative to the 5K position in all wire sizes and a mesa.	155
6.20	Comparison of the wavelength shift in exciton emission relative to the 5K position for 2 mesas and the 75nm dots and 80nm wires.	156
6.21	PL linewidth variation with temperature for a $200\mu\text{m}^2$ mesa.	158
6.22	PL linewidth variation with temperature for all dot sizes in both the 4 and 7nm QW.	159
6.23	PL linewidth variation with temperature for all wire sizes in both the 4 and 7nm QW.	160
6.24	Excitation power dependence at 2.54eV of the integrated PL intensity from the 4 and 7nm QW in the 75 and 300nm dots and the $200\mu\text{m}^2$ mesa.	161
6.25	Excitation power dependence at 2.54eV of the integrated PL intensity from the 4 and 7nm QW in the 80 and 250nm wires and the $200\mu\text{m}^2$ mesa.	162
6.26	300nm dots and 250nm wires before and after regrowth with $0.2\mu\text{m}$ layer of $\text{Al}_{0.4}\text{Ga}_{0.6}\text{As}$.	163

6.27	Comparison of the relative intensity of PL from the $200\mu\text{m}^2$ and $100\mu\text{m}^2$ mesa before and after regrowth.	165
6.28	Variation in PL spectra with temperature from the 4 and 7nm QWs from the $200\mu\text{m}^2$ mesa before and after regrowth.	166
6.29	Comparison of the variation of the relative integrated PL intensity with temperature for the 300 and 550nm dots before and after regrowth.	167
6.30	Comparison of the variation of the relative integrated PL intensity with temperature for the 150, 250 and 500nm wires before and after regrowth.	168
6.31	Variation in PL spectra with temperature from the 4 and 7nm QWs from the 500nm wires before and after regrowth.	169
6.32	Variation of the integrated PL intensity excited at 1.96eV with temperature from the 150, 250 and 500nm wires and a $100\mu\text{m}^2$ mesa.	170
6.33	Shift in exciton emission wavelength with temperature for a $200\mu\text{m}^2$ and $100\mu\text{m}^2$ mesa for the 4nm QW before and after regrowth.	171
6.34	Shift in exciton emission wavelength with temperature for a 550nm and 300nm dots for the 4nm QW before and after regrowth.	172
6.35	Shift in exciton emission wavelength with temperature for a 150, 250 and 500nm wires for the 4nm QW before and after regrowth.	173
6.36	PL linewidth variation with temperature for the 4nm QW in the mesas, dots and wires.	174
6.37	PL excited at 2.41eV from the $\text{Al}_{0.3}\text{Ga}_{0.7}\text{As}$ barriers before and after regrowth with a layer of $\text{Al}_{0.4}\text{Ga}_{0.6}\text{As}$ from a control unprocessed sample.	176
6.38	PL excited at 2.41eV from the $\text{Al}_{0.3}\text{Ga}_{0.7}\text{As}$ barriers before and after regrowth with a layer of $\text{Al}_{0.4}\text{Ga}_{0.6}\text{As}$ from a $200\mu\text{m}^2$ mesa and 300nm dots.	177
6.39	Optical behaviour of CH_4/H_2 quantum dots showing relative integrated intensities, temperature variation of the intensities and exciton emission wavelength in the 4nm QW.	184
6.40	Variation of PL linewidth with temperature for the CH_4/H_2 etched dots and mesa.	186
6.41	100nm diameter CH_4/H_2 etched dots before and after regrowth.	187
6.42	PL excited at 2.54eV from the CH_4/H_2 dots after regrowth.	188
6.43	Material structure of a $200\mu\text{m}^2$ mesa etched using CH_4/H_2 before and after regrowth.	189
6.44	Spectra obtained from overgrown and unovergrown control material.	191
6.45	PL from a SiCl_4 etched mesa after 19min temperature cycle.	192
6.46	PL from SiCl_4 etched mesa after a 12min temperature cycle.	192

List of Tables

Chapter 2

I	HRN resist thickness before and after etching with SiCl_4 and CH_4/H_2	33
II	Exposure parameters for dots in positive and negative resist	37
III	Exposure parameters for gratings in negative resist	40

Chapter 3

IV	Optimum etch conditions for quantum dot and wire reactive ion etching	63
V	Argon ion milling parameters	80

Chapter 5

VI	Details of patterned GaAs/AlGaAs samples used in obtaining the data in Fig. 5.2-5.4.	115
----	--	-----

Chapter 6

VII	Relative PL intensities for dots and wires excited using different excitation wavelengths.	179
-----	--	-----

List of Publications Arising from this Work

Chapter 2

T P Smith III, H Arnot, J M Hong, C M Knoedler, S E Laux and H Schmid: "Capacitance Oscillations in one-dimensional electron systems" Phys. Rev. Lett Vol. 59 No. 24 December 1987 pp. 2802-2805.

T P Smith III, K Y Lee, J M Hong, C M Knoedler, H Arnot and D P Kern: "Fractional quantization in ultranarrow electron channels" Phys. Rev. B. Vol. 38, No. 2, 15 July 1988-I pp. 1558-1561.

K Y Lee, T P Smith, H Arnot, C M Knoedler, J M Hong, D P Kern and S E Laux: "Fabrication and characterization of one- and zero-dimensional electron systems. J. Vac. Sci. Technol. B6 (6) Nov/Dec 1988. pp. 1856-1860.

T P Smith III, J A Brum, J M Hong, C M Knoedler, H Arnot and L Esaki : "Magnetic anisotropy of a one-dimensional electron system" Phys. Rev. Lett, Vol. 61 No. 5 August 1988 pp. 585-588.

Chapter 3

M Watt, C M Sotomayor-Torres, R Cheung, C D W Wilkenson, H E G Arnot and S P Beaumont: "Raman scattering of reactive ion etched GaAs" J. Modern Optics, 1988, Vol. 35, No. 3, pp. 365-370.

M Watt, C M Sotomayor-Torres, R Cheung, C D W wilkenson, H E G Arnot, S P Beaumont: "Raman scattering investigations of the damage caused by reactive ion etching of GaAs" Superlattices and Microstructures, Vol. 4, No. 2, 1988. pp. 243-244.

M Watt, C M Sotomayor Torres, H E G Arnot and S P Beaumont: "Surface Phonons in GaAs cylinders" Semiconductor Science and Technology, 5 (1990) pp. 285-290.

M Watt, H E G Arnot, C M Sotomayor Torres and S P Beaumont: "Surface phonon studies of nanostructures" Proceedings of the International Symposium on Nanostructure Physics and Fabrication, March 13-15, 1989. pp. 89 - 96. Edited by M A Reed and W P Kirk. Published by Academic Press Inc.

Chapter 5

H Arnot, S R Andrews and S P Beaumont: "Photoluminescence Studies of GaAs-AlGaAs Quantum Dots" *Microelectronic Engineering* 9 (1989) 365 - 368, North-Holland.

S R Andrews, H Arnot, P K Rees, T M Kerr and S P Beaumont: "Photoluminescence studies of free-standing quantum boxes" to be published *J. Appl. Phys.* 67 (7) 1990 pp. 3472-3480.

S R Andrews, H Arnot, T M Kerr, P K Rees and S P Beaumont: "Radiative Recombination in free standing Quantum Boxes" *Nato ARW Science and Engineering of 0 and 1 D Semiconductors*, Cadiz 1989.

Chapter 6

H E G Arnot, M Watt, C M Sotomayor-Torres, R Glew, R Cusco, J Bates and S P Beaumont: "Photoluminescence of Overgrown GaAs-AlGaAs Quantum Dots" *Superlattices and Microstructures*, Vol. 5, No. 3, 1989.

H E G Arnot, C M Sotomayor Torres, R Cusco, M Watt, R Glew and S P Beaumont: "Photoluminescence Studies of Overgrown GaAs/AlGaAs MOCVD and MBE Quantum Dots." *Proceedings of Quantum Wells in Optics and Optoelectronics*, Salt Lake City, February 1989. pp. 83-87 Published by the Optical Society of America, 1989 *Technical Digest Series*, Volume 10.

Summary

Fabrication of 0 and 1 dimensional structures, known as quantum dots and wires respectively, was successfully achieved in GaAs/AlGaAs, InP/InGaAs and GaAs/InGaAs semiconductor material systems. Etch masks made of either metal or resist were fabricated by electron beam lithography and the pattern then transferred to the underlying substrate using reactive ion etching with SiCl_4 , CH_4/H_2 or SiCl_4/H_2 and also argon ion milling. The smallest dots fabricated were 20nm in diameter and the smallest wires 60nm in width.

The dominant recombination mechanism for photoexcited carriers in sub-micron GaAs/AlGaAs quantum dots was found to be radiative at 5K for lateral dimensions as small as 40nm. In contrast, in GaAs/AlGaAs wires nonradiative recombination predominates as the wire width is reduced. This is the first report of quantum GaAs/AlGaAs dots as small as 40nm in diameter luminescing as efficiently as the bulk material showing that without subsequent processing the effect of any radiation induced damage is minimal. The dominant recombination mechanism in sub-micron strained layer InGaAs/GaAs quantum dots at low temperature was also found to be nonradiative.

As the temperature at which the structures were characterized was increased a size dependence was found in the relative integrated PL intensities from the dots and wires. The smaller diameter dots (75 and 150nm) and the narrower wires (80 and 150nm in width) luminesced to higher temperatures than the larger diameter dots (300 and 550nm) and the wider wires (250 and 500nm) respectively and the smaller dots luminesced to higher temperatures than the smallest wires. This was also true when comparing the larger dots to the larger wires. This temperature dependence may be due to confinement dependent on the dot diameter or wire width. Restrictions on the diffusion lengths of excitons to nonradiative sites due to the patterning of the QW into dots and wires could be the mechanism responsible for the effects seen at 5K. In wires the extra degree of freedom of the exciton contributes to the loss of luminescence at 5K as it is still possible for the excitons to diffuse to nonradiative sites within the exciton lifetime. This does not happen in the dots. This conclusion is supported by the results obtained after regrowth.

Regrowth with a layer of $\text{Al}_{0.4}\text{Ga}_{0.6}\text{As}$ on SiCl_4 etched quantum structures increased the luminescence efficiency of the 250 and 500nm wires but reduced the efficiency of the 150nm wires. The 550 and 300nm dots showed no change in efficiency either before or after regrowth. Luminescence was completely lost in the 75 and 150nm diameter dots and 80nm wide wires. This suggests that in the wires surface states contribute significantly at 5K to the nonradiative recombination rate whereas in dots they do not. The overgrown AlGaAs layer passivates the nonradiative surface states thereby increasing the luminescence efficiency of these structures.

It has been shown that shifts in exciton emission to higher energy after regrowth on samples subjected to RIE with either SiCl_4 or CH_4/H_2 are most likely due to enhanced diffusion of Al into the quantum well caused by impurities introduced during the dry etch process. This changes the profile of the well from a square potential profile to a compositionally graded well causing the shift to higher emission energies.

Chapter 1

Theory & Literature Review

1.1 Introduction

High resolution tailoring of III-V semiconductors in one dimension by epitaxial growth techniques has allowed many of the electronic properties of heterojunction structures to be precisely controlled. This has led to the development over the past few years of high mobility field effect transistors, heterostructure lasers and new quantum well devices.

Compound semiconductor materials with reduced dimensionality are increasingly being investigated for future applications and to add to our understanding of fundamental physics. The dramatic change in the energy spectrum and the density of states alter many properties of these systems. Since modern epitaxial growth techniques are capable of producing quantum well structures with sharp interfaces (of the order of one atomic layer), many interesting effects have been studied in quasi-two dimensional structures.

Quantum effects may occur in a system where the degree of freedom of the charge carrier is sufficiently restricted. In this situation the wave nature of electrons and holes becomes important. This generally happens when the particles are confined to regions smaller in dimension than their quantum mechanical (de Broglie) wavelength. Systems with one or zero degrees of freedom can be prepared starting from a two dimensional structure by patterning the layer to a lateral dimension comparable to the de Broglie wavelength of the carriers. Direct electron beam writing and highly anisotropic pattern transfer techniques such as dry etching can be used for this purpose.

This thesis will report on the fabrication techniques involved in realising one or zero degrees of freedom devices - quantum wires or dots, and in particular at the resolution limits of the electron-beam and the dry etching procedures. The optical behaviour of these structures, studied using low temperature photoluminescence techniques, will also be presented.

1.2 Background

1.2.1 Exciton Formation

When light with energy equal to or greater than the bandgap (the energy difference between the valence and the conduction band) is incident on a bulk semiconductor, an electron in the valence band may absorb this energy and make a transition to the conduction band. However by making this transition a vacancy has been created in the valence band. This unoccupied electronic state can be represented by a particle with a positive charge referred to as a "hole".

At low temperatures the band-edge optical properties of wide gap semiconductors are dominated by excitons - electron-hole pairs bound by Coulomb interactions.

In 3 dimensions the expressions for the hydrogenic Bohr radius and ionisation energy can be transferred to excitons in semiconductors by replacement of the reduced hydrogenic mass with the reduced mass of an exciton and inclusion of the relative dielectric constant.

The **ionization or binding energy** for such a system is

$$E_{\text{ex}}^{3\text{D}} = 13.6 \frac{m_{\text{ex}}^*}{\epsilon_r^2} (\text{eV})$$

where ϵ_r is the relative dielectric constant and m_{ex}^* is the reduced exciton effective mass

$$m_{\text{ex}}^* = (m_{\text{ex}}^{*-1} + m_{\text{h}}^{*-1})^{-1}$$

m_{e}^* and m_{h}^* being the electron and hole effective mass respectively. The 3D binding energy of an exciton in GaAs is 4.2meV. Free excitons can travel in the crystal and be captured by impurities and crystal defects. This alters the exciton binding energy and its lifetime.

The **diameter** of an exciton i.e. the distance at which the electron orbits the hole will vary depending on the semiconductor. A simple method of calculating the diameter of an exciton is to calculate the Bohr radius applying the same method as that used to calculate the radius of a hydrogen atom.

$$a_{\text{ex}}^{3\text{D}} = \frac{\epsilon_r}{m_{\text{ex}}^*} a_0 \quad \text{where } a_0 \text{ is the hydrogen Bohr radius given by } a_0 = \frac{h^2 \epsilon_0}{\pi e^2}$$

Obviously the diameter of an exciton will be larger than a hydrogen atom as the mass of a hole is much smaller than that of the hydrogen nucleus.

The diameter of an exciton is dependent on the effective mass of the exciton in a particular crystal. The effective mass is in turn dependent on the band structure of the semiconductor which varies between material systems and hence the diameter of an exciton will depend upon the host crystal lattice. The exciton radius in bulk GaAs is ~14nm and is ~26nm in GaInAs.

1.2.2 Heterojunctions

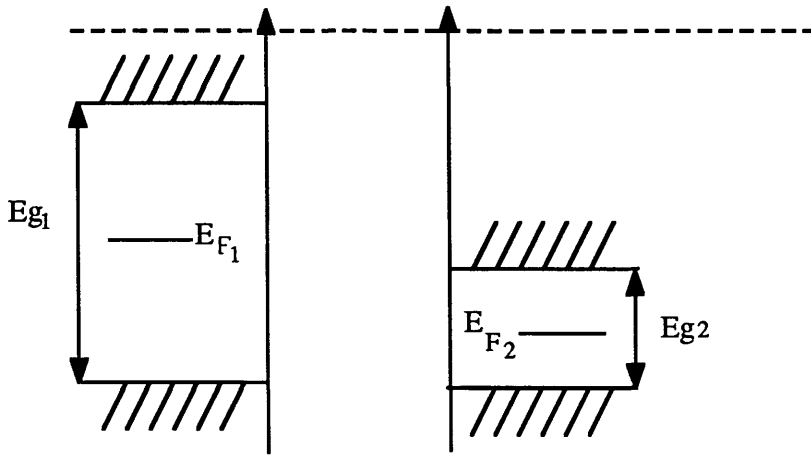
Semiconductor heterostructures are layers of two or more different semiconductors grown coherently with one common crystal structure. A heterostructure may be viewed as a single crystal in which the occupancy of the atomic sites changes at the interface. The lattice structure and constants of the two materials must differ very little if the two materials are to be grown on top of each other without introducing strain into the material. One of the most studied heterojunctions is that between GaAs and $\text{Ga}_{1-x}\text{Al}_x\text{As}$. The aluminium concentration is usually chosen to be around 20-35% to ensure that the potential barrier in the conduction band is large, that the ternary alloy is still direct gap material and to ensure that the lattice parameter matching is obtained. Above $x=0.4$ the gap becomes indirect^{1a}.

Figure 1.1 shows a) the band diagram for two bulk semiconductors with different bandgaps with the vacuum level serving as a common reference point and b) the band diagram of the heterojunction formed from these two materials. When two solids of differing electronegativity are brought together charge will redistribute in the interface bonds producing a surface dipole layer which will shift the energy of the two sides relative to each other. This causes the conduction and valence band to be offset (or discontinuous) i.e. there is potential step at the interface of the two semiconductors in the conduction and valence band. The difficulty is in knowing how the energy difference between the two semiconductor energy gaps is split between the conduction and valence bands. Does it form potential steps of equal size in both bands or is the distribution less equal?

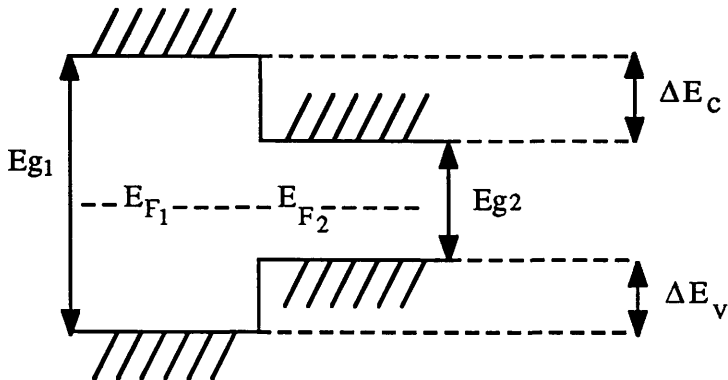
Consider a heterojunction formed by depositing a layer of $\text{Ga}_{0.7}\text{Al}_{0.3}\text{As}$ on a GaAs substrate as this is the material system used in this work. The height of the conduction or valence band offset, depends on the bulk band structures of the constituent materials (which for AlGaAs depends on the Al percentage) and on their relative position. Early results suggested that the split in a GaAs/ $\text{Al}_{0.3}\text{Ga}_{0.7}\text{As}$ heterojunction was $0.85E_g$ and $0.15E_g^2$ for the conduction and valence band respectively, where E_g is the difference in the energy gap of the two semiconductors. However later work showed that the new offset ratio (at $x=0.3$) was ~60:40³.

1.2.3 Quantum Wells

A quantum well is a thin layer (e.g. 10nm) of one semiconductor (e.g. Gallium Arsenide) sandwiched between adjacent layers of another, wider band gap material (eg Aluminium Gallium Arsenide). By cladding GaAs with AlGaAs barriers, the different relative energies of the conduction and valence bands in GaAs and AlGaAs give rise to a square well potential in the conduction band due to the conduction band offset. In undoped material a carrier thermally or optically excited into the conduction band will be confined in the low gap layers due to this band gap difference (figure 1.2). This is the physical



(a)



(b)

Figure 1.1 (a) The band diagram of two different disconnected semiconductors 1 and 2 with energies shown relative to the vacuum.
 (b) The line-up of band structures of lattice-matched semiconductors 1 and 2 forming a heterojunction. E_c and E_v are the conduction band and valence band offsets, respectively. It is assumed that the materials are undoped and that the effect of charge transfer at the interface is negligibly small. E_{g1} and E_{g2} are the fundamental gaps. (After Jaros^{1b})

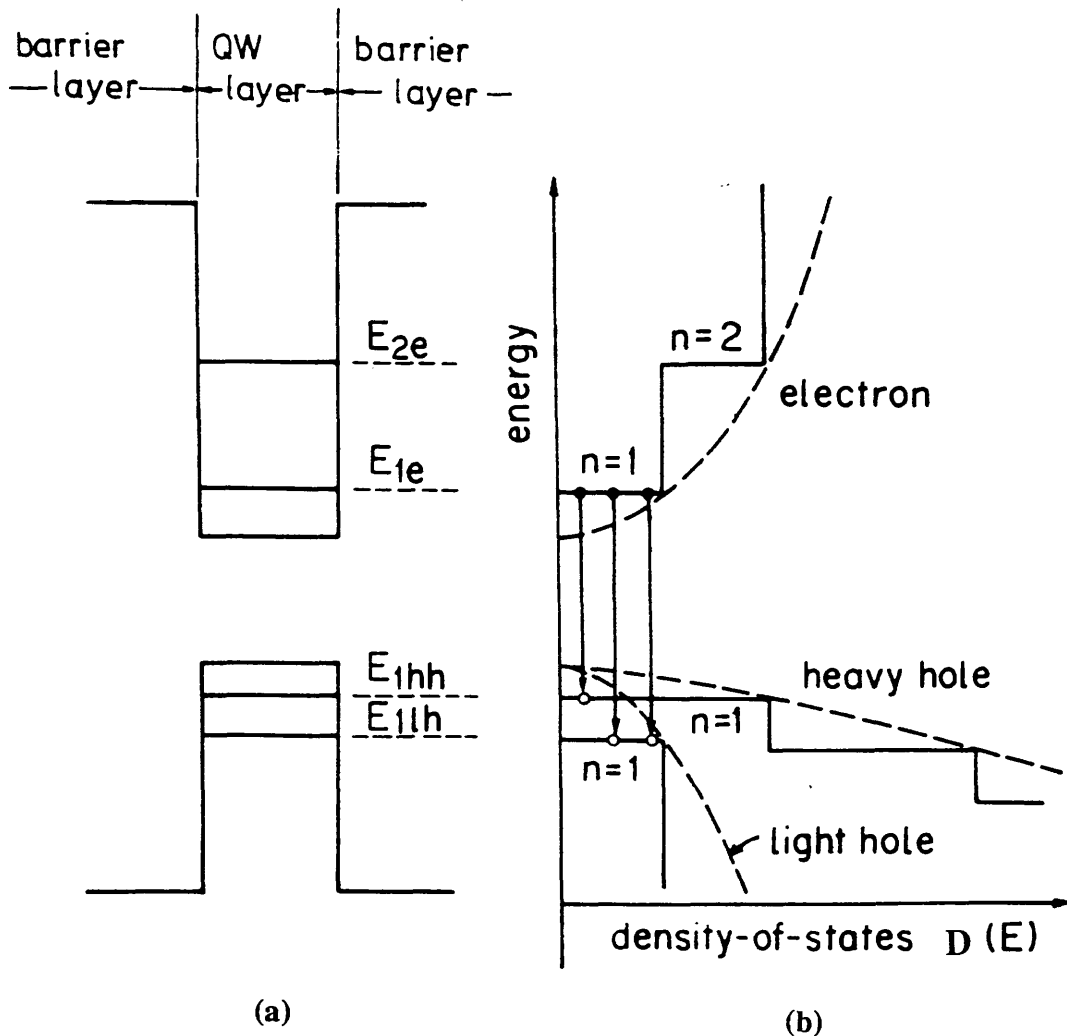


Figure 1.2 (a) Quantum energy levels in a quantum well. E_{1e} and E_{2e} are $n=1$ and $n=2$ electron levels, and E_{1hh} and E_{1lh} are $n=1$ heavy-hole and light-hole levels, respectively. (b) Density-of-states as a function of energy for a QW structure (solid line) and for a bulk crystal (broken line). (After Okamoto⁶)

realisation of the elementary quantum mechanical particle in a 1D box problem^{1b}. Coulomb attraction correlates the motion of carriers in the conduction band and valence band quantum wells in the x and y directions, forming bound electron and hole pairs or excitons. They produce very sharp resonance peaks just below the band gap, where a large oscillator strength is concentrated in a narrow spectral domain².

If the GaAs layer thickness is of the order of 10nm (less than the Bohr diameter of an exciton in GaAs - ~28nm) the motion of the carriers will be quantized along the normal to the layers (z) which will produce a series of discrete states, although the carriers are free to move in the x-y plane. The effect of the confinement on the density of states that describe the optical transitions is to transform the 3D parabolic dependence into a series of steps (figure 1.2). It also raises the degeneracy of the upper valence band of III - V semiconductors by introducing a splitting between the heavy and light holes due to their different confinement energies.

The ionisation energy and exciton radius for the ideal 2D system is given by

$$E_{\text{ex}}^{2\text{D}} = 4E_{\text{ex}}^{3\text{D}} \sim 17\text{meV} \quad (\text{ref 4})$$

for an infinitely narrow quantum well. It is 2.5 to 3 times larger than $E_{\text{ex}}^{3\text{D}}$ in a 5nm thick GaAs/AlGaAs QW. The exciton diameter has been reduced to

$$a_{\text{ex}}^{2\text{D}} = a_{\text{ex}}^{3\text{D}} \sqrt{\frac{3}{8}} \quad (\text{ref 10})$$

Exciton resonances in bulk material are difficult to observe at room temperature because in polar semiconductors longitudinal-optical (LO) vibrations produce strong electric fields that rapidly ionize the weakly bound excitons⁵. As the temperature is lowered the vibrations are reduced and hence the exciton lifetime is increased due to the reduction in the ionizing electric field. The emitted light is therefore more intense, has a narrower spectral width and shifts to lower wavelengths due to the decrease in the bandgap.

In quantum wells, the confinement increases the binding energy of the excitons so that it is more comparable with kT at room temperature. At room temperature excitons live just long enough to produce clear resonances before being ionized by interaction with LO-phonons into an e-h plasma that in turn lasts for several nanoseconds before recombining. Although the exciton still interacts with an LO-phonon and is ionized the confinement reduces the interaction channels between the excitons and the polar phonons that are responsible for the temperature broadening. The width of the exciton peak is broadened, but it remains narrow enough to be resolved at room temperature⁴.

At low temperatures quantum well excitons are considerably broader than those of high quality 3D samples; the exciton linewidth is found to increase when the layer thickness decreases. The low temperature quantum well exciton profile has been interpreted as resulting from the inhomogeneous broadening introduced by the unavoidable fluctuations of the well thickness. In the best samples these

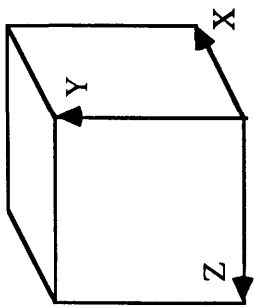
fluctuations are found to be the order of one atomic layer, and the size of the atomically smooth areas is the order of 30nm. The effects of layer roughness on the excitons produce highly interesting properties that are due to localization⁴. When the layer thickness decreases, the quantum energy levels for electrons and holes increase, thereby increasing the light emission energy⁶.

1.2.4 Quantum Wires and Dots

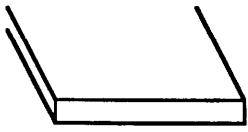
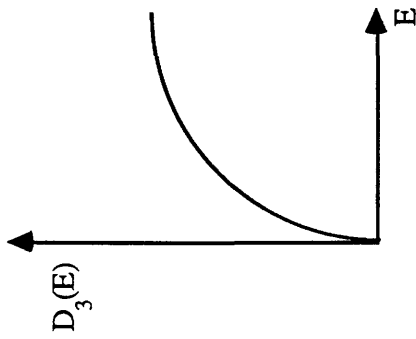
The logical extension of the concept of confining the exciton to two degrees of freedom in a quantum well is to confine it to one or zero degrees of freedom. These structures are called quantum wires and quantum dots respectively. In these structures the laterally confining potentials must be on length scales comparable with or smaller than the carrier de Broglie wavelengths. A quantum wire is obtained by patterning the quantum well in the Y direction. Carriers are therefore confined in both the Y and Z directions i.e. have one degree of freedom. A quantum dot is obtained by patterning in both the X and Y directions and the exciton therefore has zero degrees of freedom of movement (figure 1.3). This patterning of the quantum well alters the density-of-states. On reducing from three dimensions to two dimensions (3D to 2D) the density of states changes from a continuous $D(E)=E^{1/2}$ dependence to a step like dependence which is mirrored in the absorption spectrum. A 1D density of states is characterized by a series of singularities of the form $(E-E_i)^{-1/2}$ (i.e. a quantum wire) and in a 0D case (i.e. a quantum dot) the density of states is reduced to a series of delta functions (figure 1.3).

There has been considerable effort in trying to model the properties of excitons in a 1D and 0D system and therefore to predict the advantages in device performance to be gained from increasing the confinement on the exciton in these low dimensional structures. Most attention has been directed towards modelling the behaviour of quantum dots, probably because any advantages to be gained from additional confinement will be greatest in these structures. Several authors have assumed that a confined exciton can be treated as an electron-hole pair trapped in a box of infinite depth^{7,8,9} and that the effects seen will be the similar to those observed in semiconductor microcrystallites embedded in glass.

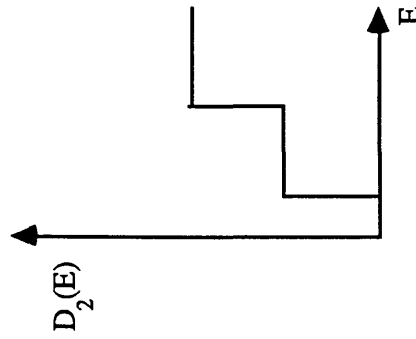
Bryant¹⁰ however has shown that quantum dots (or boxes) should be viewed as square plates of sides length L and width w. Typically the width w of the two dimensional quantum well is an order of magnitude less than the length L of the side of the dot. Therefore in quantum dots one degree of motion is always frozen out for all L. This is not the case in microcrystallites where all three dimensions are of a comparable size. From his calculations Bryant suggested that confinements effects are important even for $L \geq 100\text{nm}$ i.e. for a quantum dot 100nm in diameter. However, for these L, the exciton is much smaller than the box, and the exciton ground-state energy E_{GS} is affected little by confinement (figure 1.4). The exciton kinetic (E_{KE}) and Coulomb energies (confinement energy - E_{NI}) show a similar weak dependence on L for larger boxes. In fact E_{KE} is much larger than E_{NI} for large L. Most of the kinetic energy of an exciton in a large box is the kinetic energy due to correlation as an exciton, and only a small part is due to quantum confinement. As L decreases, E_{KE} approaches E_{NI} , indicating that the correlation effects in the exciton due to the interactions are becoming less important and that quantum confinement makes the more important contribution. Wu *et al*¹¹ showed that the broad photoluminescence peaks observed for excitons in quantum dots could result from inhomogeneous broadening due to variations in box size because the confinement energies are a sensitive function of L.



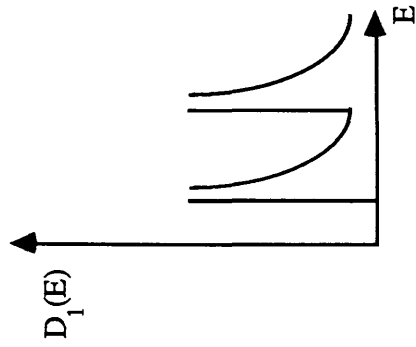
a) Bulk



b) Quantum Well



c) Quantum Wire



d) Quantum Dot

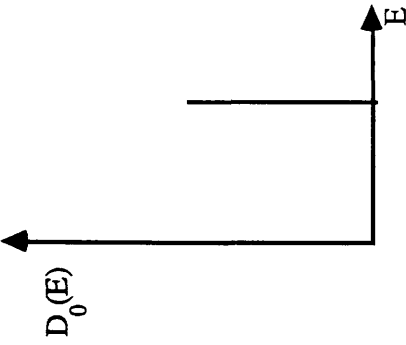


Figure 1.3 Variation of density-of-states of electrons with the increase of the quantization dimension in quantum-well structures.

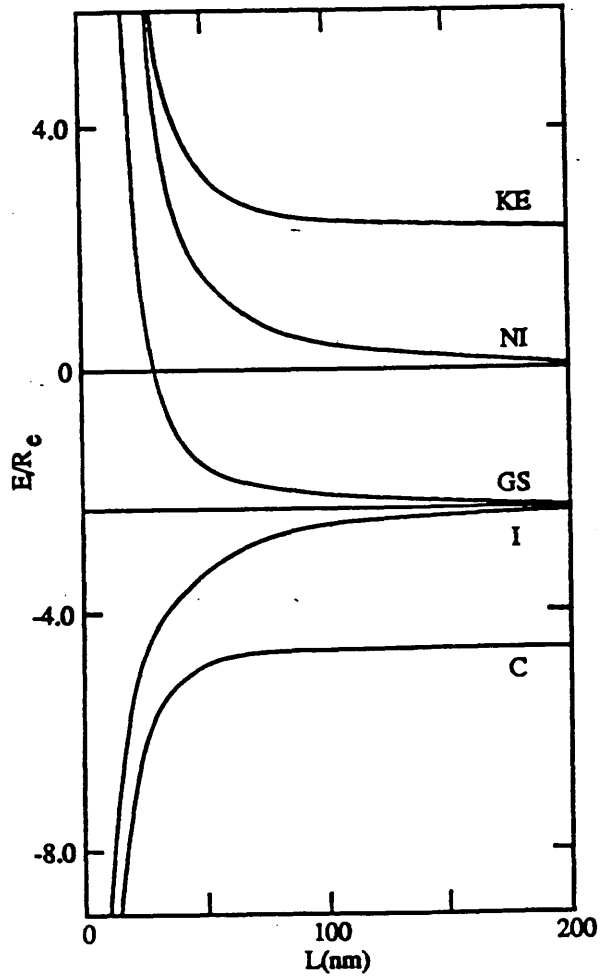


Figure 1.4 The ground-state (GS) energy of an exciton confined in a square box with sides of length L . The exciton kinetic energy (KE), Coulomb energy (C), energy of a noninteracting electron-hole pair (NI), and the interaction energy (I) are shown. (After Bryant¹⁰)

Bryant has shown that this effect is somewhat reduced taking into account exciton effects.

Austin¹² modelled the behaviour assuming that in real systems the barriers may be relatively low, so the possibility of tunnelling out of the quantum dot should be considered. Indeed Austin points out that " it is known that (in contrast to one- and two- dimensional systems) a three-dimensional system with finite barriers does not support bound states below a certain critical radius". Austin found that the electron-hole pair become more strongly bound as the dot radius decreases. The exciton binding energy passes through a maximum for Radius= $\sim 3\text{nm}$; this behaviour is similar to that found theoretically¹³ for GaAs/AlGaAs quantum wells. When the diameter of the dot is decreased from a value comparable to the bulk exciton Bohr radius ($\sim 14\text{nm}$), the electron and hole are brought closer together and the Coulomb binding energy increases; at very small radii the electron and hole wavefunctions spread appreciably into the surrounding AlGaAs and the Coulomb binding energy falls. This feature is absent in models which assume infinite barriers. A maximum binding energy of $\sim 40\text{meV}$ is predicted for a radius of 3nm and for radii above 10nm the binding energy approaches the 3D value of $\sim 5\text{meV}$. This is in contrast to Bryant¹⁰ who suggests that confinement effects could occur for a radius of $\sim 50\text{nm}$ although these effects may be small.

Another area that has been studied by several authors is the effect on optical nonlinearities when a quantum well is patterned further into a quantum wire or dot. This could lead to a new range of devices. For example Schmitt-Rink *et al*⁸ have suggested that the absorption of quantum dots might be significantly changed by local field effects and show different non-linear behaviour to quantum wells such as optical bistability. The origin of the optical non-linearity is straight forward. Electron-hole pairs created by the interband optical absorption influence the absorption spectrum. Most obviously they fill states and prevent further absorption by the Pauli Exclusion Principle and hence saturate the absorption. In bulk material Coulomb interactions due to the positive charge and negative charge on the electron and hole modify the exciton absorption resonances but it is argued that in quantum dots only state filling is important.

Bryant¹⁵ has also modelled the binding energies for the bound states of a hydrogenic impurity placed on the axis of a quantum-well wire. The QWW is a cylinder of GaAs surrounded by $\text{Al}_x\text{Ga}_{1-x}\text{As}$. Bryant found that for very small wires, the electrons leak out of the wire and behave as three dimensional electrons in $\text{Al}_x\text{Ga}_{1-x}\text{As}$. As the wire size increases, an abrupt crossover from three-dimensional to one-dimensional behaviour occurs when the radial spread of the wavefunction becomes smaller than the wire radius and the electron no longer leaks out of the wire. The binding energy is strongly enhanced. The wire remains quasi-one-dimensional out to the largest radii ($1000a_0$ where a_0 is the Bohr radius). Bryant suggests that it is expected that the luminescence from wire structures should broaden as the enhanced binding energy in a quasi-one-dimensional system is more sensitive to the location of the impurity or exciton relative to the well boundary. Further modelling changing the cross-section of the wire showed that the binding energy for impurities in wires with comparable shapes are most closely related to the cross-sectional area¹⁶.

1.2.5 Discussion

There are obviously some discrepancies in the results as Takagahara suggests that size uniformity is important if inhomogeneous broadening of the linewidth of the light emitted from QDs is to be avoided and Bryant says that this effect is smaller than previously suggested. Austin suggests that quantum dots of 20nm in radius will have binding energies approaching 3D values whereas Bryant predicts enhanced confinement energies at 50nm radius. In all these cases the authors assume different boundary conditions in trying to predict 0D behaviour. Differences will obviously occur if the quantum dot is viewed as a thin disk with the two dimensions defined by lateral confinement much larger than the width of the quantum well that defines the third dimension of the box or if it is modelled as a perfectly spherical semiconductor dot embedded in a material of a different (usually smaller) dielectric constant and also whether the barriers are modelled as being finite or infinite. For practical purposes the models which assume finite barriers and square plate like disks are more likely to yield realistic data as these are the models which most closely resemble the experimental structures. Therefore taking these considerations into account it is perhaps possible that quantum effects will be seen in quantum dots 50–60nm in diameter as Bryant¹⁰ predicts. The confinement effects may not be large enough to produce a measurable "blue" shift in the emitted light but may show up in other effects. For example Schmitt-Rink⁸ predicts that one consequence of the confinement of the electronic states is the disappearance of the temperature dependent broadening mechanism that dominates in room-temperature quantum wells⁴. In this quantum well mechanism, the exciton once created is rapidly ionized by absorbing an optical phonon to create free electrons and holes. This shortening of the exciton lifetime results in a simple lifetime broadening of the exciton line. This mechanism disappears in the QD because there need not be higher electron/or hole states of the right energy to act as final states for the phonon absorption process. Bryant also states that the properties of an exciton confined in a circular disk of radius R should be nearly the same as the properties of an exciton in a square plate with side $L=\pi R^{1/2}$. This result therefore removes the necessity of ensuring that all dots are round or square when fabricating the structures.

1.3 Optical Characterization of 1D and 0D structures

A standard method used to observe the optical behaviour of excitons confined in a quantum well is **Photoluminescence (PL)**. The PL spectrum is a measure of the number of photons emitted from a structure within a specific energy range. In general for a quantum well it will consist of one peak which is due to the electron-hole pair relaxing to the lowest energy level ($n=1$) before recombining thus emitting a photon. The PL spectrum is Stoke shifted to slightly lower energies than the exciton absorption line because excitons relax to the lowest energy states in the well before recombining. PL thus gives information on the lowest energy e1-h1 transition in a quantum well but is complicated that by the fact that the exciton might be free or bound (figure 1.5) Semiconductors are transparent to light of energy less than the energy gap separating the conduction band from the valence band. The energy at which the semiconductor starts to absorb light is known as the band edge.

Another technique is **Photoluminescence Excitation**. This is a measure of the luminescence efficiency as a function of the pump energy. Unlike the PL spectrum it gives information on the higher

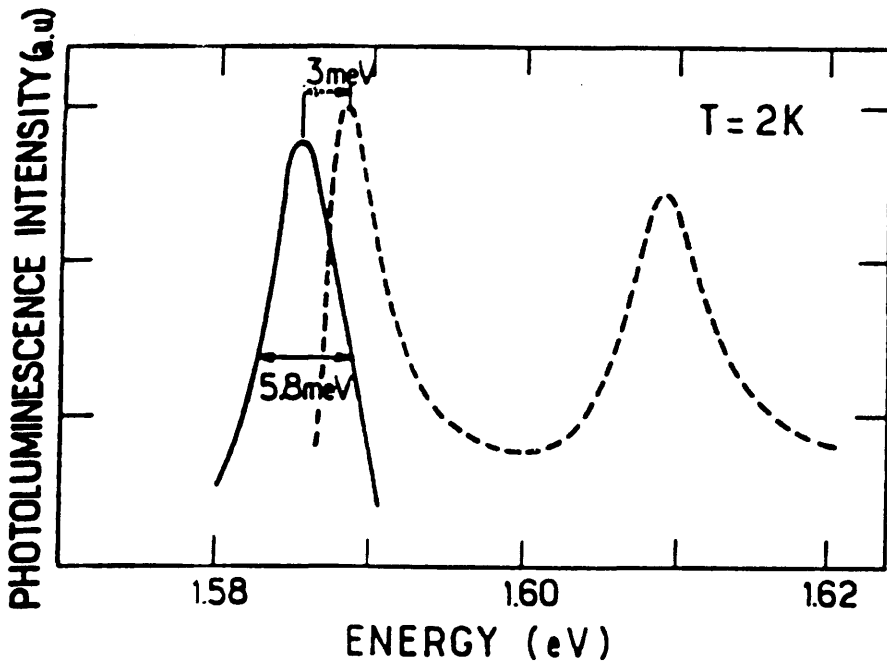


Figure 1.5 Excitation spectrum (broken line) and luminescence spectrum (solid line) of a 7nm GaAs/Ga_{0.48}Al_{0.52}As MOCVD quantum well, showing the linewidths and the Stokes shift between the free exciton heavy-hole excitation peak and the luminescence peak involving excitons bound to interface defects. (After Bastard *et al*¹⁷)

energy transitions eg e_2-h_2 . The quantum well is excited with light of energy sufficient to excite the higher energy transitions. By scanning the energy of the incident radiation from a wavelength below the main PL peak emission downwards these higher energy transitions can be observed since the PLE spectrum usually mirrors the absorption spectrum which is dominated by free exciton processes (figure 1.5). Changes in the energies of the free exciton energies (i.e. due to lateral confinement) are most easily interpreted using this technique.

Both of the above methods were used to characterize quantum structures at temperatures ranging from 2.2K to 200K. It was necessary to investigate the photoluminescence at cryogenic temperatures as lattice vibrations are sufficiently reduced at these temperatures that the excitons are not ionized in a few femtoseconds as would happen at room temperature. Bright well resolved, narrow linewidth excitonic peaks are therefore measurable. It is however interesting to investigate how the linewidth and the intensity of the signal vary as the temperature is increased and results of this are presented in Chapters 5 and 6.

1.4 Literature Review

Early optical studies of confinement in more than one dimension were almost entirely limited to colloidal preparations of II-VI semiconductor microcrystals or crystallites embedded in a glass matrix. The studies by Warnock and Awschalom¹⁸ for example, on $CdS_{0.27}Se_{0.73}$ microcrystallites reported the existence of finite size effects, where electrons trapped in tiny crystals showed the effects of quantum confinement. Blue shifts (i.e. shifts of excitonic emission to higher energy) of exciton absorption lines as a function of the crystallite size were observed by Ekimov and Onushchenko¹⁹ in CuCl microcrystallites. Banyai and Koch²⁰ predicted strong excitation-induced blue shifts due to plasma screening causing an increase in the exciton Bohr radius as well as a blue shift due to a decrease in microcrystallite size. These earlier results created interest in trying to simulate quantum confinement in compound semiconductor structures which could then be engineered into devices exploiting these quantum size effects.

1.4.1 GaAs/AlGaAs Quantum Structures

1.4.1.1 Confinement achieved using a combination of electron beam lithography and dry etching

The first report of the optical behaviour of quantum dots (QDs) was by Mark Reed *et al*²¹ who fabricated QDs in a GaAs/AlGaAs system using electron beam lithography and dry etching. Although the QD diameter in the experiment was 300nm, Reed reported blue shifts in the excitonic spectrum. This is extremely unlikely as the bulk exciton diameter in GaAs is ~ 14 nm and the QDs would need to be of the order of 30nm or less before any size effects could compress the exciton resulting in an increase in the binding energy and a decrease in the wavelength of the photon emitted on recombination. Perhaps reactive ion etch induced damage could have resulted in an area of 30nm or less of undamaged material where this effect could occur. It is significant however that this result has never

been repeated in QDs of this size.

Kash *et al*²² reported that for QDs of 100nm or less in diameter fabricated in the GaAs/AlGaAs system no blue shift was seen in the photoluminescence excitation spectrum but enhanced luminescence efficiency of up to 60-120 times greater than the bulk material was observed. They attributed this result to the suppression of the diffusion of carriers to nonradiative recombination sites within the quantum wells. This was a surprising result as it is expected that the free surfaces created by the etching procedure would function as efficient nonradiative recombination sites for the photoexcited carriers and if anything the luminescence efficiency should decrease. Enhancement of the oscillator strength is not predicted for structures of this size. It has been suggested that this enhancement of luminescence efficiency (which has never been repeated) could have been due to poor quality starting material. Subsequent processing could have removed nonradiative sites. On patterning the number of defects may have been reduced i.e. many dots may have no defects in them at all and this may account for the increased efficiency.

Further work by Kash *et al*²³ suggested that the homogeneous strain in the plane of a GaAs/AlGaAs quantum well layer induced by the patterned removal of strained material above the well, contributed a significant potential to confine the exciton in a quantum dot or wire structure. The strain is generated by the relaxation of an uniformly strained AlGaAs barrier. They investigated the effects of strain further by achieving confinement produced by inhomogeneous strain created by patterning and etching a compressively stressed overlayer of amorphous carbon²⁴. In this method the patterning of the strained overlayer imposes a corresponding pattern of strain in the underlying well, thus locally modifying its band structure. Photoluminescence spectra of the quantum wells underlying the stressor wires show band-gaps red shifted by as much as 31meV. This shift is somewhat larger than the calculated value for the strain induced by the overlayer -19.8meV. Photoluminescence excitation measurements²⁵ of the same wires showed strong polarization anisotropy of the light and heavy hole exciton absorption and this was explained by the effect of the anisotropic strain on the valence band wave functions.

Forchel *et al*²⁶ also reported PL studies of GaAs/AlGaAs quantum wires. The wires were defined by RIE in CCl_2F_2 and Ar (gas ratio 1:4) and Argon ion milling. They found that a decrease in wire linewidth from $5\mu\text{m}$ into the submicron range had the consequence of a steep decrease of the PL intensity by a factor of about 500, no matter which of the above processes were used to define the free standing wires (figure 1.6). They attributed the variation in quantum efficiency as a function of wire width to be due to non-radiative transitions at the etched sidewalls. With decreasing wire width the influence of non-radiative surface recombination increases. However they also suggested that dry etching damage may lead to the formation of optically inactive layers at the sidewalls. The results presented in Chapters 5 and 6 will refute this.

An important point to note in the presentation of all data on the optical behaviour of quantum structures is the optical geometry used to excite the structures and collect the light. In the case of the work by Forchel *et al*²⁶ a 0° scattering geometry was used where the exciting light hit the top of the wires or dots. Other authors²¹⁻²⁵ use 90° scattering geometry. The angle of incidence and the

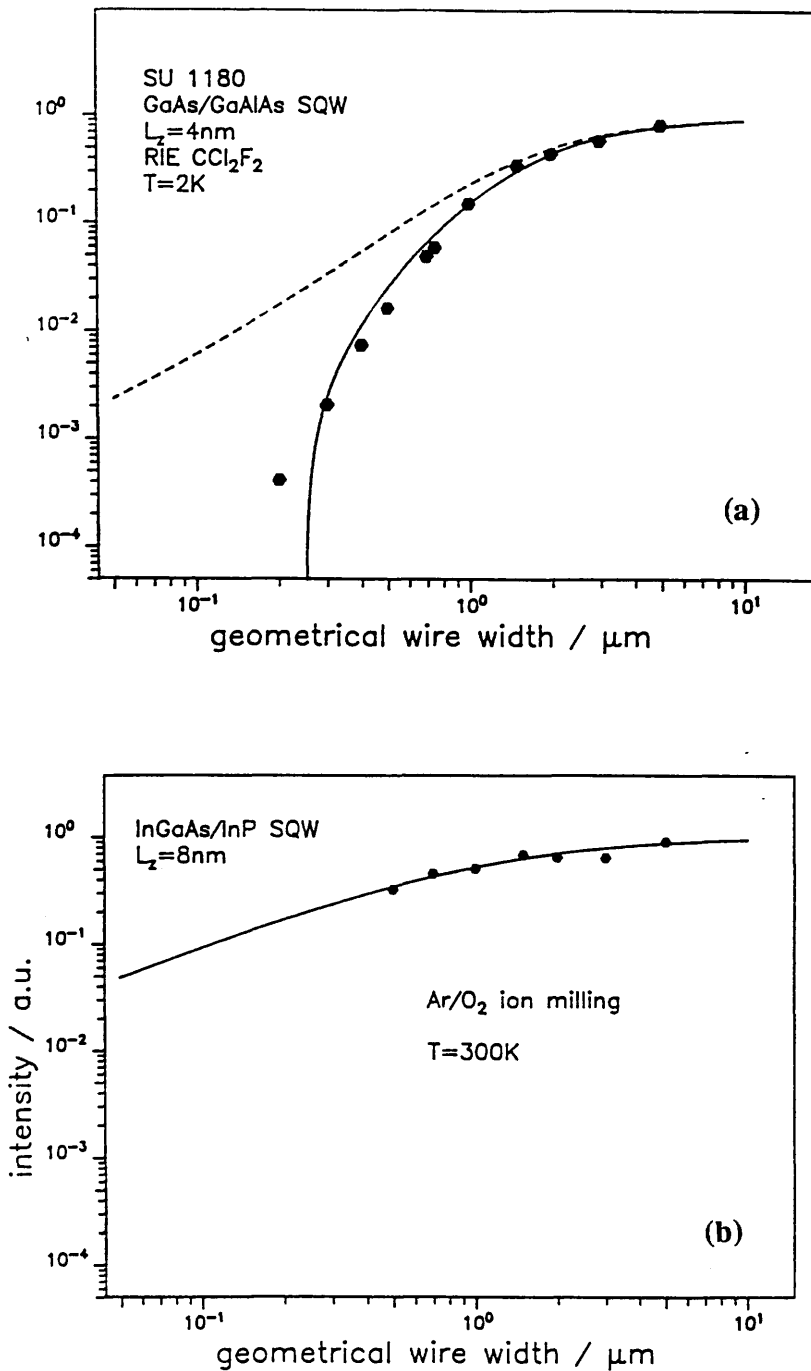


Figure 1.6 (a) PL intensity of etched GaAs/AlGaAs wires versus the wire width: broken line: experimental data calculated width dependence with a surface recombination velocity of $5 \times 10^5 \text{ cm s}^{-1}$ and no depleted surface layers; solid line - calculation including a depleted surface layer of 130 nm depth. (b) Lateral width dependence of the excitonic emission from etched InGaAs/InP wires. Broken line - experimental data; solid line - calculation using a surface recombination velocity of $5 \times 10^4 \text{ cm s}^{-1}$. (After Forchel *et al*²⁶)

polarization of the exciting radiation may significantly effect the luminescent properties of the quantum structures.

Kohl *et al*²⁷ presented the first results of quantum confinement seen in GaAs/AlGaAs quantum wire structures. These structures were fabricated using holographic lithography and reactive ion etching with SiCl₄. Interestingly they found that the PL efficiency of the active wire area was only reduced by a factor of 30 in the case of 70nm diameter wires. They attributed this to using "optimized preparation processes" which reduced the influence of the nonradiative surface recombination. The spectra were excited with normally incident light. The PLE spectra showed a blue shift of 0.2nm (0.4meV) in the hh₁₁ and lh₁₁ transitions which agreed well with the calculated value of 0.5meV. Because of this Kohl *et al* ruled out the effect of stress in the wires causing the shift. The 1D character of the transitions is manifested in a strong polarization dependence of the PLE of the wires. A magnetic field applied to the wires caused an enhancement of the reduced mass and of the exciton binding energy of the ground state hh exciton of about 15%.

1.4.1.2 Confinement achieved using ion implantation

Focussed ion beams can be used to modify the physical properties of semiconductors directly by maskless implantation or etching on the sub-100nm scale. Cibert and Petroff *et al*²⁸ used the former approach whereby carrier confinement to one and zero degrees of freedom was achieved by implantation enhanced interdiffusion of an AlGaAs/GaAs QW by Ga⁺ ions, followed by rapid thermal annealing. This removed the problem of the QD surface-air interface as implantation with the Ga⁺ ions provides an effective method for locally altering the band gap while preserving good optical quality and without introducing electrically active impurities. The carrier confinement was achieved by a built in local change in the crystal potential of the material. They reported low temperature cathodoluminescence measurements showing new luminescence lines which they attributed to transitions arising from the laterally confined states. There was little evidence of non-radiative interface recombination in the measured low temperature luminescence efficiencies. One drawback of cathodoluminescence measurements is that unlike PLE this does not mirror the absorption spectrum and shifts could occur due to the strain induced in the material by the diffusion of the Ga⁺ ions.

Leier *et al*²⁹ have also investigated this method as a means for achieving quantum confinement. Optical emission spectra of GaAs wires show two maxima, one of which is attributed to recombination in the wire sections of the sample and the other to barrier emission. As the mask width is reduced down to 40nm a wire width dependent blue shift of the wire emission up to 10meV is observed.

Although both of the above groups of researchers stated that QDs showed similar results to wires or were expected to, it is likely that it is more difficult to define a QD (a three dimensional area of undamaged material) by this diffusion process³⁰. The major problems associated with this technology are associated with obtaining the correct potential profile to achieve confinement. The lateral profile is often too flat. However this method is certainly of interest in investigating one dimensional quantization.

1.4.2 InP/InGaAs Quantum Structures

Another approach to investigate optical confinement is perhaps the most interesting and the most likely to yield the desired blue shift. Instead of using a GaAs/AlGaAs QW system, InP/InGaAs was used. This has the advantage that it offers a stable surface with a recombination velocity reduced by a factor of about 100 and consequently has very high luminescence efficiency. The exciton diameter is of the order of 30nm so that the QD diameter needed to achieve a "squeeze" on the exciton is within the limits of current processing techniques.

Temkin *et al*³¹ investigated quantum confinement in InP/InGaAs structures. The main drawback in their process was the inability to reactive ion etch the dot masks to produce free standing dots, but instead ion milling in a mixture of Argon and Oxygen was used. This is suspected to produce more damage than the RIE process. They reported that InP/InGaAs QDs down to 30nm exhibit intense low temperature photoluminescence (PL) and show the exciton shifts expected of low dimensional confinement. It has since been shown that a portion of the blue shift was related to band filling effects as they did not report that the shift was independent of the excitation intensity. They did not investigate the emission from an unpatterned mesa which was subjected to ion milling to ensure that the shift was not due to process induced damage in the material. The PL intensity from the wires was ~300 times less than the control wafer and was significantly below the filling factor of 15%. This reduction in PL intensity could be due to the surface recombination coming from the exposed InGaAs edges as in this system it is the ternary that forms the well or as a result of the ion bombardment.

Further work by Gershoni *et al*³² using a low energy (100V) ion beam was used to try and reduce this problem of process damage, and PLE measurements taken to preclude any band filling effects. They reported that transverse confinement in a quantum wire had induced exciton splitting in the optical spectrum of InP/InGaAs QW. No results of QDs were reported.

Forchel *et al*²⁶ also reported PL studies of InP/InGaAs quantum wires. The InP/InGaAs structures were etched by Ar/O₂ reactive ion beam etching (RIBE) and showed significantly smaller intensity decrease compared to GaAs/AlGaAs wires (figure 1.6). These results they suggest, were due to the different surface recombination velocities, that in InP/InGaAs possibly being much lower.

1.4.3 Quantum Dot or Wire Lasers

Perhaps one of the most useful and interesting possible application areas for quantum structures is in the manufacture of quantum dot or wire lasers. To date carrier confinement to two dimensions within the laser has been achieved by using quantum well lasers with ultra thin active layers. In quantum wells, the number of quantum states of the system is reduced due to the wavefunction quantization perpendicular to the layer plane. This reduced number of quantum states directly implies that the number of states to be inverted to reach net gain, i.e. the transparency population will be reduced as compared to the 3D Double Heterostructure laser. The square DOS in 2D leads to a more efficient use of injected carriers to create gain than in 3D: the maximum of the gain curve always lies at the bottom

QUANTUM BOX LASER

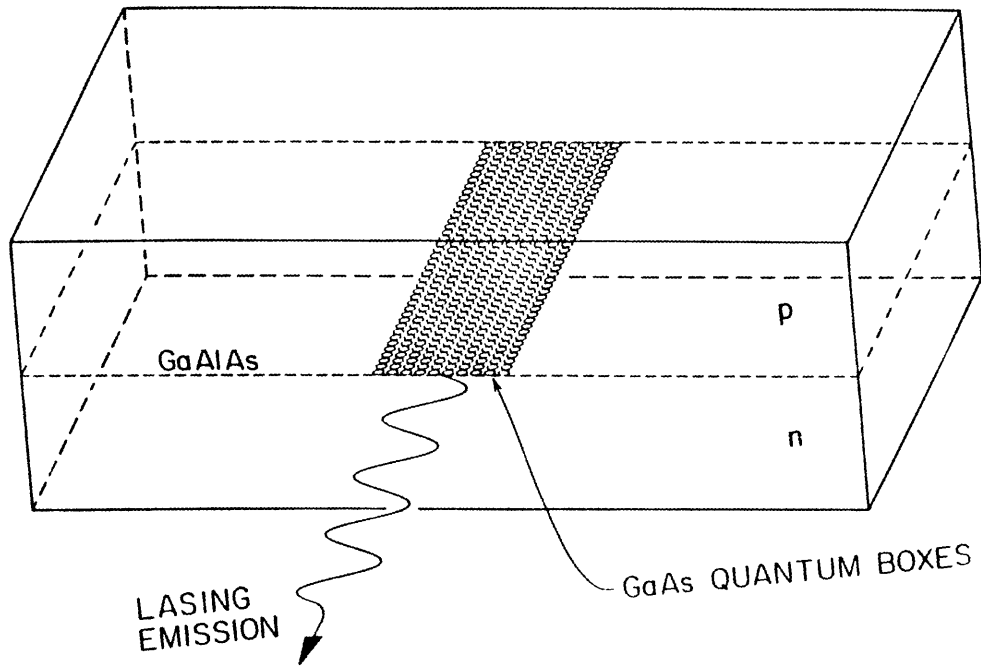


Figure 1.7 A quantum box laser in GaAs/AlGaAs system. The quantum boxes are not drawn to scale. (After Vahala³⁷)

of the quantized 2D band, instead of shifting towards higher energies due to ever increasing 3D-DOS. Therefore a larger fraction of injected carriers participate in the gain³³. These lasers have superior characteristics over the double heterostructure lasers in that they have :

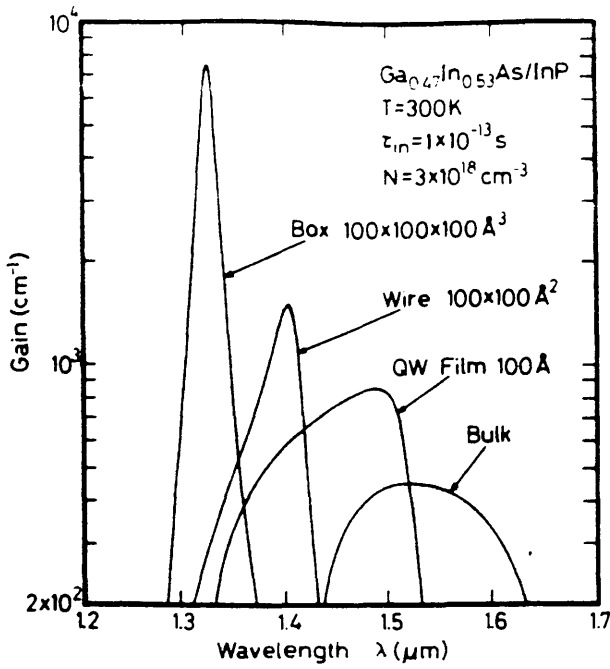
- 1) extremely low threshold current
- 2) less temperature dependence
- 3) narrow gain spectrum.

It is therefore natural to expect that using lower dimensionality structures such as quantum wires or quantum dots that will enhance the properties yet further i.e the lasers will have improved efficiency, modulation bandwidth, and temperature and frequency stability. The reduction in threshold current and hence temperature dependence helps to overcome the problem of the laser heating up when operating, as the output of the laser can vary tremendously with variation in temperature. Obviously a more stable system is desirable. Hence for future applications where high performance semiconductor lasers are required i.e. where a highly single mode and narrow field spectrum linewidths are required quantum dot or wire lasers may provide the answer.

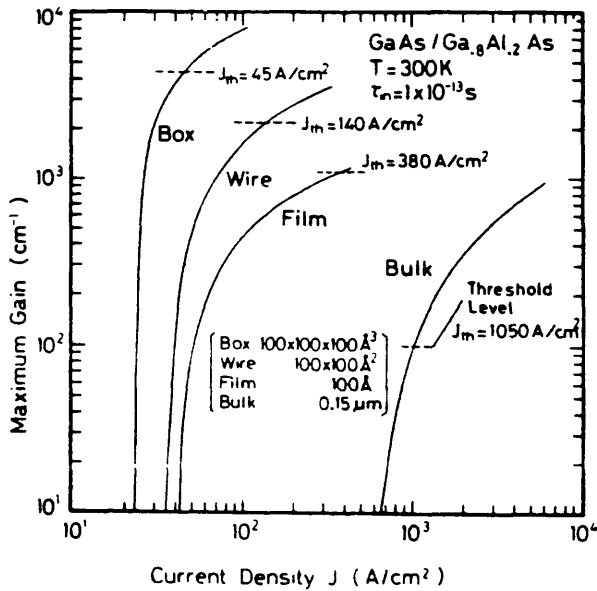
In an ideal quantum structure laser for example, the actual active layer would consist of an array of dots or wires having a characteristic size of ~10nm (ideally of the same shape and size). These structures would be fabricated from a low bandgap material and would be imbedded in a high bandgap material (e.g. GaAs in AlGaAs) (figure 1.7). Electrons and holes residing in these structures would have highly localized wave functions and the state space in each dot would be discrete as opposed to quasicontinuum of the bulk. In the ideal quantum dot laser the contribution to gain from each dot would arise from a pair of two level systems (one for each electron spin).

Asada *et al*³⁴ reported the first theoretical calculations on the expected improvement in laser performance. Calculations showed that for 10x10x10nm but still impossible to fabricate in the GaAs/AlGaAs system the gain would be increased 10 times and 15 times in the InP/InGaAs (figure 1.8) and that there would be a marked decrease in the laser threshold current (figure 1.8). The laser operation would be less temperature dependent and the gain spectrum would narrow.

Arakawa and Yariv³⁵ used magnetic fields applied to laser structures to simulate 0 and 1D confinement. By applying a magnetic field to a buried heterostructure laser they were able to simulate a quantum wire laser. In this case the electrons are only free to move in the direction of the field. The motion of these electrons is quantized in the two transverse directions (x,y) forming a series of Landau energy subbands. It was found that as the magnetic field was increased (up to 19T) the power dependent linewidth was reduced compared to the linewidth without a magnetic field. This improvement in device performance was attributed to quantum wire-like effects. Quantum dot effects were investigated by placing a GaAs/AlGaAs quantum well laser in a high magnetic field. When a magnetic field direction is normal to the quantum well plane the system becomes discrete and may be used to simulate a quantum dot laser. Evidence of the formation of full quantized effects was obtained by measuring the anisotropic properties of the spectral shift with the increase in magnetic field. Vahala *et al*³⁸ also simulated



(a)



(b)

Figure 1.8 (a) Gain spectra calculated for $\text{Ga}_{0.47}\text{In}_{0.53}\text{As}/\text{InP}$ $10 \times 10 \times 10 \text{ nm}$ cubic quantum box, $10 \times 10 \text{ nm}$ quantum wire, 10 nm thick quantum well, and bulk crystal at $T=300\text{K}$. (b) Maximum gain as a function of injection current density, calculated for $\text{GaAs}/\text{Ga}_{0.8}\text{Al}_{0.2}\text{As}$ quantum box, quantum wire, quantum well, and bulk crystal (conventional double heterostructure). Dashed line on each curve is the level of gain required for laser threshold. (After Asada et al³⁴)

quantum dot effects using this method. It was found that as the magnetic field was increased the linewidth decreased. This effect was only seen at 165K and not at room temperature. The authors attributed this to a discrete set of electronic states set up in the laser active layer.

Vahala³⁷ has raised questions as to the correctness of the theoretical predictions on the enhancement of laser performance made by Asada *et al*³⁴. In particular Vahala questions the quantum box volumetric density required to furnish a given optical gain, the limitations imposed on dot size, and the tolerances which must be maintained during fabrication. Fabrication tolerances are important as they will determine the degree to which the optical gain spectrum is inhomogeneously broadened. A quantum dot laser can be viewed as a gas laser in which the atoms are likened to the quantum dots. The overall gain spectrum produced by this gas is broadened both homogeneously by the natural linewidth of a single transition in a given dot and inhomogeneously by fabrication variations in the quantum dot sizes. Vahala predicts that there would be a two orders of magnitude gain in the threshold carrier density if the active layer was patterned into 20nm diameter quantum boxes but only if the rms roughness amplitude is held to 2nm. For larger dot sizes (~30nm diameter) he predicts that it is unlikely that the quantum dots would provide enough gain for lasing action unless they are p-doped. Smaller quantum dots (~6nm) would provide enough gain but as yet structures cannot be made this small. The larger quantum dots could be fabricated .

Miyamoto and Cao *et al*³⁸ were the first to report the fabrication of a QD laser. GaInAsP/InP quantum dot structures were fabricated from 1D QW structures grown by OMVPE by holographic lithography, wet etching and LPE regrowth. Light emission induced by current injection at the shorter wavelength than the corresponding bulk material was observed at 77K. However in this structure lasing operation was not obtained because the optical confinement factor was too small, owing to a large spacing between the quantum boxes (204nm) compared to their size (30nm). Further work by Cao *et al*³⁹ on quantum wires lasers using the same process resulted in CW lasing operation at 77K.

Miller *et al*⁴⁰ investigated the intensity-dependent PL properties at 10K of 30-40nm wide single InP/InGaAs quantum well wires grown by atmospheric pressure organometallic vapor phase epitaxy (OMPVE). The wires were fabricated by holographic photolithography and wet chemical etching and then regrown with an InP overlayer. At low laser intensities the PL shows a strong influence coming from states within the band gap which then saturate at higher intensities. An intensity-dependent shift in the PL energy coming from the wires is seen. The full width half maximum of the PL line at these higher laser intensities is less than the planar control sample, and the PL intensity from the wires as compared to the controls is higher than expected from the filling factor.

1.4.4 Electrical behaviour of Quantum Structures

The electrical behaviour of zero dimensional structures has been reported by Reed *et al*⁴¹. Electronic transport through a three dimensionally confined semiconductor double barrier resonant tunnelling structure was investigated. Fine structure was observed in resonant tunnelling through the quantum dot which corresponded to the discrete density of states of a zero dimensional system. The dot diameters were large enough (100-250nm) that any damage produced by BCl_3 RIE did not affect the conduction in

the material and the etch mask used also served as the ohmic contact, being annealed before RIE. This is the first report of electrical quantum confinement in a GaAs/AlGaAs system.

1.4.5 Summary

Kohl *et al*²⁷ have reported the first optical measurements of quantum confinement in structures as large as 60nm in GaAs/AlGaAs. Although other authors have reported results from optical measurements of quantum wires and dots none of these are conclusive. Comparison of the different reports is not straightforward since different authors use different fabrication and measurement techniques and give little indication of reproducibility. There is still the question of why quantum dots luminesce as efficiently as they do, when it is expected that surface effects would quench the luminescence.

It has been shown that enhancing the confinement in the active region of a laser should enhance device performance, but to date laser operation has only been achieved using the InP/InGaAs system and then only at liquid nitrogen temperatures.

References

- 1 (a) C Delalande and M Voos: Surf. Sci. 174 1986 pp.111 (b) M Jaros: Physics and Applications of Semiconductor Microstructures, Oxford Science Publications, Clarendon Press, 1989, see for example Appendix 2 pp. 217-219.
- 2 R Dingle, W Wiegmann and C H Henry: Phys. Rev. Lett, Vol. 33, No. 14, 1974, pp. 827.
- 3 R C Miller, D A Kleinmann, and A C Gossard: Phys. Rev. B 29 1984 pp. 7085.
- 4 D S Chemla and D A B Miller: J. Optical Soc. Am. B, Vol. 2, 1985 pp. 1155.
- 5 D S Chemla, D A B Miller and P W Smith: Optical Eng. Vol. 24, No. 4 1985 pp. 556.
- 6 H Okamoto: Jap. J. Appl. Phys. Vol. 26, No. 3 1987 pp. 315.
- 7 L Brus: J. Quantum Elect. Vol QE-22, No. 9, 1986 pp. 1909.
- 8 S Schmitt-Rink, D A B Miller and D S Chemla: Phys. Rev. B Vol. 35, No. 15, 1987 pp. 8113.
- 9 T Takagahara: Phys. Rev. B Vol. 36, No. 17, 1987 pp. 9293.
- 10 G Bryant: Phys. Rev. B Vol. 37, No. 15, 1988 pp. 8763.
- 11 W Y Wu, J N Schulmann, T Y Hsu and U Efron: Appl. Phys. Lett. 51 1987 pp 710.
- 12 E J Austin: Semicond. Sci. Technol. 3 1988 pp. 960.
- 13 R L Greene, K K Bajaj and D E Phelps: Phys. Rev. B 29 1984 pp. 1807
- 14 D A B Miller, D S Chemla and S Schmitt-Rink: Appl. Phys. Lett. 52 (25), 1988 pp. 2154.
- 15 G Bryant: Phys. Rev. B Vol. 29, No. 12 1984 pp. 6632.
- 16 G Bryant: Phys. Rev. B Vol. 31, No. 12 1985 pp. 7812.
- 17 G Bastard, C Delalande, M H Meynadier, P M Frijink and M Voos: Phys. Rev. B, Vol. 29, No. 12, 1984 pp. 7042.
- 18 J Warnock and D D Awschalom: Phys. Rev. B Vol 32, No. 8, 1985 pp. 5529.
- 19 A I Ekimov and A A Onushchenko: Sov. Phys. Semicond. 16(7), 1982 pp.775.
- 20 L Banyai and S W Koch: Phys. Rev. Lett. Vol 57, No. 21, 1986 pp. 2722.

- 21 M A Reed, R T Bate, K Bradshaw, W M Duncan, W R Frensley, J W Lee and H D Shaw: J. Vac. Sci. Technol. B4 1986 pp. 358.
- 22 K Kash, A Scherer, J M Worlock, H G Craighead and C M Tamargo: Appl. Phys. Lett. 49, 1986 pp. 1043.
- 23 K Kash, J M Worlock, M D Sturge, P Grabbe, J P Harbison, A Scherer and P S D Lin: Appl. Phys. Lett. 53, 1988 pp. 782.
- 24 K Kash, J M Worlock, D D Mahoney, A D Gozdz, B P Van der Gaag, J P Harbison, P S D Lin and L T Florez: Fourth International Conference on Modulated Semiconductor Structures, July 17-21, 1989 (to be published in Surface Science).
- 25 K Kash, J M Worlock, A D Gozdz, B P Van der Gaag, J P Harbison, P S D Lin and L T Florez: to be published in Surface Science.
- 26 A Forchel, H Leier, B Maile, and R Germann: Festkörperprobleme (Advances in Solid State Physics), Vol. 28, pp.99, Vieweg, Braunschweig 1988.
- 27 M Kohl, D Heitmann, P Grambow, and K Ploog: Phys. Rev. Lett. Vol. 63, No. 19, 1989 pp. 2124.
- 28 J Cibert, P M Petroff, G J Dolan, S J Pearton, A C Gossard and J H English: Appl. Phys. Lett. 49, 1986 pp. 1275.
- 29 H Leier, A Forchel, B E Maile, G Mayer, and J Hommel: Appl. Phys. Lett. 56 (1), Jan. 1990 pp. 48.
- 30 P M Petroff, J Cibert, A C Gossard, G J Dolan and C W Tu: J. Vac. Technol. B5 (4), 1987 pp.1204.
- 31 H Temkin, G J Dolan, M B Panish and S N G Chu: Appl. Phys. Lett. 50(7), 1987 pp. 413.
- 32 D Gershoni, H Temkin, G J Dolan, J Dunsmuir, S N G Chu and M B Panish: Appl. Phys. Lett. 53(11), 1988 pp. 995.
- 33 C Weisbuch and J Nagle: Nato Advanced Research Workshop, Eds S P Beaumont and C M Sotomayor Torres, "Science and Engineering of 1- and 0-dimensional Semiconductor Systems", Cadiz, Spain, 29th-1st April, 1989, Plenum Press, to be published.
- 34 M Asada, Y Miyamoto and Y Suematsu: J. Quantum Elect. Vol. QE-22, No. 9, 1986 pp. 1915.
- 35 Y Arakawa and A Yariv: J. Quantum. Elect., Vol. QE22, No. 9, 1986, pp. 1887.
- 36 K Vahala, Y Arakawa and A Yariv: Appl. Phys. Lett. 50 (7), 1987 pp. 365.
- 37 K Vahala: J. Quantum Elect. Vol. 24, No. 3, 1988 pp. 523.
- 38 Y Miyamoto, M Cao, Y Shingai, K Furuya, Y Suematsu, K G Ravikumar and S Arai: Jap. J. Appl. Phys. Vol. 26, No. 4, 1987 pp. L225.
- 39 M Cao, P Dsate, Y Miyamoto, Y Miyake, S Nogiwa, S Arai, K Furuya and Y Suematsu: Elec. Lett. Vol. 24, No. 13, 1988 pp. 824.
- 40 B I Miller, A Shahar, U Koren and P J Corvini: Appl. Phys. Let. 54 (2), 1989 pp. 188.
- 41 M A Reed, J N Randall, R J Aggarwal, R J Matyi, T M Moore, and A E Wetsel: Phys. Rev. Lett. Vol. 60, No. 6, 1988 pp. 535.

Chapter 2

Mask Fabrication

2.1 Introduction

To investigate quantum confinement to 1 and 0 degrees of freedom it is necessary to pattern QW material into quantum dot or wire structures. The first step in achieving this, is to pattern an etch mask onto the surface of the QW material using electron beam lithography.

Lithography is the process of transferring patterns of geometric shapes to a thin layer of radiation-sensitive material (called resist) covering the surface of a semiconductor wafer. The resist patterns defined by the lithographic process are not permanent elements of the final device but only replicas of the device features. To produce the features, these resist patterns must be transferred once more to the underlying layers comprising the device.

The size of pattern that can be transferred to resist is determined by the resolution capabilities of the exposure system used and the resist characteristics. Resolution means the smallest achievable linewidth under ideal exposure conditions. Optical lithography is the standard tool used in the semiconductor industry. Here the resist is exposed using ultraviolet light. There are several types of optical exposure techniques - for example contact printing, proximity printing and projection printing. Contact printing has a typical resolution of $\sim 0.5\mu\text{m}$ linewidth¹. However to enable quantum effects to be studied the lithographic system used needs to have a resolution of $\sim 10\text{nm}$ and only electron beam lithography can achieve this.

2.2 Electron Beam Lithography

Electron beam lithography uses a focussed beam of electrons to expose the resist. Figure 2.1 shows a schematic of the electron beam machine used for this work - a modified Philips PSEM 500 scanning electron microscope. The electrons are generated in an electron gun containing a tungsten thermionic-emission cathode as an electron source. Magnetic lenses are used to focus the electron beam to a spot which can vary from 8nm to $0.5\mu\text{m}$ in diameter. The accelerating voltage can be varied from 1.5kV to 50kV. Beam-blanking plates deflect the beam on to the objective aperture to prevent exposure of the specimen, and beam deflection coils are computer controlled to direct the focussed beam to any location

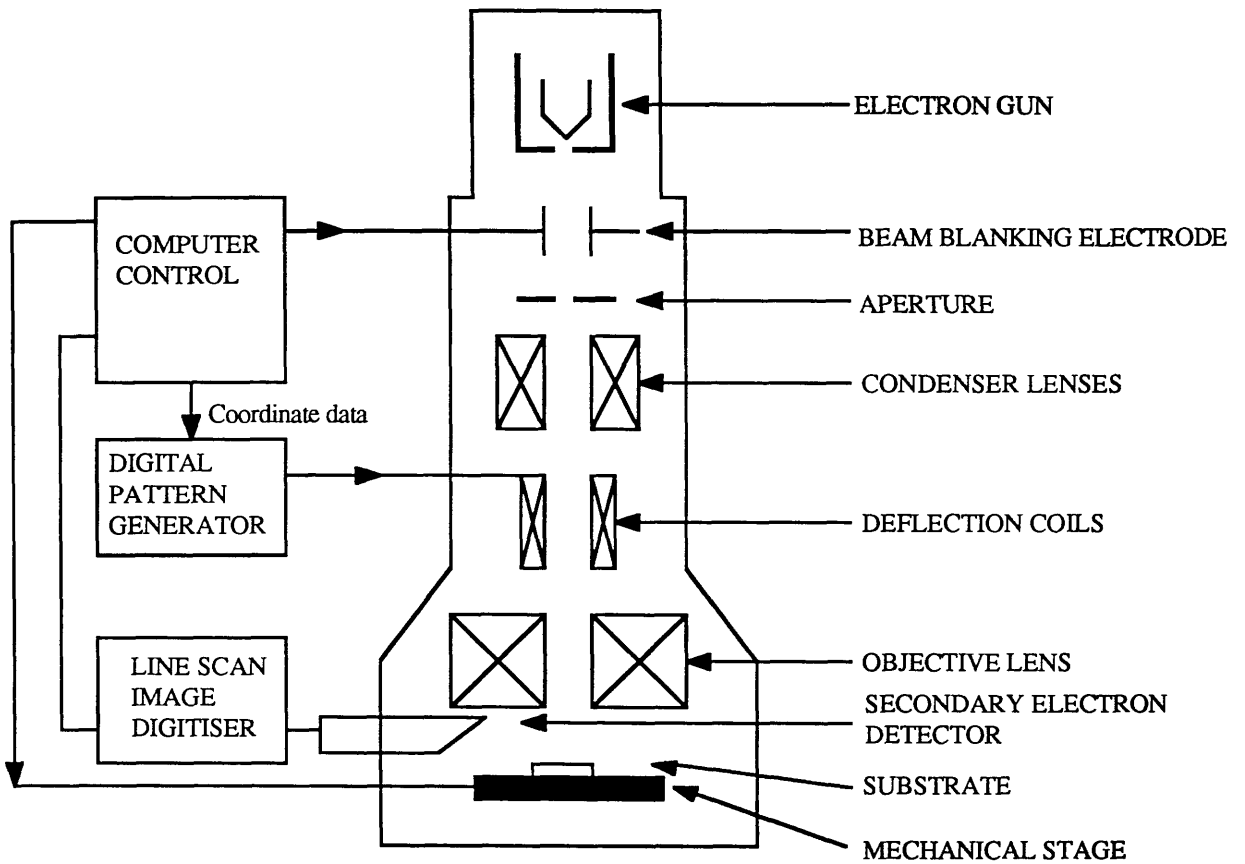


Figure 2.1 The Glasgow Electron-beam Lithographic System

in the scan field on the substrate. Because the scan field (i.e the area over which the beam can be deflected) is usually small (less than 1cm) due to lens and detector aberrations, a precision mechanical stage is used to position the substrate to be patterned.

2.3 The Proximity Effect

In optical lithography, the resolution is limited fundamentally by diffraction of light. In electron beam lithography, the resolution is not limited by diffraction (because the wavelengths associated with electrons of a few kV and higher energies are less than 1Å) but by electron scattering². When a tightly focussed beam of electrons hits a solid material, it is scattered both elastically and inelastically. The elastic collisions change only the direction of the electrons while in the inelastic collisions, energy is exchanged with the material and secondary electrons are formed. The secondary electrons are vital as it is they that expose the resist. The incident electrons will spread out as they penetrate the solid until all their energy is lost or they leave the surface after back scattering interactions³. The back scattered electrons limit the resolution of the pattern transfer process when using thin resist layers.

The back scattered electrons arise when the high energy incident electrons strike the substrate colliding elastically with the nuclei causing them to undergo large-angle scattering as they slowly lose energy. Some of the electrons scatter back into the resist outside the regions exposed by the beam and this results in a background exposure that reduces image contrast. In the regions where the exposed patterns are dense i.e. in the dot or wire areas, the back scattered electrons increase the overall exposure.

The proximity effect therefore is caused by the exposure at one point depending upon the exposure of adjacent points and it places a limit on the minimum separation between pattern features. The most usual technique for compensating for this effect is to vary the dose for each shape so that the average exposure for every shape is the same. For a complex integrated circuit pattern, the calculation required to determine the dose for each shape is very large⁴. However it proved unnecessary to perform proximity effect correction calculations when exposing small areas of dots or wires as the overall dose is simply reduced.

To reduce the problems due to the proximity effect a high beam voltage is used. By raising the beam voltage to 50kV or greater the exposure due to the proximity effect is reduced more as the centre of diffusion for the backscattered electrons is displaced further away from the surface.

2.4 Electron Beam Resists

Electron resists are commonly polymers. When an electron resist is exposed to a beam of electrons, a chemical change is induced in the resist by radiation. This change allows the resist to be patterned. The incident beam of electrons causes a change in the molecular structure of the polymer in the areas of the resist exposed to the beam. It is important to understand all the factors affecting the exposure and development of a resist because in electron beam lithography it is often limitations of the resist itself, and not those of the exposure system, that set the ultimate limit on pattern resolution.

A standard method for assessing resists is by the exposure response curve or contrast curve. It describes the thickness of the resist remaining after exposure and development versus the exposure energy and is described in detail by S R Rishton⁵. It enables the sensitivity and contrast of a resist to be ascertained. The sensitivity of a positive resist is the minimum electron dose required to completely clear out an exposed area when it is developed. Contrast is a measure of how sharply the resist changes from being under-exposed to fully exposed and cleared out when developed. A high contrast will produce sharper images.

An ideal electron resist should have high sensitivity, high contrast, high resolution and high etch resistance. A high-sensitivity resist will require a low input dose and therefore a short exposure time. For conventional organic polymer resists, which use solution development to create relief images, a high sensitivity is usually correlated with large molecular weights. Smaller molecule sizes will give better resolution but also lower sensitivity².

A high contrast resist should have a narrow molecular weight distribution (before exposure) and a sharp transition in a plot of final resist thickness (after development) versus exposure dose. The resist and its developer must be considered as a composite system in discussing contrast. Changes in developer concentration of a few percent or in temperature by a few degrees, can affect resolution and reproducibility².

When a resist mask is to be used as an etch mask it must provide a high etch resistance for the subsequent pattern transfer to the underlying substrate. Any resist erosion at the edges during pattern transfer will affect the final feature width. Resist thickness also directly affects the resolution capabilities of the system. Wilkinson and Beaumont³ showed that for a thinner resist the linewidth due to the forward scattered electrons is reduced decreasing the minimum possible feature size.

2.4.1 Positive Resist Process for Mask Fabrication

When a positive resist is exposed to an electron beam, the polymer-electron interaction causes chemical bonds to be broken (chain scission) to form shorter molecular fragments. As a result the molecular weight is reduced in the irradiated area⁶. The irradiated area can be dissolved in a developer solution that removes the low-molecular weight material and leaves a resist stencil on the substrate. This resist stencil can either be used directly as an etch mask or to enable metal to be patterned onto the substrate. A common positive electron resist is poly(methyl methacrylate), called PMMA⁷.

Cleaning The sample to be coated with resist is first cleaned by immersion and agitation in an ultrasonic bath with trichloroethylene, methanol, acetone and finally with isopropylalcohol and blown dry using nitrogen.

Spin Coating The resist is spin coated onto the substrate. This produces a thin, uniform, adherent, homogeneous film over the wafer. It is accomplished by flooding the substrate with a polymer solution and rotating it at a constant speed (1000-8000rpm) until the solvent has evaporated. The sample is then baked to remove any traces of the solvent.

Exposure A two layer polymethylmethacrylate (PMMA) resist system consists of a lower molecular weight PMMA beneath a second layer of high molecular weight PMMA. The upper layer is less sensitive to the electron beam than the lower layer because more chain scissions are required to break each molecule into sections small enough to be dissolved by the developer⁸. A larger area of the lower molecular weight resist is therefore affected on exposure. For the desired resolution to be achieved a thin resist was used i.e. there was a very small percentage (2.5%) of PMMA dissolved in the casting solvent. The resists used were a solution of 2.5% BDH in chlorobenzene with a molecular weight of 185 000 as the lower layer and a solution of 2.5% Elvacite in xylene with a molecular weight of 350 000 as the upper layer giving a combined thickness of 100nm.

Development The developer preferentially removes those areas of the polymer where chain scission has occurred because the solvent will only dissolve a polymer below a certain molecular weight. As a larger area in the lower layer is affected this results in an enhanced undercut profile (shown in figure 2.2) compared to a single layer of PMMA. The contrast of the PMMA varies with the developer. It is lower with stronger developers so it was therefore desirable to dilute the developer with a non-solvent to increase the resolution. The developers used in this work were mixtures of propan-2-ol (IPA), a nonsolvent of PMMA and 4-methylpentan-2- one (MIBK) a weak solvent.

Evaporation The resist stencil is used to pattern the substrate with a metal layer. The metal used was Nichrome or Titanium as both have a small grain size for high pattern resolution. NiCr is used with SiCl_4 etching and Ti when the gas is CH_4/H_2 as each metal has a low sputtering rate with the respective gases but a high sputter rate with the other. The etch ratio of NiCr:GaAs in SiCl_4 is >50:1 and Ti:GaAs in CH_4/H_2 >20:1.

Lift-off Soaking in room temperature or warm acetone dissolves the remaining resist and only metal deposited directly on the substrate remains. For lift-off to be successful, the resist solvent must be able to penetrate into the resist, and it is therefore desirable that the metal on the substrate is not connected to the metal on the resist. The undercut profile obtained using the two layer resist scheme achieves this. When the metal is deposited in a collimated beam with the sample at right angles to the beam, it results in the metal on the substrate being the size of the dot or wire in the upper PMMA layer, and space being left around the metal feature stuck to the substrate (figure 2.2). This then enables the solvent to penetrate the resist layers and for successful lift-off. The thickness of metal evaporated must not be thicker than the resist otherwise a continuous coating is formed and lift-off fails.

2.4.2 Positive Resist Process Steps

- 1) Spin 2.5% BDH in Chlorobenzene at 6000rpm and bake at 180°C for 30 minutes.
Spin 2.5% Elvacite in xylene at 8000rpm and bake at 180°C for 90 minutes.
- 2) Expose pattern then develop in 1:3 MIBK:IPA for 40 seconds at 23°C and then rinse with IPA.
- 3) Evaporate 20nm of metal.

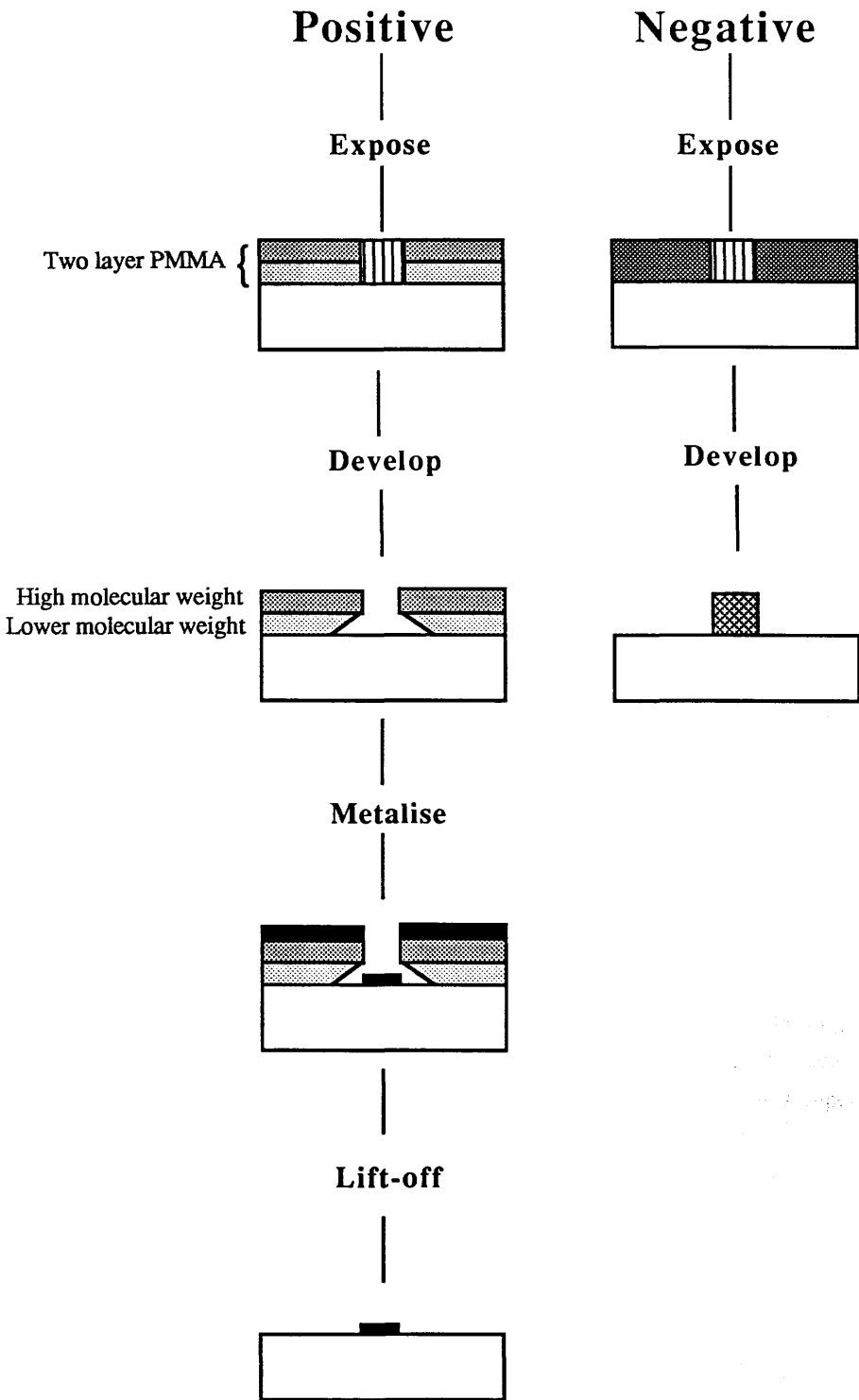


Figure 2.2 Positive and negative mask fabrication process

4) Lift-off in acetone for 30 minutes. Rinse in IPA.

2.4.3 Negative Resist Process for Mask Fabrication

In a negative electron resist, the irradiation causes radiation-induced polymer linking. The crosslinking creates a complex three dimensional structure with a higher molecular weight than that of the nonirradiated polymer⁶. The nonirradiated resist can be dissolved in a developer solution that does not remove the high molecular weight material (figure 2.2). One major drawback of a negative resist is that in the development process the whole resist mass swells by absorbing developer solvent. This swelling action limits the resolution of negative resists. Negative resists are usually more sensitive than positive resists but they generally exhibit lower contrast³. They are more resistant to dry etching and have better adhesion. The negative resist can be used as an etch mask directly without the need for evaporating metal. It also offers a further advantage in that it can be removed completely after processing using an oxygen plasma. Examples of negative electron resists are High Resolution Negative Resist (HRN) and α M-CMS⁹. S Thoms *et al*^{10,11} showed it was possible to use HRN to produce structures with dimensions in the 40nm range. Resist concentrations of 4% and 8% HRN in Microposit thinner were used giving a resist thickness of 120 and 280nm respectively.

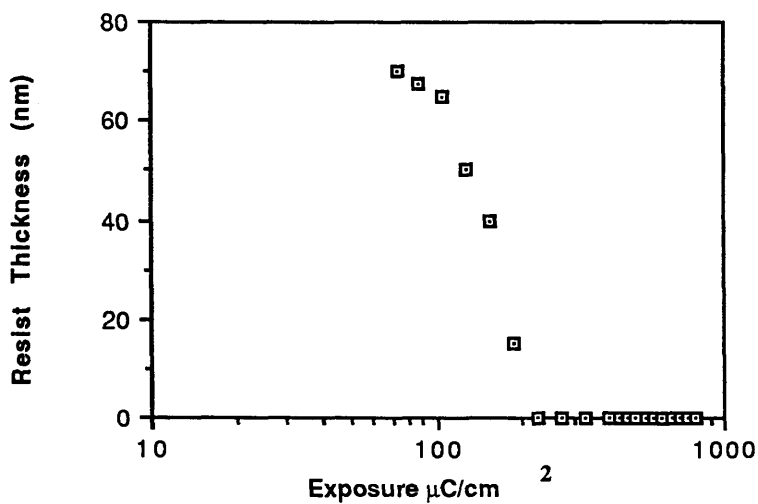
Previously it had been difficult to produce negative resists that could offer high enough contrast to be used as an electron resist. However polystyrene had been shown to have sufficient contrast to be promising and an added advantage of resistance to plasma etching. Unfortunately it also had a low sensitivity. Whipps¹² found that by using a copolymer of styrene with a compound containing an electron active crosslinking group such as p-chlorostyrene, improved sensitivity to an electron beam resulted, while maintaining the desirable properties of polystyrene such as plasma etch resistance. Two negative acting electron resists were available - HSN and HRN, both based on a copolymer of styrene with p-chlorostyrene (80:20)¹³. The difference lies in their molecular weights HSN is higher (90000) than HRN (11000) and therefore has a higher sensitivity but poorer contrast. HRN is therefore a better electron resist for high resolution applications. It was also shown that swelling of the resist on development, a problem generally associated with negative resists, did not occur to a significant extent¹³. It was thought that this because the radiation-induced cross-links appeared to bind the polymer chains closer together and reduce the possibility of solvent inclusion.

2.4.4 Negative Resist Process Steps

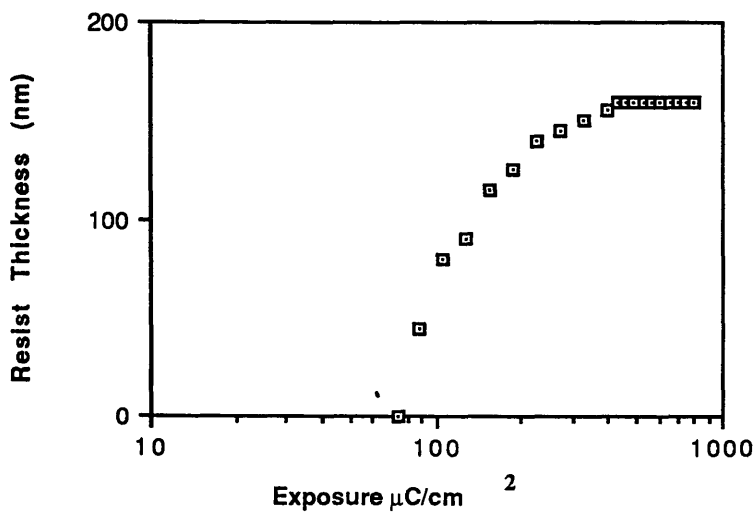
- 1) Spin coat 8% HRN at 7000rpm and bake at 120°C for 20 minutes.
- 2) Expose, and after develop for 15 seconds in MIBK then 15 seconds in IPA twice. This process was found to give optimum clearing of the undeveloped material¹⁴.

2.4.5 Comparison of the Positive and Negative Resist Processes.

The exposure response curves for 100nm thick PMMA and 280nm thick HRN are shown in figure 2.3. As expected the contrast of the positive PMMA (4.16) is better than that of the negative HRN (1.6).



(a)



(b)

Figure 2.3 Exposure response curves for a) 2.5% two layer PMMA and b) 8% HRN using a 50keV electron beam on a GaAs substrate.

This suggests that where a high packing density for quantum structures is desired the positive resist system would be better, as it will be possible to expose the structures closer together. The sensitivity of HRN is similar to that of PMMA ($106\mu\text{Ccm}^{-2}$), which is surprising as negative electron resists normally have a higher sensitivity than positive. It follows that for ultimate resolution PMMA is the better resist, but the resolution attainable with HRN is more than adequate for many applications. The two layer PMMA system has the advantage that it can give higher resolution than is possible with HRN as the contrast is better. However the metal mask is difficult to remove as the sample must be boiled in Hydrochloric acid (HCl). This process is not possible if GaAs/AlGaAs material is used as it not only removes the Nichrome but also removes the AlGaAs.

It is quicker to produce etch masks using the HRN system as fewer process steps are involved. It is advantageous in optical experiments as it is organic and is therefore transparent to light. It can also be easily removed by oxygen plasma etching for 30 minutes. Its main disadvantage is that it etches more quickly relative to GaAs than NiCr or Ti (about 10:1 as opposed to 50:1).

Due to early results from Photoluminescence measurements on QDs patterned in GaAs/AlGaAs QW material it was decided that although 4% (120nm thick) HRN, seemed to be a resistant etch mask, it was too thin and the ions bombarding the sample either passed through the mask itself or defects in the mask degrading the quality of the quantum wells beneath. 8% HRN was used instead - more than doubling the initial resist thickness from 120nm to 280nm. A comparison of resist thickness after etching in different gases is shown in Table I. By moving to a thicker resist the resolution limit of the dot diameter was increased from 40nm to 60nm.

2.5 Exposure of Dot Patterns

2.5.1 Pattern Design and Exposure Data

An array of dots is scanned by simply stepping and repeating one dot over an area. The individual dots are scanned as rectangles. The exposure for each dot i.e. the length of time the beam dwells on an area is also contained in the pattern data, as well as the distance between each dot in the X and Y direction and the number of times a dot is drawn in the X and Y direction. For example:

Exposure Data for a typical Quantum Dot Pattern

The pitch between the dots in the X then Y direction.	0 2 4 2									
The exposure value for each dot	<table border="0" style="margin-left: auto; margin-right: auto;"> <tr> <td style="border: 1px solid black; border-radius: 50%; padding: 2px 10px;">25</td> <td style="border: 1px solid black; border-radius: 50%; padding: 2px 10px;">33</td> <td style="padding: 0 10px;">160</td> <td style="border: 1px solid black; border-radius: 50%; padding: 2px 10px;">125</td> </tr> <tr> <td style="padding: 0 10px;">0</td> <td style="border: 1px solid black; border-radius: 50%; padding: 2px 10px;">750</td> <td style="padding: 0 10px;">1</td> <td style="padding: 0 10px;">0</td> </tr> </table>	25	33	160	125	0	750	1	0	The number of dots in the array in X then Y direction.
25	33	160	125							
0	750	1	0							
The starting coordinates of the quantum dot.	<table border="0" style="margin-left: auto; margin-right: auto;"> <tr> <td style="border: 1px solid black; border-radius: 50%; padding: 2px 10px;">1</td> <td style="border: 1px solid black; border-radius: 50%; padding: 2px 10px;">1</td> <td style="padding: 0 10px;">5</td> <td style="border: 1px solid black; border-radius: 50%; padding: 2px 10px;">5</td> </tr> <tr> <td style="padding: 0 10px;">0</td> <td style="padding: 0 10px;">0</td> <td style="padding: 0 10px;">0</td> <td style="padding: 0 10px;">0</td> </tr> </table>	1	1	5	5	0	0	0	0	The end coordinates of the quantum dot.
1	1	5	5							
0	0	0	0							

TABLE I

RESIST THICKNESS

Resist Thickness	8% HRN	4% HRN
Before processing	280nm	120nm
After SiCl ₄ RIE (etch depth 0.5μm)	120nm	40nm
After CH ₄ /H ₂ RIE (etch depth 400Å)	220nm	60nm

This would scan a total of 20000 dots, 4 by 4 pixels in size, 25 pixels apart in the X direction and 33 in the Y with an exposure of $750\mu\text{Ccm}^{-2}$ per pixel.

The size of the dots is limited by the resolution of the resist, the beam diameter and also the speed at which the scan generator can blank the beam. Improvements to the scan generator enabled single pixel dots to be exposed. A thin positive or negative resist was used as described in Section 2.4 and a spot size of 8nm for the smallest dots and 16nm for the larger. When a larger spot size is used the beam current is increased and the length of time taken to expose a pattern is reduced. Therefore the three factors which can be varied are:

- 1) the dot size (i.e. the number of pixels scanned)
- 2) the pitch between the dots
- 3) the exposure.

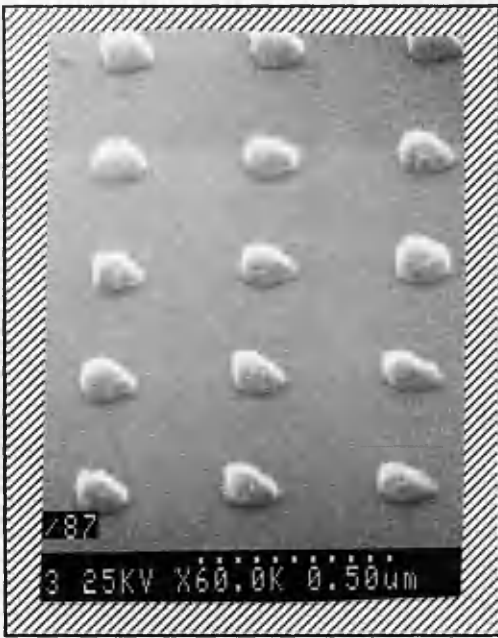
The main aim was to be able to consistently produce a specific size of dot and the smallest dot possible within the limits of the resist system used. The pitch between the dots (centre to centre spacing) is less important as a greater number of dots in an area should not affect the physical effects seen. However as a reduction in the pitch creates problems of overexposure due to the Proximity Effect (Section 2.3), the distance between the dots was large enough that this problem could be ignored i.e. a pitch either 3 or 5 times the dot diameter for HRN masks and a pitch 2 or 4 times the dot diameter for NiCr masks.

60nm and 100nm patterns were scanned using a $25\mu\text{m}\times 19\mu\text{m}$ frame size and a 8nm spot. A pixel is one point that can be addressed by the scan generator. Each dot consists of an array of pixels each one of which is scanned by the beam. There are 4096×4096 points in each frame. The pixel size is determined by dividing the frame size by the number of points in each frame. Therefore a frame size of $25\times 19\mu\text{m}$ has a pixel size of 6.1nm in the X and 4.64nm in the Y direction. The smaller the frame size the smaller the pixel size and hence the higher the resolution. 250nm dots were scanned using a $100\mu\text{m}\times 76\mu\text{m}$ frame and a 16nm spot. There was no need to use high resolution frame and spot size for such large structures. If a direct conversion from desired dot size to number of pixels was made, the resulting dots were larger than required, so a reduced number of pixels was scanned.

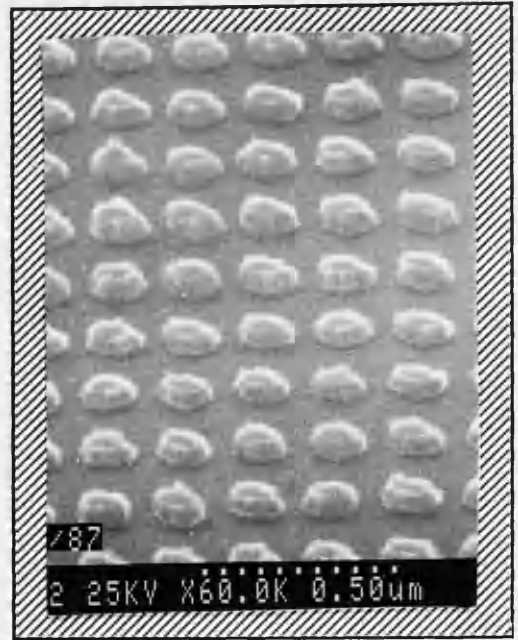
2.5.2 Results

Nichrome and Titanium dot masks 40nm, 60nm 100nm and 250nm in diameter can be routinely achieved using the two layer positive resist scheme outlined in Section 2.4.3 (figure 2.4).

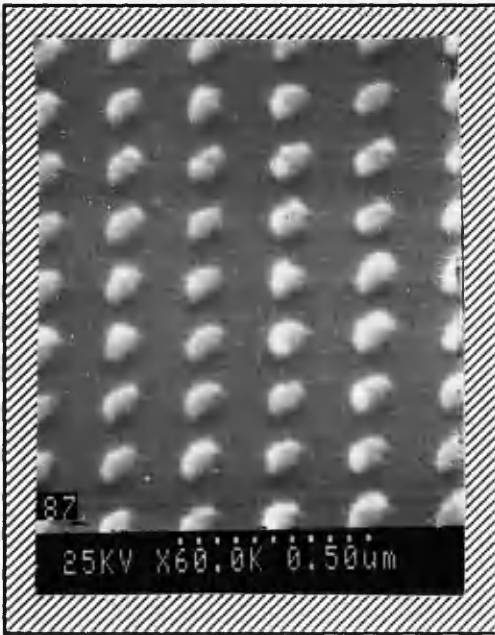
HRN dot masks 60-70nm, 100nm, 250nm and 500nm in diameter are routinely achieved (figure 2.5). When it was tried to expose single pixel dots in HRN the dwell time needed to cross link the resist was too high i.e. beyond the capability of the scan generator. 3×3 pixel dots are the smallest rectangles that can be exposed successfully. The exposure parameters for both positive and negative resists are given in Table II.



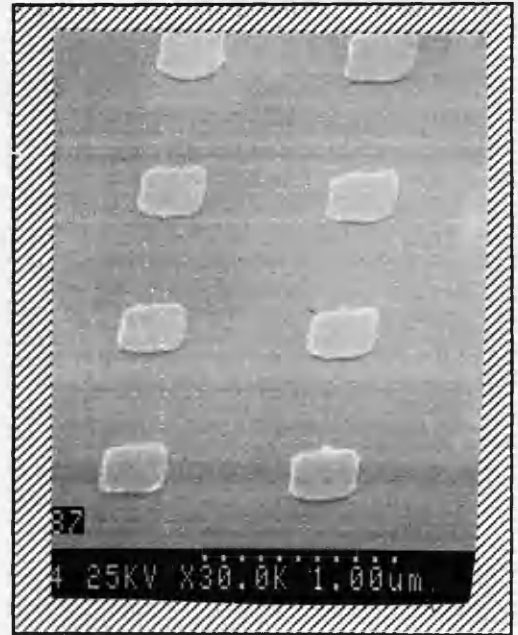
(a)



(b)

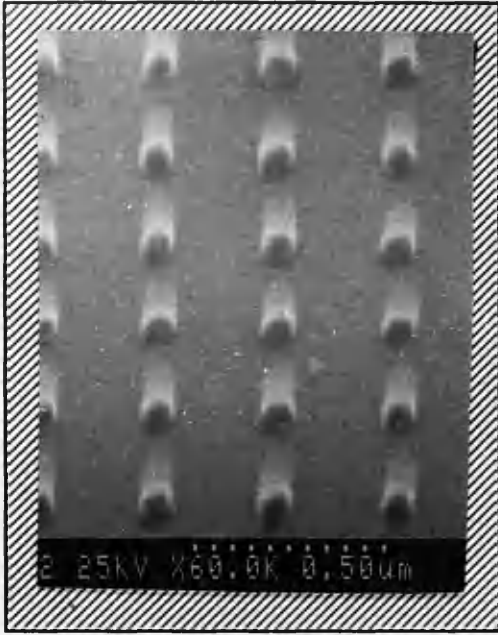


(c)

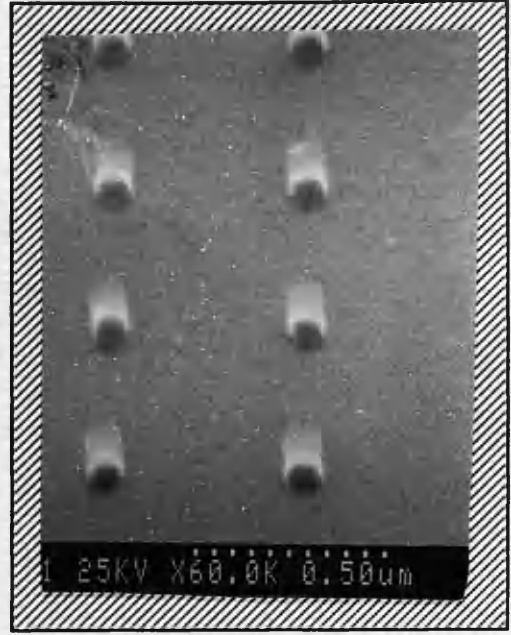


(d)

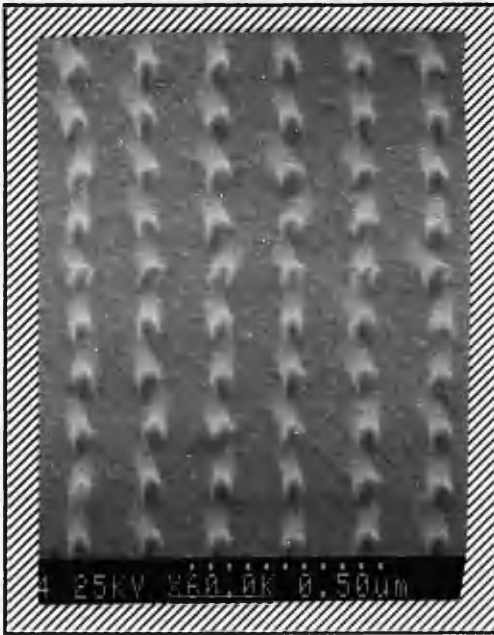
Figure 2.4 Quantum dot 20nm thick Nichrome etch masks with diameter a) 100nm on 200nm pitch b) 100nm on 400nm pitch c) 60nm on 200nm pitch and d) 300nm on 1000nm pitch.



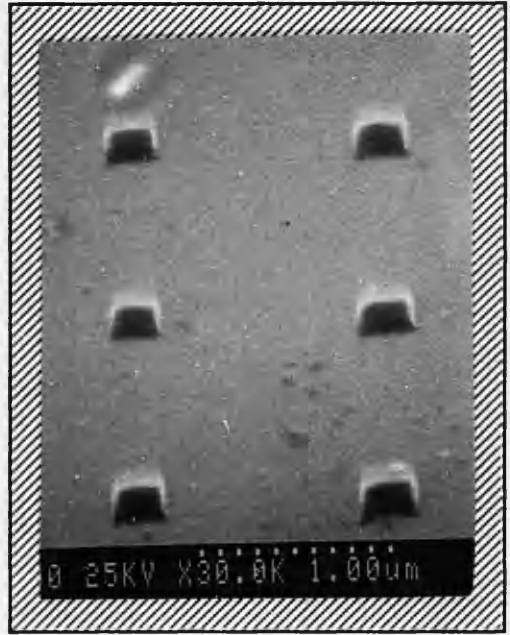
(a)



(b)



(c)



(d)

Figure 2.5 Quantum dot 250nm thick HRN etch masks with diameter a) 100nm on 300nm pitch b) 100nm on 500nm pitch c) 50nm on 200nm pitch and d) 300nm on 1000nm pitch.

TABLE II
EXPOSURE PARAMETERS FOR DOTS

DOT Diameter	MAG	SPOT SIZE	POSITIVE RESIST			NEGATIVE RESIST		
			rectangle size(pixels)	PITCH (pixels)	EXPOSURE ($\mu\text{C}/\text{cm}^2$)	rectangle size(pixels)	PITCH (pixels)	EXPOSURE ($\mu\text{C}/\text{cm}^2$)
60nm	5000	8nm	3x3	33x44	4000	4x4	50x65	9000
100nm	5000	8nm	9x11	66x87	2000	9x12	82x108	2000
250nm	1250	16nm	9x11	41x54	3000	7x12	52x66	2000
500nm	1250	16nm	-	-	-	15x25	49x37	2000

2.6 Exposure of Wire Patterns

Quantum wire array (or grating) resist etch masks can be obtained using either positive or negative resists. When a negative resist is used the area exposed to the beam forms the mask. When a positive resist is used the area not exposed to the beam forms the mask.

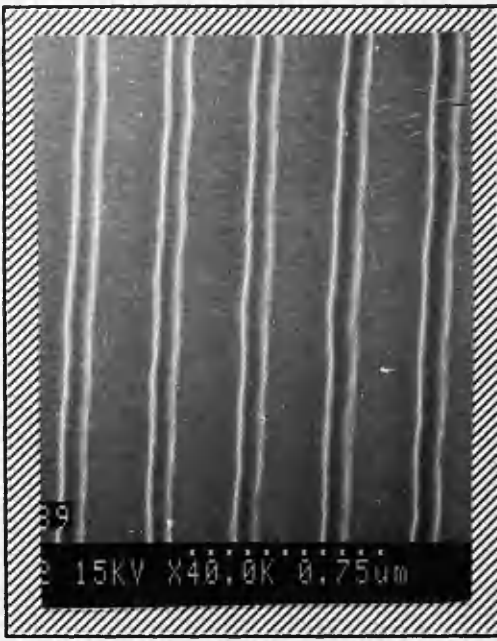
2.6.1 Exposure of Negative Resist Wire Masks

The negative resist masks were exposed using the modified Philips PSEM-500 scanning electron microscope with a 16nm spot size and a 50kV beam. The 100 μ m by 76 μ m frame size was used. This enabled wires 100 μ m in length to be exposed without the need for the stitching together of smaller frames. Two different sets of patterns were designed. In the first the pitch was kept constant and in the second the filling factor. The filling factor is the percentage of material left after processing. If it is to be kept constant the pitch between the wires must be reduced as the wire width is reduced. The scan data was generated using the matrix option in the "Design" program (original version written by W S Mackie⁹ and updated by S Thoms). Grating patterns could be routinely exposed with wire widths of 75nm, 100nm, 200nm, 300nm and 400nm routinely achievable (figure 2.6). A summary of the exposure data is given in Table III.

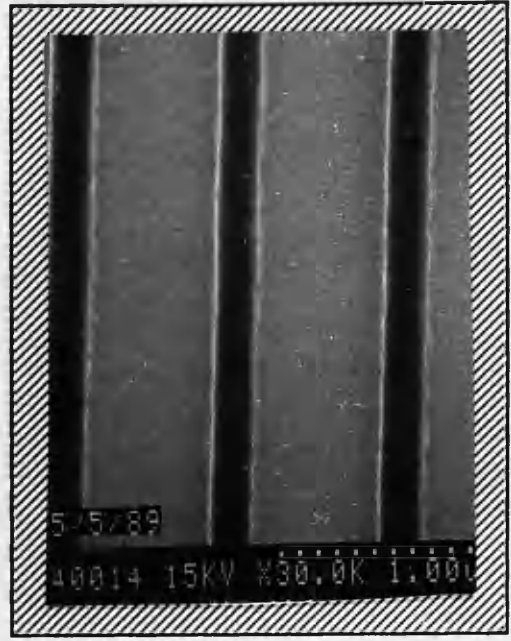
2.6.2 Exposure of Positive Resist Wire Masks

To investigate the density of state (DOS) in a 1D system quantum wires were fabricated in a two dimensional electron gas system formed in a modulation doped GaAs/AlGaAs heterostructure. In a quantum wire the electron motion is confined in two directions to a width comparable to the Fermi wavelength but smaller than the inelastic scattering length. Electron energies are quantized in the confined directions producing a dramatic change in their physical properties. The confinement scheme relies on the fact that the removal of the GaAs cap depletes the two dimensional electron gas (2DEG) beneath. To do this reactive ion etching is used. Hence a 1DES can be obtained by structuring the GaAs capping layer into very narrow lines or wires. Capacitance measurements verified that quantization had been achieved. This work was carried out at IBM Thomas J Watson Research Centre, Yorktown Heights, New York. The quantum wires were fabricated by myself and the capacitance measurements were performed by T P Smith III. Further details of the results can be obtained from references 15-17.

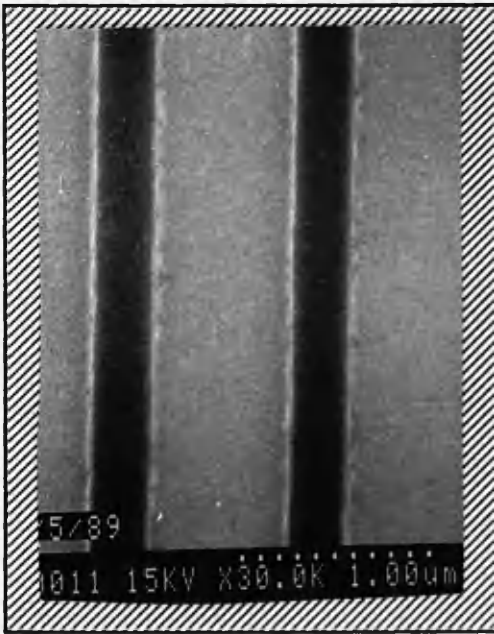
The positive resist masks were exposed using the IBM VS-6 system. Wires 100, 200 300 and 400nm and periods of 200, 400, 600 and 800nm, respectively, were written into 100nm thick PMMA [molecular weight 360 000] with a 50pA beam of 25keV electrons in a 250x250 μ m fields using a high-resolution electron beam pattern generator¹⁸. Figure 2.7 shows 300nm lines on a 600nm pitch. An averaging process was used to produce extremely smooth, regular lines¹⁹. The developed resist layer was used as the stencil for the subsequent reactive ion etching step. By using a positive resist, the higher contrast enabled a smaller pitch to be obtained than would have been possible with a negative resist. This was desirable as in these structures the confinement was achieved by introducing a potential variation in the 2DEG and by using an equal spacing between wires to wire width ratio, a



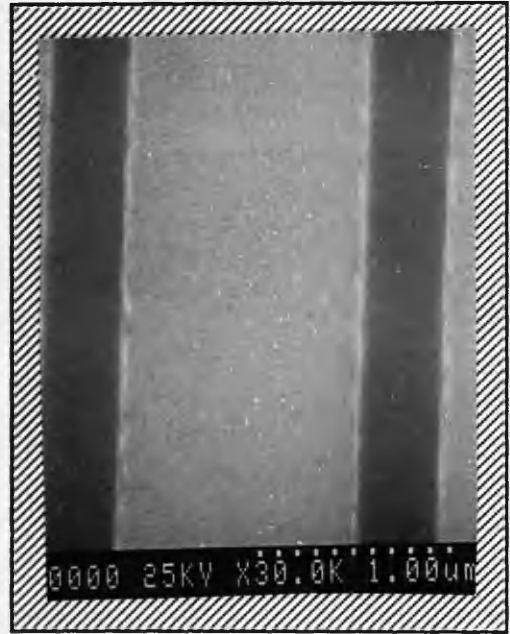
(a)



(b)



(c)



(d)

Figure 2.6 Quantum wire 250nm thick HRN etch masks with diameter a) 75nm on 300nm pitch b) 200nm on 900nm pitch c) 300nm on 1.1 μ m pitch and d) 400nm on 1.64 μ m pitch.

TABLE III**EXPOSURE PARAMETERS FOR GRATINGS ON NEGATIVE RESIST**

WIRE DIAMETER (nm)	Constant filling factor = 0.25		Constant Pitch = 1000nm
	PITCH (nm)	EXPOSURE $\mu\text{C}/\text{cm}^2$	EXPOSURE ($\mu\text{C}/\text{cm}^2$)
75	300	500	1000
100	400	375	750
200	800	380	450
300	1200	380	350
400	1580	380	275

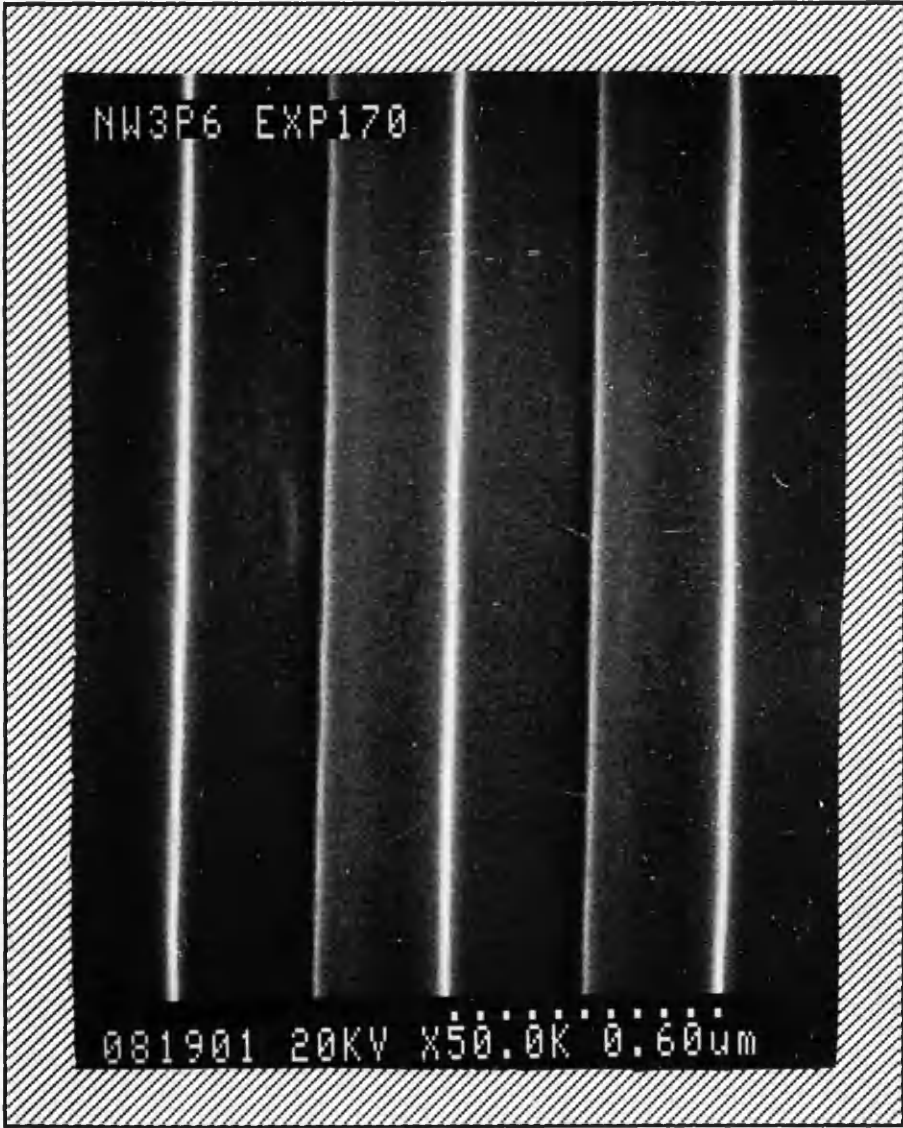


Figure 2.7 300nm wires on 600nm pitch exposed in single layer PMMA on GaAs

smooth potential would be obtained leading to better confinement. Uniformity is also extremely important as any variations would smear out the potential. As positive resists do not suffer from swelling on development as do negative resists the wire profile is less likely to vary.

2.7 Sample Design for Optical Spectroscopy

2.7.1 Design and Fabrication of Alignment Marks

To enable the photoluminescence signal from quantum dots and wires to be measured and comparisons made between different sizes of structures, the dots and wires were exposed in a square area in the centre of an alignment window. This helped to locate the dots when viewing the sample in a low temperature optical cryostat. An area $100 \times 100 \mu\text{m}$ is difficult to see on a sample, even with some optical magnification, without any other marks as a reference point. Several designs for this alignment window have been used. The basic design requirement is shown in figure 2.8. It was necessary to have many windows (8 - 12) so several different dot and wire sizes could be exposed on the sample for comparison purposes. It is also extremely important to expose square areas of unpatterned material to act as a control. It is not enough to use another piece of material to give a control signal. While this would give information on the peak positions due to the quantum well width, it would not enable a comparison of relative intensities to be made between patterned and unpatterned areas. It is necessary to know the exact area of quantum well material being excited. It is also important that the unprocessed areas should be subjected to the same process procedures so effects due to processing can be assessed. These areas of unpatterned material or mesas were exposed as large squares either $100 \mu\text{m}^2$ or $200 \mu\text{m}^2$ using a frame size of $1.56 \times 1.18 \text{mm}$ and a $0.25 \mu\text{m}$ spot.

Initially the sample was completely covered with a gold mask and windows were patterned in the metal into which the quantum structures could be exposed. First attempts to achieve this design were done by using a negative resist called polyimide.

- 1) A layer of $0.3 \mu\text{m}$ thick polyimide (10% Polyimide solution solvent 35:65 by volume of acetophenone:xylene) was spin coated at 5000rpm onto the sample, baked for 1-2hrs at 180°C and the square alignment windows exposed on it.
- 2) The sample was then developed in 1:1 acetophenone:xylene at 23°C for 1min and then rinsed thoroughly in IPA.
- 3) Evaporate $0.1 \mu\text{m}$ thick of NiCr/Au/NiCr and lift-off by boiling in acetophenone to dissolve the polyimide for 30 minutes then rinse thoroughly in IPA.

Unfortunately very poor edge definition was achieved by this method as the polyimide exposure did not produce the desirable undercut profile. In order to obtain this the metal-on-polymer (MOP) mask process was used. This normally consists of a 800nm thick Germanium layer on $0.3 \mu\text{m}$ layer of polyimide. This is fabricated using a bilayer resist comprising of a $1 \mu\text{m}$ thick 185 000 PMMA layer on a $0.3 \mu\text{m}$ thick layer of polyimide. This process is normally used to protect active areas of a device when boron implantation is used to achieve electrical isolation - for example in the fabrication of Field

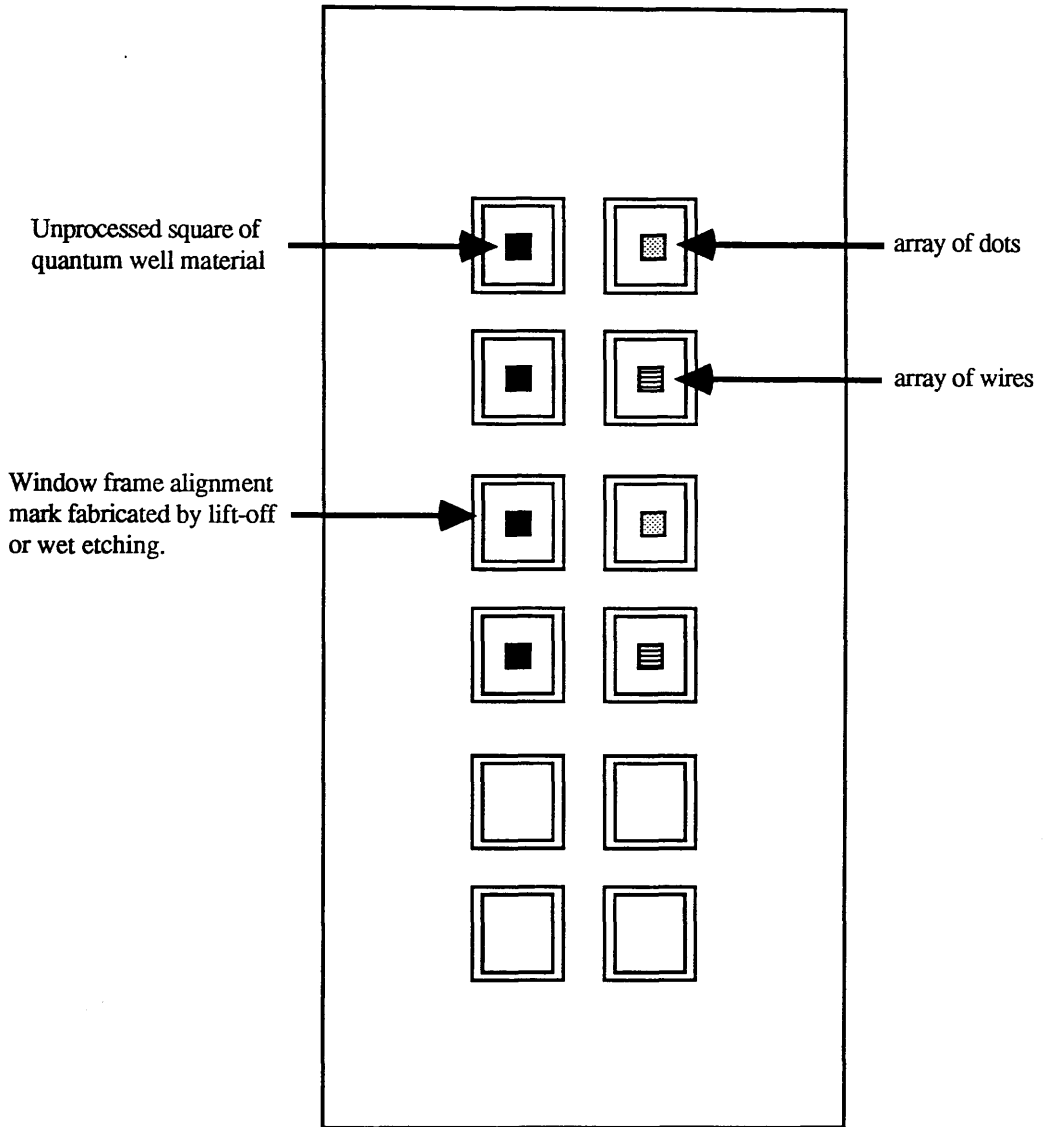


Figure 2.8 Alignment mark design for optical experiments.

Effect Transistors (FETs) type devices.

- 1) Spin coat a 0.3 μm thick layer of polyimide using a 10% Polyimide solution (solvent 35:65 by volume acetophenone:xylene) at 5000rpm and bake at 180°C for 1 hour.
Spin coat a 1 μm thick layer of 185 000 PMMA using a solution of 18% BDH in chlorobenzene at 5000rpm and bake at 180°C for 1 hour.
- 2) Expose alignment windows on BDH layer and develop using 1:1 MIBK:IPA at 23°C for 1 minute.
- 3) Evaporate 20nm of Nichrome and 400nm of Germanium. The NiCr is only used to help the Germanium stick. It was not necessary to evaporate such a thick layer of Ge as is required for boron implantation so the thickness of Ge evaporated was halved from 800nm.
- 4) Lift-off with acetone.
- 5) Develop polyimide as above.
- 6) Evaporate NiCr/Au/NiCr to a thickness of 0.1 μm .
- 8) Lift-off polyimide as above.

The polyimide under the BDH layer is also exposed and hence crosslinked. By using the MOP mask process an undercut profile is obtained because when the polyimide is developed only the sides of the windows are removed and not the top as it is protected by the germanium mask. By overdeveloping an undercut profile results. Further details of MOP mask fabrication are given by K Y Lee in reference 20. After the second evaporation and lift-off well defined regular square windows of GaAs/AlGaAs are left onto which the positive or negative resist could be spun and dots and wires subsequently exposed (figure 2.9).

It was realised however, once several samples had been characterised, that it was unnecessary to cover the complete sample with a mask. In fact it was desirable to remove as much of the unpatterned quantum well material as possible to reduce the possibility that stray excitation of this material could contribute to the overall signal. It was therefore decided to simply outline a gold window frame. This removed the need to use polyimide.

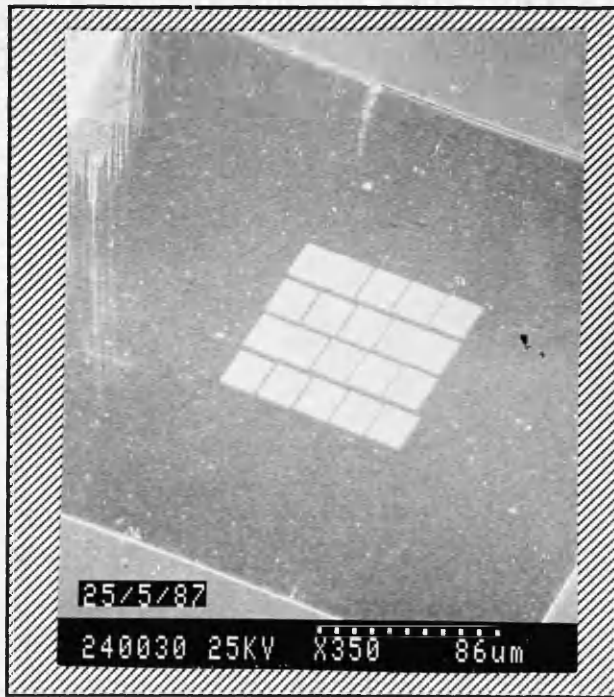
- 1) Spin coat 18% BDH in chlorobenzene at 5000rpm and bake at 180°C for 1 hour.
- 2) Expose the window frame outline and develop in 1:1 MIBK in IPA.
- 3) Evaporate NiCr/Au/NiCr to a thickness of 0.1 μm and lift-off in acetone as outlined in Section 2.4.2 .

The quantum structures could then be exposed in the centre of these window frames (figure 2.10).

Finally it was realised that it was desirable to remove all traces of the quantum well material from the sample except in the quantum structures. This was achieved by wet etching the alignment windows as opposed to evaporating metal and then lifting off. The wet etch used was 20 Hydrochloric acid : 1 Peroxide for 2 minutes (figure 2.11). This process also had the added advantage of cutting down on the number of process steps and also increasing the resolution as the wet etched marks proved better to focus on when exposing the sample in the e-beam machine than the the Au lift-off marks. The wet etched marks provided a sharper focussing edge.



(a)



(b)

Figure 2.9 GaAs/AlGaAs sample completely covered in gold with arrays of dots exposed in the middle of the windows a) part of the sample b) detail of one of the windows showing a $25 \times 19 \mu\text{m}$ frame size stepped & repeated 20 times.

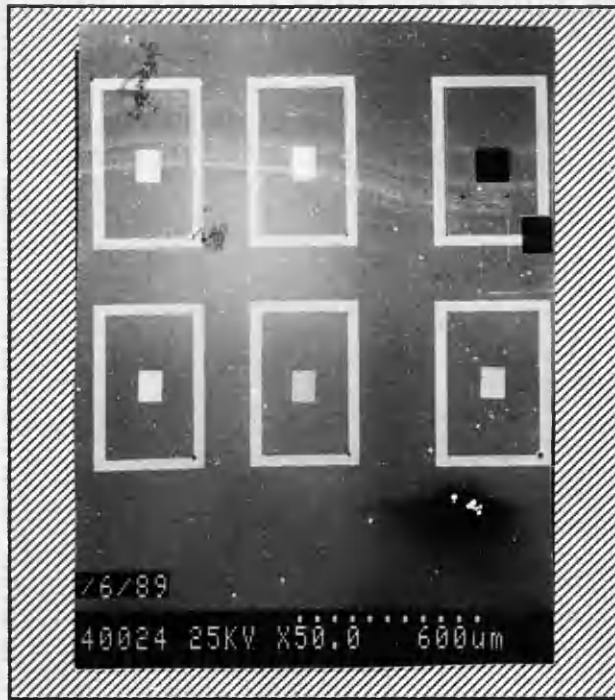


Figure 2.10 GaAs/AlGaAs sample with gold lift-off alignment marks and areas of dots or wires exposed in the centre. A mesa is exposed in the top right hand corner.



Figure 2.11 GaAs/AlGaAs sample with wet etched alignment marks and a mesa (foreground) and wires (background) exposed in the centre of the window.

2.7.2 Alignment and Exposure of Pattern Areas

The 60 and 100nm dot patterns were exposed using a 25 μ m x 19 μ m frame size. In order for these dots to cover an area approximately 100x100 μ m the smaller frame must be stepped and repeated 4 times in the X-direction and 5 times in the Y-direction. By focussing on the top and bottom left of the alignment windows a registration position is obtained. A position file specifies where the first frame should be exposed and the subsequent distance and number of steps in each direction. Using this information the pattern is automatically exposed. The pattern can then be stepped out in the desired location using the automatic step and repeat facility of the control program²¹.

2.8 Quantum Dot Fabrication using Laser Holography¹

One of the main drawbacks of electron beam lithography for fabricating dots and wires is the small area of sample that can be practically patterned. For example as the area to be patterned increases from 100x100 μ m to 200x200 μ m, the time taken to expose the area increases four fold from 10 to 40 minutes. The area over which the sample is in focus is also small 500 μ m² and therefore if too large an area of coverage is attempted the dots or wires exposed at the extremities would be out of focus and therefore the wrong size or exposure fails completely. By using the holographic process larger areas may be covered.

2.8.1 Background

It is possible to use an interference pattern made by the crossing of two laser beams to produce small period gratings over areas up to 1cm² in photoresist. The period of the grating is determined by the laser wavelength and the angle of intersection of the beams, and can be calculated from

$$\Lambda = \lambda_0 // 2n \sin\theta$$

where Λ is the grating period (equal to the period of the interference fringes); 2θ is the angle of intersection of the beams; and n is the refractive index of the medium in which the fringes are formed, usually air.

To record the fringes, a substrate (glass, GaAs, or Si) coated with a photoresist such as Shipley AZ1350J is placed at the point where the fringes are formed. When a reflecting substrate such as GaAs is used, a standing wave is set up in the resist creating planes of maximum and minimum exposure parallel to the substrate. This can have serious effects on small period structures ranging from poor profiles to the collapse of the entire structure. The standing wave period P is given by :

$$P = \Lambda \{ 4n^2 (\Lambda/\lambda_0)^2 - 1 \}^{-1/2}$$

¹ This work was done in conjunction with J J Thompson using the process developed by K Thomas²² for producing holographic gratings.

where n is the refractive index of the resist. The standing wave period is determined principally by the grating period. The resist thickness must be chosen so that a plane of maximum exposure intensity lies at the top surface. As a plane of minimum exposure always lies at the substrate-resist interface, the resist thickness is thus chosen to be $(m+0.5)P$, where m is an integer. Figure 2.12 shows the apparatus used to make gratings.

2.8.2 Quantum Dot Fabrication on GaAs

A layer of AZ1350J photoresist $0.5\mu\text{m}$ thick is spun onto a GaAs substrate, which should be no smaller than 5mm by 5mm , and square to ensure a uniform coating of resist. The resist is baked at 90° for 30 minutes. It is then exposed to an Argon ion laser, wavelength 457.9nm twice, rotating the sample through 90° for the second exposure. The sample is then developed in 1:2 developer:water for 15s, which develops only the top $0.05\mu\text{m}$ of the crossed gratings (figure 2.13).

It is possible to take the developed photoresist dot array and etch this in the oxygen plasma until only small peaks of resist are left on the substrate surface (figure 2.14). These then form an etch mask for the RIE etching of the GaAs in SiCl_4 or CH_4/H_2 to produce arrays of quantum dots (figures 2.15). It is essential that the development gives a profile suitable for etching into a mask for dots, ie high, clearly defined peaks in both grating directions, and a good overcut profile as undercut profiles tend to fall over during etching.

A large number of samples were made with a range of exposure and development times to determine the parameters necessary to give good profiles. As the development time increases, highly raised peaks are formed, and then undercut until they fall off, leaving a flat surface. This is then repeated with the next layer of resist. The change in profile is caused by the standing wave effect. It is possible to develop the dots down to the substrate, but it is not possible to control the time and development rate and time sufficiently well to ensure that all the peaks are left intact, with no areas under or overdeveloped. Thus a short development time of 15s was chosen, with exposure times of 15s and 20s, as this produces a satisfactory etch mask array after oxygen etching. The exposure times affect the relative strengths of the two gratings, although there does not appear to be any clear relationship between the relative exposure times and the grating strengths. Also, a range of exposure times gives good etch masks, and thus seems to be slightly less critical than the development time. Developing each grating after exposure was also tried, but the results were markedly better only for long (30s) development times.

Thus the best parameters for the production of arrays of quantum dot masks are two exposures of 15s and 20s respectively, with a single development of 15s in 1:2 developer: water. The development time is the most critical parameter.

The developed dot array is then etched (see Chapter 3) using the Plasmfab 340 machine in an oxygen plasma for 4 minutes, with an RF power of 0.31Wcm^{-2} and an etch pressure of 16mTorr to leave photoresist peaks 40nm high. It is important to choose the etching parameters carefully in order to avoid over or under etching areas, which in this case leads to variations in the final sizes of the

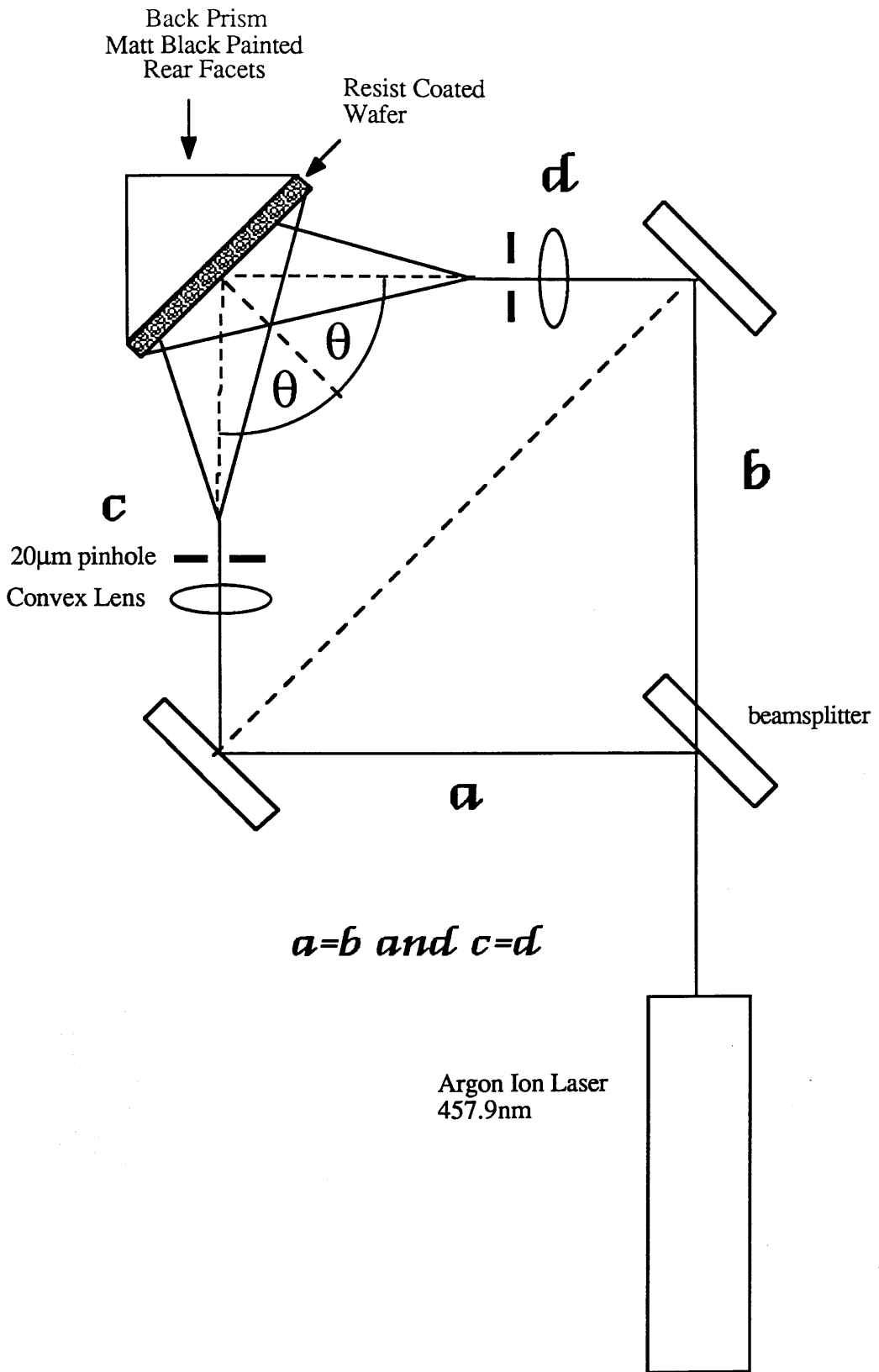
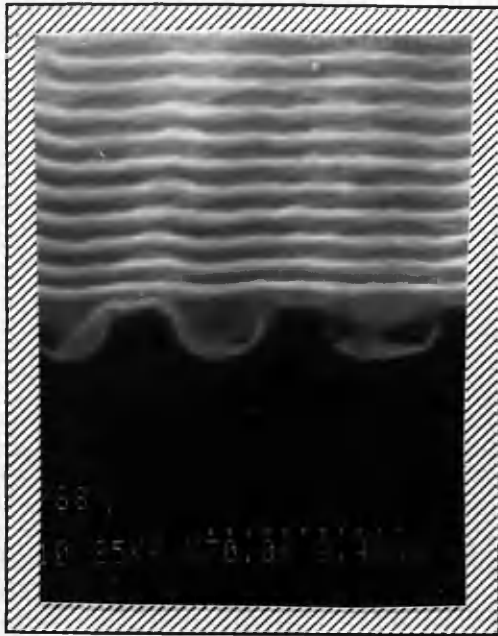
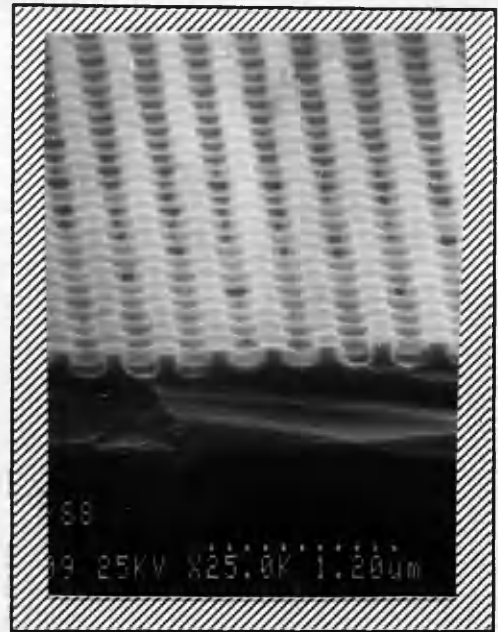


Figure 2.12 Laser interferometer arrangements for generating holographic gratings using 457.9nm line to generate gratings with periods greater than 0.3µm.
(After Thomas)



(a)



(b)

Figure 2.13 Crossed gratings in photoresist viewing a) the grating exposed first b) 2nd grating exposed end on.

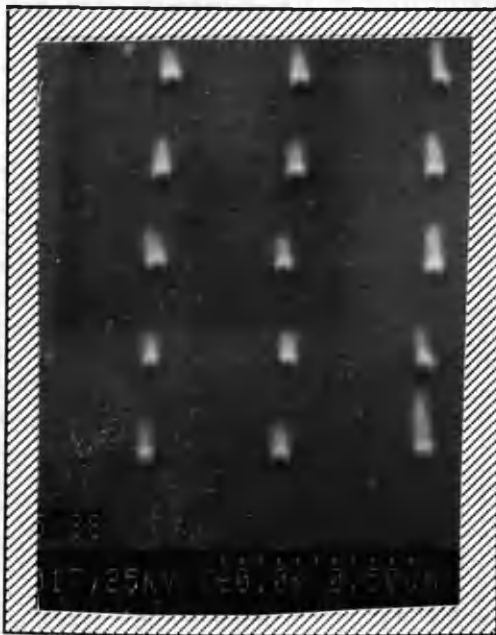


Figure 2.14 Mask remaining after oxygen plasma etching of crossed gratings.

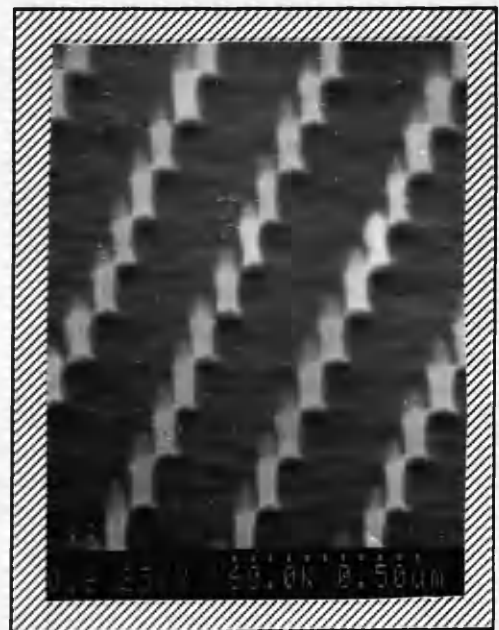


Figure 2.15 Quantum dots obtained after RIE in SiCl_4 of mask in figure 2.14.

quantum dots. The masks are typically 100nm in diameter, which is larger than the size desired for quantum dots, but this can be reduced by etching in the oxygen plasma for longer, which reduces the dot diameter and also the etch mask thickness.

This holographic method is capable of producing consistent arrays of quantum dots of 40nm to 100nm in diameter over 20mm² with careful control of the development and etching parameters, which is a much larger area than can easily be covered with electron beam lithography. It could therefore perhaps be used as a method by which quantum dots could be made commercially as electron beam lithography is unlikely to prove cost effective.

There are two main disadvantages of using this method for fabricating quantum dots and wires. The first is that only dots or wires of one size can be exposed on the one sample. It is therefore impossible to learn anything of the behaviour of quantum structures by observing the differences between dots or wires of different sizes, or between dots and wires themselves. The second disadvantage is that the wires and dots will always be of a constant pitch as this is dependent on the wavelength of light used. For applications such as quantum dot or wire lasers it is desirable that the filling factor be as high as possible i.e the pitch between the structures to be as small as possible. This factor can be varied in e-beam lithography and using positive resist to fabricate wires it has been shown that a filling factor as high as 50% can be achieved. This is not possible using laser holography as although filling factors of 50% are achieved with larger wires as the mask is oxygen plasma etched to reduce the overall wire width the pitch between the wires increases thus reducing the overall filling factor.

2.9 Summary

Metal quantum dot masks 40 to 250nm in diameter with pitches of two and four times the dot diameter can be routinely fabricated using a two layer positive PMMA resist scheme and Nichrome or Titanium as the evaporated metal. A negative resist (HRN) has been used successfully to fabricate quantum dot masks 60 to 500nm in diameter with pitches three times and five the dot diameter. This mask could be completely removed after dry etching - see Section 3.8.

HRN has also been used to fabricate quantum wires 75 to 500nm in width and 100µm in length with either a constant pitch of 1000nm or a constant filling factor of 25%. PMMA has been used to fabricate quantum wires 100 to 400nm in width with a filling factor of 50%.

Samples have been fabricated which consist of window frame alignment marks delineated either by using the standard lift-off techniques or wet etching and in the centre of these marks arrays of quantum dots or wires. The area of dot coverage is either 100x98µm or 200x190µm with a filling factor of approximately 4-5% depending on the size of the dot. The area of wire coverage is 100x76µm and a filling factor of 25%. These samples are then characterised by using low temperature photoluminescence spectroscopy.

Laser holography combined with oxygen plasma etching has been shown to be a viable method for fabricating quantum dots as small as 40nm over areas as large as 20mm².

References

- 1 For a more detailed discussion of optical lithography see M C King: N G Einspruch, Ed., VLSI Electronics, Vol 1, Academic, New York, 1981 pp. 42.
- 2 M P Lepselter and W T Lynch: N G Einspruch, Ed., VLSI Electronics, Vol 1, Academic, New York, 1981 pp. 84.
- 3 C D W Wilkinson and S P Beaumont: Proceedings of the Winter School Les Houches, France, March 25 - April 5, 1986. Editors M J Kelly and C Weisbuch, Springer Proceedings in Physics 13 pp. 36.
- 4 A N Broers: Proceedings of the Winter School Les Houches, France, March 25 - April 5, 1986. Editors M J Kelly and C Weisbuch, Springer Proceedings in Physics 13 pp. 2.
- 5 S R Rishton, Thesis, Glasgow, 1984.
- 6 E D Roberts: Vacuum Vol. 26, No. 10/11 pp. 459.
- 7 J S Greeneich: J. Electrochem. Soc. July 1975 pp. 970.
- 8 W S Mackie, Thesis, Glasgow, 1984.
- 9 B E Maile, A Forchel, R Germann, A Menschig, H P Meier and D Grutzmacher: to be published, 1988.
- 10 S Thoms, S P Beaumont, C D W Wilkenson, J Frost and C R Stanley: Microcircuit Engineering 5 (1986) pp. 249. Elsevier Science Publishers B.V. (North-Holland).
- 11 S Thoms, I MacIntyre, S P Beaumont, M Al-Mudares, R Cheung and C D W Wilkenson: J. Vac. Sci. Technol. B 6 (1), 1988 pp. 127.
- 12 P W Whipps: Proceedings Microcircuit Engineering 1979 (Aachen) pp. 118.
- 13 P W Whipps: Proceedings Microcircuit Engineering 1983.
- 14 C Reeves, Thesis, Glasgow, 1987.
- 15 T P Smith III, H Arnot, J M Hong, C M Knoedler, S E Laux, and H Schmid: Phys Rev Lett. Vol. 59 No.24 1987 pp. 2802
- 16 T P Smith, K Y Lee, J M Hong, C M Knoedler, H Arnot and D P Kern: Phys Rev B, Vol 38, No. 2, 1988 pp. 1158.
- 17 K Y Lee, T P Smith III, H Arnot, C M Knoedler, J M Hong, D P Kern and S E Laux: J. Vac. Sci. Technol. B6 (6), 1988 pp. 1856.
- 18 D P Kern. P J Houzago, P J Coane, and T H P Chang: J. Vac. Sci. Tech. B 1 1983 pp. 1096
- 19 D P Kern and H Schmid: (private communication).
- 20 K Y Lee, Thesis, Glasgow, 1987.
- 21 J Adams, Thesis, Glasgow, 1990.
- 22 K Thomas, Thesis, Glasgow, 1989.

Chapter 3

Etching

3.1 Introduction

Once the resist pattern defining the desired size and shape of the quantum dots (QDs) or quantum wires (QWWs) has been produced it must be transferred to the semiconductor material on which it was exposed. One method of transferring the patterns is to selectively remove the unmasked portions of the material to produce surface relief, a process generally known as etching. There are many different types of etching but the four investigated for the production of quantum structures were Wet Chemical Etching, Plasma Etching (PE), Reactive Ion Etching (RIE) and Ion Beam Milling (IBM). There are four requirements of the etching or milling process which must be fulfilled if quantum structures are to be obtained : -

- 1) **Anisotropy** - The extent to which the wall profiles are truly vertical. In order to achieve this there must be no etching in the lateral direction in order that the pattern is transferred with perfect fidelity.
- 2) Surface and sidewall **smoothness** which depends on mask quality and etch parameters.
- 3) The extent to which etching produces **surface and sidewall damage** and therefore affects the electrical and optical performance of the device. This greatly depends on the ionic energy and chemistry. The term *damage* means any change to the semiconductor material such as the introduction of crystal defects which might degrade the electrical or optical properties from the bulk.
- 4) Etching **selectivity** between the mask and the substrate and also between the various layers of a device. This generally depends on the chemistry of the etching technique.

It should be emphasised that while all the above points are important in many applications where pattern transfer to the underlying substrate is used, anisotropy and surface damage are especially important in the production of working quantum structures. The etch process used must be capable of very high resolution transfer of the pattern to the underlying substrate as the critical feature size can be as small as 20nm and in order to achieve this the anisotropy of the etch is essential. Low damage is also important as sidewall damage of a few nanometres could modify the behaviour of such small structures. In order to meet the above requirements several different processes were investigated. -

Reactive Ion Etching with SiCl_4 , CH_4/H_2 and SiCl_4/H_2 , Ion Beam Milling with Argon and Wet Chemical Etching.

3.2 Wet Chemical Etching

Attempts were made to fabricate QDs by wet chemical etching. The main advantage of wet etching is that it is a very low damage method for removing material. It relies on the reactivity of the etch with the material to be removed and not on ionic bombardment as in plasma etching. The mechanism for wet chemical etching involves three essential steps (1) the reactants are transported (e.g. by diffusion) to the reacting surface, (2) chemical reactions occur at the surface, and (3) the products from the surface are transported away (e.g. by diffusion). Both agitation and the temperature of the etchant solution will influence the etch rate. The main problems associated with wet etching are undercutting and orientational selectivity. Quantum wires have been successfully etched by S Thoms *et al*¹ using an etch system of $\text{H}_2\text{O}:\text{NH}_3:\text{H}_2\text{O}_2$ in the two ratios 1000:20:7 or 3000:20:7. They found that width control using wet etching was difficult but that quantum wires with widths of the order of $0.1\mu\text{m}$ were possible. While wires of 100nm are sufficiently small to be of interest in transport measurements, they are still too large to show modified quantum confinement effects in the optical properties. It is unlikely that wet etching will be able to achieve the resolution of the dry etch process.

To produce GaAs/AlGaAs QDs two methods were tried. In the first HRN dot masks 240nm in diameter were etched in GaAs using a wet etch of Potassium Chlorate : H_2O : HCl (2g of Potassium Chlorate in 100mls of H_2O then 2mls of this with 100mls of HCl). This failed completely as there seemed to be a residue of HRN which is removed by dry etching and does not affect the final result, but in wet etching left the surface speckled. The material did not etch evenly and after 1 hour the masks began to distort in shape. This method was therefore abandoned.

The second method was to first etch the dots by RIE in SiCl_4 and then to wet etch with the isotropic etch described above. It was hoped that this etch would reduce the diameter of the pillars evenly with an etch rate of 100nm in 30 minutes and also remove any "damaged" layer that might exist on the surface. Unfortunately the etch rate along the $\langle 011 \rangle$ and $\langle 101 \rangle$ crystal planes of GaAs is different and the quantum dots began to etch preferentially along certain planes (figure 3.1) after 1 hour in the etch solution. This method was therefore also abandoned.

3.3 Plasma Etching

Plasma-assisted pattern transfer techniques rely on partially ionized gases consisting of equal numbers of positive ions and negative electrons, and a component of un-ionized neutral molecules and fragments, produced by low pressure ($\sim 10^{-4}$ to 10^+1 torr) electric discharges. The generic term 'plasma assisted etching' includes ion milling, sputter etching, reactive ion beam etching, reactive ion etching and plasma etching. These techniques differ in the specifics of discharge conditions, type of gas and apparatus; the common thread is the discharge, often referred to simply as the plasma.



Figure 3.1 Wet etch of QDs after RIE in SiCl_4

3.3.1 Self-Sustained Glow Discharges

When an electric field of sufficient magnitude is applied to a gas, the gas breaks down. This process begins with the release of an electron by some means such as photoionization or field emission. The released electron is accelerated by the applied field and gains kinetic energy, but in the course of its travel through the gas, it loses its energy in collisions with gas molecules. There are two types of collisions, elastic and inelastic. Elastic collisions deplete very little of the electron's energy because of the great mass difference between electrons and molecules. Ultimately the electron energy becomes high enough to excite or ionize a molecule by inelastic collisions. In ionizing collisions the electron essentially loses all of its energy. Ionization frees another electron which is accelerated by the field, and so the process continues. Therefore electron impact ionization involves the removal of an electron from a molecule or atom by the primary electron, producing a positive ion and two electrons. The two electrons produced by the ionizing collision can then be accelerated by the electric field until they too produce ionization. It is by this multiplication process that the glow discharge is maintained. If the applied voltage exceeds the breakdown potential, the gas rapidly becomes ionized throughout its volume.

Electrons released in ionizing collisions and by secondary processes are lost from the plasma by drift and diffusion to the boundaries and by recombination with positive ions. The discharge reaches a self-sustained steady state when electron generation and loss processes balance each other.

Nonionizing, inelastic collisions between electrons and gas molecules or atoms also occur. Two important types of nonionizing collisions are electronic excitation of molecules (or atoms) and molecular fragmentation. In the excitation process the bound electron jumps to a higher energy level within the atom with a corresponding quantum absorption of energy. Electronically excited molecules and atoms account for much of the luminous glow of the plasma by emitting photons as they relax to lower-lying electronic states. Molecular fragments are often highly reactive atoms and free radicals. A free radical is a molecular fragment having an unpaired electron.

The electron density for the plasmas of interest ranges from 10^9 to 10^{12} cm^{-3} . As the density of gas molecules at 1 torr is about 10^{16} cm^{-3} it can be seen that these discharges are weakly ionized. This results in a gas temperature near ambient, despite a mean electron temperature of about 10^4 to 10^5 K. The relatively low gas temperature permits the use of thermally sensitive materials, such as organic resists as etch masks².

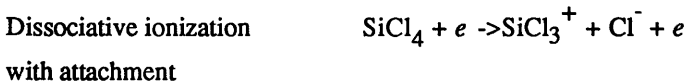
In summary, the application of an electric field to a gas results in the conversion of electrical energy to potential energy of activated gaseous species such as ions, atoms, and free radicals which can be used to produce etching by physical and chemical interactions with solid surfaces. The energy is transferred by free electrons colliding inelastically with gas molecules.

3.3.2 Physical and Chemical Phenomena in Gas Discharges

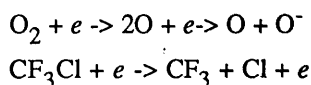
The production of atoms and radicals in molecular gas discharges is essential to etching, because the feed gases themselves are almost always virtually unreactive. As an example, CF_4 is a relatively inert gas that does not react with Si at any temperature up to melting point (1412°C). However, when a discharge is initiated in CF_4 , one of the by-products is atomic fluorine which reacts spontaneously with Si at room temperature to form volatile SiF_4 . Similarly, O_2 does not attack photoresists significantly at or near room temperature, but the atomic oxygen produced in an O_2 discharge rapidly converts resist to volatile by-products such as CO , CO_2 and H_2O^2 . The rate of production of ions, atoms and radicals depends on discharge parameters such as pressure, power density, frequency, and feed-gas flow rate.

The plasma is the source of the species that result in etching. The steady-state constitution of any discharge is governed by the rates of production and loss of the various species.

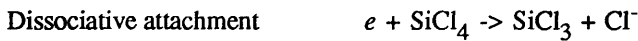
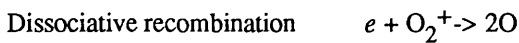
Production of ions, atoms and radicals. Electron impact is the primary mechanism of ion production in noble and molecular gas discharges. In molecular gases, ionization may also occur with fragmentation, in which case dissociative ionization is said to occur. The process of dissociation is the breaking apart of a molecule. An oxygen molecule can be dissociated into two oxygen atoms, but an atomic gas such as argon cannot be dissociated at all. A normal result of dissociation is an enhancement of chemical activity, since the products are usually more reactive than the parent molecule. Attachment may also occur whereby an electron colliding with an atom may join on to the atom and form a negative ion. Noble gases, including argon, already have filled outer electron shells and so have little or no propensity to form negative ions. Halogen atoms however have an unfilled state in their outer electron shells; they therefore have high electron affinities and so readily form negative ions. For example:



Electron impact can also result in molecular dissociation (fragmentation) without ionization, which generally requires less energetic electrons. Most atoms, radicals, and in some cases negative ions are produced by these impact events. For example:



Loss mechanisms Electrons are lost from a discharge by drift, diffusion, recombination, and attachment. In molecular gases the recombination and attachment events can be dissociative. An electron joins with a positive ion to form a neutral atom. For example,



Ions can also drift to the electrodes or diffuse to the walls and be lost.

Atoms and radicals can be lost either by reactions which occur in the plasma or reactions that take place on the surfaces available in the etch chamber.

3.3.3 Plasma Production using DC or AC Discharges

DC Discharges In dc discharges positive ions are accelerated toward the cathode and cause ejection of secondary electrons. The secondary electrons are accelerated away from the cathode causing a space charge of less mobile positive ions to form. This region is known as the dark space sheath and has a relatively low conductivity, because it is depleted of the more mobile electrons and consequently most of the applied voltage is dropped across it. One of the most obvious features of a discharge is that it glows and this is due to the relaxation of atoms excited by electron impact. The glow intensity therefore depends on the density and energy of the exciting electrons. Since the electron density is lower in the area of the dark space it does not glow as much hence the name. When the secondary electrons have been accelerated to a high enough energy, they collide with the gas molecules and ionization takes place. The voltage across the dark space sheath directly influences the energy with which the ions strike the substrate. The ions enter the dark space with a very low energy. They are then accelerated by the sheath voltage and in the absence of collisions in the sheath, would strike the substrate with a kinetic energy equivalent to the dark space voltage.

AC Discharges In an ac discharge a rf frequency alternating field is applied across two metal electrodes in a partially evacuated chamber causing their polarity to change every half cycle, so that each electrode alternates as the negative electrode (cathode). The ions and electrons can both follow the field and establish a glow discharge. As the frequency of the applied field is increased, a point is reached where ions created during breakdown cannot be extracted from the gap prior to field reversal. As the frequency is increased still further, a large fraction of the electrons have insufficient time to drift to the positive electrode during a half-cycle. These electrons then oscillate in the interelectrode gap and undergo collisions with the gas molecules. It is these electrons that cause ionisation, so this process is not reliant on the secondary electron yield from the electrode and chamber walls as in a dc plasma. The lower limit of frequency for oscillations depends on the electron mobility, the electrode spacing and the amplitude of the applied field. The frequency limit is typically in the rf range.

The main advantage of using a rf discharge is that electrons can pick up sufficient energy during their oscillations in the gap to cause ionization and the probability of ionizing collisions is enhanced by these electron oscillations allowing operation at pressures as low as $\sim 10^{-3}$ torr.

3.3.4 Plasma Etching and Reactive Ion Etching

Plasma etching (PE) and reactive ion etching (RIE) rely, to various degrees on both chemical reactions that form volatile or quasi-volatile compounds and physical effects such as ion bombardment. The gases selected produce fragments which react with the materials of interest to form volatile compounds at temperatures low enough to be appropriate for pattern transfer. Halogen containing gases are often used due to their reactivity with semiconductors such as Silicon or Gallium Arsenide³, but recently new gases such as Methane have been investigated^{4, 6}.

RIE produces anisotropic etching compared to PE which generally produces an isotropic profile. In PE electrodes are energised at radio frequency to produce a chemically active plasma from a suitable gas or mixture of gases at a low pressure (typically 100mTorr) and the sample is placed on a grounded electrode. RIE also uses electrodes within a vacuum chamber to produce a chemically active plasma. The electrode plates differ in area so that when energised at a high frequency (13.56MHz in most cases) a d.c. bias is formed between the smaller plate and the plasma so that ions are directed across a dark space onto the sample. A negative dc or self bias voltage is formed on the target plate due to the build up of negative charge caused by the much greater mobility of electrons in a plasma compared to ions. To begin with when an alternating voltage supply is used the target is negative for one half cycle. It is bombarded by positive ions in this half cycle and the voltage on the target becomes slightly less negative. The voltage then switches positive, but this time the voltage decays much more rapidly towards zero as the positive charged target now draws a large electron current. After a few cycles the voltage waveform will become repetitive and displaced towards the negative. It is this bias which enables almost continuous bombardment of the target by positive ions. An asymmetric system is used whereby the target (or cathode) is smaller in area than the anode as a larger voltage sheath will appear at the smaller electrode thus enabling the bombarding ions to be accelerated by a larger voltage.

It has been shown that as the etch rate increases with an increase in the self bias voltage that this is evidence of the physical component of the RIE process (see figure 3.13). This increase due to the bias voltage or energy of the bombarding species can be detrimental in device formation as material damage can result and affect the required performance. RIE is therefore partly chemical in nature and partly physical.

Each target sample constituent should form volatile products upon reaction with the etchant, so that unwanted chemical rich surfaces do not result⁷. In general RIE or dry etching can leave three kinds of surface defect: Deposition (leaving a surface residue or cone forming micromasks), diffusion (of plasma constituent and/or products) and dislocation of the crystal lattice⁸. The extent to which etching damages the sample surface or alters its composition depends on the nature and energy of the gases and ionic species. The process which leaves the least amount of crystal dislocation is probably that which employs the lowest ion energies.

The plasma assisted etching process can be summarised in five steps

- 1) The process begins with the generation of the etchant species in the plasma.
- 2) The reactant is then transported by diffusion through the dark space to the surface.
- 3) The reactant is adsorbed on the surface.
- 4) This is followed by chemical reaction (along with the physical effects such as ion bombardment) to form volatile compounds.
- 5) These compounds are desorbed from the surface, diffused into the bulk gas, and pumped out by the vacuum system.

3.3.5 Reactive Ion Etch Parameters

To achieve successful etching of microstructures the correct parameters for the particular etch system being used must be established. The etch rate and the anisotropy of the etch are interdependent on the pressure, power density, flow rate and temperature.

Lowering pressure and increasing power density, increases the mean electron energy and the energy of ions incident on surfaces. An increase in power also increases the density of radicals and ions in the plasma. Thus if etching is ion-assisted, a decrease in pressure or an increase in power favours etch rate anisotropy.

In general etch rates increase monotonically with power, although at a diminishing rate. As all the applied power is ultimately dissipated as heat at very high power densities, substrates require heat sinking to avoid undesired effects such as resist flow or loss of selectivity.

The flow rate of the feed gas determines the maximum possible supply of reactant. The etch rate is determined by the generation rate of reactive species in the discharge, but is limited by the lack of reactant gas at low flows and by pumping of active species at high flows where the pump rate has to be increased to maintain a low pressure. However under normal operating conditions, flow rate has only a small influence on etch rate.

The temperature influences etch rate in reactive etching primarily through its effect on the rates of chemical reactions. However in the RIE system used in these experiments the temperature was held constant at 40°C. The actual substrate temperature is not known as it is thermally isolated from the electrode on which it sits.

Where a mixture of gases is used the ratio of one gas to the other i.e. the composition also affects the etch rate and selectivity. The addition of one gas can either slow down or speed up the etch rate. For example in the etching of Silicon with CF₄-containing mixtures the addition of a small amount of oxygen increases the etch rate. If however hydrogen is added the etch rate decreases².

3.4 SiCl₄ Reactive Ion Etching

Some of the etch gases and or gas mixtures used to etch GaAs and related compounds are chlorine based gases such as SiCl₄, BCl₃, Cl₂, CCl₂ or CCl₂F₂. Gases containing fluorine alone cannot be used as although arsenic forms volatile products with fluorine at workable temperatures, gallium does not, so that the well documented fluorine chemistry used in silicon technology cannot be utilised. Chlorinated gases can be used successfully as both AsCl₃ and GaCl₃ have reasonably high vapour pressures at processing temperatures and are gaseous at typical RIE operating pressures^{7,9}. One advantage of SiCl₄ over chlorinated halocarbons is that it will not produce chlorinated polymer films which can contaminate the sample, and inhibit etching¹⁰. Furthermore SiCl₄ has been shown to possess high selectivity over many common masking materials¹¹.

3.4.1 The Etch Mechanism in SiCl₄ RIE

In SiCl₄ RIE the chlorine radicals form volatile products with the GaAs namely gallium chlorides and arsenic chlorides at low temperatures which are removed in the exhaust. There is also an element of physical sputtering perhaps due to the silicon chloride compounds. This physical component of the etch is important as it enables the native oxide which is unreactive to Cl atoms to be removed thereby enabling the GaAs to be etched by the chemically reactive Cl. In the reactive ion etching of GaAs with Cl₂ plasma the oxide must first be removed by, for example, a H₂ plasma¹¹.

It has been reported that when SiCl₄ is mixed with argon the etch characteristics of anisotropy and smoothness are improved to some extent^{3,11,12}. This is to be avoided as addition of argon has been shown to increase damage¹³. The thickness of the damaged sidewall is of crucial importance when fabricating structures 30nm or less in diameter.

It has been suggested by Hu *et al*¹³ that in samples etched in Cl₂, Auger Electron Spectroscopy (AES) revealed an excess of Cl on the sidewalls as compared to the substrate surface and this chloride layer limited the lateral etch rate of the sidewalls. Sonek *et al*¹⁴ also explained the high degree of anisotropy achieved in BCl₃ RIE by suggesting that species are adsorbed onto the etched sidewalls and behave as surface inhibitors during the etching process, either by reacting with the etchant species, or by preventing the etchant species from reaching the etching surface. It has been established that RIE of GaAs with Cl₂ leads to As depleted surfaces and high chlorine coverage. This is attributed to a "poisoning" of the surface with low volatile gallium chloride species¹⁵. Vodjdani *et al*¹⁶ suggested that the removal of Ga products is highly enhanced by ion bombardment while arsenic removal is more chemical and depends on partial pressure. It is therefore likely that in gases where the ionic component is lower (desirable for low damage etching) excess Ga will occur.

3.4.2 Results

In this work a Plasmatechnology RIE80 machine operated at 13.56Mhz was used. The cathode and anode are anodised aluminium. The load capacitance was tuned according to the etching conditions to

yield the minimum reflected power. The temperature of the electrode was maintained at 40°C throughout. The temperature at a real sample surface during etching was not measured, but it is likely to be higher because of the temperature rise caused by ion and electron bombardment. However, no evidence of resist flow is seen therefore temperatures cannot be greater than the glass transition temperature of the resist. With SiCl₄ there were problems with reproducibility perhaps due to slight variations in pressure, pump down time or even temperatures. Every attempt was made to keep the parameters constant.

Quantum dots and wires from 40nm to 500nm have been successfully fabricated on the same chip using SiCl₄. The optimum conditions for etching both 1D and 0D structures are given in Table IV and examples of the etching achieved are shown in figures 3.2 and 3.3. Aspect ratios in the region of 1:5, diameter:etch depth are easily obtainable. Extremely vertical sidewalls are routinely achieved under optimum conditions using a power density of 0.65Wcm⁻². The smallest QDs fabricated with SiCl₄ are 20nm in diameter and etched ~50nm deep (see figure 3.4). Below this undercut profiles were obtained. It is important to keep the applied power as low as possible to achieve the required profile as increasing the power increases the d.c. bias and hence the ionic bombardment of the sample. This increases the contribution to the etching from the sputtering process (i.e. the transfer of momentum) and is hence more likely to increase the crystallographic damage. No selectivity was found for GaAs over AlGaAs or vice versa.

The limiting factor in the fabrication of quantum structures using SiCl₄ is the fast etch rate of ~0.2µm/min. For very small structures i.e.10nm in diameter an etch depth of 50nm (aspect ratio 1:5) would require etch times of only 15 seconds. It is known that there is an induction period when virtually no etching takes place of perhaps 10 to 20 seconds. This period varies from day to day and therefore reproducibility is a major problem when etching structures of this size. It would therefore be desirable to slow the etch rate in some way while retaining the useful properties of SiCl₄ of low damage and high anisotropy. This was achieved by diluting SiCl₄ with H₂ and the results of this are presented in Section 3.5.

Several experiments were also done to investigate the possibility of reducing the dot diameter after the initial RIE with SiCl₄ has produced the free standing pillars. Throughout these experiments the power was kept constant. Only the flowrate (and hence the pressure) or the pump speed were varied.

Experiment 1 Etched quantum dots (at conditions given in Table IV) were subjected to a further Plasma Etch at 150mTorr and 0.43Wcm⁻² of 1min to 5min duration without the sample being removed from the etch chamber or the flow of SiCl₄ being stopped. As plasma etching is isotropic it was thought that this may reduce the diameter of the dots as now the sidewalls would be etched at the same rate as the mask. After 1min there was virtually no change in the dot profile but after 3min trenching around the base of each dot had occurred and after 5min crystallographic etching of the dots had resulted (see figures 3.5 & 3.6)¹². This experiment was repeated but with a reduced power of 0.22Wcm⁻². Now however the dots undercut so quickly that they fell over completely in a 2min etch. The surface was still extremely rough.

TABLE IV

OPTIMUM ETCH CONDITIONS FOR QUANTUM DOT AND WIRE RIE

GASES	SiCl₄	SiCl₄	H₂	CH₄	H₂	CH₄	H₂
MATERIAL SYSTEM	←	→	GaAs/AlGaAs or GaAs/InGaAs		→		InP/InGaAs
GAS FLOW (sccm)	8	6	10	6.9	25	12	8
Relative Partial Pressure		1	5	1	5	3	2
ETCH PRESSURE (mTorr)	10	11		20		16	
R F POWER DENSITY (W/cm²)	0.65	0.65		0.75		0.75	
D C SELF BIAS (V)	310	360		1030		1030	
TEMPERATURE (°C)	39	39		30		30	
ETCH RATE	0.2 μm/min	0.1 μm/min		250 Å/min		750 Å/min	

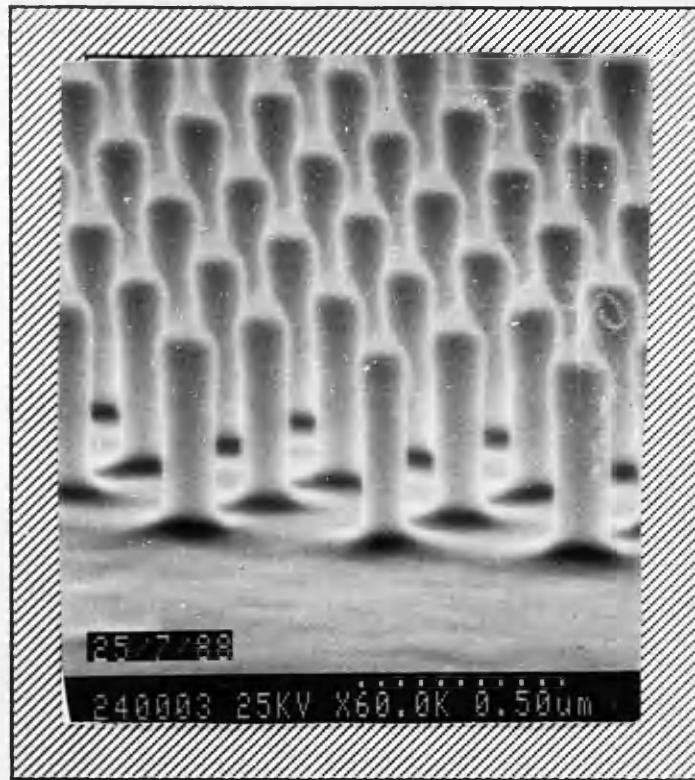


Figure 3.2 Quantum dots etched by SiCl_4

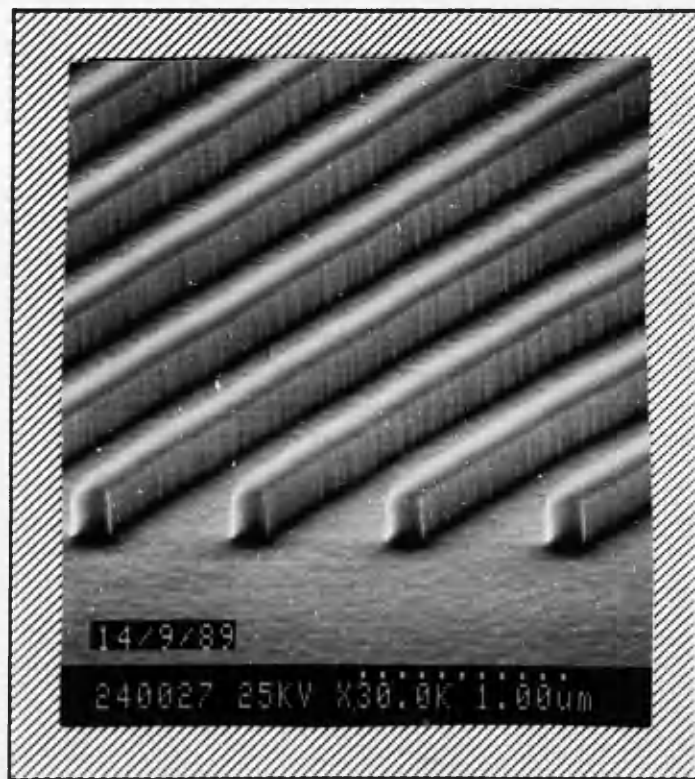


Figure 3.3 Quantum wires etched by SiCl_4

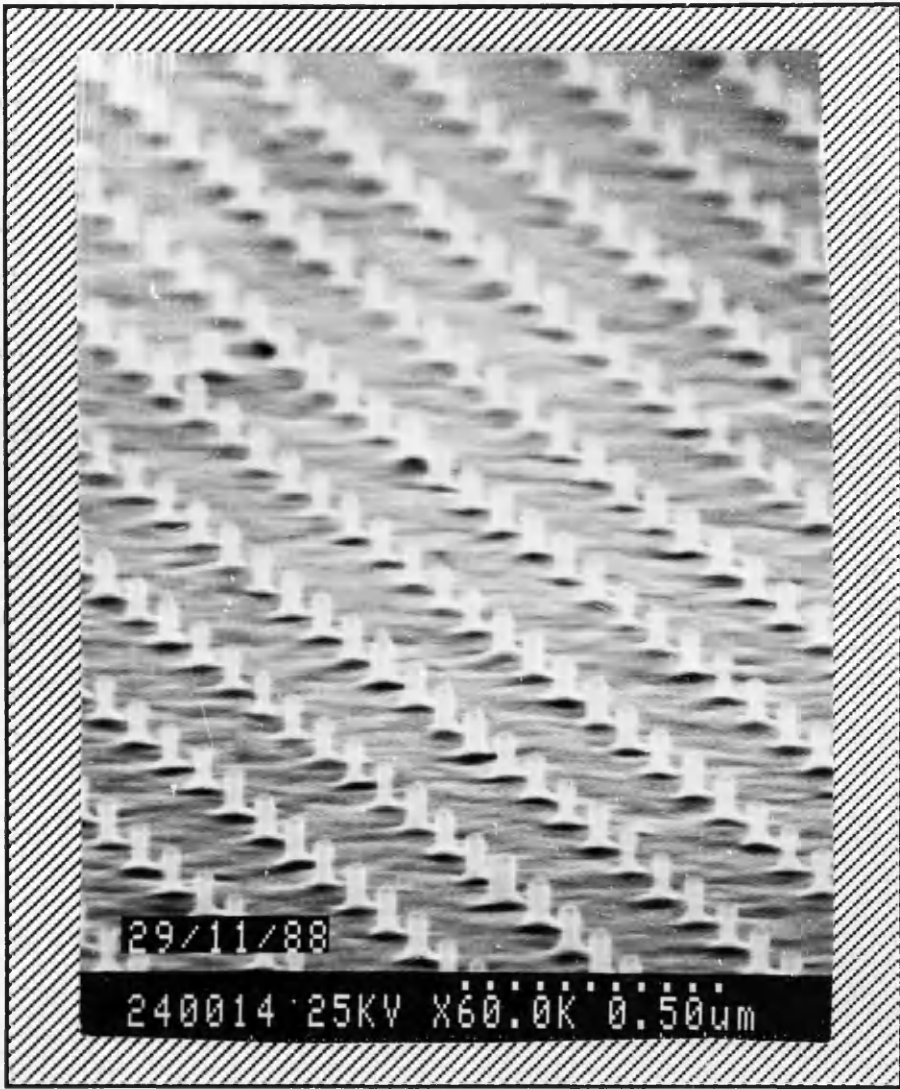


Figure 3.4 20nm QDs exposed using the JEOL and etched using SiCl_4

Experiment 2 Identical etch conditions to Table IV but the etch pressure was increased from 11 to 22mTorr. This resulted in much more severe undercutting, with many of the dots falling over in a 2min etch (figure 3.7 and see Section 3.3.6).

Experiment 3 A dot array was etched using the anisotropic etch conditions given in Table IV. The sample was removed from the chamber thereby oxidising it and returned and subjected to an increased pressure etch (44mTorr as opposed to 11mT) with all other conditions constant. This resulted in dot profiles whereby the first part of the dot was vertical and the second part was much more undercut (figure 3.8).

In summary it is suggested that these experiments show that a resistant rate limiting layer may form on the dots either during etching or after^{3, 14} as it is impossible to change the profile of a quantum dot by any subsequent plasma etching after it has been etched initially with SiCl_4 . This layer may be a chlorine coating due to excess gallium chloride as described in Section 3.4.1 as it proved impossible to change the dot profile in Experiment 1 even when SiCl_4 continuously surrounded the sample. However in the RIE process itself there will be far more etching vertically on the sample parallel to the plasma. Species will not bombard the sidewalls but only hit at glancing angles. This does not explain why in PE the sidewalls do not etch. It would be expected that the ions would have enough energy to remove the oxide layer but this appears not to happen. Perhaps the density of ions bombarding the surface is still much higher than on the sidewalls so the oxide on the surface etches away much quicker than on the sidewalls. As GaAs has a faster etch rate than its oxide the dots then undercut quickly and fall over due to the high pressure and nondirectionality of the plasma etch, before any effect can be seen on the previously etched portion of the dots.

SiCl_4 was also used to successfully etch GaAs/InGaAs QDs using the same conditions for GaAs/AlGaAs etching. The starting material consisted of 2.5, 6 and 9.5nm thick $\text{In}_{0.11}\text{Ga}_{0.89}\text{As}$ quantum wells and this material was patterned into dots ranging in size from 75nm to 500nm. No selectivity of the InGaAs over the GaAs or vice versa could be seen. It is likely that no problems due to the involatility of In at the etch temperature of 40°C were encountered due to the low percentage of In in the overall material makeup - only 11% in the three wells.

3.5 SiCl_4/H_2 Reactive Ion Etching

Several authors had reported the improvement of the etch characteristics of different gases by diluting either with hydrogen or oxygen^{17, 18} or helium¹⁹. One major drawback of using SiCl_4 for the etching of quantum structures is the high etch rate of $\sim 0.2\mu/\text{min}$. While this is desirable for the etching of optical devices such as lasers or waveguides where the required etch depth is several microns it is less desirable when the etch depth required is 50nm or less. It is almost impossible to control the etch reproducibly in the first 30 seconds of the etch period and it would therefore be an improvement if the etch rate could be slowed. This induction period is perhaps due to the oxide layer which at first would only be removed by the ion sputter etching component of the process which is small, until a chemically active surface appears²⁰. Further evidence of this was reported by Smolinsky *et al*¹⁸ in their studies of plasma etching of III - Vs in which they found that chlorine reacted only with GaAs and

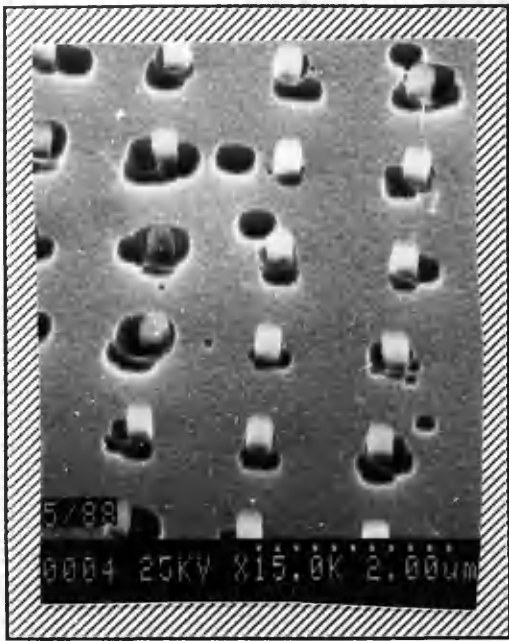


Figure 3.5 Anisotropic SiCl_4 etch followed by 3min PE.

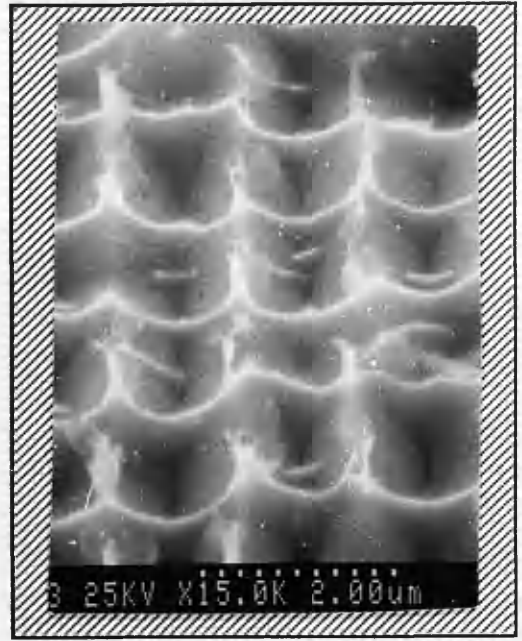


Figure 3.6 Anisotropic SiCl_4 etch followed by 5min PE.

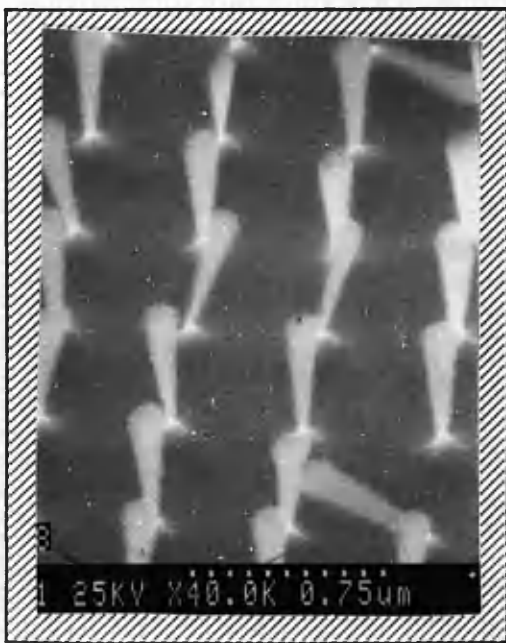


Figure 3.7 SiCl_4 RIE at 22mTorr



Figure 3.8 Anisotropic RIE at 11mTorr followed by RIE at 44mTorr.

left the oxide completely untouched. One method of diluting reactive ion etch gases which has been studied is to use a noble gas such as argon²¹. While this has the advantage that it is chemically unreactive and therefore should only contribute to the physical component of the etch process it has a higher molecular weight than the reactive species and is likely to increase the "damage" caused by the etch. The advantage of hydrogen is that it is a low molecular weight gas and would therefore not be expected to increase the damage. Indeed Semura *et al*²² reported that when CCl_4/H_2 was used to etch GaAs, and Raman Spectroscopy was used to analyse the crystal structure, this gas mixture showed as little damage as the wet etched surface for H_2 ratios above 0.6. Therefore diluting with hydrogen may also have the advantage that the surface damage is reduced.

3.5.1 The Etch Mechanism in SiCl_4/H_2

The reaction chemistry of SiCl_4 with H_2 is also well documented as this is one of the gas mixtures used to grow epitaxial silicon. The effect of adding one gas to another to improve the etch characteristics can be explained in terms of creation or suppression of chemically active species in the plasma by the additive gas. Semura *et al*^{17,22} reported that the etching characteristics of CCl_4 , Cl_3F and CCl_2F_2 were greatly improved by diluting with hydrogen. They found that RIE in pure CCl_4 produced isotropic etching and surface roughness which they suggest may be due to the high reactivity of the gas. First they investigated diluting the gas with oxygen. On diluting with O_2 the Cl content of the plasma and hence the etch rate increased because the O combines with the carbon which would otherwise require Cl and reacts with the CCl_3 to liberate Cl. The surface was also rough and covered with thin black films due to carbon deposits. Continued addition of O_2 reduced the etch rate due to adsorption of atomic oxygen onto the surface.

When the effects of mixing H_2 with CCl_4 were studied they found that as the H_2 flowrate increased, the etching rate gradually decreased and the etched surface morphology was markedly improved. From their measurements using XPS and Raman Spectroscopy they concluded that the damage decreases with increasing H_2 flowrate.

They suggest the following mechanism to account for this: the hydrogen scavenges chlorine from the CCl_4 by forming HCl and unsaturated compounds. The saturated compounds are then accelerated by the self-bias voltage and etch the substrate as physical ions resulting in a more anisotropic profile²². Why this should reduce the damage is uncertain as it is thought that the larger the physical component of an etch the more damage is caused.

The effects of mixing a fluorocarbon or chlorofluorocarbon gas with oxygen to improve etch properties has been extensively studied for silicon etching^{23,24}. It is worth discussing this mechanism as it is perhaps illustrative of the effects of gas mixture etching. From his studies of silicon and silicon dioxide etching by CF_4 diluted with either oxygen or hydrogen Mogab has proposed a different explanation to account for the improved etch characteristics. The etch rate of Si and SiO_2 in a CF_4 plasma are relatively low, but when O_2 is added the etch rates of Si and SiO_2 increase (figure 3.9). However a maximum etch rate for both Si and SiO_2 is not obtained for the same O_2 concentration - the maximum

for Si being approximately half the O_2 content for maximum SiO_2 etching. With the continued addition of O_2 , the etch rates decrease more rapidly for Si than for SiO_2 . These effects can be explained by considering the plasma and surface chemistry involved. Fluorine atoms are active in the etching of Si and the addition of O_2 to a CF_4 plasma results in an increase in the F atom concentration. This increase in concentration is due to the oxygen reacting with the CF_3 radicals to form COF_2 , CO and CO_2 which reduces the consumption of F atoms within the plasma leaving more to contribute to the etching of the silicon. Ultimately the F atom concentration decreases because of dilution.

If oxygen affected only the plasma chemistry, it would be expected that the maximum etch rates for both Si and SiO_2 to occur at the O_2 concentration which produces a maximum of F atoms. However the maxima for Si and SiO_2 are not coincident because the oxygen is also involved in the surface chemistry. In the case of Si etching, oxygen tends to chemisorb on the surface, thereby partially blocking direct access by F atoms. Since this effect increases as more oxygen is added, the maximum etch rate for Si does not occur at the maximum F atom concentration. A similar effect is absent for etching of SiO_2 because the surface is in effect covered with oxygen to begin with. Consequently the maximum etch rate for SiO_2 occurs when oxygen is first added producing a maximum F atom concentration in the plasma. Oxygen chemisorption also accounts for the more rapid decrease of etch rate for Si beyond the maximum²⁵. F atoms react much more rapidly with Si than with SiO_2 , so CF_4 - O_2 plasmas offer high selectivity of Si over SiO_2 .

If H_2 is added to a CF_4 plasma, quite different effects are noted. In reactive ion etching, at relatively low pressure, the etch rate of SiO_2 is nearly constant for H_2 additions up to about 40% while the etch rate for Si decreases monotonically to a value near zero at this concentration (figure 3.10). Adding H_2 in amounts exceeding ~40% causes unwanted polymer formation on the SiO_2 . It is therefore possible to selectively etch SiO_2 over Si by adding H_2 to CF_4 .

The difference in the behaviour of the etch when hydrogen is added is explained by Mogab as follows. CF_3 radicals etch SiO_2 by an ion-induced reaction which ultimately results in formation of SiF_4 . The C derived from these radicals is removed from the surface by combining with oxygen from the SiO_2 to form CO, CO_2 and possibly COF_2 gases. A similar reaction path with Si is unavailable, because there is no way to remove the adsorbed C, which blocks the fluorine from reaching active surface sites. The role of hydrogen then is twofold. It combines with F atoms to form stable HF thus removing a potential Si etchant, and particularly at higher pressures, it changes the plasma chemistry so that higher concentrations of etchant CF_3 are produced.

It may be that a similar reaction occurs to that of CF_4/O_2 when H_2 is added to $SiCl_4$ to etch GaAs or GaAs/AlGaAs. (As there is no preferential etching of GaAs over AlGaAs or vice versa it can be assumed that the results on GaAs only would be the same on GaAs/AlGaAs quantum well layers.) When H_2 is added to the feed gas a maximum etch rate is reached at about 25% H_2 (figure 3.11). The etch rate decreases with the continued addition of H_2 . If Cl atoms are formed in the same way as F atoms - by electron impact dissociation of $SiCl_4$ and consumed by combination with $SiCl_x$ radicals, the same mechanism may occur whereby added hydrogen results in the depletion of $SiCl_x$ radicals by

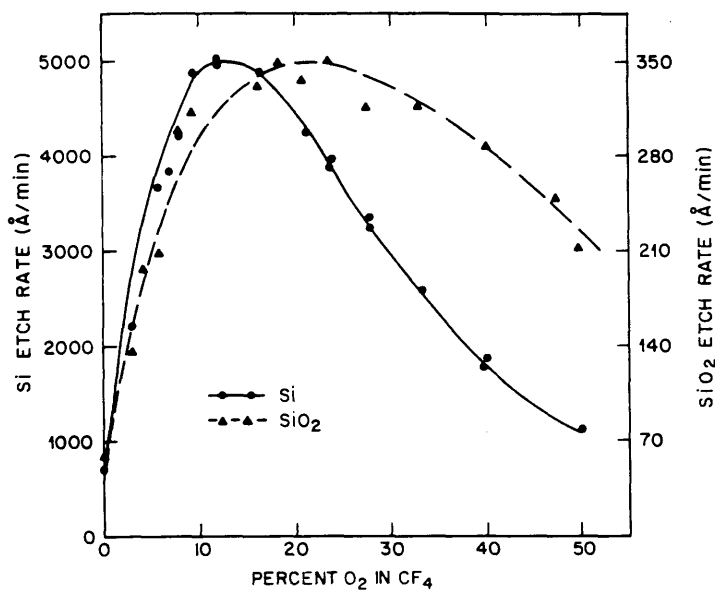


Figure 3.9 The addition of O₂ to a CF₄ plasma affects the rate of etching of both Si and SiO₂. (After Mogab. ref 2).

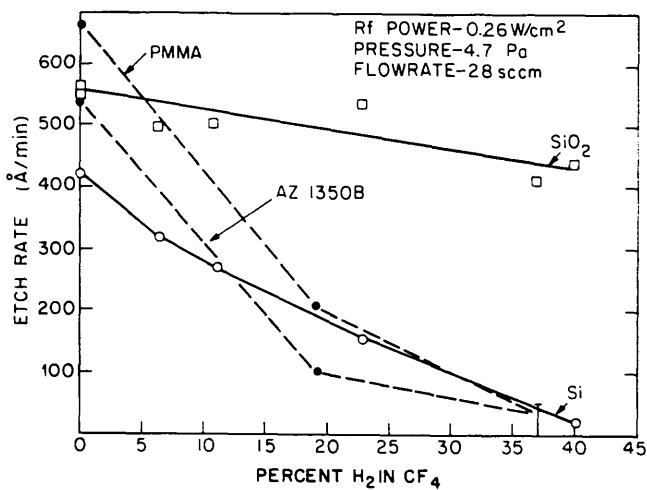


Figure 3.10 The addition of H₂ results in a rapid decrease of the etch rate of Si relative to SiO₂. (After Mogab. ref 2).

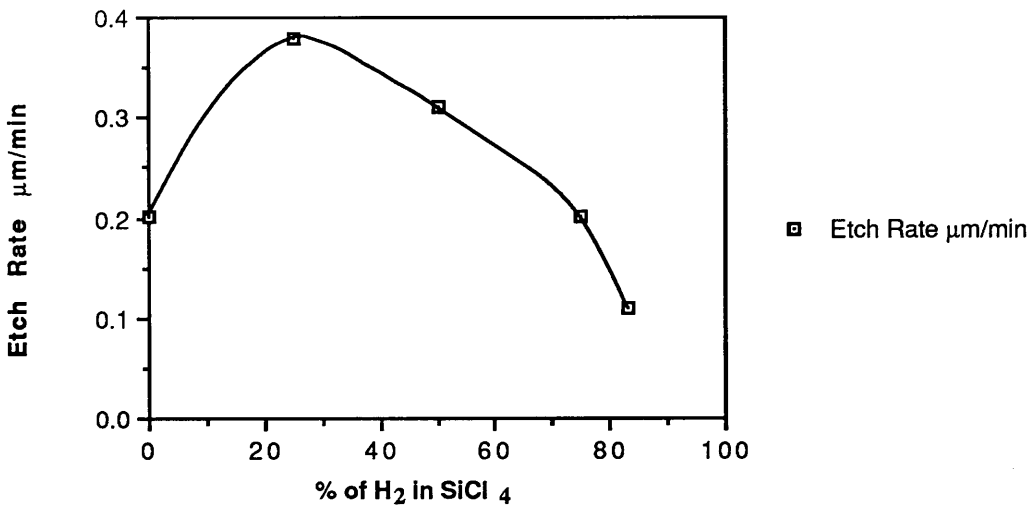


Figure 3.11 Etch Rate $\mu\text{m}/\text{min}$ versus the percentage of H_2 in SiCl_4 .

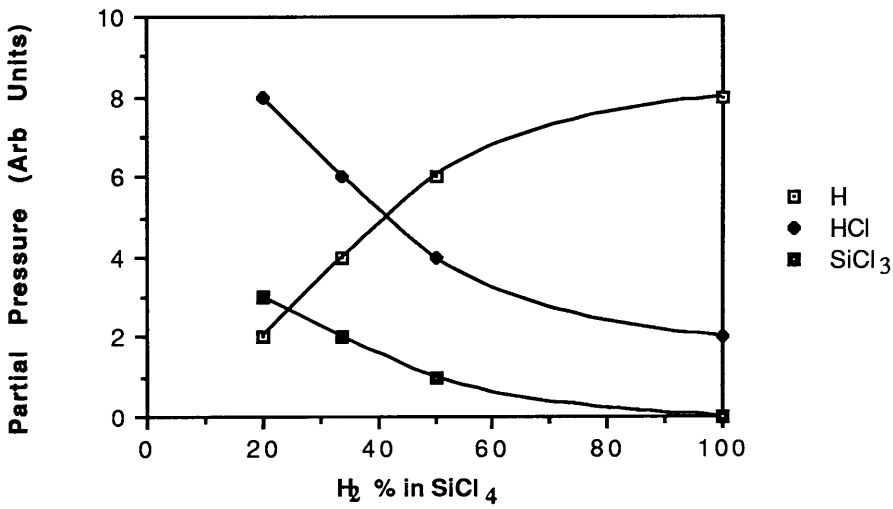


Figure 3.12 RGA analysis as the percentage of H_2 in SiCl_4 is increased.

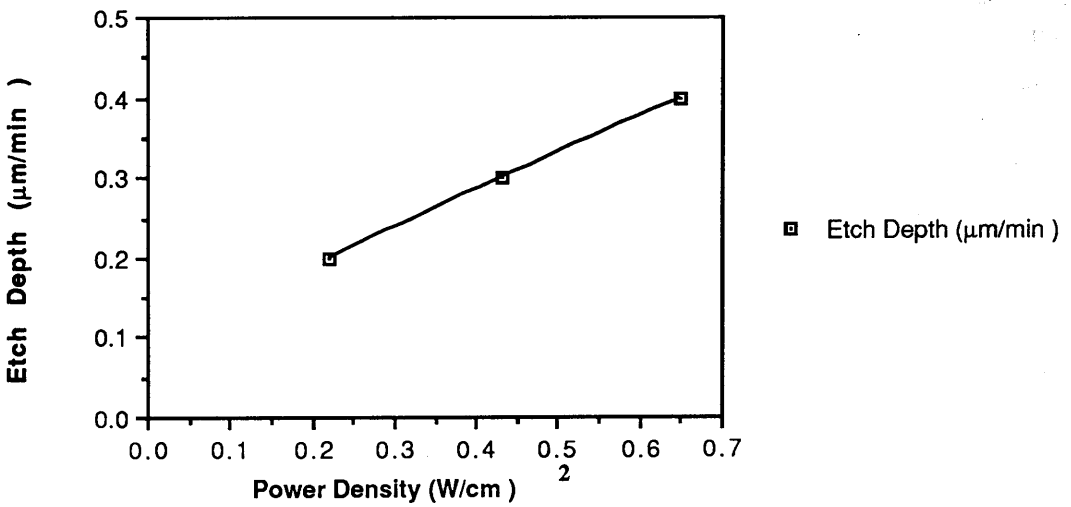


Figure 3.13 Etch depth $\mu\text{m}/\text{min}$ versus applied Power Density W/cm^2 .

the formation of $\text{SiCl}_x\text{H}_{4-x}$ which reduces the consumption of Cl atoms. The net result would be an increase in the Cl atom concentration and a corresponding increase in the etch rate.

There may also be a small contribution to the etch rate from etching by H atoms whereby the GaAs forms volatile hydride compounds²⁶.

There is also however the competing process suggested by the results of CF_4/H_2 . Here the Cl reacts with the H to form HCl thus removing a potential GaAs etchant. A similar result was found by Smolinsky *et al*¹⁸ when H_2 was added to CCl_2F_2 . As can be seen from the RGA analysis (figure 3.12) there is an increase in the HCl concentration which decreases as the percentage of SiCl_4 decreases. This is as expected as the amount of Cl available to react with the H is reduced as the percentage of H_2 in the feed gas is increased.

Other effects may also contribute to the change in etch rate observed. Hydrogen does perhaps contribute towards a cleaning effect in the chamber. Adsorbed oxygen on the chamber walls and water vapour are present in the etch chamber and oxygen may limit the etch process by causing a gallium oxide layer to form which slows down the etch rate.

3.5.2 Results

The main reason however for diluting SiCl_4 with H_2 was not to speed up the etch rate but to slow it down. The experimental equipment used is described in Section 3.3 - SiCl_4 RIE. This has been achieved by using a gas ratio of 1:5, $\text{SiCl}_4:\text{H}_2$ (see Table IV) whereby the etch rate was reduced to $0.1\mu\text{m}/\text{min}$ and quantum dots successfully etched with this gas mixture (figure 3.14).

An interesting result was obtained using a ratio of 1:1 SiCl_4/H_2 when the flowrate was increased to 24sccm for SiCl_4 and 8sccm for H_2 , hence increasing the pressure to 20mTorr. The etch rate increased to $0.4\mu\text{m}/\text{min}$ and an etch time of 1 minute was used. This resulted in anisotropic as well as isotropic etching and the etched quantum dot being much smaller than the mask (figure 3.15). An overall size reduction of 100nm could be obtained on 250nm QDs. Unfortunately dots of 80nm or less fell over as a slightly undercut profile also resulted, which caused the smaller dots to undercut completely before any reduction in overall diameter could be seen. The same affect was not obtained when the pressure was increased to 20mTorr by reducing the pumping and keeping the flowrate comparable to that used for SiCl_4 etching alone - 6sccm for SiCl_4 and 2sccm for H_2 . This change in profile described above, is perhaps due to the combined effect of the increased supply of the reactive species due to the increased flowrate and the higher pressure increasing the isotropic component of the etch. The addition of the hydrogen perhaps inhibits the forming of the gallium chloride layer by possibly increasing the volatility of these species which are thought to prevent lateral etching of the dots. This then enables etching to take place in both directions but the components must be balanced in such a way that a vertical profile results.

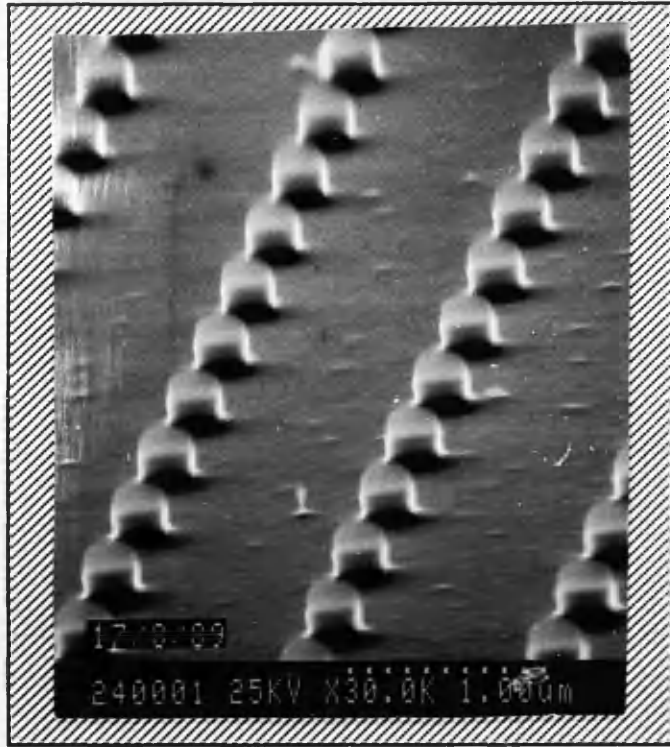


Figure 3.14 SiCl_4/H_2 RIE 1:5 ratio Etch Rate $0.1\mu/\text{min}$



Figure 3.15 SiCl_4/H_2 Ratio 1:1 Pressure 18mTorr
Isotropic and anisotropic etching.

Using a gas ratio of 1:3 SiCl₄:H₂ with a constant pressure of 10mtorr and temperature of 40°C, the applied power density was varied. As expected when the applied power density was increased the etch rate increased (figure 3.13) and the etch profile of the QD structures also changed. An applied power density of 0.65Wcm⁻² produced the most anisotropic etching (figure 3.18) and when the power density was reduced to 0.22Wcm⁻² a "necking" effect was seen showing that there was some sidewall bombardment i.e. the etch was less anisotropic (figures 3.16 & 3.17). This result is in agreement with the mechanisms outlined in Section 3.3.6.

It has been shown that H₂ can successfully mixed with SiCl₄ to slow down the etch rate and therefore increase the controllability of the etch process. The anisotropic undercutting of the etch mask could well be a worthwhile mechanism to utilise to reduce the overall size of quantum structures. No damage assessment measurements have yet been carried out to see if the damage characteristics of this gas mixture is improved over SiCl₄ etching.

3.6 CH₄/H₂ Reactive Ion Etching

A method of etching nanostructures was developed at Glasgow University by R Cheung, C D W Wilkinson *et al*¹⁴ which appears to give little crystallographic damage and can etch InP/InGaAs at room temperature unlike chlorinated gases where the etching must take place at elevated temperatures. They suggested that the action of CH₄/H₂ in etching GaAs was in some sense the inverse of metal organic chemical vapour deposition with the formation of (CH₃)₃Ga and AsH₃ as reaction products.

3.6.1 The Etch Mechanism in CH₄/H₂ RIE

Niggebrugge *et al*^{4,5} reported the first successful etch of InP with CH₄/H₂. They concluded that in CH₄/H₂ the etching mechanism is more chemical in nature than physical. They did so because if CH₄ is replaced by Ar, an efficient sputtering species, the etch rate decreased and the surface morphology degraded considerably. Secondly they found that if a photoresist mask was used a resistant film was deposited on the mask throughout etching making, in theory, infinite etching possible. If the physical sputtering was a dominant mechanism this layer would have been sputtered away. It is thought that if the etch is more chemical in nature, the sidewall damage would be reduced due to a reduction in the bombardment of the heavy ionic species. This is extremely advantageous for nanostructure fabrication. In order to see quantum confinement effects in the GaAs/AlGaAs system the QD has to be 30nm or less in diameter therefore if there is substantial sidewall damage it may be extremely difficult to obtain luminescence from the dots and wires.

CH₄/H₂ offers several advantages over Halogen gases for etching of InP, as at room temperature the chlorides of gallium are volatile, but those of indium are not²⁷. In III - V compounds the group III and group V halides have different volatilities. As has been shown by Balooch *et al*¹⁵ this can result, in the case of GaAs in a gallium rich surface. This layer results because the group V element - the arsenic is selectively removed from the surface leaving a layer enriched in the group III element. Like AsCl₃ and GaCl₃ in GaAs, PCl₃ in InP has a higher vapour pressure than InCl₃ (10 Torr as opposed to

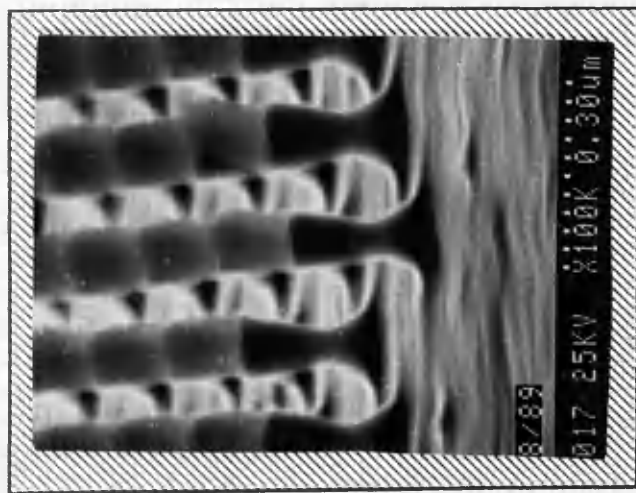


Figure 3.16 SiCl₄/H₂ Ratio 1:3
Power Density 0.22W/cm²

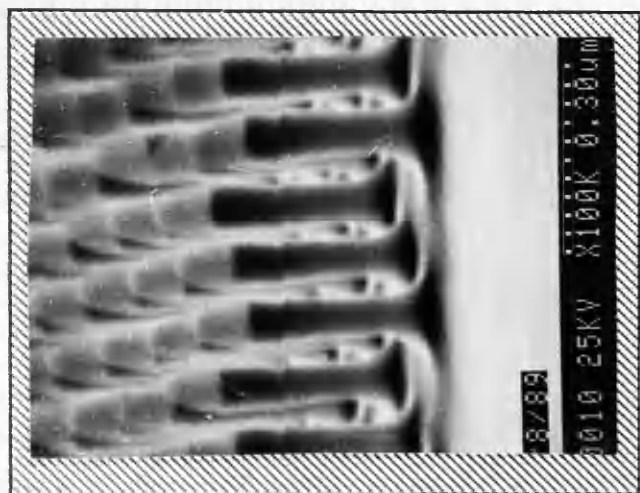


Figure 3.17 SiCl₄/H₂ Ratio 1:3
Power Density 0.43W/cm²

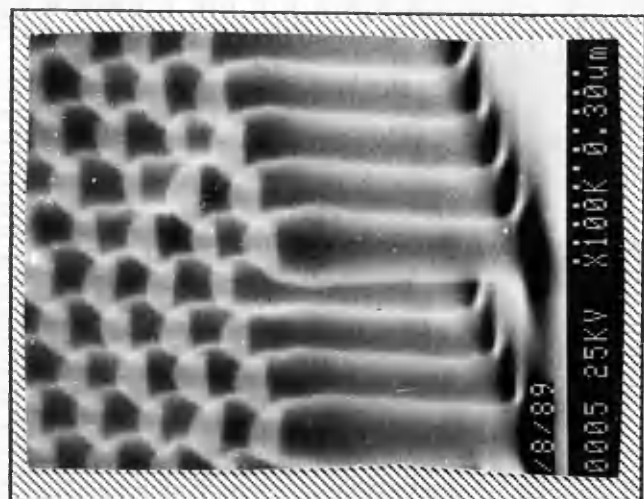


Figure 3.18 SiCl₄/H₂ Ratio 1:3
Power Density 0.65W/cm²

1×10^{-4} Torr)²⁷. However unlike GaCl₃ which has a high thermal evaporation rate at room temperature, InCl₃ does not, and physical sputtering is the dominant method of removal at room temperature. This results in an In residue being left which does not occur in the etching of GaAs at room temperature. A temperature above 150°C is required to plasma etch InP with chlorine (derived either from pure chlorine or from chlorocarbon gas, sometimes mixed with oxygen), and the temperature of the substrate must exceed 250°C to obtain a smooth surface²⁸ as at these elevated temperatures the indium chlorides can evaporate from the surface. Hirata *et al*²⁹ however reported successful etching of InP gratings at temperatures of 50°C using a mixture of CCl₄/O₂ and Hu and Howard¹² reported successful etching of GaAs and InP at the same temperature (not given) using a mixture of CCl₂F₂/Ar/O₂ in a 1:1:1 ratio. Several authors^{27,29} have reported that a rate limiting layer of carbon is adsorbed on the InP surface when carbon containing gases are used. However when oxygen is added to the feed gas it reacts with the obstructive carbon thereby enhancing the etch rate. Unfortunately mixing an etch gas with oxygen produces problems due to degradation of organic resist masks such as photoresist or HRN. As already stated above, it is thought that the methane is the dominant etchant species in CH₄/H₂. However Tu *et al*³⁰ have shown that hydrogen can also contribute to the etching of InP, although again an In rich surface results for the reasons described above.

CH₄/H₂ therefore offers significant advantages over chlorine containing gases as etching of InP can take place at room temperature, and a constant etch rate much slower than that obtained when using chlorine containing gases results when etching GaAs. In both cases there is little or no degradation of organic resist masks and a smooth surface and an anisotropic etch profile are easily obtainable.

3.6.2 Results

CH₄/H₂ etching was performed in an Electrotech SRS Plasmfab 340 RIE machine. The anode and cathode are made of aluminium with a nominal anode/cathode area ratio of 3:1. In addition the cathode is coated with Titanium oxide. The machine is operated at 13.56Mhz. The substrate was mounted on the cathode the temperature of which was kept constant at 30°C.

Using the conditions outlined by Cheung *et al*⁶ and listed in Table IV successful fabrication of GaAs/AlGaAs quantum dots was achieved (figure 3.19). Unfortunately it was almost impossible to obtain vertical sidewalls as CH₄/H₂ always seems to give an overcut profile on QDs although extremely vertical walls are obtained on QWWs. The two competing processes of (1) redeposition and/or adsorption of nonvolatile or less volatile products onto the sidewalls and (2) sputtering and/or desorption from the etched sidewalls determine the slope of the overcut. The applied power was raised to 0.75Wcm⁻² and this increased the verticality of the walls although the etching achieved using this gas was never as truly anisotropic as that achieved using SiCl₄. As increasing the applied power, increases the dc bias and hence the momentum of the bombarding ions, this would increase the "damage" to the QDs and QWWs and therefore the applied power was not increased further in an effort to achieve perfectly vertical sidewalls. Increased anisotropy can also be achieved by lowering the pressure but as the etch pressure was already low at 10mtorr, any lower pressure would have reduced the reactant concentration more and slowed down the etch rate further.

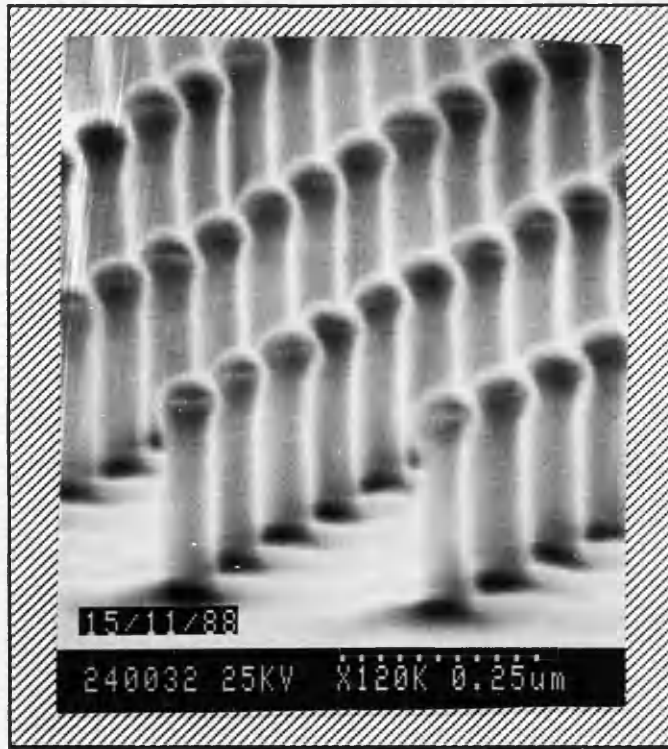


Figure 3.19 CH₄/H₂ Etched GaAs QDs

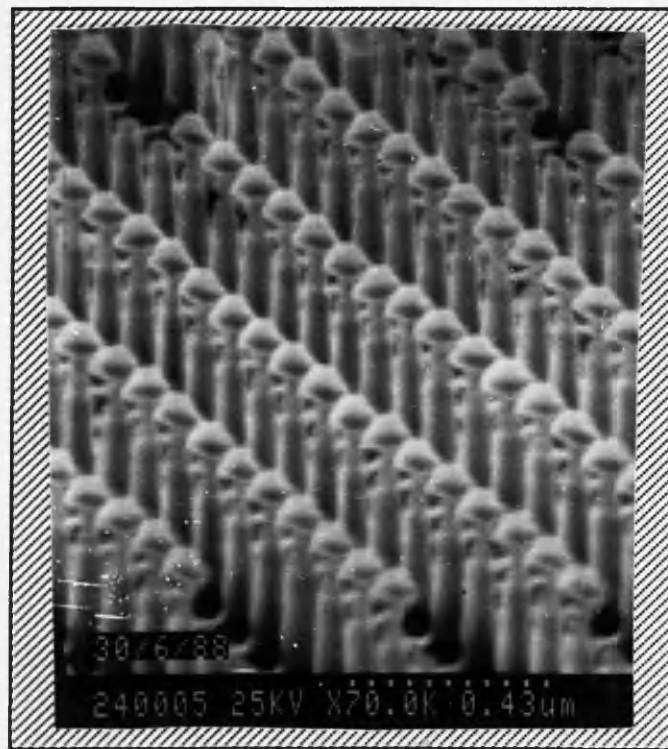


Figure 3.20 CH₄/H₂ etched InP/InGaAs QDs

CH_4/H_2 has also been used to successfully etch quantum dots in InP/InGaAs. Using a gas ratio of 3:2 (CH_4/H_2) and an operating pressure of 16mTorr or below and a power density of 0.75Wcm^{-2} , an etch rate of 75nm/min (as opposed to 25nm/min for GaAs/AlGaAs) was obtained. The etch profiles are however still slightly overcut. If the SEM micrograph in figure 3.20 is observed closely the slight variations in the width of the dot can be seen. It is thought that this is due to preferential etching of the InGaAs QW. Etching at the gas ratios successful for producing GaAs/AlGaAs QDs resulted in preferential etching of the P and unreacted In being left on the surface as "bumps".

Finally the one major drawback for CH_4/H_2 RIE or any gas mixtures using H_2 , is that H_2 acts as a passivator of donors or impurities. For electrical measurements passivation of donors can have catastrophic results. However complete restoration of free carrier concentration occurs by annealing the sample at temperatures above 300°C for a time dependent on the type of doped material used and the thickness of the layer³¹. For optical applications hydrogen passivation of defects and impurities which could act as nonradiative recombination centres could in fact be a positive affect by increasing the luminescence efficiency²⁰. Results reported in Chapter 5 and 6 show that the hydrogen does not enhance or reduce the PL efficiencies from CH_4/H_2 etched quantum well structures.

3.7 Ion Beam Milling

Measurements of the photoluminescence efficiency from QDs etched using SiCl_4 or CH_4/H_2 suggested that the effect of the high surface recombination velocity of GaAs which was expected to quench the luminescence from the structures in the submicron range was small (see Chapter 4, Section 4.4.1).

It was thought that perhaps the chlorine or methane acted as some sort of passivating agent combining with broken bonds at the surface and thus passivating defects. This might restore the luminescence efficiency of the QDs³². It is known that an etched surface is contaminated with the etching species to a depth of the order of 1nm²². A further effect may be the difference in the composition of the surface and sidewalls after etching as it is known that the surface is gallium rich due to excess gallium chlorides¹⁴.

To investigate this QDs were fabricated using argon ion milling, a simple sputtering process with no reactive component. If reactive species were important the photoluminescence efficiencies from these milled structures should be greatly reduced.

3.7.1 Comparison of Ion Beam Milling and Reactive Ion Etching

Ion Beam Milling (IBM) and RIE have similar resolution capabilities, but each have some unique advantages. RIE is a material selective process depending on the choice of the plasma gas. Ion milling however does not require reactive compatibility between the etchant and the etched material. One disadvantage of ion milling is that material sputtered from the bombarded area is partially deposited on the adjacent walls³³ resulting in an overcut profile (see figure 3.21). The profile formed during etching is therefore not as vertical as that obtained from the anisotropic etching process such as SiCl_4 RIE.

3.7.2 The Etch Mechanism in Ion Beam Milling using Argon

When a solid is bombarded by ions or neutral atoms, material is removed from the surface of the solid. This process is called sputtering. This is achieved in IBM by using a beam of collimated monoenergetic ions extracted from a gas plasma. Electrons are injected into the ion beam so that the overall charge of the beam is neutral. Removal of material from the bombarded surface occurs as a result of the transfer of momentum from the incident ion to the atoms of the solid provided that the energy transferred to the atom in the collision process exceeds the chemical binding energy and when the momentum imparted to the atom is directed away from the surface.

The most important material property in ion etching is the sputter yield which is defined as the number of sputtered target ions per incident ion. The sputter yield depends on the material being etched, the bombarding atoms and their energy and the angle of incidence. The sputter yield bears a relation to the binding energy of the target atoms. It is low for elements such as carbon, silicon and titanium and high for gold and platinum. Obviously titanium will then make a good etch mask for IBM and gold a poor one. The sputter yield increases with increasing energy and usually saturates above a few keV as the penetration of the ion into the target increases without a corresponding increase in the energy lost close to the surface. For this reason ion etching is usually done with energies below a few keV. Noble gases, which are used in most cases, exhibit a higher sputtering yield relative to other atoms and also avoid a possible chemical reaction. The sputtering yield usually increases as θ increases ($\theta = 0^\circ$ at normal incidence). The increase is due to the longer path the bombarding ion travels closer to the surface, which permits more excited atoms to escape from the surface. With further increase in θ the sputter yield reaches a critical angle above which ion reflection and subsequent reduction in the sputtering yield occurs².

3.7.3 Results

These experiments were carried out using an Oxford OAR2255 ion beam system with a current density of 0.14mAcm^{-2} at 20° tilt and continuous rotation. In order to successfully etch GaAs/AlGaAs QDs the the beam voltage (a) and the angle of incidence of the beam on the sample (b) had to be chosen.

It is known that the efficient operating regime for IBM is for beam energies between 100 to 1000V. Above 1000V channeling effects and surface layer damage become important and below 100V the incident ions do not have sufficient energy to eject atoms from the material³⁴. A beam voltage of 500V was therefore used and this produced an adequate sputter rate of GaAs.

The second major parameter, the angle of incidence of the incoming beam effected the sidewall profile of the QDs. Etching at $\theta=20^\circ$ tilt was found to produce slightly overcut dots. When the angle was increased to 30° this effect became worse. An angle of 20° was used. A contribution to this overcut profile could come from redeposition. Since most of the sputtered atoms are of low energy and obey a cosine distribution some of the sputtered material may simply redeposit on opposite surfaces. A summary of the parameters used is shown in Table V. Titanium was used as the masking material.

TABLE V**ARGON ION MILLING PARAMETERS**

Pressure	0.4μbar
Cathode Current	6.17A
Discharge Current Voltage	0.64A 51V
Accelerator Current Voltage	7.4mA 105V
Beam Current Voltage	15mA 500V
Current Density	0.14mAcm⁻²
Neutraliser Current Bias Filament Discharge	1.5mA 58.7V 3.6 A 0.14A

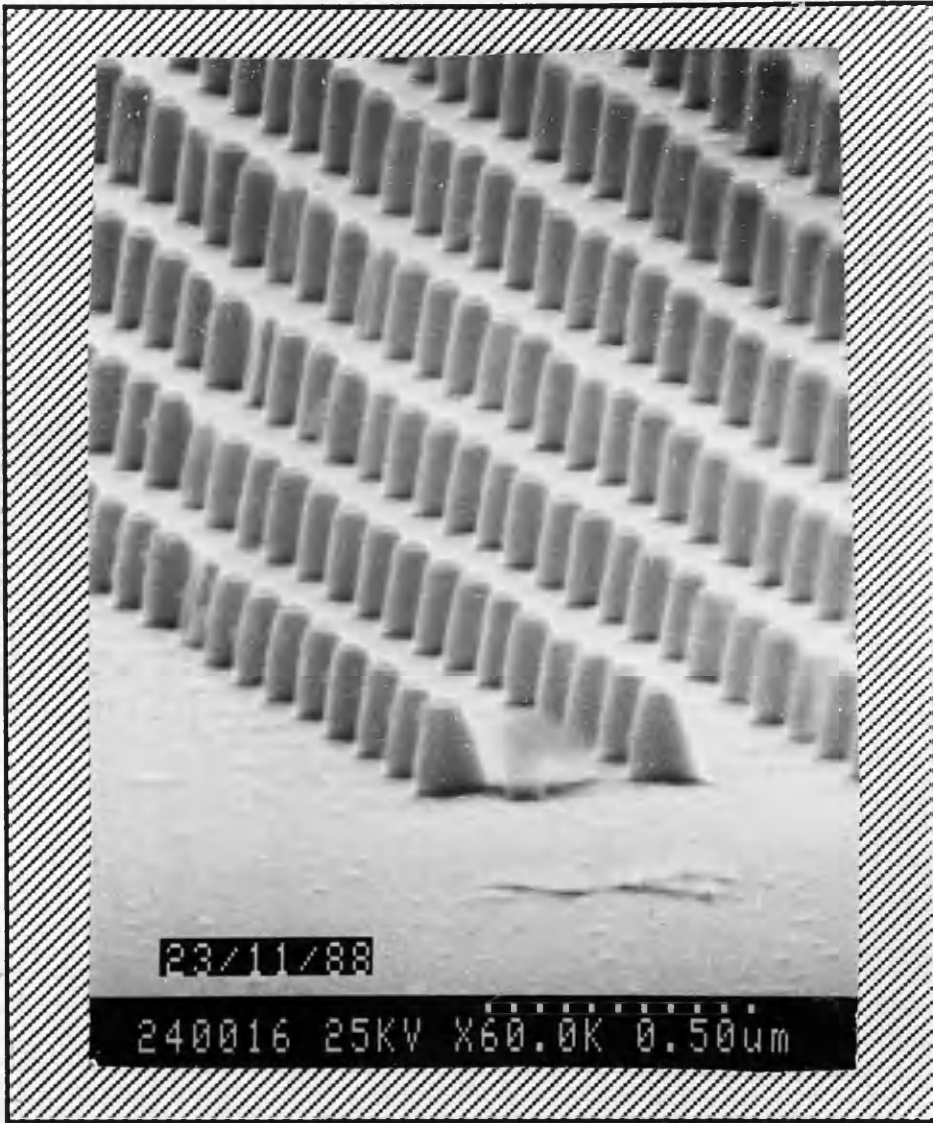


Figure 3.21 Argon Ion Milled GaAs/AlGaAs QDs

Nichrome and HRN had too high a sputter yield (i.e the efficiency with which incoming ions remove material).

QDs were successfully fabricated on GaAs/AlGaAs quantum well material down to 100nm in diameter. It is difficult to be precise about the diameter due to the overcut profile as can be seen in figure 3.21.

3.8 Oxygen Plasma Etching

In order to see if the organic HRN mask left on the dots during the optical characterisation process, attenuated the signal in any way, the HRN was removed by oxygen plasma ashing. The atomic oxygen produced in the O₂ discharge rapidly converts the resist to volatile by-products such as CO₂ and H₂O². This was done in a Plasmafab 505 oxygen barrel etcher at a power of 60W, a flowrate of 40sccm, a pressure of 100mTorr and etch time of 30 minutes.

3.9 Reactive Ion Etch Induced Damage

As already mentioned in Section 3.1 dry etch damage refers to any change to the semiconductor material such as distortion of the crystal lattice brought about by the material being subjected to the etching effects of a plasma, which stops it behaving electrically or optically, like the perfect unprocessed material. The effects of damage are especially important when fabricating quantum structures as relatively small amounts of damage - 10nm on a sidewall for example - are relatively unimportant when fabricating structures with dimensions in the μm size range but could be very important when the structure has an overall diameter of 30nm.

In anisotropic RIE there is also a difference between surface and sidewall damage. This difference is due to the way in which the bombarding ions hit the material. In surface damage the surface is being constantly bombarded with ions whereas sidewall damage is caused by ions reflecting off the surface and hitting the sidewalls. It has been shown by Cheung *et al*³⁵ that surface damage is independent of etch depth but sidewall damage increases with time. Surface damage is not important in the optical excitation experiments carried out in this work as the areas which are to be investigated are always protected by a metal or organic resist mask. It is unlikely that there is any significant ion penetration through the mask and therefore it is the sidewall damage which is of crucial importance.

3.9.1 Damage assessment by current carrying devices

Many authors^{31,36-38} have reported the effects of dry etching on GaAs on the electrical characteristics of GaAs devices. A common technique is to fabricate Schottky diodes on the etched surfaces and then characterize the diodes by their barrier height and ideality factor derived from the I-V characteristics. Since Schottky diode formation requires only a metal evaporation on the front surface after RIE and no high temperature processing steps, the damage induced in the GaAs can be obtained without having to take into account the effects of subsequent processing. The barrier height and the ideality factor give a measure of the extent of the damage. The higher the ideality factor the greater the damage. Using this

method Pang³⁶ demonstrated that IBM with Ar caused more surface damage than RIE with Cl₂, SiCl₄, CCl₂F₂ and CF₄. Pang³⁷ also showed that the amount of damage could be minimized by reducing the ion penetration distance into the substrate by reducing the ion energy.

To investigate the sidewall damage different methods must be used. Thoms *et al*³⁹ investigated the effect of dry etching by fabricating a rib (or wire) in a doped epilayer on an undoped substrate. This method would give an indication of the sidewall damage by measuring the resistance of wires of varying width. It was found that as the energy of the bombarding ions was increased the depletion width in the wire increased i.e. the effects due to damage had increased. Pang *et al*⁴⁰ measured the damage on sidewalls by fabricating structures which consisted of narrow conducting channels between Ohmic pads. They observed channel conduction with channel widths down to 0.08μm. The difficulty with using electrical measurements to assess sidewall damage is that there is an intrinsic depletion width on the sidewall. Thoms *et al*³⁹ were able to obtain a control for this by wet etching a wire and measuring the minimum depletion width from such a low damage process. This was not done by Pang *et al*⁴⁰ and the depletion width had to be estimated before a measure of the actual damage could be obtained. Cheung *et al*³⁰ also employed the method outlined by Thoms *et al*³⁹ to compare the cut-off widths of n⁺ wires etched using SiCl₄, CH₄/H₂ and wet etched wires. Damage of 30nm on each sidewall was measured for SiCl₄ and 20nm for CH₄/H₂.

3.9.2 Damage assessment by photoluminescence measurements

Due to the many areas in which dry etching is now employed to fabricate devices, it is also necessary to know the effect dry etching has on the optical performance of semiconductor materials. It may be that the factors which affect transport properties do not effect radiative recombination. Photoluminescence (PL) can give a measure of the extent to which a semiconductor has been affected by the exposure to RIE by comparing the intensity and the width of the PL peak before and after processing (or with a control sample). Results by Namba *et al*⁴¹ showed that optically, doped GaAs samples were affected by Ar sputter etching. An indication of the depth of the damage could be given by exciting the sample with different laser lines as this changes the penetration depth of the light. For example the 633 line of a He-Ne laser has a penetration depth of 240nm and the 488nm line of an Argon Ion laser to 88nm. Yuba *et al*⁴² reported PL degradation from GaAs and InP etched by Ar IBM and that InP withstands the process better than GaAs which shows a higher and deeper degree of damage. No explanation is given for this finding.

Rossabi *et al*⁴³ also used temperature dependent PL to compare the amount of damage caused by RIE with HCl or Cl₂ and wet etching after MBE regrowth. Suprisingly they found that Cl₂ produced less damage than wet etching as at lower temperatures the Cl₂ etched sample had the highest intensities. This is extremely unlikely. As only GaAs was used and not quantum well material it is likely that the dry etching introduced exciton binding defects emitting luminescence at high intensities at low temperatures. Unfortunately no spectra for the control sample are shown as this would have clarified the expected intensities from the material.

All of the above methods of assessing dry etch damage optically are only able to look at the surface damage. It has already been shown electrically that surface and sidewall damage are different. Quantum dots offer a unique method for optically assessing the sidewall damage and the results of these experiments are presented in Chapter 5 and 6.

3.9.3 Damage assessment by cathodoluminescence measurements and transmission electron microscopy

Other methods used to assess dry etch damage are cathodoluminescence (CL), cross-sectional transmission electron microscopy (TEM), and Raman scattering. Wong *et al*⁴⁴ used CL to obtain a profile of the depth of the RIE induced damage by using material containing multiquantum wells of different widths at different depths in the sample. Each quantum well has a unique spectral signature dependent on its width and by placing these wells at varying depths from the sample surface a correspondence between CL peak position and sample depth is obtained. Argon sputtering and RIE with $\text{CCl}_2\text{F}_2/\text{BCl}_3$ gas mixture at different bias voltages were investigated. CL was performed before and after annealing at 350°C for 20 minutes. This is a particularly elegant method for assessing the depth of the damage and Wong *et al*⁴⁴ showed that as the bias voltage was reduced the depth of the damage was reduced. Interestingly they showed that as the etch time is increased the damage did not penetrate any deeper into the sample but it did increase in magnitude. It was also shown that more damage was obtained when ions of lower mass were used by comparing the damage from Ar sputtered samples (40amu) and He (4amu). Helium produced by far the greater damage. However since light ions impart less energy to the host atoms upon collision the damage created should be less severe. This was found to be the case as the QWs recovered significantly more than the Ar etched samples on annealing. When RIE was used no damage could be seen. This is because the first well was 30nm from the surface and this shows that the RIE damage must occur in the first 30nm. Obviously by situating a well in the first 30nm more information on the extent of the damage could be obtained. Finally they showed that significant recovery of the CL intensity could be achieved by a post etch anneal at 350°C for 20 minutes with the sample sandwiched between two GaAs wafers to prevent arsenic outdiffusion.

Cathodoluminescence can also offer significant advantages in assessing the damage in quantum dots as a signal could be obtained from one dot only and not from an array of dots as is necessary in photoluminescence. GaAs/AlGaAs QD samples were assessed using CL by Prof J Steeds and Jiannong Wang at Bristol University. The material structure is described in Chapter 5 Section 5.3. When the dots are imaged using cathodoluminescence, the detector can image at different wavelengths enabling a picture of the luminescence from wells at different depths to be seen. Figure 3.22 shows the image from 100nm QDs detected at (a) 780.2nm and (b) 804.0nm. Photograph (a) shows the luminescence from the 5nm QW and (b) from the 10nm QW. The arrow points to a quantum dot where the lower 10nm well luminesces but the 5nm well does not. This suggests that this upper well has been damaged by the dry etching. This is perhaps due to the mask on this dot disintegrating. This method is useful as it is possible to see the optical behaviour of individual dots whereas in Photoluminescence it is the behaviour of a complete array of dots that is measured.

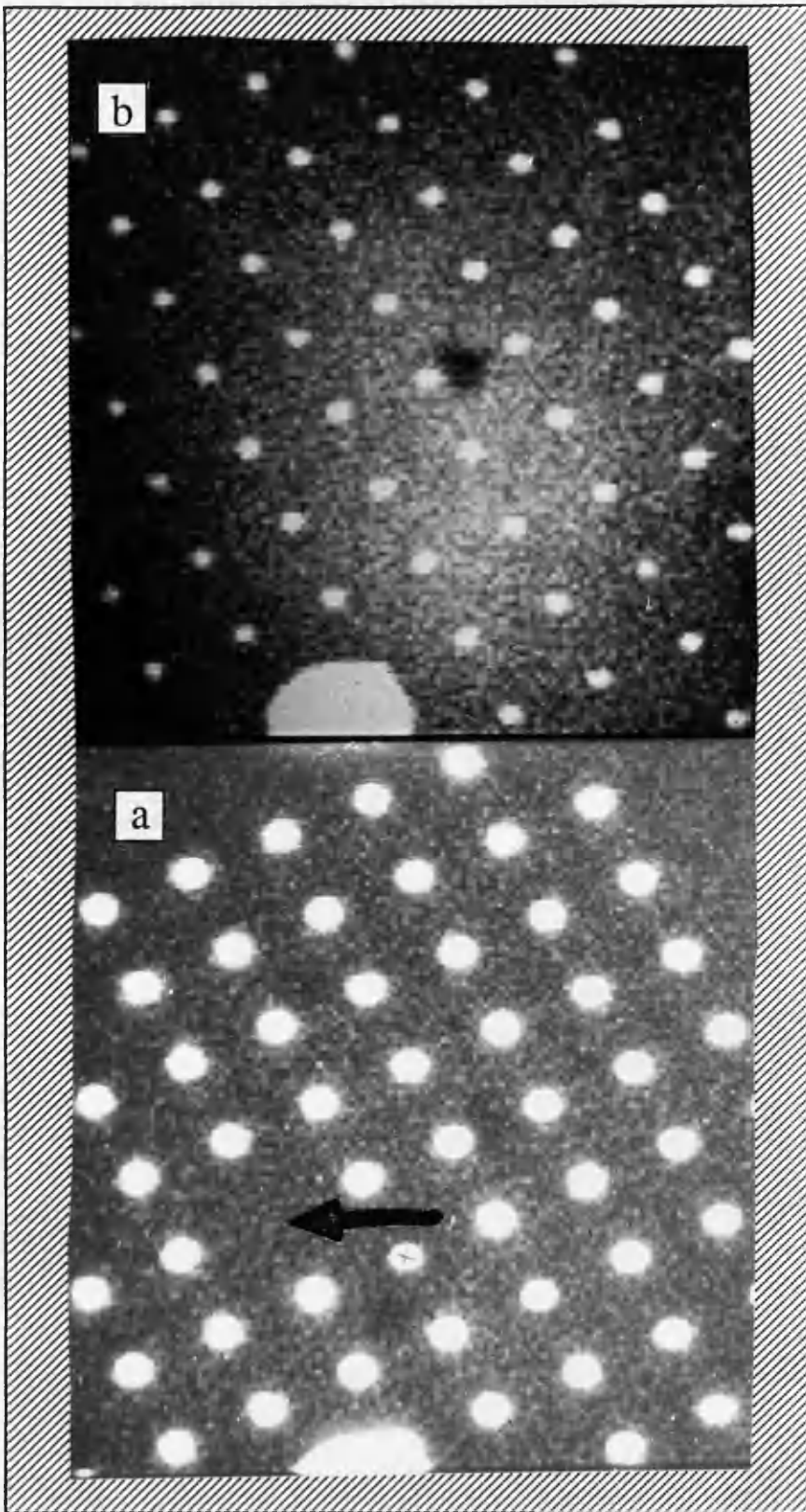


Figure 3.22 Cathodoluminescence micrograph of QDs fabricated in GaAs/AlGaAs QW material. Luminescence from (a) the 5nm QW and (b) the 10nm QW.

TEM has been used to assess the microscopic nature of the damage. By etching a quantum wire on a mesa Cheung *et al*⁴⁵ were able to assess the sidewall damage. This showed that the crystallinity of the wire was maintained right to the edge but that there was a change in composition graded over some 50nm which the authors ascribed to the absence of arsenic.

3.9.4 Damage assessment by Raman Scattering

As it is believed that RIE induced damage occurs within several tens of nanometres of the surface it is desirable to utilise a technique which has a high sensitivity for surface layers. Raman scattering is a technique which enables the study of lattice vibrations (or phonons) to be made. The features seen in a Raman spectrum arise from the interaction between incident laser light and the variation in crystal potential caused by quantized lattice vibrations⁴⁶. Theoretically, the Raman scattering selection rules for the optical phonons of GaAs based on the back-scattering configuration used, predict that only the LO phonon is observed from the (100) GaAs surface⁴⁷. The TO mode is symmetry forbidden. When the crystal symmetry is changed in some way, for example distortion of the lattice by ion bombardment from a plasma which reduces the long range crystalline order, it becomes possible for the TO phonon to be observed and this mode is then seen in the Raman Spectrum along with the LO mode. A measure of the extent of the damage to the crystal can be obtained by calculating the TO/LO intensity ratio. As this increases the damage is thought to increase. The advantage of Raman Scattering, like photoluminescence measurements, is that by varying the wavelength of the incident laser light the penetration depth changes, so the depth of damage can be reasonably accurately ascertained. As the light goes from blue to red the penetration depth increases⁴⁷.

Detailed studies of the Raman Spectra obtained from dry etched surfaces and QDs were made by Dr M Watt and Dr C M Sotomayor Torres. First dry etch damage to plain unprocessed GaAs (doping $2 \times 10^{17} \text{cm}^{-3}$ with Si) was investigated. These samples were supplied by R Cheung. Various etch powers were investigated. Figure 3.23 shows the Raman Spectrum obtained from two samples etched in SiCl_4 , one at a power density of 0.43Wcm^{-2} and the other 0.22Wcm^{-2} . While both the etched samples show the TO mode which is supposedly forbidden for this scattering geometry, the control sample shows only the LO mode. The TO/LO ratio for the 0.43Wcm^{-2} sample is 0.3 and 0.17 for the 0.22Wcm^{-2} sample. These results suggest that the sample etched with the higher power suffered more crystalline damage. When the exciting light was varied from 482.5 through 530.9 to 647.1nm changing the penetration depth from 35nm to 145nm it was found that only the sample etched at 0.43Wcm^{-2} showed a TO mode with a penetration depth of 65nm, which was not apparent at a depth of 145nm.

From these results Watt *et al*⁴⁷ concluded that the TO mode appears when the crystal is damaged and increases in intensity as the damage increases. Secondly they concluded, that as the scattering volume increases by increasing the laser penetration depth, and the TO phonon intensity decreases, the contribution to the spectrum from the damaged volume decreases. This results suggest that the crystalline damage lies close to the surface of the material. Watt *et al*⁴⁷ also showed that the damage to the crystal was isotropic.

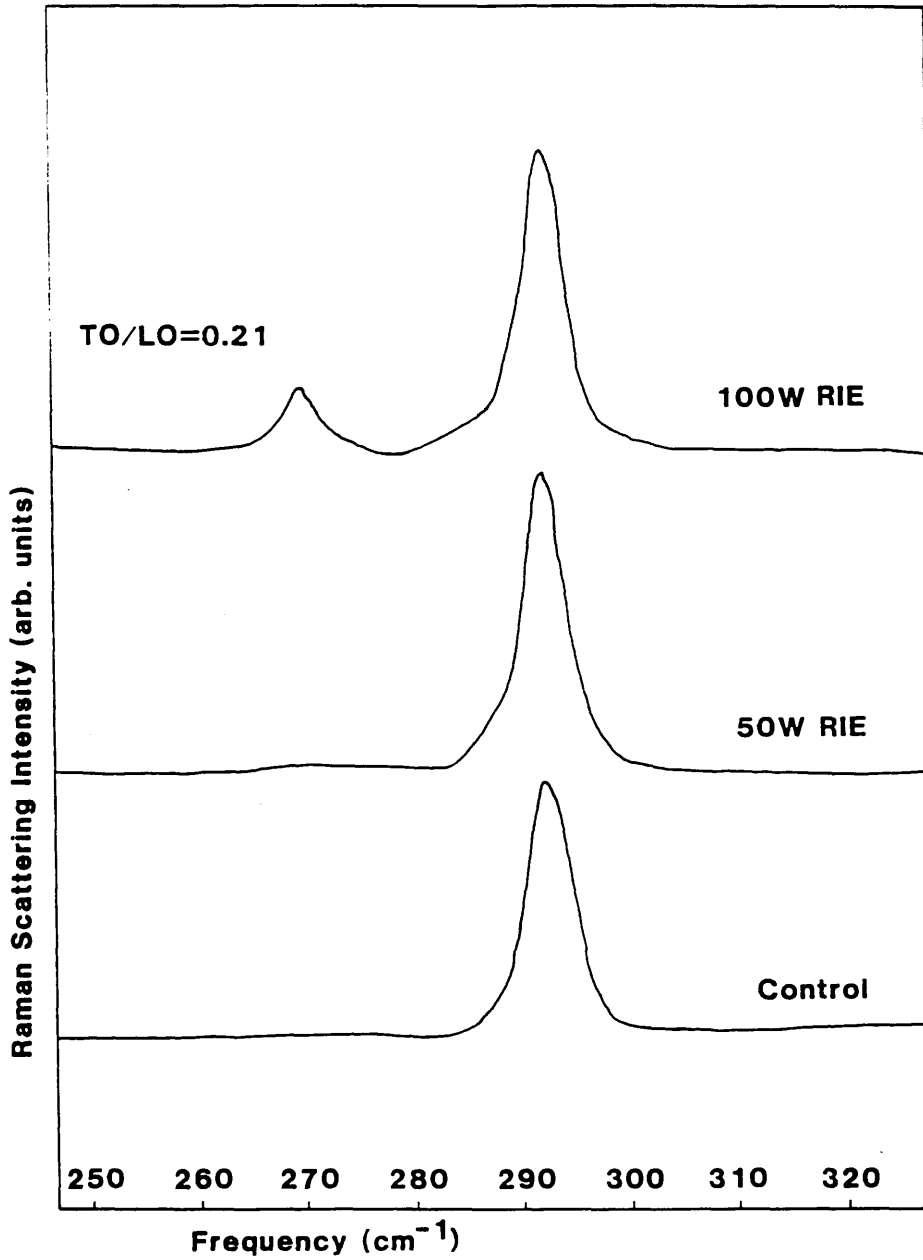


Figure 3.23 Raman scattering spectra from two etched samples and the control sample. (After Wait⁴⁷)

Samples were fabricated using the process outlined in Chapters 2 and 3 on undoped bulk GaAs. As the material did not contain any quantum wells these structures are called quantum cylinders and not quantum dots. Ten samples in all were fabricated with quantum cylinders of different dimensions varying from 60 to 200nm in diameter and etch depths from 150 to 570nm. Three samples showed a new spectral feature at an energy between the LO and TO phonons (figure 3.24). The TO phonon is seen with intensity of the same order as the LO phonon because it is no longer a forbidden mode: by patterning the surface with the cylinders the scattering geometry is now changed, and the TO mode becomes an allowed mode. Interestingly the off-pattern spectra show only the LO phonon indicating that the sample surface after etching is quite smooth and has minimal damage⁴⁹.

In the three samples which showed a new spectral feature, the quantum cylinders had dimensions of 80nm or less (60, 60 and 80nm) and were etched to a depth greater than 200nm (290, 210 and 310nm). The etch profile on these samples was vertical with little or no under or overcut. The same diameter is therefore maintained throughout the length of the cylinder. The etch depth is also important as in small vertical cylinders of diameter 60nm, but etch depth of only 150nm, no additional spectral feature was seen. It is thought that this is because these cylinders were too short to sustain the mode corresponding to the additional spectral feature. Watt *et al*^{47,48} investigated the possibility that the additional spectral feature seen, was due to an amorphous signal from the RIE induced damage layer, in particular from the gallium chloride layer that is discussed in Sections 3.4.1 and 3.4.2. This possibility was discounted as the spectrum of amorphous GaAs would contain a broad band reflecting the phonon density of states and this was not observed.

It was therefore concluded that this spectral feature could be due to a surface phonon of the cylinder. When the experimental data is plotted on a graph of theoretical surface mode frequency as a function of cylinder radius (figure 3.25) good agreement is obtained⁴⁸. However two characteristics must be demonstrated in order to identify a surface phonon: the frequency must be shown to change with both cylinder radius and the dielectric constant of the surrounding medium. The first criterion has been fulfilled as can be seen from figure 3.25. To investigate if the frequency changes with dielectric constant one sample was coated with a layer of CVD-grown silicon nitride. The additional spectral feature did indeed shift to lower energies confirming that it is indeed a surface phonon mode. As a surface phonon mode is seen this would suggest that the crystallinity of the surface has been preserved and the effect of the dry etch damage on the optical behaviour of quantum cylinders is minimal. This result is in agreement with those presented in Chapter 5 - Photoluminescence studies of free standing MBE Quantum Dots and Chapter 6 - Photoluminescence studies of Overgrown Quantum Dots and Wires. Similarly when the angle of the incident light was varied with respect to the sample surface a stronger intensity was obtained with light incident at 45° again agreeing with the results presented in Chapter 5.

3.10 Summary

GaAs/AlGaAs QDs down to 20nm diameter and QWWs down to 50nm diameter have been successfully fabricated by RIE using SiCl₄, SiCl₄/H₂ and CH₄/H₂. InP/InGaAs QDs down to 40nm in diameter have been fabricated using CH₄/H₂. GaAs/InGaAs QDs down to 60nm in diameter have been fabricated

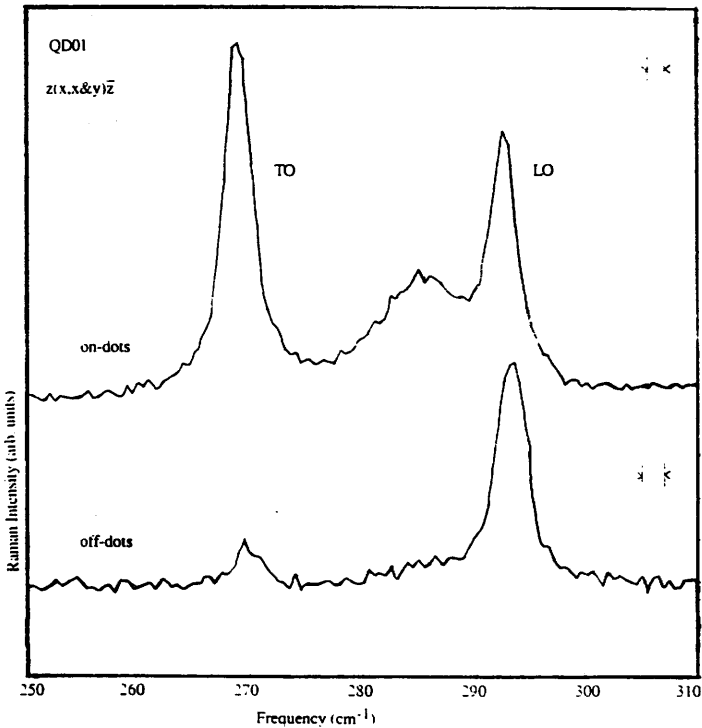
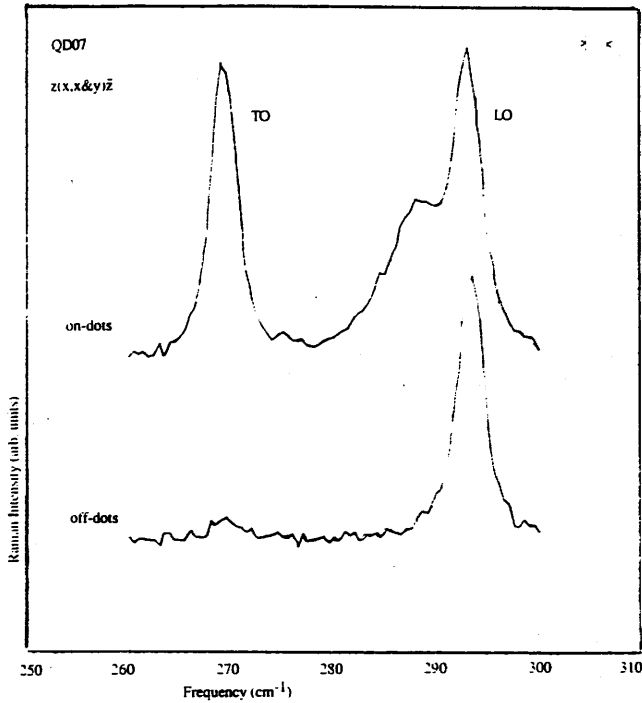


Figure 3.24 Raman Spectra of 2 quantum dot samples both on and off the patterned area. Notice the spectral feature between the TO and LO mode. In both cases the dot diameter was 60nm and the etch depth 290nm for QD01 and 210nm for QD07. (After Watt⁴⁷)

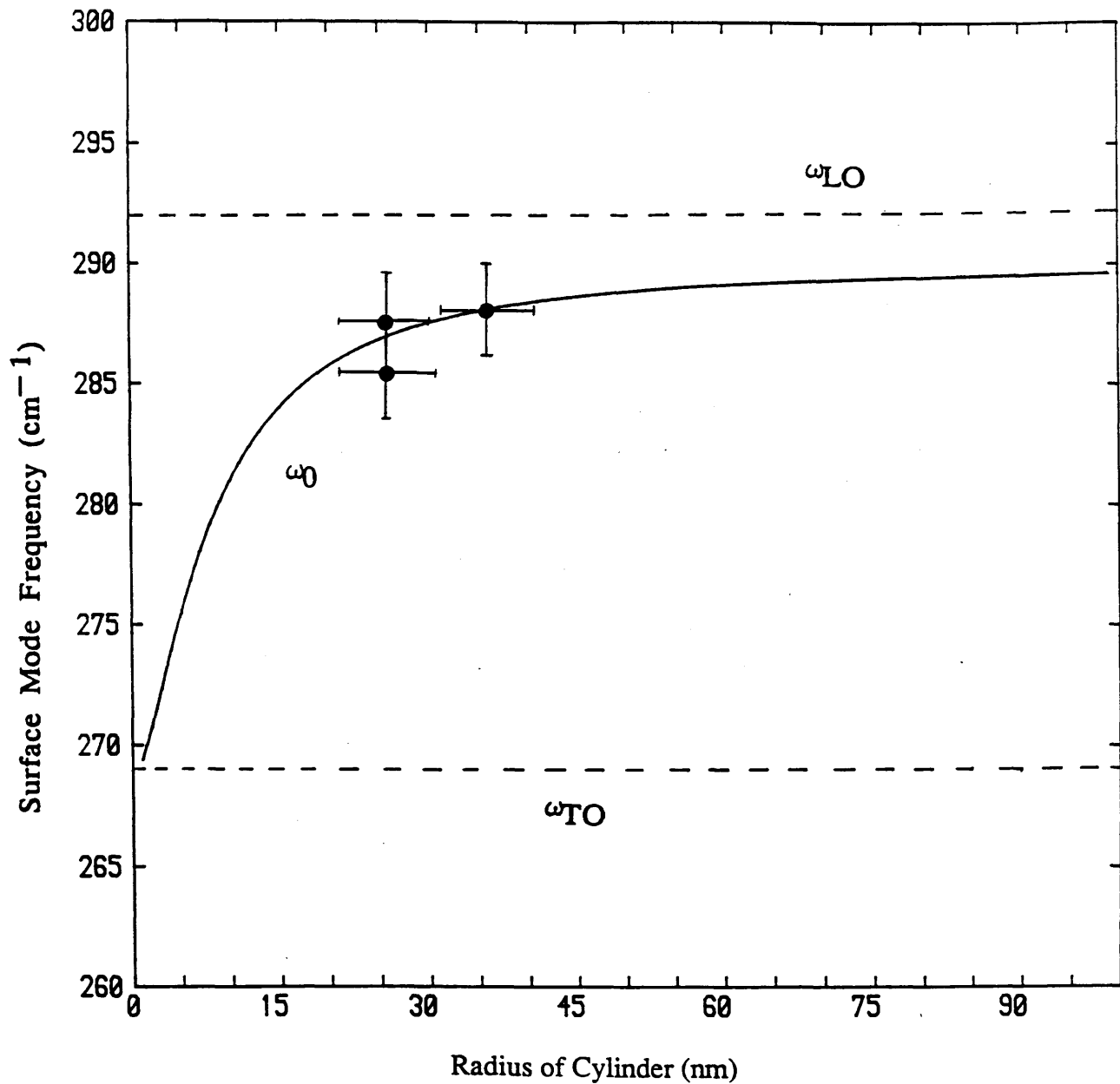


Figure 3.25 Plot of the experimental data points of the additional Raman feature and theoretical calculations for the surface phonon frequency. (After Watt⁴⁹)

using SiCl_4 . GaAs/AlGaAs QDs down to 80nm have been fabricated using Argon Ion Milling. SiCl_4 produces the most vertical sidewall profiles but has a considerably higher etch rate ($0.2\mu\text{m}/\text{min}$ as opposed to $25\text{nm}/\text{min}$) compared to CH_4/H_2 and is therefore more difficult to control accurately.

SiCl_4/H_2 produces isotropic as well as anisotropic etching resulting in a reduction of the dot diameter compared to the original etch mask and at ratios of 1:5 $\text{SiCl}_4:\text{H}_2$ the etch rate is reduced from $0.2\mu\text{m}/\text{min}$ for SiCl_4 only, to $0.1\mu\text{m}/\text{min}$ thus increasing the controllability of the process.

Raman Scattering experiments on quantum cylinders have shown the presence of a surface phonon mode. This confirms that the crystallinity of the sidewalls is maintained after dry etching. This alteration of the phonon spectrum due to patterning may have some bearing on the other optical properties of quantum dots, for example the luminescence efficiency from these structures and this will be discussed in Chapter 6.

References

- 1 S Thoms, I MacIntyre, S P Beaumont, M Al-Mudares, R Cheung & C D W Wilkinson: J. Vac. Sci Technol. B 6 (1), 1988, pp. 127.
- 2 C J Mogab: VLSI Technology, Chapter 8, pp. 303, Edited by S M Sze, Published by McGraw-Hill Book Company.
- 3 E L Hu & R E Howard: J. Vac. Sci. Technol. B2 (1) 1984 pp. 85.
- 4 U Niggebrugge, M Kling & G Ganes: Proc 12th Synp on GaAs & related compounds. Karwizawa, Japan, 1985, pp. 367.
- 5 U Niggebrugge, P Albrcht, W Doldisson, H P Nolhig & H Schmid: Self-aligned low-loss totally reflecting waveguide mirrors in InP/InGaAsP
- 6 R Cheung, S Thoms, S P Beaumont, G Doughty, V Law & C D W Wilkinson: Elec. Letts, Vol 23 No 16, 1987 pp. 857.
- 7 A P Webb: Semiconductor 84, Birmingham 25 - 27 Sept 84.
- 8 G F Doughty: Semiconductor International 85 Conference, Birmingham, 1 - 3 Oct 1985.
- 9 R E Klinger and J E Greene: J. Appl. Phys. 54 (3) 1983 pp. 1595.
- 10 R A Gottscho, G Smolinsky and R H Burton: J. Appl. Phys. Vol 53, No. 8, 1982 pp. 5908.
- 11 M B Stern and P F Liao: J. Vac. Sci Technol. B 1 (4) 1983 pp. 1053.
- 12 J Z Li, I Adesida & E D Wolf: J. Vac. Sci. Technol. B3 (1) 1985 pp. 406.
- 13 E L Hu and R E Howard: Appl. Phys. Lett 37 1980 pp. 1022.
- 14 G J Sonek and J M Ballantyne: J. Vac. Sci. Technol. B2 (4) 1984 pp. 653.
- 15 M Balooch, D R Orlander and W J Siekhaus: J. Vac. Sci. Technol. B4 1986 pp. 796.
- 16 N Vodjdani and P Parrens: J. Vac. Sci. Technol. B 5 (6) 1987 pp. 1591.
- 17 S Semura & H Saitoh: J. Vac. Sci. Technol. A2 (2) 1984 pp. 474.
- 18 G Smolinsky, R P Chang and T M Mayer: J. Vac. Sci. Technol., 18 (1) 1981 pp. 12 .
- 19 Alan Seabaugh: J Vac. Sci. Technol. B 6 (1) 1988 pp. 77.
- 20 Hirohito Yamada, Hiromasa Ito, and Humio Inaba: J. Vac. Sci. Technol. B3 (3) 1985 pp. 884.
- 21 J Chaplart, B Fay and N T Linh: J. Vac. Sci. Technol. B Vol. 1 No 4, 1983 pp. 1050 see also

references 3, 9 and 10

- 22 S Semura, H Saitoh and K Asakawa: *J. Appl. Phys.* 55 (8) 1984 pp. 3131.
- 23 see for example J Parasczak and M Hatzakis: *J. Vac. Sci. Technol.* 1981 Nov/Dec pp. 1412.
- 24 C S Korman: *J. Vac. Sci. Technol.*, 20 (3)1982 pp. 476.
- 25 C J Mogab, A C Adams and D L Flamm: *J. Appl. Phys.* 49 (7)1978 pp. 3796.
- 26 R P H Chang, C C Chang and S Darack: *J. Vac. Sci. Technol.*, 20 (1) 1982 pp. 45.
- 27 R A Barker, T M Mayer, and R H Burton: *Appl. Phys. Lett.* 40 (7) 1982 pp. 583.
- 28 L A Coldren and J A Rentschler: *J. Vac. Sci. Technol.*, 19 (2) 1981 pp. 225.
- 29 K Hirata, O Mikami, and T Saitoh: *J. Vac. Sci. Technol.* B2 (1) 1984 pp. 45.
- 30 C W Tu, R P H Chang and A R Schlier: *Appl. Phys. Lett* 41 (1) 1982 pp. 80.
- 31 R Cheung, S Thoms, I MacIntyre, C D W Wilkinson, and S P Beaumont: *J. Vac. Sci. Technol. B* 6 (6) 1988 pp. 1911.
- 32 H Arnot, S R Andrews and S P Beaumont: *Microcircuit Engineering* 9 (1989) pp. 356. Elsevier Science Publishers B.V. (North Holland)
- 33 S Somekh: *J. Vac. Sci. Technol.* Vol 13 No 5, 1976 pp. 1003.
- 34 P G Gloersen: *J. Vac. Sci. Technol* Vol 12, No 1, 1975 pp 28.
- 35 R Cheung, Y H Lee, C M Knoedler, K Y lee, T P Smith III and D P Kern: *Appl. Phys. Lett.* 54 (21)1989. pp. 2130.
- 36 S W Pang: *J. Electrochem. Soc.* Vol. 133, No. 4, 1986 pp. 784.
- 37 S W Pang, M W Geis, N N Efremow and G A Lincoln : *J. Vac. Sci. Technol. B* 3 (1) 1985 pp. 398.
- 38 K Nagata, O Nakajima and T Ishibashi: *Jap. J. Appl. Phys.* Vol 25, No 6, 1986, pp. L510.
- 39 S Thoms, S P Beaumont, C D W Wilkinson, J Frost and C R Stanley: *Microcircuit Engineering* 5 (1986) pp. 249 Elsevier Science Publishers B. V. (North-Holland).
- 40 S W Pang, W D Goodhue, T M Lyszczarz, D J Ehrlich, R B Goodman, and G D Johnson: *J. Vac. Sci. Technol.* B6 (6) 1988 pp. 1916.
- 41 S Namba, M Kawabe, N Kanzaki and K Masuda: *J. Vac. Sci. Technol.*, Vol. 12, No. 6, 1975 pp. 1348.
- 42 Y Yuba, K Gamo, H Toba, X G He and S Namba: *Jap. J. Appl. Phys.* Vol. 22 No. 7, 1983. pp. 1206.
- 43 J Rossabi, M Dutta, M W Cole and D D Smith: Santa Clara 1989.
- 44 H F Wong, D L Green, T Y Liu, D G Lishan, E L Hu, P M Petroff, P O Holtz and J L Merz: *J. Vac. Sci. Technol.* B6 (6) 1988 pp. 1906.
- 45 R Cheung, A Birnie, J N Chapman, S Thoms and C D W Wilkinson: to be published *Appl. Phys. Letts.*
- 46 M Watt, C M Sotomayor Torres, R Cheung, C D W Wilkinson, H E G Arnot and S P Beaumont: *J. of Modern Optics*, 1988, vol. 35, No. 3, pp. 365.
- 47 M Watt, Thesis, Glasgow University 1988.
- 48 M Watt, H E G Arnot, C M Sotomayor Torres and S P Beaumont: *Proceedings of Nanostructure and Physics and Fabrication*, College Station, Texas, March 13-15, 1989 pp. 89 Published by Academic Press (London) Ltd.
- 49 M Watt, C M S Torres, H Arnot and S P Beaumont: *Semicond. Sci. Technol.* 5 1990 pp. 285.

Chapter 4

Experimental and Material growth methods

4.1 Introduction

To characterize the structures fabricated using the processes detailed in Chapters 2 and 3 Photoluminescence measurements (Chapter 1, Section 1.3) were carried out. In this chapter the set-up of the experimental apparatus used for these measurements carried out by myself at Glasgow University is described. Much of the experimental apparatus was originally set-up by Dr M Watt and as such, a detailed description of it is found in reference 1. The different methods employed to grow the starting material used in these experiments and the quality of the material, especially the interfaces between the binary and tertiary that form the quantum well are discussed.

4.2 Experimental Apparatus

To investigate the optical behaviour of these structures a high resolution, low temperature photoluminescence system was used (figure 4.1). Low temperature measurements required the sample to be placed in a cryostat and cooled. A laser was used to photcreate electron-hole pairs to obtain luminescence spectrum. The emitted radiation was dispersed by a monochromator and detected using photon counting techniques.

4.2.1 Lasers

Three lasers were used to excite the sample and hence obtain photoluminescence spectra.

- 1) an Argon ion laser either directly or as a pump for
- 2) a dye laser
- 3) a Helium Neon laser.

Varying the pump wavelength changes the penetration depth of the laser light into the semiconductor crystal (see Section 3.9.2). The Argon ion laser was a Spectra Physics model 2030 updated to a model 2045. The dye laser was a Coherent model 599-01 and could be used with a number of dyes depending on the laser optics. A Spectrolab prism monochromator ensured only single line excitation of the sample and was important for removing the laser plasma background when using the photon counting system. The transmission of the monochromator depended on the beam size and generally a maximum transmission of around 50% was achieved.

4.2.2 Focussing and Collecting Optics

4.2.2.1 Nearly Backscattering Geometry

In the initial experiments to measure the PL spectra from QDs (Section 6.3 and 6.4) a nearly backscattering geometry was used to collect the emitted light¹. The laser beam was focussed onto the sample in a spot approximately 50 μ m in diameter using a small lens placed at about 50 to 60° to the sample surface normal. The laser spot was focussed onto the 100 μ m square dot arrays by moving the X and Y controls on the mirror deflecting the light through the focussing lens. This was not an ideal method as the control on the mirror was not fine enough to accurately control the positioning of the laser spot. In order to focus the spot onto the dot arrays the sample in the cryostat was viewed by looking through a pair of binoculars. This method was also not ideal and the accuracy with which the laser spot was focussed onto an array was greatly improved by changing to the 90° scattering geometry and new collection optics described in Section 4.2.2.2.

The laser spot was then transferred by means of the collection optics to a similarly focussed spot on the entrance slit of the spectrometer. In order to collect as much of the scattered light as possible lenses of 10cm in diameter were used as the collection optics. A pair of such lenses were used: the first had the sample in its focal plane and the collimated beam from this lens was focussed by the second lens onto the spectrometer slit. The second lens provided all the fine adjustment necessary to couple the signal into the spectrometer. The lenses were made of optical crown glass (type HC 519604).

4.2.2.2 90° Scattering Geometry

In later experiments the system was modified by myself to use a 90° scattering geometry (figure 4.1). This utilized two cryostat windows at an angle of 90° to each other. The light was focussed onto the dot and wire arrays using a Ealing microscope Objective of 60mm/0.07NA focal length mounted in an X-Y-Z translation stage with micrometer control. The sample was mounted on a copper plate using Bostick Glue which was then screwed to the insert and set at an angle of approximately 45° to the focussing laser beam. Additional white light illumination of the sample was needed to enable the patterned areas to be seen clearly.

The collecting optics used was a commercially available 60-300mm Sirius Zoom lens (F4.5-6) also mounted on an X-Y-Z translation stage. Using this zoom lens the image of the sample was focussed onto the entrance slits of the spectrometer along with the incident laser spot reflected off the sample. In an experiment such as this it may be difficult to find the weak PL signal from the dots or wires (~4% of mesa signal strength in the dots and 25% in the wires). By reflecting the laser light along the same line of sight as the PL onto the spectrometer entrance slit, a signal from the quantum wells is easily found which can then be peaked using the controls on the focussing and collecting optics. The advantage of this system over the back scattering system was that by adjusting the focal length of the lens a magnified image of the sample in the cryostat could be obtained. This was of crucial importance in these very high resolution experiments as it was necessary to focus the laser spot onto an area of

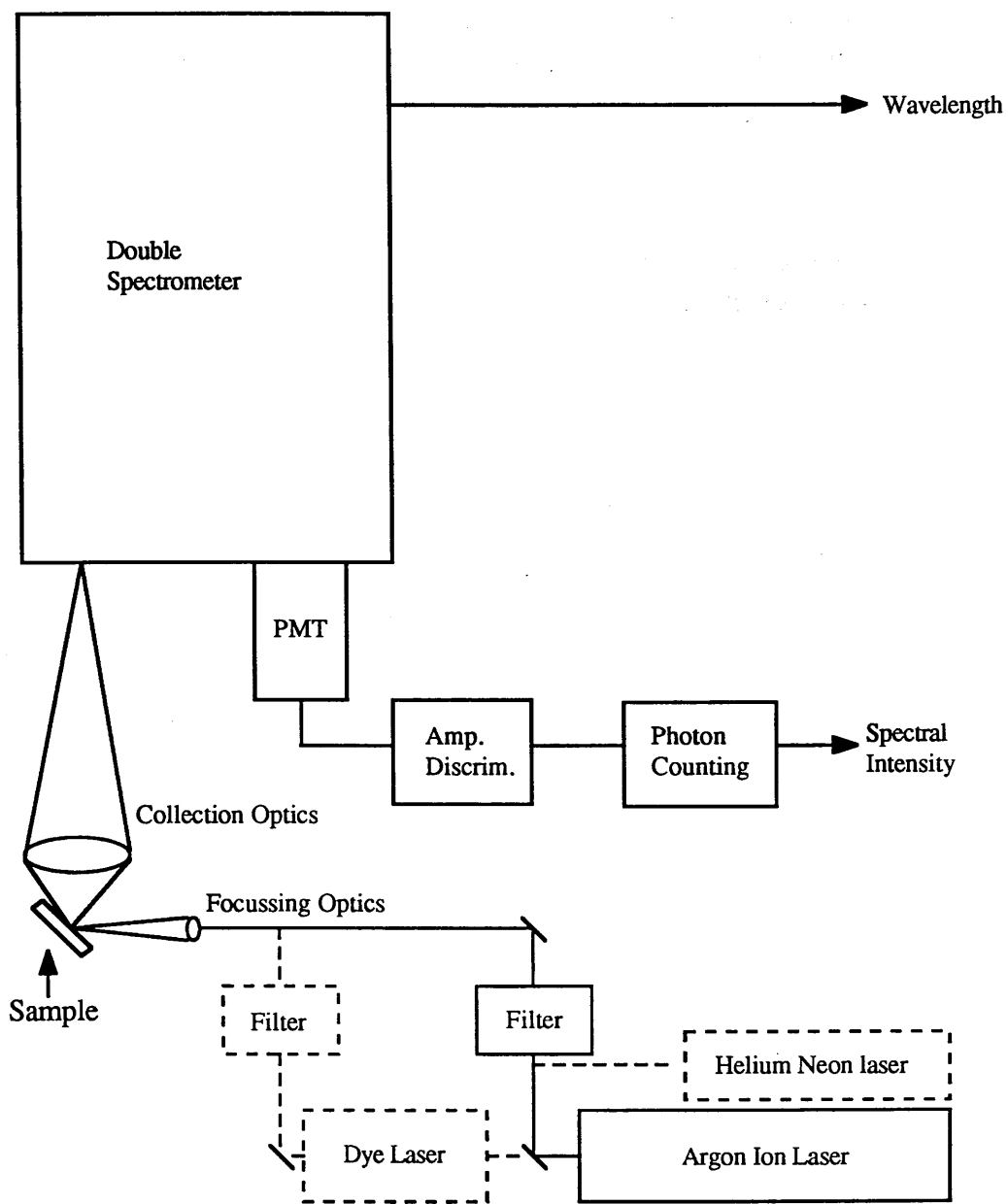


Figure 4.1 Schematic of the 90° scattering geometry photoluminescence apparatus showing the photomultiplier tube (PMT) with its amplifier discriminator. The components shown in dotted lines are alternative alignments of the system when the dye laser or Helium Neon laser is used.

dots or wires 100 μ m square. By having a magnified image of the sample and micrometer movement on the focussing optics, the laser spot could be positioned very accurately, completely overlapping the array of dots or wires. As both the focussing and collecting optics had X-Y-Z movement control this ensured that the maximum signal could be obtained by adjusting all six movements. The importance of the alignment system cannot be overemphasized. When relative efficiency measurements of different areas are done the laser must be exciting the whole array every time.

4.2.3 The Spectrometer

The spectrometer used was a Jobin-Yvon Ramanor U1000. This is a 1m focal length double grating spectrometer, i.e. two single spectrometers side by side with the gratings attached to a single shaft to eliminate any relative movement. The image of the exit slit of the first spectrometer falls upon the entrance slit of the second spectrometer. The gratings are coupled additively in that the second grating further disperses the light incident upon it. The light path in the spectrometer is shown in figure 4.2. The gratings used were a holographic pair with 1800 grooves/mm. As the double spectrometer has extremely good stray light rejection it did not matter that the laser spot from the sample was focussed into it. If however a single spectrometer is used a filter must be inserted to remove the laser line either just before or after the entrance slit. To calibrate the spectrometer absolutely a monochromatic light source of known wavelength must be used e.g. one of the laser lines.

4.2.4 Photon Counting Techniques

Photon counting is a technique used in conjunction with a photomultiplier tube. Whenever a photon is incident on a photosensitive photocathode an electrical impulse is produced. This is amplified by a dynode chain before reaching the anode. A pulse height distribution occurs associated with noise from the dynode chain, but since the gain between the first dynode and photocathode is greatest, pulses originating at the photocathode dominate. The signal is then amplified and fed into a discriminator which rejects all pulses below a given size. The remaining pulses are then converted into either TTL or ECL logic pulses. Photon counting is limited by thermal noise particularly from the first dynode and photocathode, resulting in a count even when the tube is darkened. This dark count is reduced by cooling the tube. In these experiments a Hamamatsu R943-02 type tube was used. This type of tube is designed specifically for photon-counting applications as it has a gain of 5×10^5 and a very low dark noise. The tube was cooled to about -25°C in a Pacific Instruments Thermoelectrically-cooled housing with a built in amplifier and discriminator. Further details on the specifications and operation of the tube are supplied in Reference 1.

4.2.5 Spectral Response of the system

The combined spectral response of the gratings and the detector is shown in figure 4.3. In these experiments the wavelength region of interest is from 640 to 830nm. As can be seen the response drops considerably over this region. It is only necessary to normalize the spectra if the relative intensity of the signals from different well widths, emitting at different wavelengths, are being compared. If however the comparison is of the signals obtained from the same well widths subjected to different

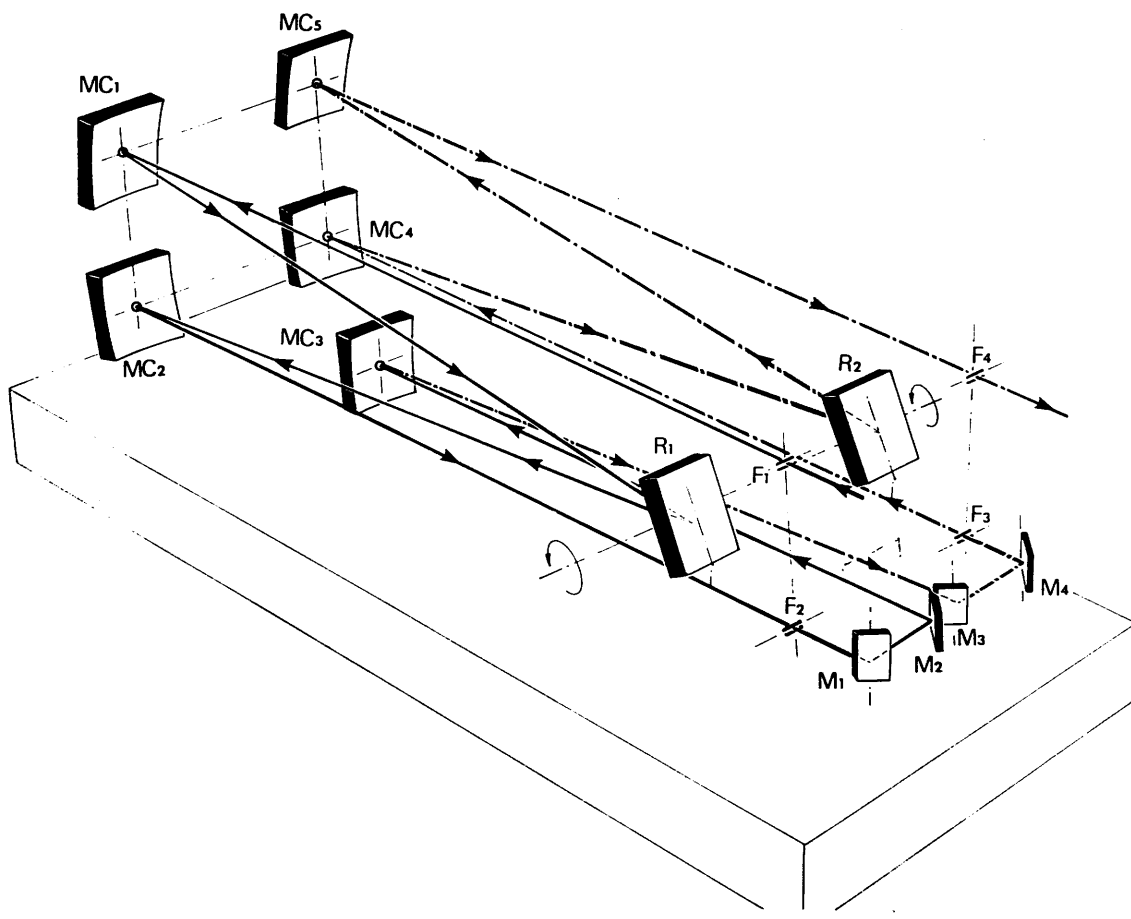


Figure 4.2 Schematic representation of the light path within the double spectrometer.
(After Jobin-Yvon Operating Manual)

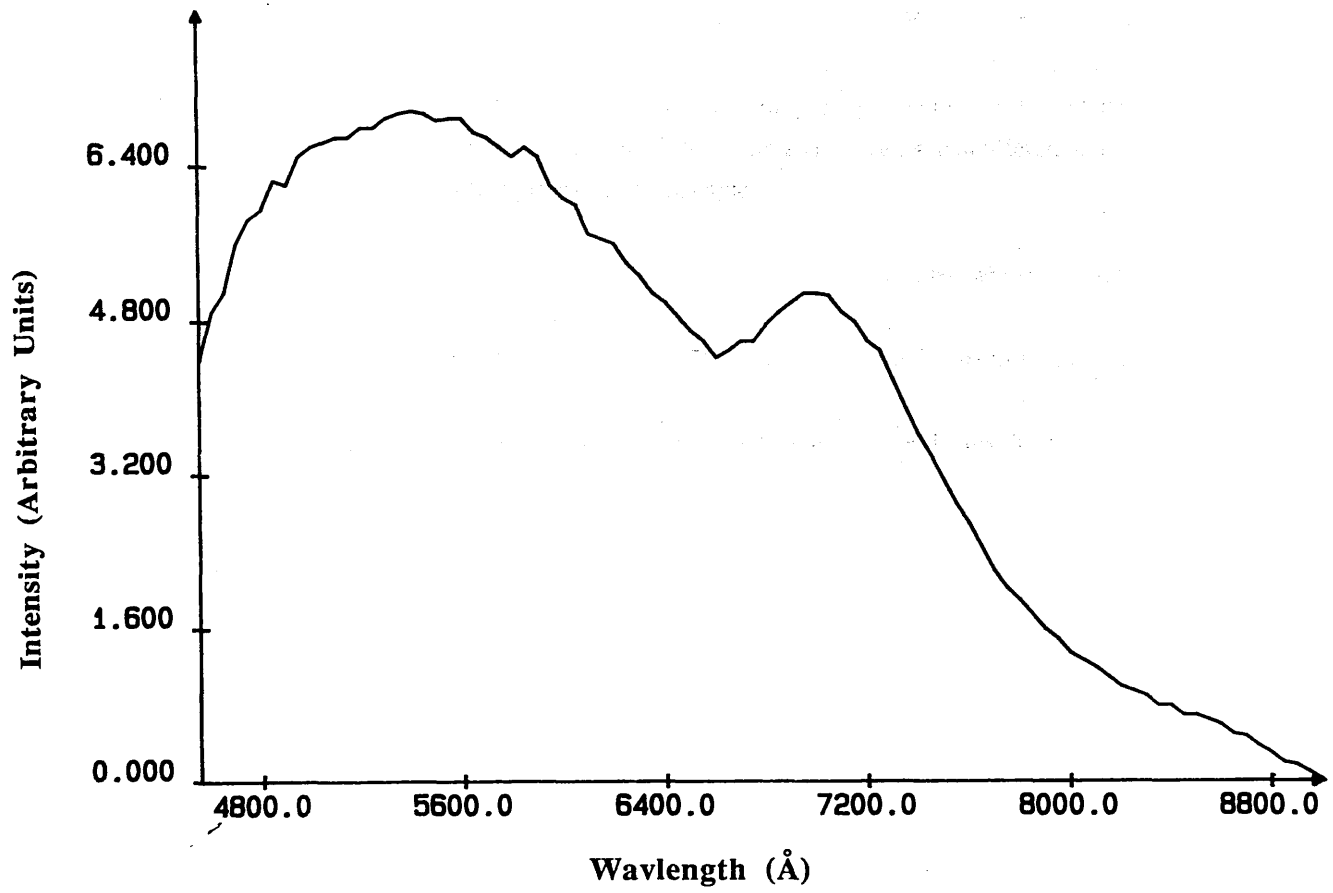


Figure 4.3 The combined spectral response of the spectrometer gratings and the photon detector.
(After Watt¹)

processing, it is not necessary to normalize the results.

4.2.6 Computerisation and Software

Initial computer control of the system was developed by M Watt using an IBM Model 30. A detailed explanation of this system is given in Reference 1. From November 1989 onwards an Instruments S A Prism Software Package was used which ran on an Elonex computer and enabled integrated spectrometer control and data acquisition. Prism is a completely integrated series of programs and special routines for the acquisition and treatment of spectroscopic data which offered many advantages over the in-house data acquisition program. For example

- 1) It was faster as it did not need to count at a wavelength for a specified whole number of seconds but could sample for times down to 0.2 secs.
- 2) It plotted the spectrum on the VDU as the data was obtained and if required the scan could be interrupted immediately.
- 3) It could count with time while sitting at one wavelength and plot the results.
- 4) Its data manipulation was improved. For example it offered facilities such as calculating the integrated intensity under a curve and removing plasma lines or severe noise spikes from a spectrum.

The main advantage gained from the improvement in software was the speed with which data could be acquired. This was increased by approximately a factor of three on the old system. The printing options available were not as flexible and this section of the package could be improved.

4.2.6 Cryostats

4.2.6.1 Large Bore Optical Cryostat

Two optical cryostats were used. The first was a large bore Quantum Production optical cryostat, a detailed description which is given in Reference 2. The cryostat could be operated in either bath or gas-flow modes i.e. either by immersing the sample in liquid Helium and cooling to below the lambda point so that the liquid was superfluid (temperature $\sim 2.2\text{K}$) or else by maintaining a flow of cold gas sufficient to keep a constant temperature (range 4.2-300K). The main drawback of this cryostat was the difficulty in a) maintaining a constant temperature and b) changing the temperature due to its design and the poor seal on the windows. It became apparent as the experiments progressed that it would be desirable to be able to easily change the temperature between 5K and 200K. Due to the large thermal mass of this cryostat this would take a long time (8 hours) and it would also be difficult to stabilize the temperature at different points as the cryostat warmed up to take data. It was therefore decided to use a Oxford Instruments Continuous Flow cryostat as it could fulfil the above specifications.

4.2.6.2 Continuous Flow Cryostat and Flow Controller

The Oxford Instruments CF1204 is a hybrid continuous flow (CF) cryostat with a dynamic facility allowing helium to be accumulated in the sample space which when pumped on operates below 2.2K. However in these experiments the cryostat was always used in gas mode where the sample was cooled by a continual flow of cold gas passing over it and exhausting at the top of the sample space. The CF gas flow system is shown in figure 4.4a.

The CF cryostat operates by controlling the transfer of helium to a vacuum insulated, radiation shielded, sample space in the cryostat. Sample temperature is maintained by balancing the flow through the cryostat with power applied to an electrical heater within a heat exchanger. Coolant flow is produced by pumping on the helium return line of the transfer tube thereby sucking the helium from the storage dewar.

The flow and pressure through the cryostat is monitored and controlled by a flow control unit. This consists basically of a vacuum gauge, needle valve and flowmeter (figure 4.4a). The gas from the cryostat enters the unit, passes through the needle valve into the gas flow pump and flows along the helium exhaust line through a calibrated flowmeter. A negative pressure gauge is connected to the gas flow line after it enters the unit from the cryostat. This indicates the line pressure and will also show any air leaks in the CF system. A diaphragm pump is used for the CF system as it is oil-free and provides an airtight helium return line.

The cryostat sample chamber uses indium mounted spectroil quartz window units which are 20mm in diameter. The outer vacuum jacket windows are 25mm in diameter. The sample space is fitted with a 34 Ω wire wound heater, an Oxford Instruments rhodium iron (RhFe) resistor on the heat exchanger and a RhFe resistor mounted on the insert cold finger to which the sample is mounted (figure 4.4b). Both resistors could be used for controlling the temperature in gas flow mode. However a more accurate control of the temperature of the sample was gained by using the resistor on the insert.

Temperature control and stability is an important consideration when using a cryostat particularly above liquid helium temperatures. This can only be achieved with a temperature control unit using a feedback system. The required temperature was first approximately obtained by controlling the flow of cold gas through the needle valve on the transfer tube. The temperature controller was preset to the required temperature and provided an error signal relating to the difference between the set point and the actual temperature. The error signal gave a proportional level for the electrical heat input to the cryostat heat exchanger to balance the cooling by the cold gas. An Oxford Instruments ITC4 temperature controller provided the three term control to damp any unstable feedback oscillations. Two sensors on the controller were programmed for the RhFe resistors. These channels were calibrated by providing a reference value of known temperature, for example liquid nitrogen or liquid helium, as the lowest reference point and room temperature as the highest reference point. This procedure was repeated several times until consistent readings were obtained for known temperatures.

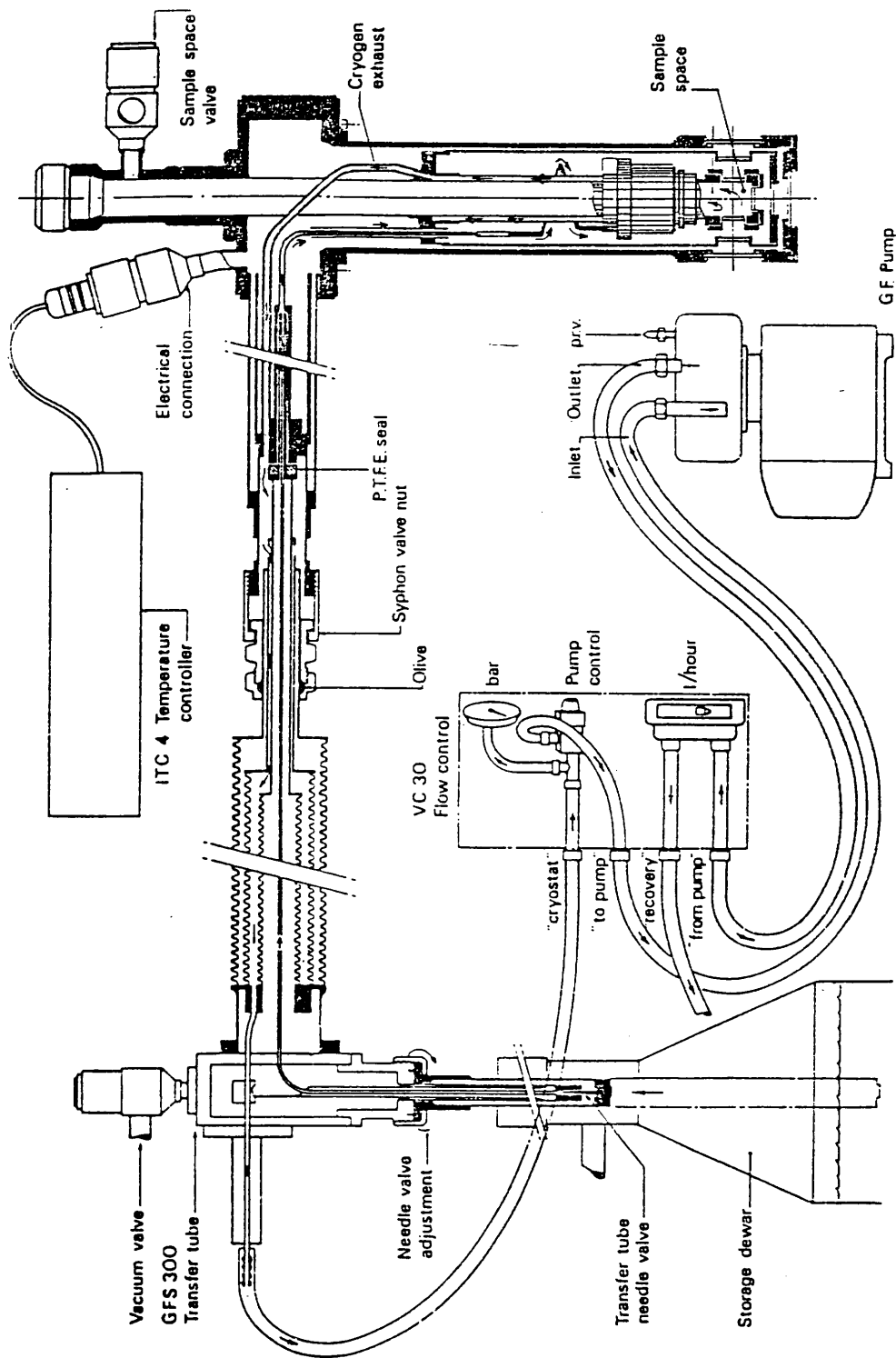


Figure 4.4a Schematic of the continuous gas flow system.
 (After Oxford Instruments Operating Manual)

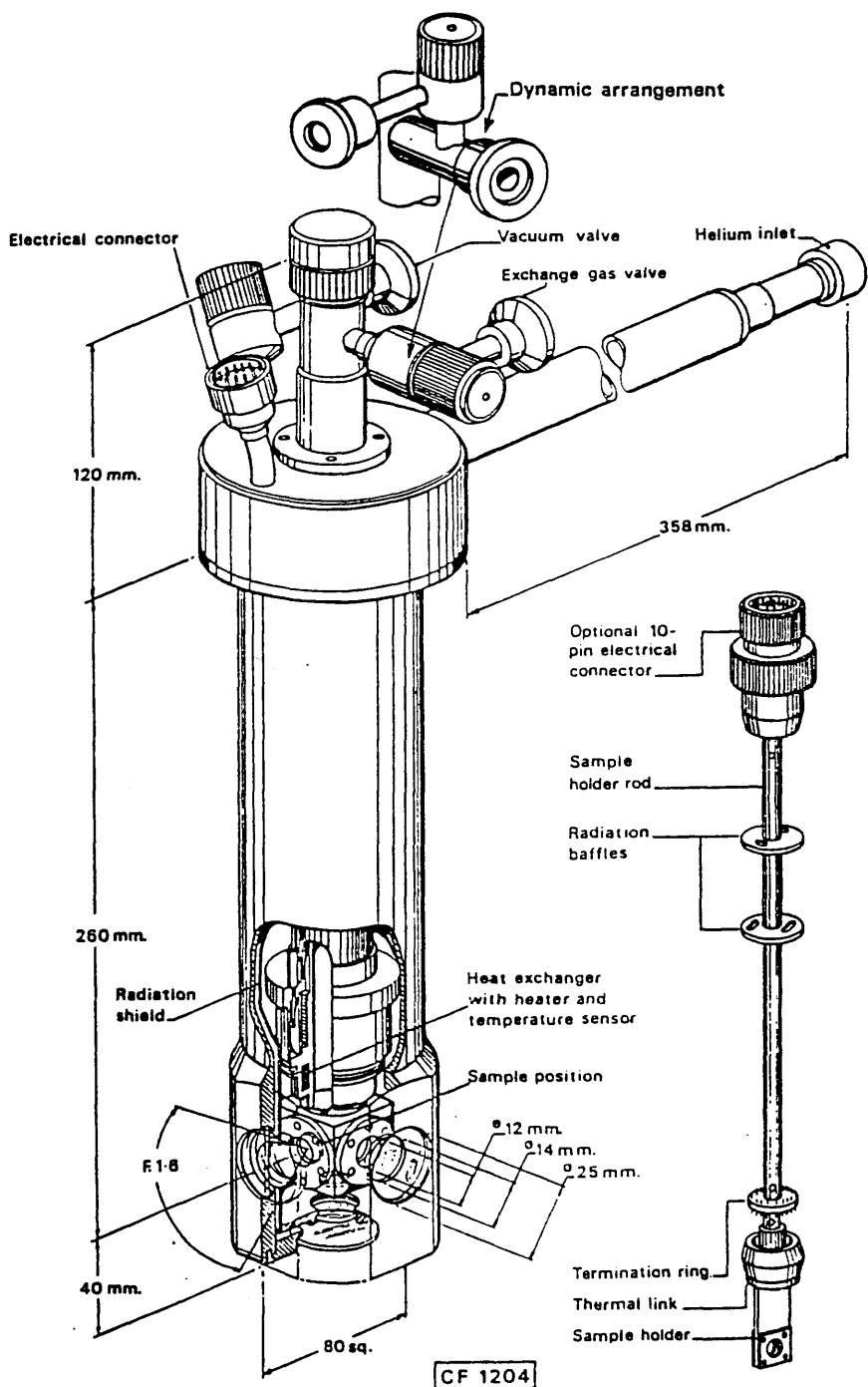


Figure 4.4b CF 1204 Cryostat and Insert.
(After Oxford Instruments Operating Manual)

Many advantages were gained from using this cryostat over the wide bore cryostat. The obvious improvements were in the temperature control which was accurate to within 1 Kelvin. The CF cryostat could maintain any temperature between 5K and 300K for hours on end. The other major gain was improvement in the speed of data acquisition as scans were no longer aborted due to the helium level dropping below the sample in the middle of a scan as occurred when the wide bore cryostat was being used in bath mode. Time was no longer wasted in trying to stabilize the temperature (an art in itself on the old system) and the time taken to move between set temperatures was vastly reduced. The flow cryostat can warm from 5K to room temperature in 30 minutes. These improvements resulted in a much greater efficiency in the use of helium.

4.3 Quantum well growth methods by MOCVD and MBE

Many different techniques have been developed for the epitaxial growth of III-V compound semiconductors. These include liquid-phase epitaxy (LPE), vapour-phase epitaxy (VPE), metal organic chemical vapour deposition (MOCVD) and molecular beam epitaxy (MBE). The growth control allowed in MOCVD and MBE, has enabled the production of III-V compound structures with near monolayer definition³ in heterojunctions and alloy composition controllable to within one percent (but this is limited by intermixing and desorption at higher temperature). In the experiments described in this thesis the material is grown by either of these methods. Chapter 5 reports on the Photoluminescence obtained from dots patterned into MBE grown material and in Chapter 6 mainly MOCVD dots and wires are investigated.

4.3.1 MBE

MBE is an evaporation process involving the reaction of one or more thermal beams of atoms or molecules (Ga, Al, As etc) with a hot crystalline surface under ultrahigh vacuum conditions ($\sim 10^{-10}$ Torr). Growth occurs, with the required stoichiometry, as atoms and molecules arrive and react on the substrate surface. The growth rate can be controlled reliably with remarkable precision down to 0.01 atomic layers per second. However the standard practical growth rate is usually one monolayer per second or $1\mu\text{m}$ per hour. It is this low growth rate, combined with almost instantaneous interruption of growth using shutters over each molecular source that allows growth control down to monolayer thickness.

The MBE crystal growth process is a two-step phenomenon, in which the first step involves the incident atom or molecule sticking to the crystal surface and the second step involves motion on the surface to the point of incorporation into the crystal. These steps are species dependent, temperature dependent and crystal surface dependent. At low temperatures, motion on the surface is slow, and rough or noncrystalline growth may occur. At ideal temperatures (500-700°C), lateral motion occurs to atomic step edges where the atom is bound. The crystal surface may be strongly smoothed at the atomic level because the growth proceeds more rapidly at the lowest points on the surface. At high temperatures, reevaporation from the surface becomes significant and it is difficult to determine exact growth rates and therefore quantum well thicknesses and alloy composition.

4.3.2 MOCVD

In MOCVD room-temperature vapours are used to transport the film constituents. For example alkyls of the group III metals, and hydrides of the group V elements usually are used as precursor species. Dilute vapours of these chemicals are transported at or near room temperature to a hot zone where a pyrolysis reaction occurs⁴. The formation of GaAs is described by



and the formation of AlAs by



If more than one reaction such as Equations 1 and 2 occurs simultaneously, the resultant solid becomes a mixed alloy of the type $\text{Ga}_{1-x}\text{Al}_x\text{As}$. The alloy composition x is determined by the relative rates of the two reactions which in turn depend upon a number of factors including gaseous diffusion, unknown intermediate steps, thermodynamics and reactor gas dynamics⁴.

The gas velocities and temperature gradients in the vicinity of the hot susceptor play a significant role in the deposition process. Transport of the alkyls (or some unknown partially cracked intermediate) from the gas to the growth interface occurs mainly by diffusion through a boundary zone near the wafer. The nature of the temperature gradients, concentration gradients, chemical species, and reactions taking place within the boundary layer are complex.

4.4 Comparison of the MBE and MOCVD growth processes

Unlike MBE where the growth is uniform across the wafer under ideal conditions, the growth across a MOCVD wafer is not uniform. In MBE the wafer is rotated during growth but in MOCVD it is static in the reactor. Ehlers *et al*⁵ showed using scanning photoluminescence that there are considerable variations in the growth rates in both the transverse and longitudinal directions on wafers grown in a horizontal MOCVD reactor. This therefore affects the well width across the wafer.

It is known that, under optimum conditions MBE can produce structures with interface roughness down to one or two monolayer fluctuations⁶, and the purest material, as it is grown under high vacuum conditions. In MBE there are many in situ surface diagnostic tools such as reflection high-energy electron diffraction (RHEED), Secondary-ion mass spectroscopy (SIMS), Auger electron spectroscopy which monitor the quality of the material and in the case of RHEED the flatness and crystalline state of the epilayer surface as it is grown⁷. This is possible as MBE growth takes place in an UHV environment whereas in MOCVD the growth is at atmospheric pressure. While this simplifies the MOCVD growth process it does not lend itself to the application of similar diagnostic procedures as may be used in MBE. To this end the actual growth mechanism in MOCVD is less well understood although techniques are being developed to try and overcome this problem⁸.

4.4.1 Interface Quality

The differences in material purity and the abruptness and flatness of the interfaces between different semiconductor layers produced by each growth method, are of major importance to this work. The high quality and purity of MBE material make it attractive as the method used to grow material for investigating 0 and 1D confinement. However the area of application of quantum dots and wires that is being investigated is the incorporation of one and zero degrees of freedom structures into the active region of a quantum well laser. MOCVD is often used to grow lasers in a commercial environment so it is important to investigate the results of fabricating these structures in the essentially poorer quality MOCVD material.

Low-temperature excitonic linewidths in luminescence and excitation spectra are frequently employed as a sensitive monitor of interface abruptness and material purity^{9,10}. Narrow linewidths and high luminescence intensity are obtained from high quality QWs as the dominant line broadening mechanism is scattering with acoustic phonons¹¹ (homogeneous linewidth). Broad linewidths and poorer luminescence intensity are seen in poorer quality material perhaps due to well width fluctuations and interface roughness, chemical composition fluctuations at the interface, impurities in the well barrier regions and at interfaces¹² (inhomogeneous linewidth).

It is known that the quality of AlGaAs grown on GaAs (generally referred to as the normal surface) is much higher than the quality of GaAs grown on AlGaAs (inverted surface)¹³⁻¹⁶ and it is thought this is due to the higher concentration of defects in the AlGaAs. The quality of the quantum wells themselves is not independent of the quality of the confining bulk AlGaAs layers. Defects generated during the growth of the lowest AlGaAs layer may propagate into the quantum wells creating nonradiative recombination centres and mechanisms for linewidth broadening. This is due to the strong Al-O bond, which favours the reaction of Al with residual contaminants in the growth chamber (e.g. H₂O, CO) leading to the incorporation of oxygen, or, by the reduction of CO, of free carbon into the growing layer. Oxygen containing species such as H₂O and CO normally present in the MBE growth chamber having sticking coefficients on Al_xGa_{1-x}As at least one order of magnitude greater than on GaAs, resulting in enhanced unintentional impurity incorporation and thus more non-radiative recombination centres¹⁷. Improved UHV technology, higher purity of starting materials and elevated growth temperatures have helped to overcome these difficulties.

The quality of the material obtained using MBE growth is extremely high. Linewidths of ~0.5meV in wells 13.5 and 28nm thick have been obtained¹¹. As the material is grown in an ultra high vacuum the purity is excellent and this is shown by high luminescence efficiencies obtained as few nonradiative traps are introduced during growth. One of the main inhomogeneous broadening mechanisms in MBE grown samples results from growth steps at the interfaces causing fluctuations of the quantum well thickness. The local excitonic energy levels thus vary strongly in a lateral direction and the excitonic line becomes broadened. This interface disorder consists of island-like structures having one monolayer height and varying lateral size. If the exciton Bohr diameter is smaller than the island size⁶ the excitons can be localized at one of these island-like structures, as at low temperatures the exciton will diffuse to the lowest energy level (corresponding to the thicker well regions)¹⁸. If the lateral island size

is smaller than the exciton Bohr diameter the exciton will experience an averaging of the well width fluctuations and this broadens the linewidth¹⁹ (figure 4.5).

To reduce the effect of interface roughness on linewidth growth interruption has been used¹³⁻¹⁶. Interruption between growing the AlGaAs and GaAs layers for example, allows time for the atoms to migrate to energy favourable nucleation sites on the interfaces. In this manner, using PL and PLE as the characterization tool, extremely sharp luminescence peaks have been observed, corresponding to atomically flat island sizes in the micron range^{18,20}. Large area variations of 1 or 2 monolayers (ML) in the QW thickness have been reported^{10,12-17}, where one ML= $a/2=0.283\text{nm}$ and a is the GaAs lattice constant, due to interface growth defects where AlGaAs protrudes into the well of GaAs or GaAs extrudes towards the AlGaAs barrier. These fluctuations can be seen by splitting in the main free exciton peak. The energy difference between these peaks is equal to fluctuations in well width corresponding to monolayer (or multiples thereof) fluctuations in well thickness. The confinement energy of the exciton is therefore dependent on its position in the well¹⁰. Miller *et al*¹⁴ suggested however that multiple peaks could also be due to excitons bound to impurities introduced by interrupting the growth. Radiative efficiencies were reduced probably due to nonradiative traps at impurity sites.

In MOCVD grown material it is not possible to obtain as abrupt interfaces as those in MBE. It is likely that due to the finite time needed to switch from one gas phase composition to another there will be a gradation in the Al composition across the interfaces²²⁻²⁴. The quality of the interfaces is therefore not as high as in MBE grown material and this is shown in the PL linewidths obtained from MOCVD material. Pistol *et al*²⁵ have reported MOCVD linewidths of 6meV in a 2nm well. This linewidth suggests that at most the well width fluctuations are of the order of 1-2 MLs. Unlike MBE where the interface maybe smooth over a distance of $\sim 30\text{nm}$ ⁶ before a monolayer fluctuation in well width occurs, MOCVD material may have fluctuations over a much smaller distance. For example Kawai *et al*²³ report PL studies of MOCVD grown QWs where the linewidth of 3,4,7, and 10nm wells at 4.2.K is 8.4, 7.6, 5.7 and 6.4meV respectively. They suggest that these small linewidths are due to island like structure formed by well width fluctuations over the interface smaller than one half the lattice constant, and that the islands formed are not large enough to trap an exciton. This "pseudo-smooth" nature of such interfaces could lead to the sharpening of the PL¹⁷. How this difference in interface formation might effect exciton localization is considered in Chapter 6.

The quality and type of interface in GaAs/AlGaAs QWs will be extremely important when they are patterned down to 0 and 1 DOF structures. It is known that as MBE grown QWs become thinner, the affect of interface fluctuations is more apparent in the PL spectra. In wider wells of 50-60 ML and upwards, ML fluctuations in well widths only slightly perturb the exciton energy¹⁵. Weisbuch's *et al*⁶ model of growth islands of GaAs in AlGaAs or AlGaAs in GaAs proposes a distance of 30nm between these islands. If the lateral extent over which the exciton can move is only 60nm due to patterning into dots, it is not unreasonable to expect that this might significantly affect the expected exciton behaviour seen in the bulk. The exciting laser light is generally focussed to a spot 50 μm in diameter. The spectra obtained from bulk material will therefore be the average of the affects seen over

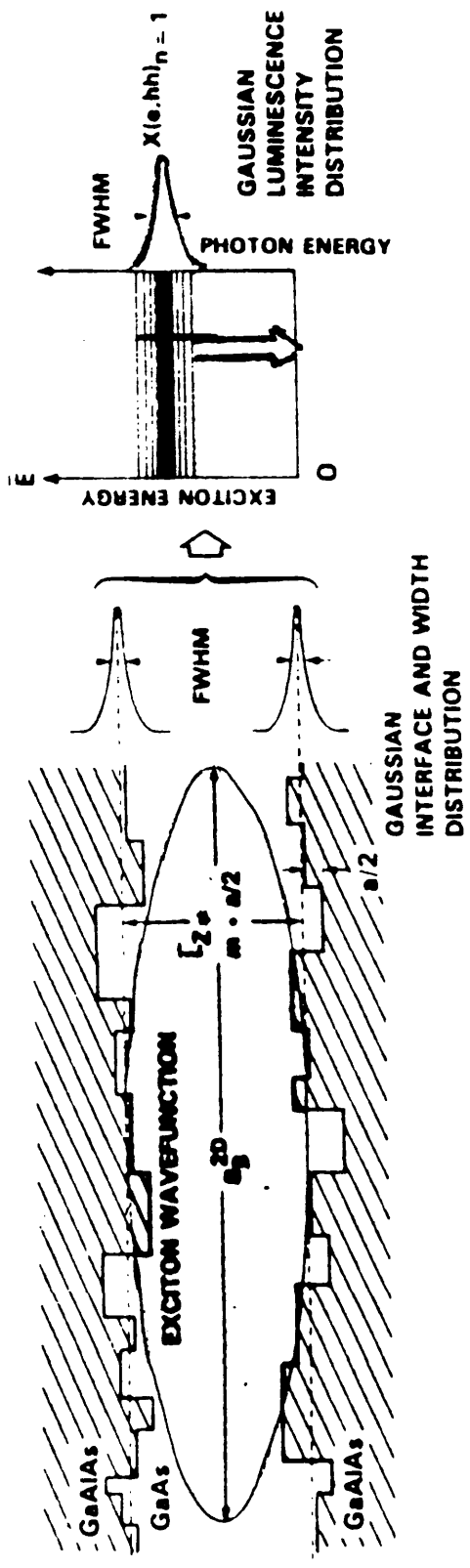


Figure 4.5 Model for the interface disorder of an AlGaAs/GaAs/AlGaAs QW grown without interruption showing how the disorder inhomogeneously broadens the exciton (e, hh) linewidth. (After Bimberg et al²⁰)

the area of sample excited - in this case $50\mu\text{m}^2$. Once dots have been patterned into the QWs this will not be the case as the largest area excited will be $0.5\mu\text{m}$ in diameter, the diameter of the largest dot. The situation is different in wires because the exciton is free to move distances comparable with the bulk in one direction as the wires in these experiments were $100\mu\text{m}$ long. It is therefore important to assess the quality of the interfaces in the starting material and to take these affects into account when trying to understand any differences in optical behaviour brought about by the additional confinement.

References

- 1 M Watt, Thesis, Chapter 4, Glasgow 1988.
- 2 I Ferguson, Thesis, Chapter 2, St Andrews 1989.
- 3 A C Gossard: J. Quantum Elect. Vol QE-22, No. 9, Sept 1986 pp. 1649.
- 4 M J Ludowise: J. Appl. Phys. 58 (8), Oct 1985 pp. R31.
- 5 H L Ehlers, A W R Leitch and J S Vermaak: J. Crystal Growth 96 1989 pp. 101.
- 6 C Weisbuch, R Dingle, A C Gossard and W Wiegmann: Solid. State Comm. Vol 38, 1981 pp. 709
- 7 W T Tsang: Semiconductors and Semimetals, Vol 22, Part A, Chapter 2, Section IV.
- 8 F H Pollak and H Shen: J. Crystal Growth 98 1989 pp. 53.
- 9 J Lee, E S Koteles and M O Vassell: Phys. Rev. B, Vol. 33 1986 pp. 5512.
- 10 B Deveaud, A Regreny, J Y Emery and A Chomette: J. Appl. Phys. 59 (5) 1986 pp. 1633.
- 11 L Schultheis, A Honold, J Kuhl, and K Köhler: Phys. Rev. B Vol. 34 1986 pp. 9027.
- 12 K Meiyng, S Dianzhau, L Jiben, H Yunneng and Z Yiepen: J. Elect. Mat. Vol 16, No 6, 1987 pp. 417
- 13 W T Masselink, Y L Sun, R Fischer, T J Drummond, Y C Chang, M V Klein and H Morkoc: J. Vac. Sci. Technol. B, Vol 2, No 2 1984 pp. 117.
- 14 R C Miller, C W Tu, S K Sputz and R F Kopf: Appl. Phys. Lett. 49 (19) 1986 pp. 1245.
- 15 F Voillot, A Madhukar, J Y Kim, P Chen, N M Cho, W C Tang and P G Newman: Appl. Phys. Lett. 48 (15) 1986 pp. 1009.
- 16 K K Bajaj , D C Reynolds, C W Litton, J Singh, P W Yu, W T Masselink, R Fischer and H Morkoc: Solid State Elect. Vol 29, No 2 1986 pp. 215
- 17 M Tanaka and H Sakaki: J. of Crystal Growth 81 (1987) pp. 153.
- 18 C W Tu, R C Miller, P M Petroff and R F Kopf: J. Vac. Sci. Technol. B6 (2) 1988 pp. 610.
- 19 D Bimberg, D Mars and J N Miller: J. Vac. Sci. Technol. B4 (4) 1986 pp. 1014.
- 20 D Bimberg, J Christen, T Fukunaga, H Nakashima, D E Mars and J N Miller: J. Vac. Sci. Technol. B5 (4) 1987 pp. 1191.
- 21 Y L Sun, R Fischer, M V Klein, H Morkoc and E Mendez: Thin Solid Films 112 1984 pp.213
- 22 J N Schulman: J. Vac. Sci. Technol. B1 (3) 1983 pp.644.
- 23 H Kawai, K Kaneko and N Watanabe: J. Appl. Phys. 56 (2) 1984 pp. 463.
- 24 J Y Anderson and U Westergren: J. Crystal Growth 93 1988 pp. 307.
- 25 M E Pistol, S Nilsson, P Silverberg, L Samuelson, M Rsk and G Landgren: Superlattices and Microstructures, Vol 2, No 6, 1986 pp. 501.
- 26 B A Wilson, R C Miller, S K Sputz, T D Harris, R Sauer, M G Lamont, C W Tu and R F Kopf: Inst. Phys. Conf. Ser. No. 83 Chapter 4, Papaer presented at the Int. Symp. GaAs and Related Compounds, Las Vegas, Nevad, 1986 pp. 215.

Chapter 5

Photoluminescence studies of free-standing MBE quantum dots

5.1 Introduction

This work was carried out in conjunction with Dr S R Andrews of GEC Hirst Research Centre. All fabrication was done by myself and the photoluminescence experiments were carried out by Dr S R Andrews. It was felt necessary to present the PL measurements done by Dr S R Andrews and myself (Chapter 6) into separate Chapters to differentiate the work. However there was much interaction between us with results obtained by Dr S R Andrews, especially in the area of temperature variation of QD PL intensity, suggesting the way forward in the overgrowth work.

In this chapter the effects of patterning MBE grown QW material into submicron free-standing lattice matched GaAs/Al_{0.3}Ga_{0.7}As and strained layer In_{0.11}Ga_{0.89}As/GaAs quantum dots with relatively large surface-to-volume ratios will be presented and the affect that this patterning has on the recombination of photoexcited carriers will be discussed.

5.2 Surface Recombination Velocity

Oxygen-exposed GaAs surfaces (and presumably InGaAs surfaces for small enough In mole fractions) possess a large density of extrinsic states near the middle of the forbidden energy gap which effectively pin the surface Fermi level at that position. This midgap pinning is associated with trapping centres, which can give rise to a large non-radiative surface recombination velocity (SRV) at room temperature¹ and can limit the performance of minority carrier devices such as bipolar transistors and light emitting diodes. These extrinsic states may be due to the oxidation of the GaAs which results in the formation of excess arsenic, As₂O₃ and Ga₂O₃ on the surface^{2,3}. Heterojunction interface recombination velocities are generally small by comparison⁴.

It is expected that when GaAs/AlGaAs quantum well material is patterned into wires or dots, the effect of the surface recombination velocity will be greater as the surface area to volume ratio has been greatly

increased. There will be many more states available on the surface where excitons can recombine nonradiatively and hence in very small submicron structures it is thought that the luminescence will either be reduced or even quenched. The surface recombination velocity varies between semiconductors. In the InP/InGaAs system the surface recombination velocity is approximately two orders of magnitude less than the GaAs/AlGaAs system and therefore it is expected that submicron structures in this system will show little evidence of surface recombination. Chapter 1, Sections 1.4.1 and 1.4.2 reviews the results obtained by different authors in fabricating quantum structures in these two material systems. The results presented here will attempt to ascertain the affect these surface states have on the luminescence from submicron structures.

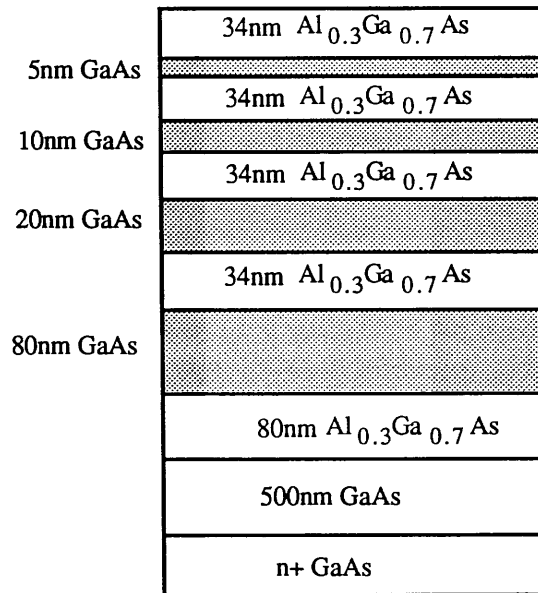
5.3 Experimental Details

The GaAs/AlGaAs quantum dot structures were made from material grown by molecular beam epitaxy and the material structure is shown in figure 5.1a. The 80nm AlGaAs layer was included to inhibit diffusion of photoexcited carriers from the substrate to the quantum wells. The InGaAs/GaAs quantum dots were fabricated from material with the structure shown in figure 5.1b. The well and barrier thicknesses were verified to 10% accuracy by transmission electron microscopy. Patterning of the material was done using electron beam lithography as described in Chapter 2 and then the free standing pillars containing the quantum dots were defined either by reactive ion etching or argon ion milling as described in Chapter 3.

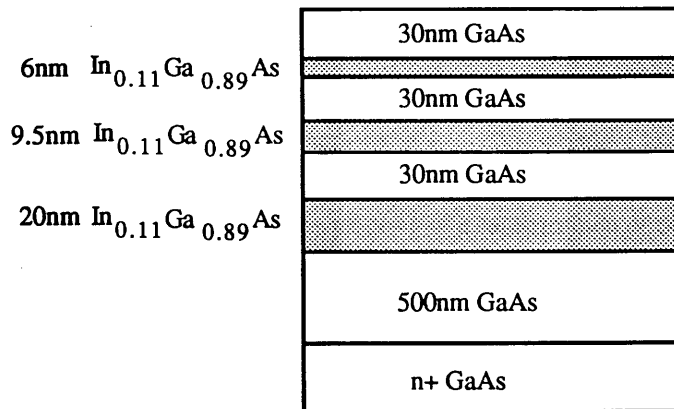
Dots with various nominal diameters between 40nm and 500nm were patterned in the form of arrays of free standing pillars in squares 100 μ m on edge with typical pillar spacings of between three and five times the pillar diameter, corresponding to filling factors of 4-9%. The pillar arrays were delineated using one of the alignment patterns outlined in Chapter 2 Section 2.7. The pillar diameters could be measured to an accuracy of ± 5 nm in the SEM. The pillar diameter variations within the array were of the same order. The uppermost two quantum wells were etched through in all cases. Typically 10 different arrays of pillars were patterned at a time with a spacing of 1mm between adjacent arrays. Square control mesas 100 μ m on edge were also exposed between the arrays to assess etching damage and act as standards of luminescence efficiency. The masks were not generally removed after fabrication. With metal masks, this resulted in attenuation of the optical signal by a factor of 5-30 depending on the final mask thickness. The HRN mask caused negligible attenuation.

Another sample designed to allow comparative investigations of low temperature surface recombination rates at broad area GaAs free surfaces was also etched at the same time as some of the GaAs/AlGaAs quantum dots. The sample consisted of undoped GaAs and Al_{0.3}Ga_{0.7}As layers grown in the following order on a semi-insulating substrate: 400nm GaAs buffer, 500nm AlGaAs, superlattice buffer (consisting of ten periods each of 5nm GaAs, 5nm AlGaAs), 40nm AlGaAs, 500nm GaAs, 40nm AlGaAs, 10nm GaAs. Square windows 400 μ m on edge were photolithographically created in a 2 μ m thick layer of positive resist. Subsequent etching then revealed the 500nm GaAs layer.

Photoluminescence and Photoluminescence excitation experiments were carried out using a similar experimental set up to that outlined in Chapter 4. The main difference was in the alignment of the laser



(a)



(b)

Figure 5.1 (a) The GaAs/AlGaAs material structure grown by MBE. (b) The InGaAs/GaAs material structure grown by MBE.

spot onto the QD array. The 30 μm focal spot of the exciting laser light and the patterned sample areas were observed at x100 magnification through a pinhole at the entrance of the spectrometer using a periscope equipped with a TV camera instead of using a zoom lens. The pinhole provided effective spatial filtering to help discriminate against PL excited in other areas of the sample by scattered light and by using a TV camera to image the sample it was possible to position the infrared light used for PLE measurements.

PL was excited above the AlGaAs band gap using the 632.8nm (1.96eV) line of the He-Ne laser and below the AlGaAs band gap using an Argon ion pumped Pyridine 2 or Styryl 9 dye laser with the sample mounted in a variable temperature helium atmosphere. A 90° scattering geometry was used with the exciting incident light focussed down to 30 μm and typically making an angle θ of between 33° and 67° to the sample surface normal. For θ larger than about 40° the measured luminescence intensity was approximately independent of angle. However, for θ smaller than 40° the collected luminescence intensity decreased rapidly with decreasing θ , especially for small diameter and metal masked samples. This possibly indicates improved coupling of light into the dots (for example by sidewall illumination) at larger angles of incidence and the measurements discussed below were made with a fixed incident angle of 50° unless otherwise stated. The PL was spectrally dispersed using a 0.85m focal length double grating spectrometer with a resolution of 0.2meV (full width at half maximum, FWHM).

5.4 Experimental Results

5.4.1 GaAs/AlGaAs Quantum Dots

Representative PL spectra of the GaAs/AlGaAs quantum well sample before and after patterning into pillars of 60nm diameter are shown in figure 5.2. The peaks near 775, 802, 814 and 818nm in the spectra of the starting material, figure 5.2a arise from the ground state free exciton recombination in the 5, 10, 20 and 80nm (and thicker) layers respectively. The peaks near 802nm and 814nm are doublets at low excitation powers with the longer wavelength component corresponding to a defect bound exciton. The other important feature in the spectrum of figure 5.2a is the broad, relatively weak background between 800nm and 850nm. This appears to be made up of a superposition of two broad peaks centred at 830nm and 822nm which is tentatively attributed to transitions involving an electron bound to a neutral carbon acceptor and an exciton bound to a defect, (d,X), such as a gallium vacancy complex^{3,4} respectively. The 100 μm control mesas on the patterned samples showed similar spectra to the starting material, figure 5.2a, but with the exciton peaks typically broadened by about 1meV, possibly because of the strain associated with differential thermal contraction between mask and sample on cooling or because of radiation damage. The spectra of the patterned material in figures 5.2b,c,d clearly show peaks associated with recombination in the 5nm and 10nm wells. Linewidths (FWHM) in the starting material were 4meV and 1.2meV for the transitions in the 5nm and 10nm wells respectively. In the smallest patterned structures there was typically further broadening of 2-4meV which can be attributed mainly to radiation damage. In the samples patterned using SiCl₄ RIE and Argon ion milling (figures 5.2b,c) there is a broad (~60meV) (d,X) peak with absolute intensity similar to that in the starting material, together with a narrow (<1meV, FWHM) dip at the free exciton energy of 1.515eV. For

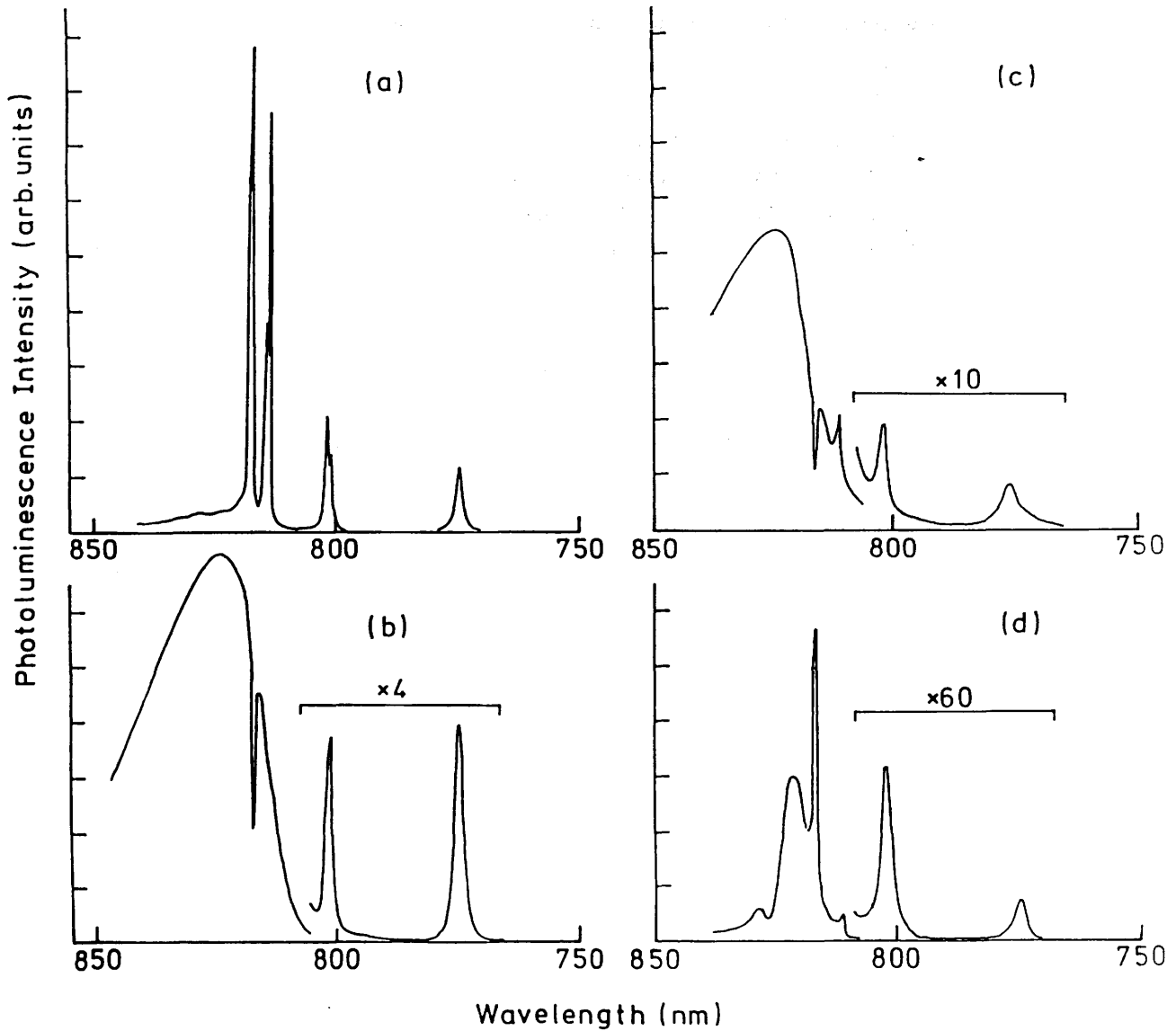


Figure 5.2 Representative PL spectra obtained at 5K with excitation at 1.65eV and 1Wcm^{-2} for GaAs/AlGaAs quantum well sample before patterning (a) and after patterning into (b) 60nm pillars (250nm pitch) etched to depth of $0.2\mu\text{m}$ using SiCl_4 RIE (c) 60nm pillars (200nm pitch) etched to depth of $0.12\mu\text{m}$ using Ar ion milling, (d) 60nm pillars (180nm pitch) etched to depth of $0.1\mu\text{m}$ using CH_4/H_2 RIE.

wavelengths longer than 810nm the spectrum from the patterned areas is very similar to that of the uniformly etched regions of the samples. This structure may be due to scattering from radiation induced defects or the creation of a surface depletion region in the GaAs buffer or 80nm layer exposed during the etching. In the CH_4/H_2 etched samples the spectrum in the region 800-850nm is somewhat different. figure 5.2d shows a relatively narrow (10meV, FWHM) peak centred at 822nm and about ten times more intense than the background at that wavelength in the starting material which again is probably related to defect bound excitons. Note that a bulk-like free exciton peak is apparent in figure 5.2d, presumably because the smaller etch depth in this sample leaves the 80nm GaAs layer buried. Some CH_4/H_2 etched samples were annealed at 400°C for 5 minutes after removing the HRN resist in an oxygen plasma. Hydrogen is known to passivate shallow acceptors and donors in GaAs but can be removed by annealing. Its effects on radiative recombination are not known but no significant differences between the spectra of annealed and unannealed samples were observed.

The energy dependence of the PL intensity (i.e. the photoluminescence excitation or PLE spectrum) in many of the box arrays was measured and it was found that the luminescence efficiency has a similar variation with energy in both mesas and dots except for a broadening of 2-4meV in the latter. There was no enhancement in the PL efficiency at high excitation energy relative to low energy as reported by Kash *et al*⁵. The shape and position of the n=1 heavy hole exciton resonance in the excitation spectrum was not found to vary with detection energy suggesting that the dominant line broadening mechanism is intrinsic to each quantum dot (radiation damage) rather than reflecting size variations between dots. No significant variation in ground state exciton energy with dot size was found within the experimental uncertainty of $\pm 2\text{meV}$. These observations are consistent with calculations of the bound state energies for 5nm wells in 50nm boxes with $\pm 5\text{nm}$ lateral size variations which give (taking into account the electron-hole interaction⁶ a blue shift in the exciton bound state energy of approximately 3meV and an inhomogeneous broadening of 1meV.

Figures 5.3 and 5.4 show the relative intensity of luminescence from the 5nm and 10nm quantum wells after patterning into dots of lateral extent 40nm-500nm using SiCl_4 and CH_4/H_2 RIE respectively. The relative intensity is the ratio of the integrated intensity of the quantum well luminescence from the dot array (divided by the box filling factor) to that from an adjacent 100 μm mesa. Typically the measurements are reproducible to within factors of order 2 or 3. The luminescence efficiency of the mesas was found to be the same as that of large, similarly masked pieces of the starting material. A relative intensity of 1 therefore indicates a luminescence efficiency which scales with the volume of excited quantum well material. Although some data show lower efficiency, possibly because of processing problems, the majority of points for both etching processes do approximately support such a scaling. Possible processing problems include poor mask quality resulting in radiation damage and poor anisotropy in the etching, resulting in over or under cutting leading to a reduction in surface coverage. The results in figures 5.3 and 5.4 were obtained at 5K with excitation at 1.96eV which is above the AlGaAs band gap. Similar results were obtained with excitation below the AlGaAs band gap at 1.65eV.

Table VI Details of patterned GaAs/AlGaAs samples used in obtaining the data of Figures 5.3, 5.4 and 5.5.

Figures	Symbol	Mask	Etch Depth (μm)
5.3	Triangle	0.12 μm HRN	0.6
	Square	0.12 μm HRN	0.2
	Circle	25nm NiCr	0.2
	Diamond	0.28 μm HRN	0.3
5.4	Circle	0.28 μm HRN	0.1
	Square	25nm TI	0.1
5.5	Circle	20nm Ti	0.12
	Square	20nm Ti.	0.2

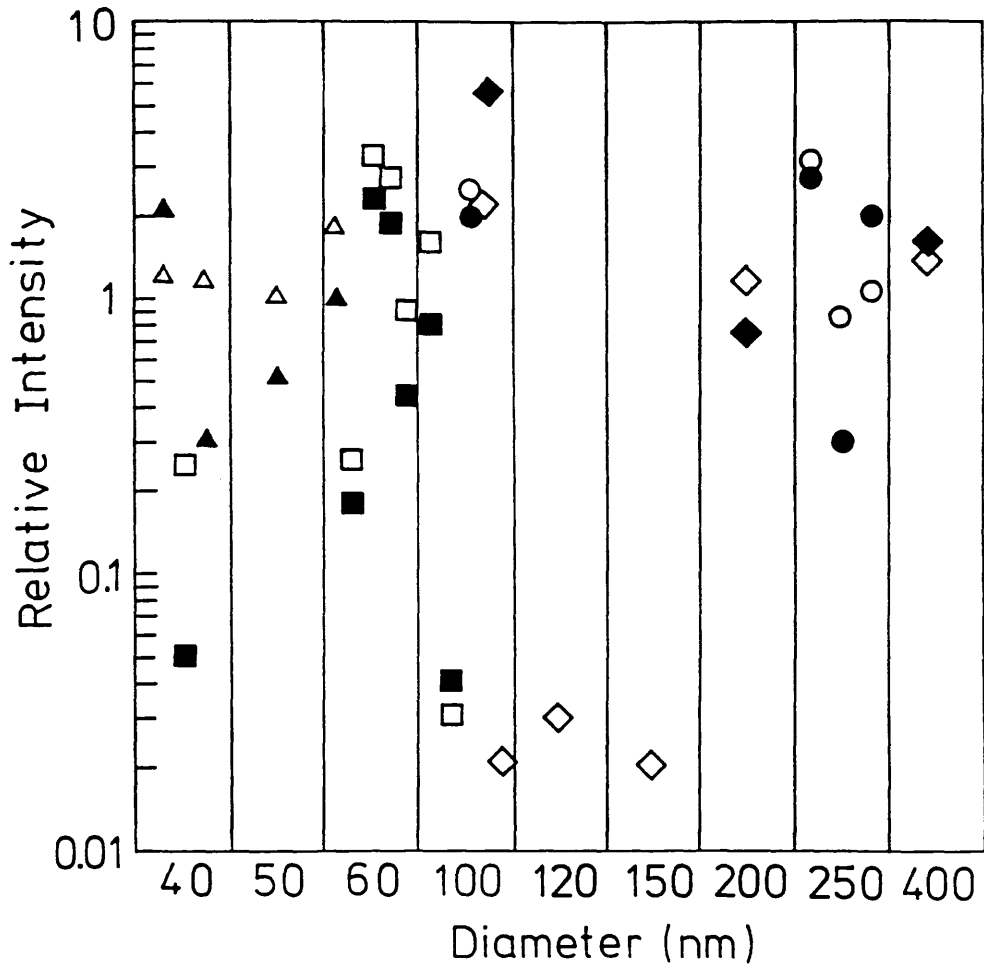


Figure 5.3 Integrated intensity of PL excited at 1.96eV in four SiCl_4 etched GaAs/AlGaAs quantum well samples (as shown by the key) with various pillar diameters relative to that in the control mesas on the same samples. The PL intensities are scaled by the volume of quantum well material excited as discussed in the text. Data from the 5nm quantum well is shown by open symbols and the 10nm well by filled symbols.

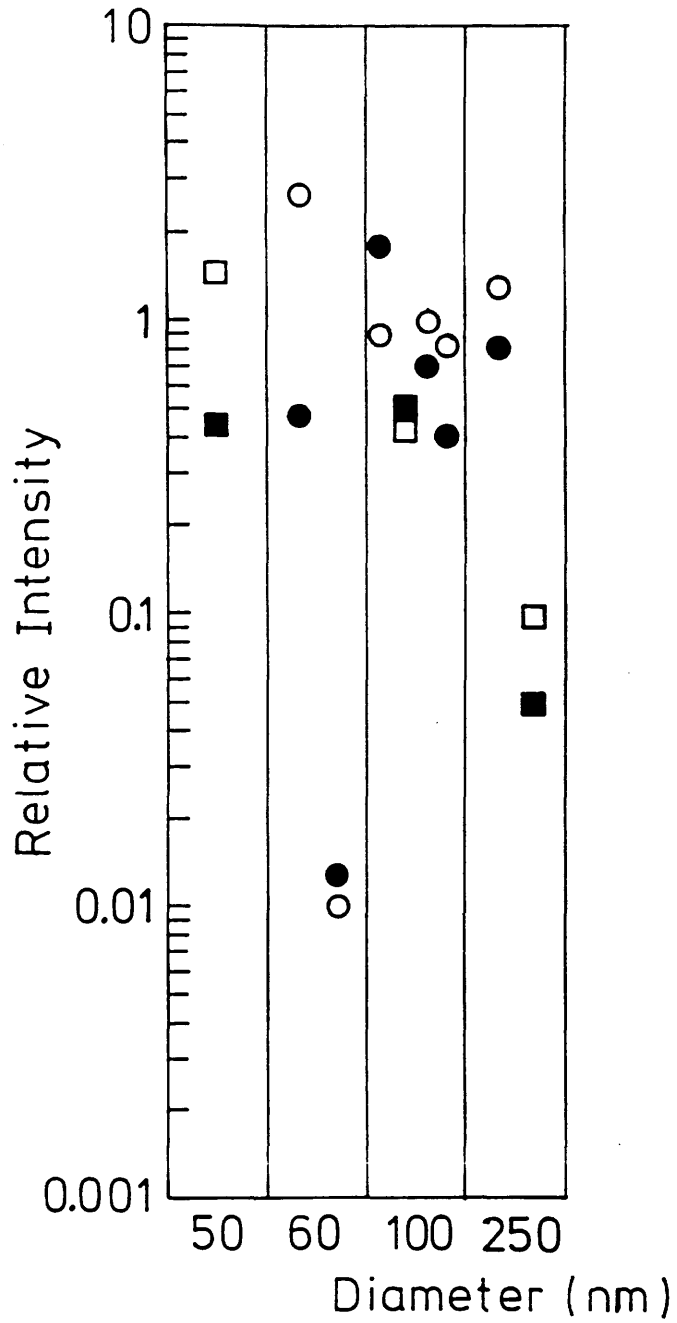


Figure 5.4 Relative Intensity of PL excited at 1.96eV in two CH₄/H₂ etched in GaAs/AlGaAs quantum well samples as shown by the key. Open symbols refer to 5nm quantum well and filled symbols to 10nm well.

After these results were obtained from dots fabricated by SiCl_4 and CH_4/H_2 , passivation of broken bonds at the GaAs surface was suggested as the mechanism enabling efficient luminescence to be obtained from the dots⁷. For example it was suggested that the Cl layer discussed in Section 3.4.1 could perhaps passivate these states. In order to investigate this possibility dots were fabricated using Argon ion milling. This is a purely physical sputtering process (see Section 3.7) with no chemistry involved and therefore no means of chemical passivation of surface states. The results are shown in figure 5.5a and were obtained using the same excitation conditions as those described for figures 5.3 and 5.4. The relative luminescence efficiencies from these dots are ~ 1 with a slight decrease of an order of magnitude for the smallest structures. These results therefore show that chemical passivation of surface states is not the mechanism which results in efficient luminescence from the dots. It might have been expected that these structures would have been more severely damaged as it is thought that by increasing the chemical component of a reactive ion etch process reduces the resulting damage and this has been shown in direct sputter etching of broad areas⁸. As can be seen this is not the case and this suggests that the mechanism of damage to the sidewalls of the pillars is different. This might be expected since they predominately suffer indirect ion bombardment. In figure 5.5b the effect of reducing the angle of incidence of the exciting light on the measured relative intensity of the PL is illustrated.

At first sight the results in figures 5.3, 5.4 and 5.5a indicate that non-radiative surface recombination at the air exposed free surfaces created by patterning is not effective in quenching the luminescence at low temperature. Typical behaviour of the quantum well integrated luminescence intensity with exciting power for an efficiently luminescing array is shown in figure 5.6. A linear dependence is found, characteristic of radiative recombination, down to the lowest powers which could be investigated. Similar behaviour was found for less efficiently emitting arrays. This tends to support the conclusion that centres for non-radiative recombination are ineffective in these samples under typical experimental conditions. The temperature dependence of the integrated PL intensity from the 5nm and 10nm wells in the 60nm diameter CH_4/H_2 etched pillars is compared with that of the starting material in figure 5.7. The luminescence efficiency of the pillars is seen to decrease relative to that of the starting material with increasing temperature. This behaviour is discussed in Section 5.4.

The most important feature of the data which must be explained is the existence of samples showing high luminescence efficiency at low temperature rather than some also show relative low efficiency. Passivation of surface states has been ruled out as a possible mechanism due to the results from the Argon ion milling experiments. It is therefore worthwhile to consider whether enhancement of the radiative recombination rate or photocarrier generation rate within the pillar or a reduction in the non-radiative recombination, not associated with the free surfaces, could be the responsible mechanism.

It seems unlikely that the radiative recombination rate could be increased because the dots are too large to show clear signs of lateral confinement. A further point to consider is whether the number of carriers created in the wells scales with the volume of the quantum well. This assumption appears reasonable as there is no obvious mechanism leading to significant enhancement of the optical field within the pillars (although the dependence of the PL intensity on the angle of incidence of the exciting light is not fully understood) and diffusion of photoexcited carriers from material between the pillars into the quantum

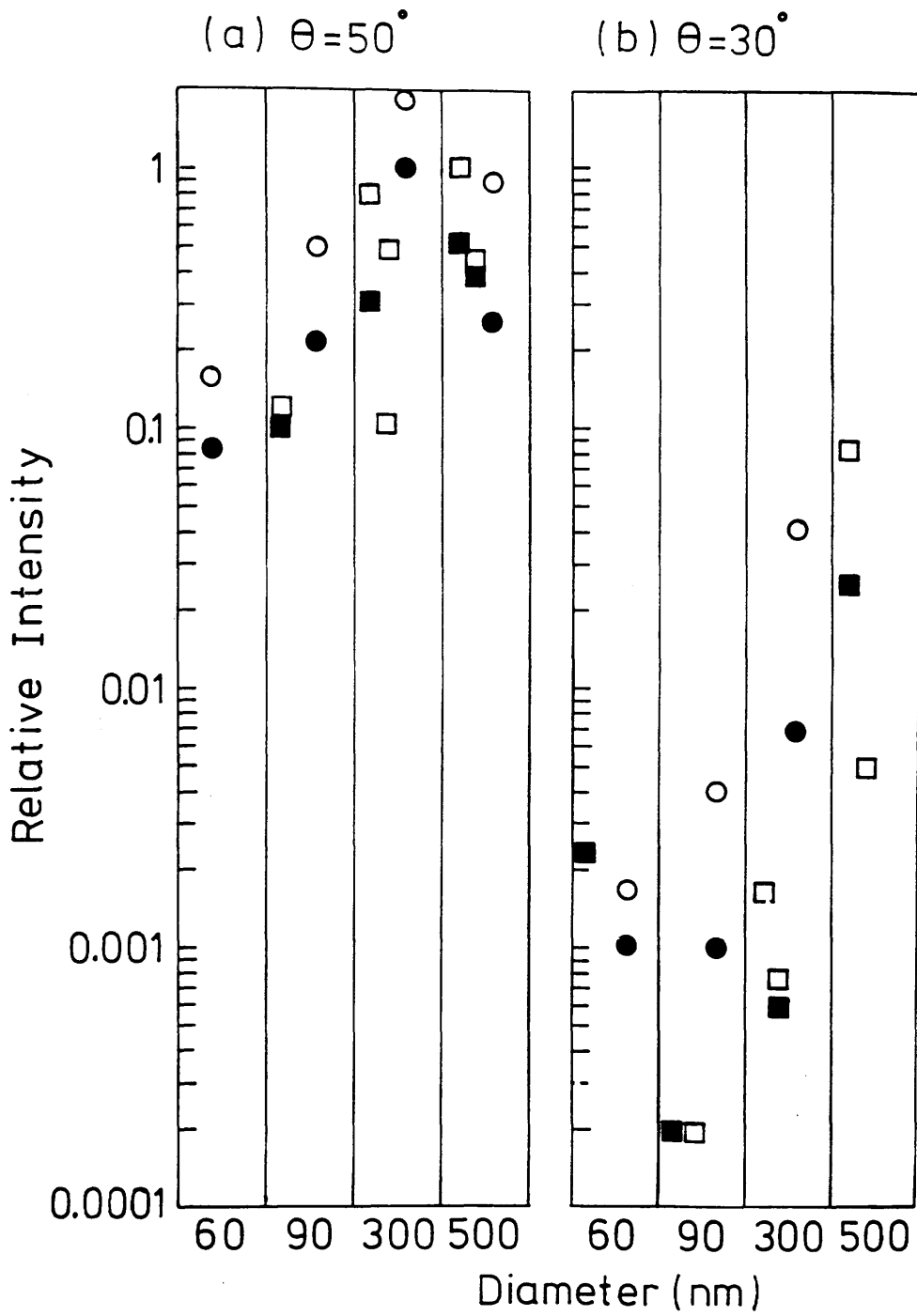


Figure 5.5 Relative Intensity of PL from GaAs/AlGaAs quantum wells excited at 1.65eV with angles of incidence of (a) 50° and (b) 30° in two Ar ion milled samples, as shown in the key. Open symbols refer to 5nm quantum well and filled symbols to 10nm well.

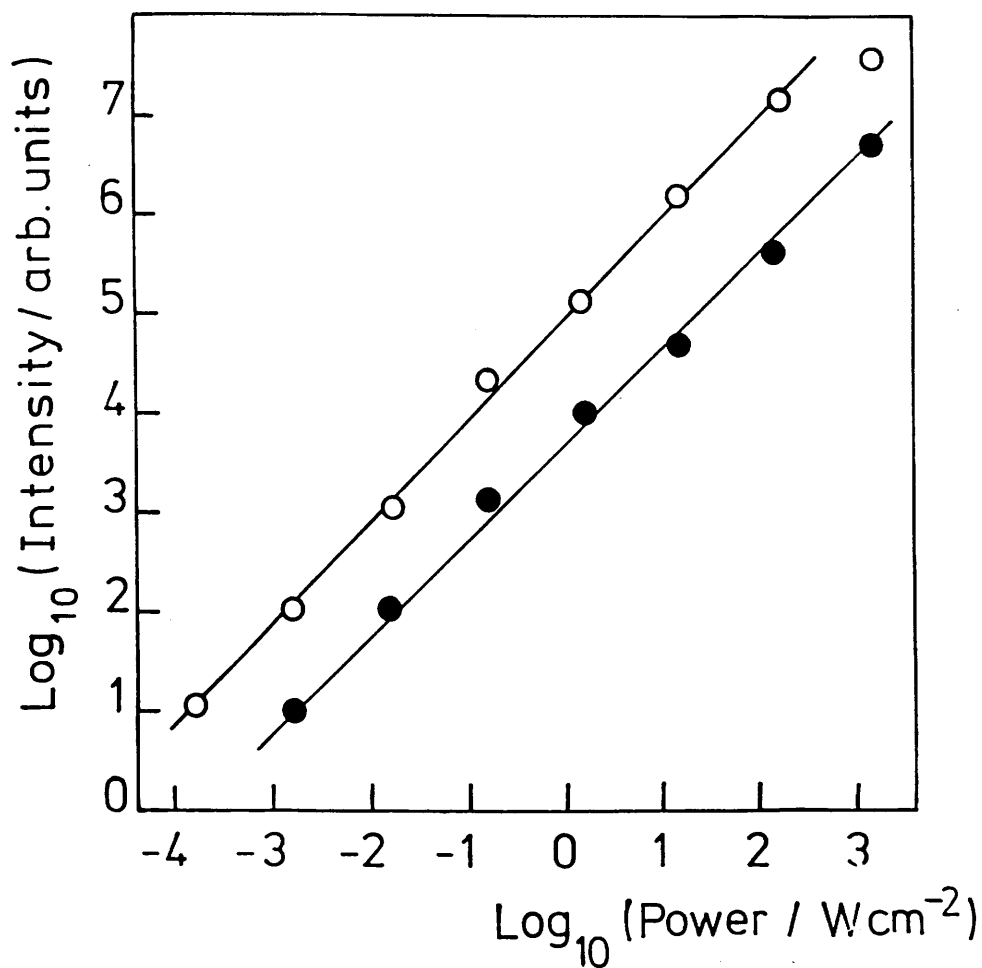


Figure 5.6 Excitation power dependence at 1.65eV of integrated PL intensity from 10nm well of GaAs/AlGaAs sample fabricated into an array of 60nm dots (filled circles) and a control mesa (open circles) in a sample etched using CH_4/H_2 with a $0.28\mu\text{m}$ HRN resist mask.

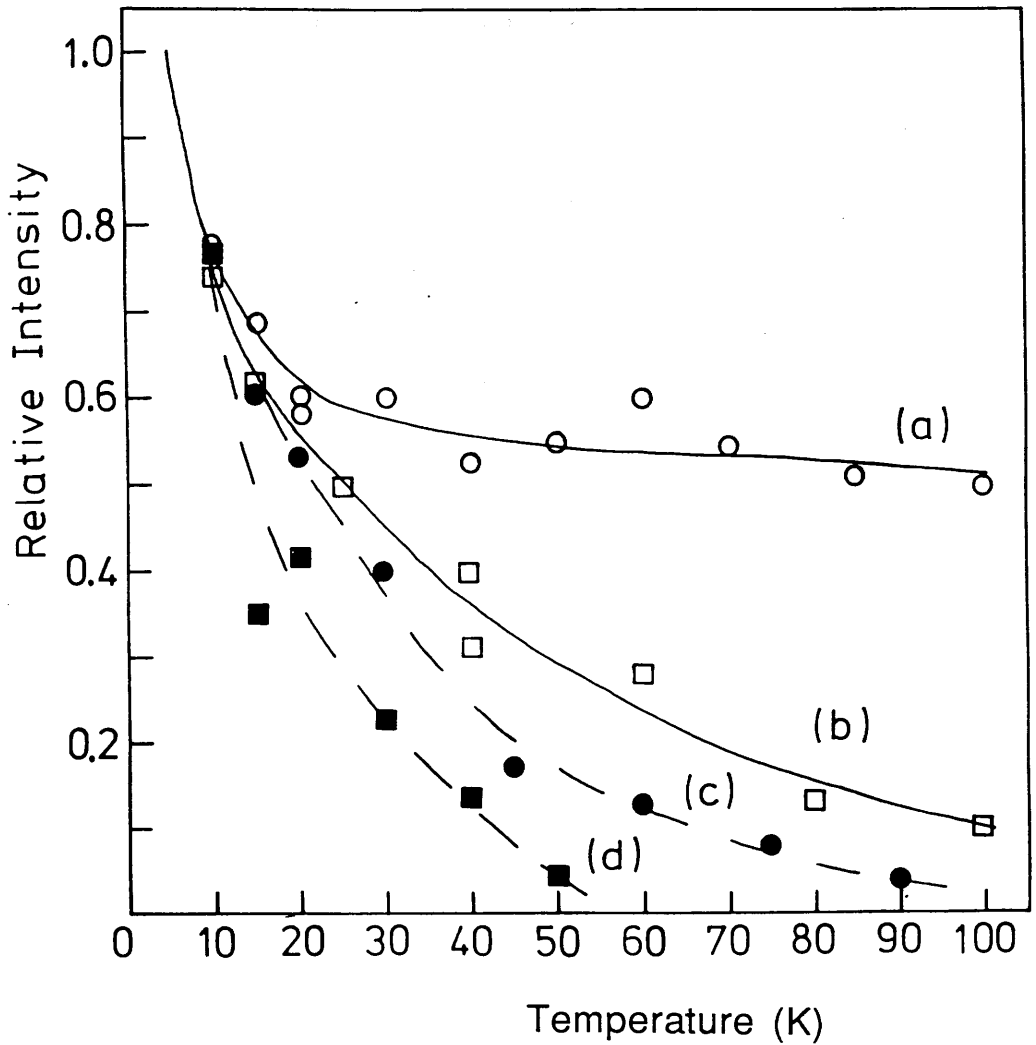


Figure 5.7 Temperature dependence of integrated luminescence intensity relative to that at 5K in (a) 5nm quantum well of GaAs/AlGaAs sample before processing and (c) after patterning into an array of 60nm pillars by CH_4/H_2 RIE. Curves (b) and (d) similarly before and after processing for 10nm well.

wells seems to be ruled out by the fact that no quantum well luminescence is observed if excited at energies below that of the well gap. Note similar results were obtained with excitation at energies above and below the barrier band gap so that the mechanism whereby carriers photoexcited in the barriers are transferred into the wells need not concern us. In connection with 'bulk' non-radiative recombination, it should be noted that Kash *et al*⁵ have observed an enhancement of the luminescence efficiency of quantum wires and dots with dimensions 40–45nm by an excitation energy dependent factor of up to 50-100 compared with the unpatterned material. It was suggested that patterning might eliminate many non-radiative recombination centres in the quantum wells, thus increasing the luminescence efficiency. A similar argument has previously been used to explain the high luminescence efficiency of quantum wells compared with bulk semiconductors⁹. In the latter case, exciton confinement in the growth direction impedes transport to non-radiative centres. If an enhancement mechanism is operating in these samples, then it must be balanced by increased surface non-radiative recombination. Although this effect cannot be ruled out, such a fortuitous balance seems unlikely and it is believed that these experiments show that surface recombination need not be significant in GaAs/AlGaAs dots at low temperature.

5.4.2 InGaAs/GaAs Quantum Dots

Typical PL spectra of the InGaAs/GaAs sample after processing into a 100 μ m mesa and array of 500nm diameter pillars with 4% surface coverage are shown in figure 5.8. The peaks at 847, 861.5 and 847.5nm arise from the ground state recombination in the 2.5, 6 and 9.5nm thick In_{0.11}Ga_{0.89}As quantum wells respectively. In contrast to the GaAs/AlGaAs dots, the relative luminescence intensities in InGaAs/GaAs dots with lateral dimensions of less than 0.5 μ m fabricated using both SiCl₄ and CH₄/H₂ RIE were found to be dramatically less than in the starting material or large mesas for excitation both above and below the GaAs bandgap, indicating that surface recombination plays an important role in the latter system. For 500nm dots, the relative intensities were found to be between 0.1 and 0.01 of that in the 100 μ m mesas. The luminescence from the dots with diameters of 300nm and less was too weak (relative intensity less than 10⁻³) to discriminate against the background GaAs luminescence.

5.4.3 Broad Etched Areas¹

The results presented in Section 5.3 show that nonradiative surface recombination is not a dominant recombination mechanism in the GaAs/AlGaAs quantum dots and that the process is mainly radiative - shown by the high relative luminescence efficiencies of the dots at low temperatures. This raised the question of whether the surface recombination velocity was the same at room temperature and at 5K, the temperature at which the dots were measured. The following experiment was designed to try and answer this question.

¹ In this section the samples were fabricated by Dr S R Andrews, and all calculations on the surface recombination velocity were done by him. The dry etching was done by myself using the same parameters as the dot etching.

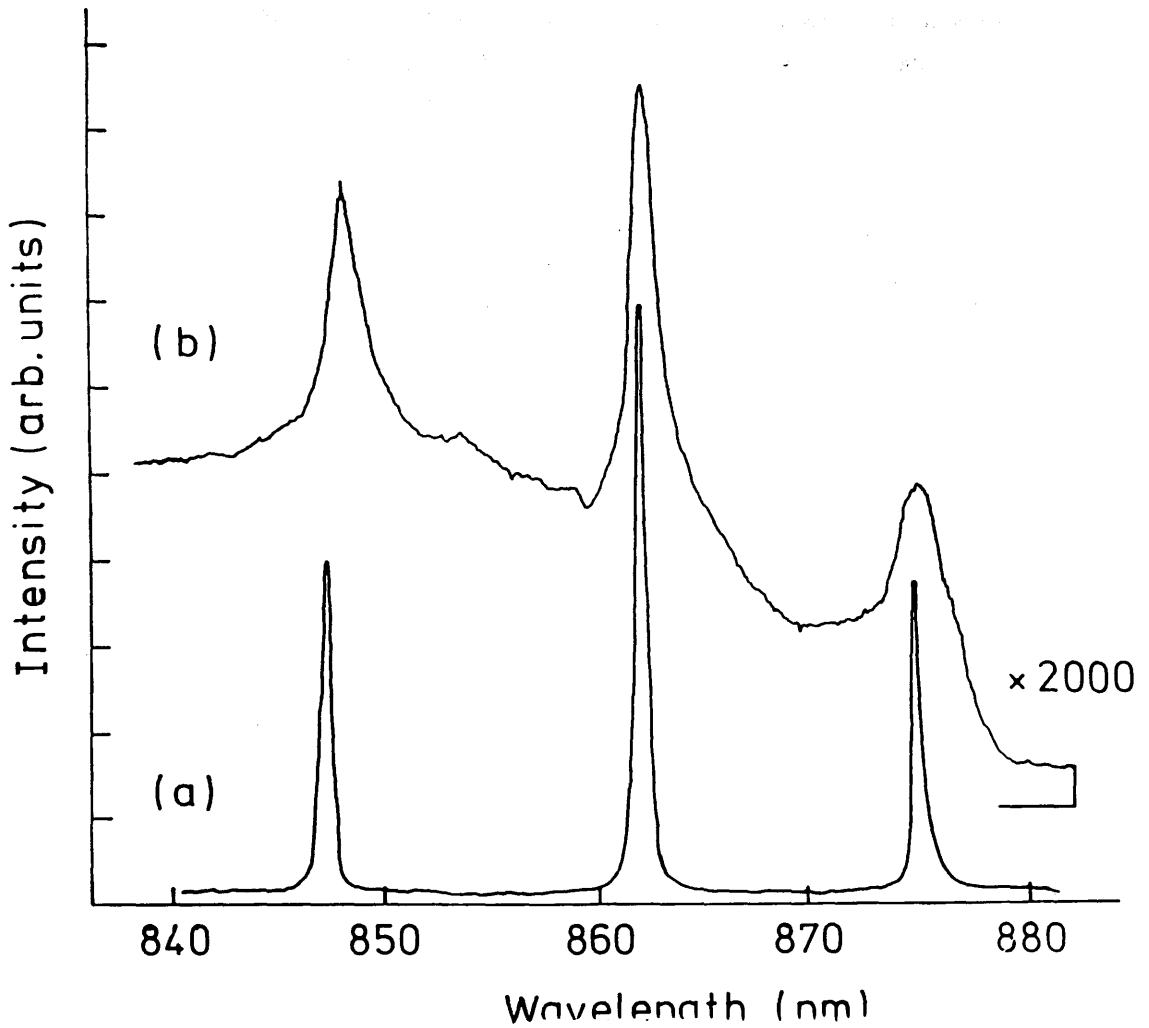


Figure 5.8 PL spectra of InGaAs/GaAs samples at 5K excited at 1.49eV (a) 100 μ m mesa and (b) array of 500nm pillars (pitch 2500nm, etch depth 0.3 μ m) fabricated using SiCl₄ RIE and a 0.28 μ m thick HRN etch mask.

At the same time as some of the quantum dot arrays, samples from the wafer containing a 0.5 μm thick nominally undoped GaAs layer bounded by AlGaAs barriers in such a way as to expose areas of free GaAs surface were also etched. At 5K, the PL spectrum of the GaAs layer was dominated (for power densities as low as 0.01Wcm⁻²) by a strong free exciton peak at 1.519eV in both the as-grown and etched samples, but with peak intensity reduced by a factor of about 100 in the latter. Figure 5.9 shows the temperature dependence of the relative integrated luminescence intensity from buried and exposed regions of a sample prepared by reactive ion etching with SiCl₄. Similar results were obtained using CH₄/H₂ and also wet chemical etching with H₂O:H₂O₂:HCl (12:1:1). Neglecting bulk non-radiative recombination and reabsorption, and assuming that the luminescence intensity is proportional to τ/τ_r where $\tau^{-1}=\tau_r^{-1}+S/d$, τ_r is the radiative lifetime, S is the surface recombination velocity and d is the thickness of the GaAs layer (assumed smaller than the diffusion length) then it is estimated that $S\sim 10^6\text{cm}^{-1}$ at 5K using a radiative recombination time of 3ns¹⁰. Figure 5.9 suggests that the surface recombination velocity decreases with increasing temperature but since τ_r increases with temperature it is possible that this picture is modified. The temperature dependence suggested by figure 5.9 is however in qualitative accord with phenomenological models of non-radiative recombination which take into account trap occupation factors^{11,12} and a low value at room temperature is consistent with the data reviewed by Aspnes¹.

Another approach to look at the question of the effects of the surface states is to try and alter the surface after the behaviour of oxygen exposed surfaces has been measured. One way to do this, is to regrow with a layer of a semiconductor and results utilizing this method are presented in Chapter 6. Another way to treat the exposed surfaces is by immersion in NH₄OH saturated with H₂S following a brief wetting etch in 1:1:500 H₂SO₄:H₂O₂:H₂O for 5 seconds (etch rate $\sim 0.5\text{nms}^{-1}$). This treatment is reported to lower the surface state density, possibly by the formation of passivating surface Ga-S bonds which inhibit oxidation^{13,14}. As can be seen in figure 5.9 the effect of this surface passivation treatment is to increase the PL intensity in the surface exposed regions by a factor of about 5 at room temperature, although there is little effect at 5K as also found by Skromme *et al*¹⁵. Similar experiments were carried out on several GaAs/AlGaAs and InGaAs/GaAs quantum dot samples. No significant change in luminescence efficiency was found in these structures at 5K, but it is difficult to regard this as confirmation of a low surface recombination rate because of the small effect found in the broad area etched sample at 5K and also because it may be difficult to wet the surface of the dots.

5.5 Discussion²

With the provisos mentioned in Section 5.4 concerning changes in the bulk non-radiative recombination and coupling of light into the structures, the overall conclusion from this work is that the non-radiative surface recombination rate in GaAs/AlGaAs dots remains small compared with the radiative recombination rate for lateral dimensions down to 40nm but is relatively large in those InGaAs dots smaller than 500nm. Taking a typical exciton radiative lifetime of 300ps for a 5nm GaAs quantum well at 5K¹⁶ then a negligible non-radiative rate in the smallest GaAs/AlGaAs pillars implies

² Calculations done in this section by Dr S R Andrews

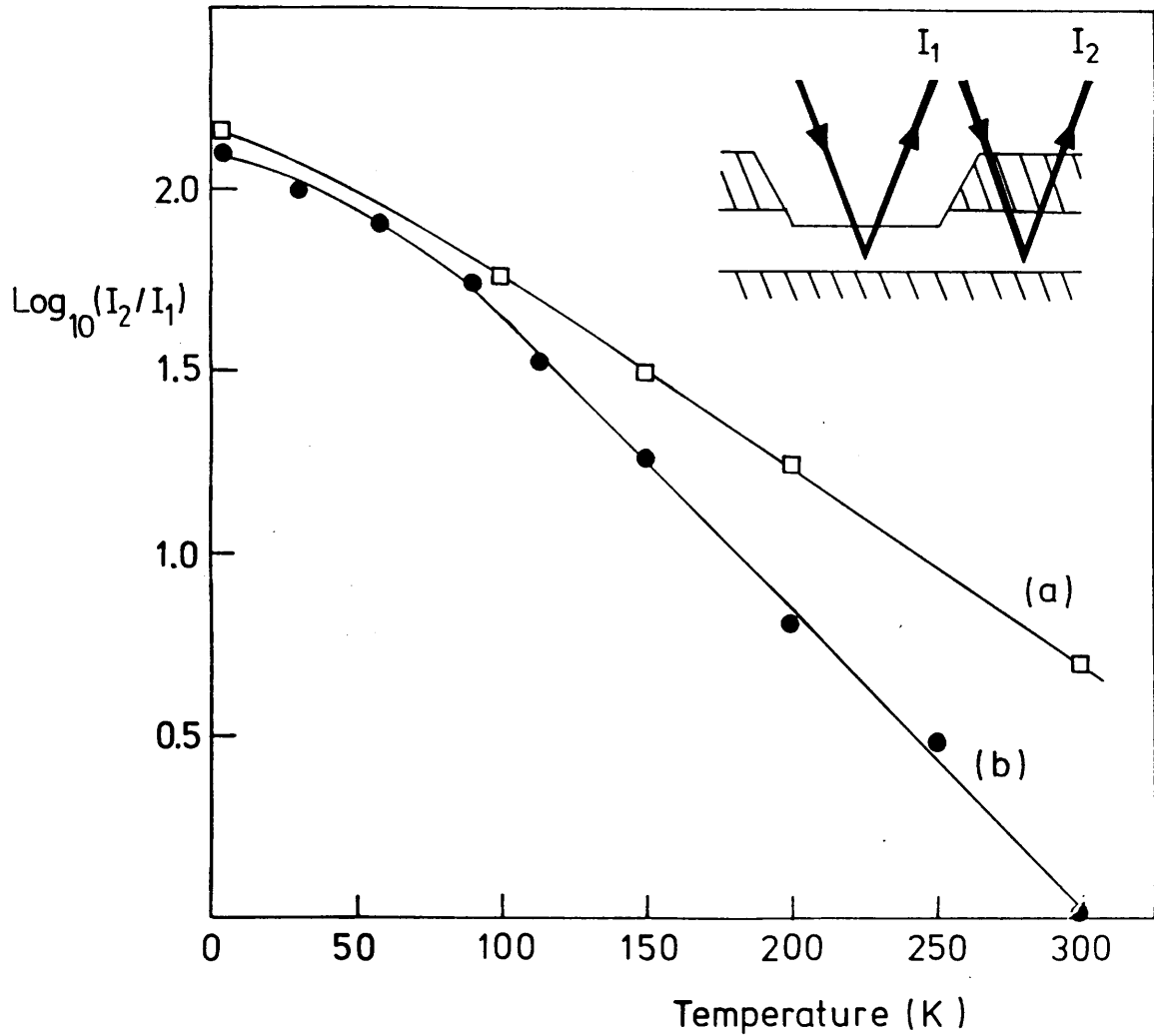


Figure 5.9 Temperature dependence of ratio of luminescence intensity of GaAs epilayer with top surface bounded by AlGaAs relative to that with oxygen exposed surface revealed by SiCl₄ RIE (0.11μm of material removed in 20s) as indicated schematically in inset. Circles (lower curve) show behaviour after attempted passivation with (NH₄)₂S and squares (upper curve) behaviour before passivation.

that the surface recombination velocity, S , is less than 10^4cm s^{-1} . This result is different to that obtained by Forchel *et al*¹⁷ and Maile *et al*¹⁸ for their $\text{CCl}_2\text{F}_2/\text{Ar}$ (1:4) RIE and Argon ion milled GaAs/AlGaAs quantum wires. They observed strong luminescence quenching consistent with a value for S of $5 \times 10^5 \text{cm}^{-1}$. This is similar to that observed at the broad etched surfaces and in the InGaAs/GaAs dots where $S \sim 10^6 \sim 10^7 \text{cm s}^{-1}$ at 5K is estimated. Leaving aside the possibility of large surface recombination rates being attributable to excessive lattice damage incurred during etching it is necessary to consider in what ways the recombination kinetics in a quantum dot could be different to that in a large crystal.

Carrier transport in quantum wells is very different to that in the bulk. Not only are excitons localised perpendicular to the layers (which increases the radiative recombination rate compared with the bulk¹⁹) but also the lateral potential fluctuations associated with local variations in well width (or impurities) which inhomogeneously broaden the exciton transitions can also laterally localise excitons²⁰ (see Section 4.4.1). Exciton diffusion coefficients^{20,21} at 5K can consequently be very small ($< 1 \text{cm}^2 \text{s}^{-1}$) with small associated diffusion lengths (typically $< 100 \text{nm}$). In unpatterned quantum wells at low temperatures, hot photoexcited carriers rapidly form excitons and lose energy by phonon emission until within a few meV of the bottom of the band when excitons generally relax into localised states where further thermalisation within the exciton lifetime is inhibited²². In quantum dots, localisation competes with further thermalisation to, and trapping at, mid-gap surface states. It is suggested that localisation may successfully compete in these GaAs/AlGaAs dots where there are fairly large potential fluctuations (of order 4meV in the 5nm well as inferred from the Stokes shift between emission (PL) and absorption (PLE)). In the InGaAs/GaAs dots, the lateral potential variations appear to be much smaller with, for example, Stokes shifts of less than 0.2meV in the 2.5nm well so that localisation might compete less successfully. Note that it must be supposed that the localisation sites are distributed on length scales of order or smaller than the smallest pillar diameters so that, if lateral disorder arising from well width fluctuations or other defects is responsible, then it must be relatively short range compared with the exciton diameter. An extreme case of the localisation proposed above would be that due to radiation induced mixing of well and barrier at the surface of the dots. The latter mechanism seems unlikely in view of the similar results obtained with a variety of etching methods.

Another possibility is that excitons are laterally localised in the GaAs/AlGaAs dots as a result of relief of the mismatch strain ($\sim 0.04\%$) in the AlGaAs barrier layers caused by removing the surrounding material²³. If the strain is inhomogeneous in the pillars, in particular if it is greatest at the side walls, then a strain induced lateral confining potential of the order of a few meV seems possible. Although the lattice mismatch is larger in the InGaAs/GaAs system (0.8%) it is expected that the strain relaxation will have a similar effect because the relatively thick barriers are lattice matched to the substrate resulting in a similar stored strain energy. In either system it is difficult to predict the effect of strain on the lateral potential variation in the dots. Another possibility is that differential contraction between mask and semiconductor might impose significant strain on cooling. This possibility was investigated by measuring the luminescence efficiency of GaAs/AlGaAs dots etched using CH_4/H_2 in which the HRN mask was subsequently removed in an oxygen plasma. No significant differences were found between the luminescence efficiency of samples cooled with and without HRN masks in place or between HRN and metal masked samples. This tends to suggest that strain effects associated with the

masks are not sufficiently large to influence these results.

If surface recombination in the patterned GaAs/AlGaAs structures is inhibited by lateral exciton localisation then a change in luminescence efficiency with increasing temperature as carriers thermally activate into delocalised states and then thermalise to mid-gap surface traps might be observed. In both the dots and starting material there is a decrease in luminescence with increasing temperature (figure 5.7) as the radiative recombination rate decreases relative to the non-radiative rate. In the starting material this effect is due partly to a thermally activated increase in diffusion length leading to an increase in bulk non-radiative recombination and partly to an increase in exciton lifetime because of the effects of acoustic phonon scattering on the coherence volume of the wavefunction¹⁶. What is significant is that the luminescence intensity in the quantum dots falls faster than that in the starting material for temperatures above 10-20K, indicating a higher non-radiative recombination rate in the dots than in the starting material at these temperatures. This behaviour could be attributed to the existence of a thermally activated non-radiative decay channel at the dot free surfaces. The integrated luminescence intensity of the quantum wells in the InGaAs/GaAs starting material showed similar behaviour to that in GaAs/AlGaAs, whilst in the smallest InGaAs/GaAs patterned structures for which luminescence could be observed it was approximately independent of temperature between 5K and 100K. These observations are consistent with the conjecture that surface recombination can be thermally activated in the GaAs/AlGaAs dots but is already activated in the InGaAs/GaAs dots at 5K.

5.6 Summary

To summarise, the dominant recombination mechanism for photoexcited carriers in sub-micron lattice matched MBE grown GaAs/AlGaAs quantum dots was found to be radiative at temperatures below 20K for lateral dimensions as small as 40nm. In contrast, the dominant recombination mechanism in the sub-micron strained layer InGaAs/GaAs quantum dot system at low temperatures was found to be non-radiative. It is suggested that non-radiative surface recombination is inhibited by the existence of lateral potential barriers in the GaAs/AlGaAs dots but not in the InGaAs/GaAs dots. The origin of such potentials is unclear. Two possibilities have been suggested: disorder in the plane of the well (with surface disordering as an extreme case) and strain. Of these models, that involving lateral potential fluctuations intrinsic to the quantum wells is possibly consistent with surface recombination being more important in InGaAs/GaAs dots. On the basis of this model it is possible that measurements of luminescence efficiency made on samples in the same material system but grown under different conditions (giving rise to different interface morphology) might show different behaviour with decreasing lateral dimensions and this possibility is investigated in the following Chapter.

References

- 1 D E Aspnes: Surf Science 132, 1983 pp. 406.
- 2 E Yablonovitch, C J Sandroff, R Bhat and T Gmitter: Appl. Phys. Lett. 51 (6) 1987 pp. 439.
- 3 S D Offsey, J M Woodall, A C Warren, P D Kirchner, T I Chappell and G D Pettit: Appl. Phys. Lett. 48 (7) 1986 pp. 475.
- 4 R J Nelson, J S Williams, H J Leamy, B Miller, H C Casey, B A Parkinson and A Heller: Appl. Phys. Lett. 36(1) 1980 pp. 76.
- 5 K Kash, A Scherer, J M Worlock, H G Craighead and M C Tamargo: Appl. Phys. Lett. 49 1986 pp. 1043.
- 6 G W Bryant: Phys. Rev. B. B37 1988 pp. 2635.
- 7 H Arnot, S R Andrews and S P Beaumont: Microelectronic Engineering 9 1989 pp. 365 Elsevier Science Publishers B.V. (North Holland).
- 8 S W Pang: J. Electrochem. Soc: Solid State Science and Tech. 133 1986 pp. 784.
- 9 S F Ren and J D Dow: J. Luminescence 33 1985 pp. 103.
- 10 G W 't Hooft, W A J A Van der Poel, L W Molenkamp and C T Foxon: Phys. Rev. B35 1987 pp. 8281.
- 11 W Schockley and W T Read: Phys. Rev. 87 1952 pp. 835.
- 12 D T Stevenson and R J Keyes: Physica 20 1954 pp. 1041.
- 13 J-F Fan, H Oigawa and Y Nannichi: Jap. J. Appl. Phys. 27 1988 pp. L1331.
- 14 M S Carpenter, M R Melloch, M S Lundstrom and S P Tobin: Appl. Phys. Lett. 52 1988 pp. 2157.
- 15 B J Skromme, G J Sandroff, E Yablonovitch and t Gmitter: Appl. Phys. Lett. 51 1987 pp. 2022.
- 16 J Feldman, G Peter, E O Gobel, P Dawson, K Moore, C Foxon and R J Elliott: Phys. Rev. Lett. 59 1987 pp. 2337.
- 17 A Forchel, H P Meier, B E Maile and R Germann: Festkörperprobleme (Advances in Solid State Physics) 28 1988 pp. 99
- 18 B E Maile, A Forchel, R Germann, K Strubel, F Scholz, G Weimann and W Schlapp: Microcircuit Engineering 6 1987 pp. 163.
- 19 E O Göbel, H Jung, J Kuhl and K Ploog: Phys. Rev. Lett. 51 1983 pp. 1588.
- 20 J Hegarty, L Goldner and M D Sturge: Phys. Rev. B30 1984 pp. 7346.
- 21 H Hilmer, S Hansmann, A Forchel, M Morohashi, E Lopez, H P Meier and K Ploog: Appl. Phys. Lett. 53 1988 pp. 1937.
- 22 Y Masumoto, S Shionoya and H Kawaguchi: Phys. Rev. B29 1984 pp. 2324.
- 23 K Kash, J M Worlock, M D Sturge, P Grabbe, J P Harbison, A Scherer and P S D Lin: Appl. Phys. Lett. 53 1988 pp. 782.

Chapter 6

Photoluminescence Studies of Overgrown GaAs/AlGaAs Quantum Dots and Wires

6.1 Introduction

Recently it has been suggested that substantial improvements to semiconductor laser operation can be made by confining the carriers in two or three dimensions, as in a quantum dot or wire laser (see Section 1.4.3 and references 34–40 in Chapter 1). One method of achieving this is to pattern the quantum structures by electron beam lithography and reactive ion etching and then overgrow by MOCVD. The first step towards fabrication is therefore to investigate the optical behaviour of the buried quantum dots and it is this process which will be investigated in this Chapter.

6.2 Experimental Details

The aim of these experiments was to investigate the optical behaviour of quantum dots and wires before and after overgrowth with a layer of $\text{Al}_{0.4}\text{Ga}_{0.6}\text{As}$. The overgrown layer (or overlayer) is always grown by MOCVD but the starting material is grown by either MBE or MOCVD. All MOCVD growth was performed in an atmospheric pressure horizontal reactor equipped with a vent run manifold. The growth was carried out Dr R Glew of STC Technology, Harlow. The sample substrates and the overgrowth layer were grown at 750°C . The Al concentration was increased to 40% in the overgrowth layer as

- a) it makes it possible to differentiate between the signal obtained from the 30% AlGaAs in the barriers and the 40% AlGaAs in the overgrown layer
- b) 40% AlGaAs emits at about 625nm and it is therefore possible to use a HeNe laser with a laser line at 633nm to excite the barriers and not the overgrown layer. This is desirable as the overgrown layer could contribute to the overall efficiency of emission if the excitons in this layer were excited.

The MBE grown samples were supplied either by T Kerr of GEC Hirst Research Centre, Wembley or by the MBE Group at Glasgow University. The sample from GEC was grown in a VG V80H MBE system at 700°C and the Glasgow material was grown using a Varian Modular Gen II MBE machine at 700°C.

Patterning was performed using the process described in Chapter 2, Sections 2.4 to 2.7. A negative resist (HRN) was used throughout as this could be removed before regrowth by oxygen plasma etching as described in Chapter 3, Section 3.8. This is necessary because if the mask is not removed problems with the regrowth layer above the dots and wires could result. For example it could be non-crystalline or heavily contaminated with carbon residue. The free standing dots were defined by reactive ion etching with either silicon tetrachloride or methane hydrogen (see Chapter 3, Table I for parameters).

Low temperature photoluminescence spectra were obtained using the set-up described in Chapter 4. Various laser lines were used to excite the samples and these will be detailed with the results.

6.3 Comparison of MOCVD QDs etched using SiCl₄ or CH₄/H₂ before and after regrowth

Early results by Cheung *et al*¹ had suggested that CH₄/H₂ produced less damage than SiCl₄ etching. However it was not known which etch would be most successful when regrowth was also done. Perhaps one etch would introduce more impurities than the other. It was therefore felt necessary to compare the photoluminescence from quantum dots etched using either of the gases both before and after regrowth to see which etch was most compatible with the regrowth process.

6.3.1 Sample Details

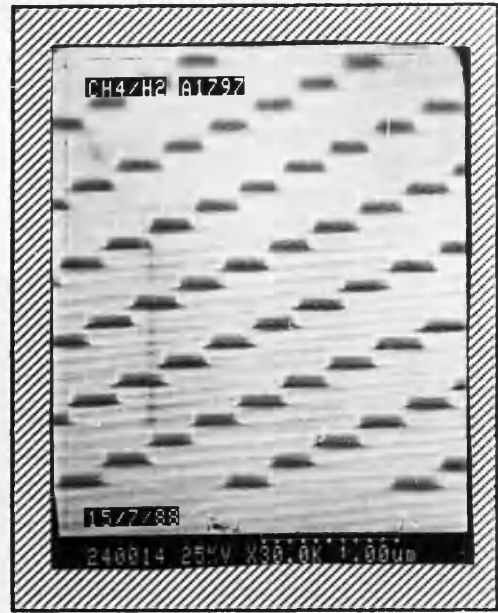
The starting material consists of a single 10nm quantum well in Ga_{0.7}Al_{0.3}As grown by MOCVD, 50nm from the surface on an n⁺ substrate.

Several dot sizes were investigated - nominally 70, 110, and 350nm diameter dots in 100µm² arrays with a separation between the dots of 300, 500 and 1000nm respectively (figure 6.1). The smaller dots were circular but the larger dots square. Two identical samples were fabricated but different gases - SiCl₄ and CH₄/H₂ were used in the reactive ion etching. The SiCl₄ etched dots were three times deeper (300nm) than those etched in CH₄/H₂. Beside each 100µm² array of dots was a 100µm² unpatterned mesa to provide a control. Complete coverage of the dots was achieved by overgrowing by MOCVD with 0.2 µm of Ga_{0.6}Al_{0.4}As and a 40nm GaAs cap (figure 6.2).

Low temperature photoluminescence measurements were taken at 60K using the large bore optical cryostat described in Chapter 4 and the excitation source was a 633nm line of a Helium Neon (HeNe) laser. The typical spectral resolution was 1nm. A temperature of 60K was used as the large bore optical cryostat would not at this time maintain a temperature of 5K due to a leak.

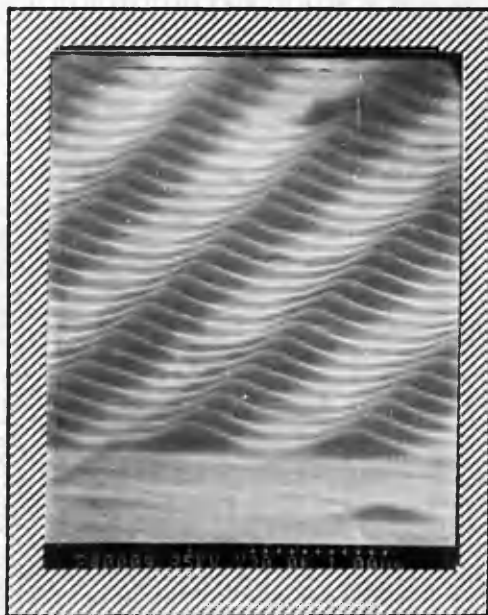


(a)

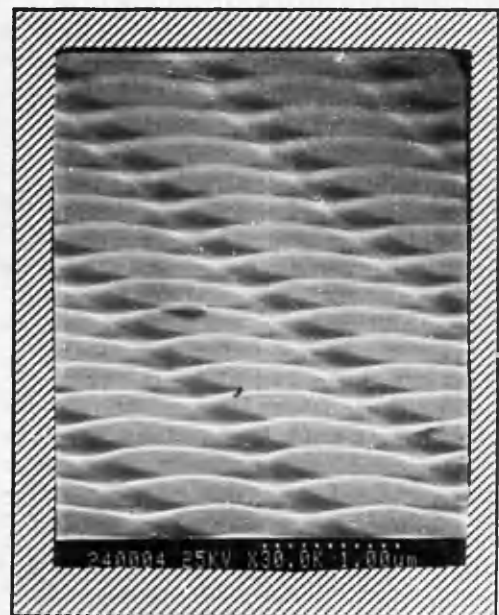


(b)

Figure 6.1 SEM micrographs 350nm diameter quantum dots after RIE with a) SiCl_4 and CH_4/H_2 .



(c)



(d)

Figure 6.2 SEM micrographs 350nm diameter quantum dots after regrowth with $0.2\mu\text{m}$ of $\text{Al}_{0.4}\text{Ga}_{0.6}\text{As}$ on a) SiCl_4 and CH_4/H_2 .

6.3.2 Results and Discussion

Prior to regrowth, quantum well (QW) emission was obtained only from the mesas on each sample. It is expected that a significant contribution to the PL intensity will come from the photoexcited carriers excited in the $\text{Ga}_{0.7}\text{Al}_{0.3}\text{As}$ barriers which then recombine in the GaAs well. After regrowth over the SiCl_4 etched QDs, QW emission was recovered in the 350nm dots and remained in the mesas but in the CH_4/H_2 etched dots and mesas no quantum well emission was obtained.

The photoluminescence spectra for the SiCl_4 etched sample are shown in figures 6.3 and 6.4. In figure 6.3 spectrum A is the QW emission from the mesa before regrowth and spectrum B after. The emission has shifted approximately 3nm to higher energies and the intensity has decreased by a factor of about 7 after regrowth. In figure 6.4 spectra C and D are the QW emissions from the 350nm QDs before and after regrowth. Spectrum E corresponds to the adjacent mesa. Both the 350nm QDs and the $100\mu\text{m}^2$ mesa show an emission peak at 796nm thus the QW emission from the dots has been recovered. The luminescence efficiency scales approximately with the volume of QW material remaining in the dots relative to that of the overgrown mesa.

From these initial results it was suggested that the reduction in the integrated PL intensity from the mesas after regrowth could have been due to nonradiative traps present in the regrown interface. However the reduction could also have been due to differences in the alignment of the PL system when the two measurements were taken. It was further suggested that the shift in PL emission wavelength could have been due to vertical diffusion of the aluminium into the QW on regrowth² and this will be discussed further in Section 6.11. It was not clear why emission was not obtained from either set of dots before regrowth as luminescence was being readily obtained from MBE dots etched using either SiCl_4 or CH_4/H_2 (see Chapter 5) and why only the SiCl_4 etched dots recovered their luminescence after regrowth. Several explanations were put forward to try and account for the before regrowth behaviour. For example it was suggested that perhaps emission recovered after regrowth due to the annealing out of sidewall damage at the regrowth temperature. It may only be seen in the larger dots as:

- a) RIE could completely destroy the QW in the smaller dots whereas the greater volume of material in the larger dots would be able to recover sufficiently on annealing to give a measurable signal
- b) the effect could occur in the smaller dots but the signal is too weak compared to the background
- c) on regrowth the aluminium can diffuse completely through the smaller quantum dots destroying any structure in the material.

Later measurements however both my S R Andrews³ and myself⁴ showed that the luminescence efficiency of the QDs is reduced with increasing temperature (see figure 5.7). As these measurements were taken before regrowth at 60K, it is likely that the signal was so small that it could not be measured with the alignment system used. No mechanism could be found to explain the results from the CH_4/H_2 etched dots and this will be discussed further in Section 6.10.

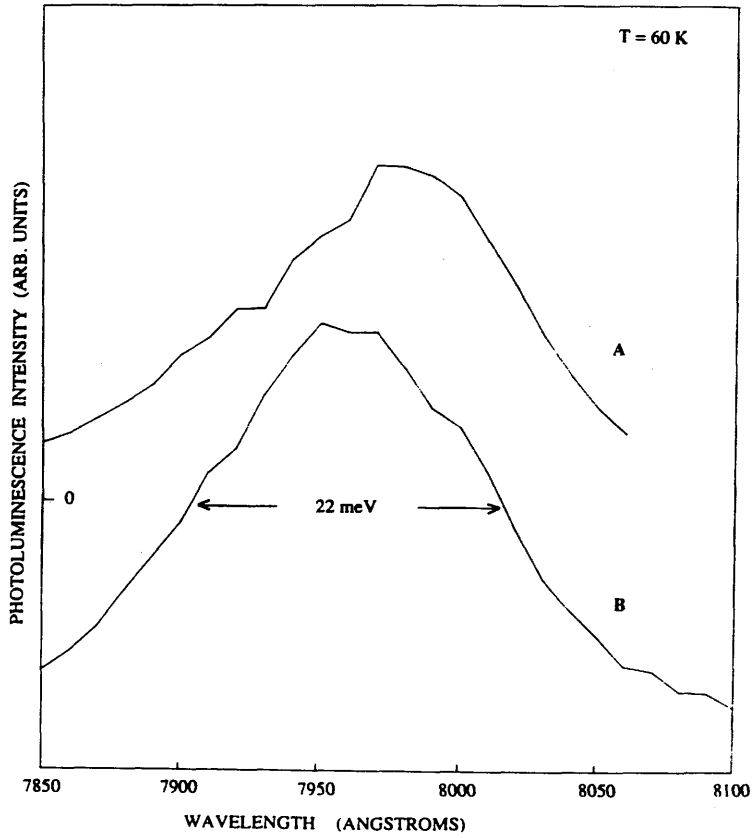


Figure 6.3 Quantum well photoluminescence emission from SiCl_4 etched mesa (A) before and (B) after regrowth.

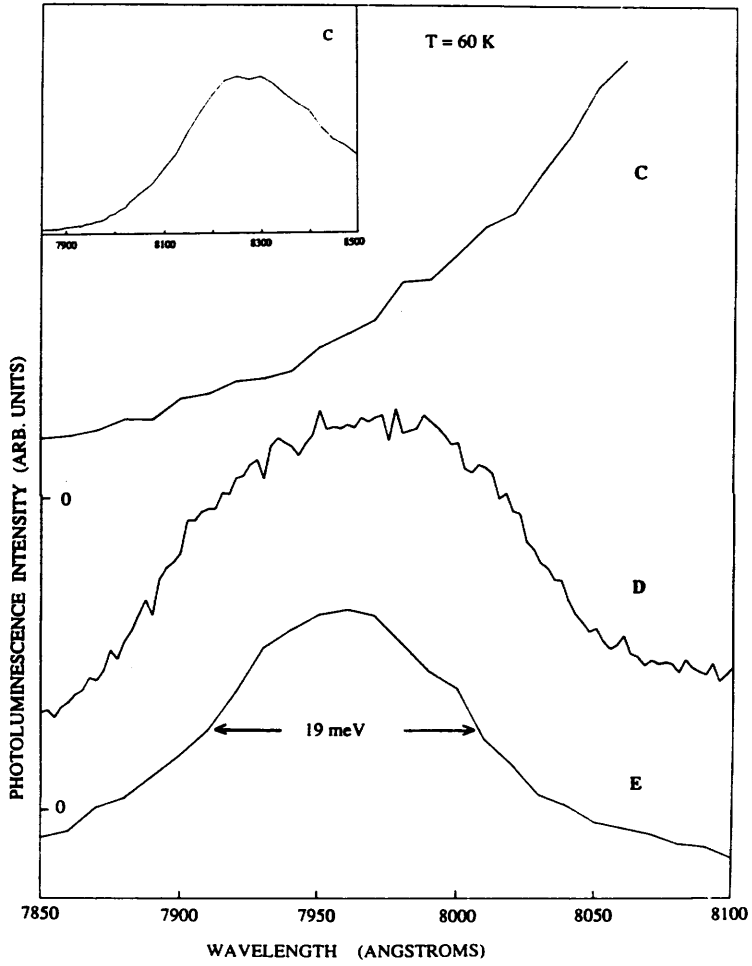


Figure 6.4 Quantum well Photoluminescence emission from the SiCl_4 etched 350nm dots before regrowth (C), after regrowth (D) and from the corresponding mesa (E).

The most uniform planar regrowth seems to have been on the CH_4/H_2 etched sample (see figure 6.2). However in this case, this is most likely to be a depth effect because the CH_4/H_2 etched dots are only one third as deep as those etched by SiCl_4 . In a previous experiment where the regrown layer on 350nm SiCl_4 etched dots was thicker, the overgrown profile of the dots was almost identical to that of the shallower overgrown CH_4/H_2 etched dots reported here⁵. It was also found that an increase in growth time resulted in planarisation of the surface because the growth between the dots is faster than the growth on the dots. For fabrication of a quantum dot laser this is important for the regrowth of the remaining laser structure.

6.3.3 Summary

These initial results were the first report⁶ showing that it was possible to regrow AlGaAs over quantum dots defined by electron beam lithography and RIE with SiCl_4 and CH_4/H_2 . It was not clear why the CH_4/H_2 etched dots showed no Photoluminescence. It is most likely to be due to lack of sensitivity in the measuring equipment that no signal was found. At 60K Photoluminescence emission was recovered in the overgrown QDs etched by SiCl_4 and the intensity scales with the volume of material remaining after patterning. It was thought that the difference in behaviour lay in the starting material and not in the experimental technique and therefore the next step seemed to be to attempt the overgrowth of dots fabricated in MBE material.

6.4 Overgrown MBE Quantum Dots

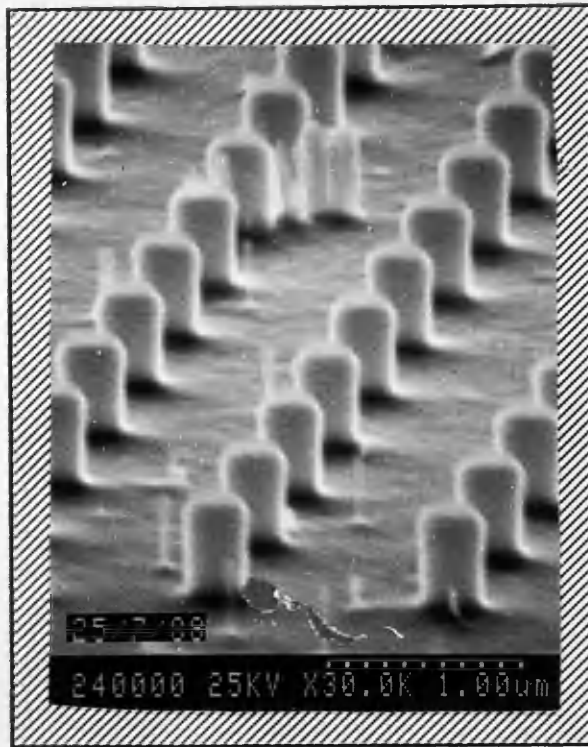
6.4.1 Sample Details

The starting material, grown using MBE by T Kerr at GEC, consisted of 11.5, 5.7, 2.8 and 1.4nm undoped GaAs wells bounded by 20nm thick $\text{Al}_{0.3}\text{Ga}_{0.7}\text{As}$ barriers (apart from the 1.4nm well top AlGaAs barrier which is 100nm thick) grown in that order on a n^+ GaAs substrate with an intervening undoped GaAs buffer layer and a 1.4nm GaAs cap. Only results for the 1.4nm QW will be presented. This material was not of ideal design for a QD experiment but was used while new material was being grown. The free standing dots were defined by reactive ion etching with SiCl_4 .

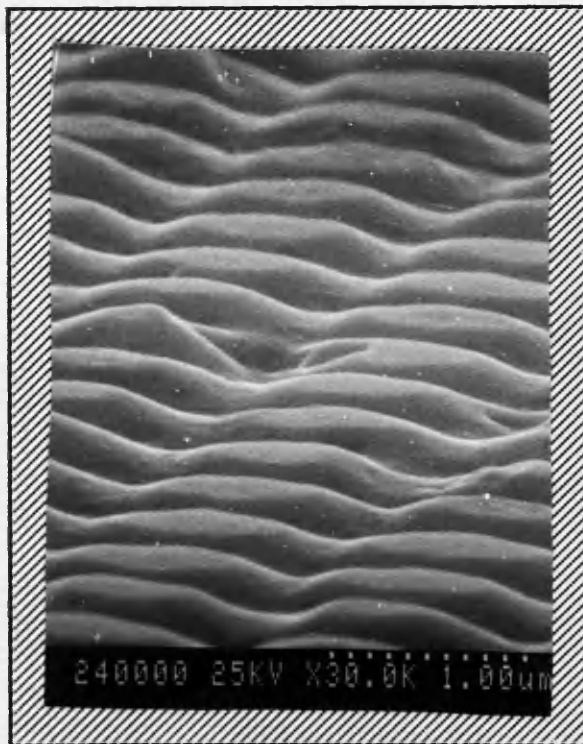
Several dot sizes were investigated - nominally 70, 110, and 300nm diameter dots in $100\mu\text{m} \times 100\mu\text{m}$ arrays with a separation between the dots of approximately five times the dot diameter. Beside each array of dots was a $100\mu\text{m} \times 100\mu\text{m}$ unpatterned mesa to provide a control. The dots were then overgrown with $0.6\mu\text{m}$ of $\text{Al}_{0.4}\text{Ga}_{0.6}\text{As}$, both with a 40nm GaAs cap (figure 6.5). Low temperature (2.2K) measurements were obtained using the set-up described in Section 6.3. as the large bore optical cryostat could now be operated using superfluid helium.

6.4.2 Results and Discussion

Before overgrowth the mesas and all dot sizes down to 75nm diameter luminesced. It is expected that a significant contribution to the PL intensity will come from the photoexcited carriers excited in the



(a)



(b)

Figure 6.5 SEMs of MBE 300nm diameter dots a) after RIE
b) after regrowth.

$\text{Ga}_{0.7}\text{Al}_{0.3}\text{As}$ barriers which then recombine in the GaAs well. In this sample the QW emission remained in the mesas and the 300nm QDs but was lost in the smaller 75nm and 110nm diameter dots after regrowth.

Figure 6.6 shows the QW emission from the largest QDs and corresponding mesa patterned in the MBE (Spectra A and B) starting material respectively before (solid line) and after (dashed line) overgrowth. Spectra A and B show that the dot and corresponding mesa emission are both at 697.5nm and after regrowth the dot and mesa emission have both shifted, 10nm and 7.5nm respectively, to higher energy. Three out of four mesas measured showed a significant shift of between 6 and 8nm with only one shifting less than 2nm.

The integrated luminescence intensity of the dots relative to that of the mesas scales with the volume of material excited before and after regrowth but the overall intensity is reduced by up to an order of magnitude after regrowth for both the mesas and the dots.

6.5 Comparison of MOCVD and MBE QDs

The shift seen in the emission from both the MOCVD and MBE mesas and dots, both etched using SiCl_4 , could be due to the vertical diffusion of aluminium into the wells perhaps enhanced by impurity diffusion at the regrowth temperature of 750°C. The observation of larger energy shifts in the MBE mesa emissions compared to that in the MOCVD sample could be a result of the longer exposure to the 750°C regrowth temperature. The overgrowth layer was 3 times thicker on the MBE sample than on the MOCVD as the MBE dots were 0.6 μm high whereas the MOCVD dots were 0.2 μm high.

When Photoluminescence spectra were measured at 2.2K QW emission was obtained before regrowth from QDs down to 75nm in diameter fabricated in MBE material. After regrowth only the larger 300nm diameter dots luminesce. QDs fabricated in MOCVD material only luminesce after regrowth when the measurements are taken at 60K and then only in the larger 350nm diameter dots. In both cases the intensity scales with the volume of material remaining. In both cases no quantum well emission is obtained from the smaller dots after regrowth possibly due to the complete lateral diffusion of aluminium through the wells. This effect may be enhanced by any impurities on the sidewalls introduced by the RIE step which could then diffuse into the wells on regrowth.

6.6 Experiments to answer questions raised in Sections 6.3 and 6.4

These preliminary results created many unanswered questions. Later results^{3,4} showed that the difference in luminescence efficiency found in dots fabricated in MOCVD and MBE material could be ascribed to the temperature at which the QDs were measured. However the shifts of the PL peak position after regrowth had not been explained. It had been suggested that these shifts could be due to vertical diffusion of aluminium in the wells², diffusion of impurities introduced by RIE or even lateral diffusion of Al from the overgrown layer. This effect was seen in both the MOCVD and MBE etched dots. It was also suggested that the shift could be due to strain on the quantum dot pillars due to the

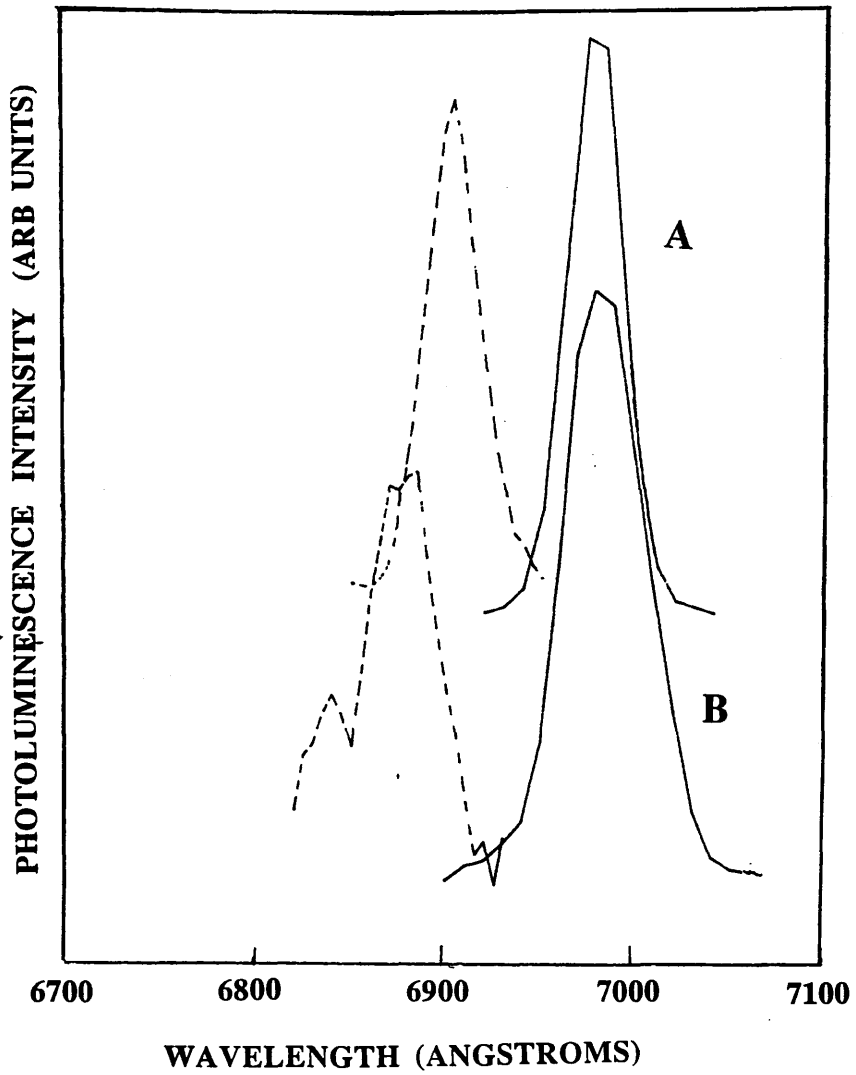


Figure 6.6 Quantum well emission from the mesa (A) and the 300nm dots (B) patterned in MBE starting material before regrowth (solid line) and after regrowth (dashed line).

overgrown layer. There are two ways this question could be answered.

- 1) If the PLE spectrum from the dots was measured the energy difference between the heavy hole and light hole exciton would change after regrowth if strain was the cause of the shift in the peak position of the PL spectrum.
- 2) The second method (and the one used here as PLE was not available in Glasgow) which would enable an investigation of the actual cause of the PL shift is to measure QDs before regrowth and then subject them to different regrowth temperature cycles in an arsenic atmosphere (as at 750°C, the regrowth temperature, As would evaporate from the surface unless an arsenic atmosphere is used). If a shift was still seen then strain and lateral migration of Al from the growth of the AlGaAs overlayer could also be ruled out.

The effect of dry etch impurities could also be investigated by comparing the effects of this procedure on QDs fabricated by RIE in SiCl_4 and CH_4/H_2 .

In Chapter 5 it was found that the relative integrated PL intensity from dots decreased with increasing temperature at a rate faster than the mesas. This was explained by suggesting that at 5K, the excitons were localized in low energy well areas and the predominate recombination mechanism was radiative. As the temperature was increased the excitons were able to diffuse to nonradiative sites, the majority of which were thought to be on the surface of the dot. This is because GaAs has a high surface recombination velocity and when QWs are patterned into quantum structures it is thought that this nonradiative recombination will be the dominant recombination mechanism as the ratio of surface area to unit volume has been greatly increased by the patterning (see Chapter 5, Section 5.2). Therefore to prove if the regrowth layer affected the surface states by removing nonradiative sites for the excitons and allowing luminescence to be seen at higher temperatures, it was necessary to investigate the temperature dependence of the photoluminescence from a range of sizes of quantum dots (QDs) and wires (QWWs).

It has been suggested that MOCVD material is in some way incompatible with CH_4/H_2 etching and in order to investigate this fully QDs should be fabricated on MOCVD material and then etched using this gas and the PL spectra from dots taken both before and after regrowth.

Finally results by other authors (Chapter 1 references 22 & 26) had showed that at submicron dimensions the luminescence efficiency of GaAs/AlGaAs quantum wires decreases with wire width and is 4 orders of magnitude smaller in wires ~100nm wide. The results presented in Sections 6.3 and 6.4 showed that submicron QDs could luminesce as efficiently as the control mesas and at worst showed an order of magnitude drop. These results were backed up by the collaboration with Dr S R Andrews and the results presented in Chapter 5. It was therefore decided to fabricate quantum dots and wires down to submicron dimensions on the same sample and thus enable a direct comparison of the luminescence efficiency of 0 and 1 DOF structures subjected to identical fabrication and measurement techniques.

6.7 Photoluminescence obtained from MOCVD quantum dots and wires before and after overgrowth

6.7.1 Material Design

In order carry out the experiments outlined in Section 6.6, material was designed consisting of 10nm, 7nm and 4nm undoped GaAs quantum wells bounded by 20nm thick $\text{Al}_{0.3}\text{Ga}_{0.7}\text{As}$ grown in that order on an n^+ substrate with an intervening undoped GaAs buffer layer. There was no capping layer so that when the AlGaAs overlayer was grown a new QW was not formed at the interface. The top well was designed to be 4nm thick as this is within the capabilities of the MOCVD growth process. Several wells at different depths were included as this would enable some measure of the effect of the fabrication processes, if for example the top well was affected more by the RIE step or the temperature gradient at the regrowth step which might occur along the length of the pillar. The wells are grown in order of decreasing well width because if the order was reversed the light emitted from the thinner wells would be absorbed in the thicker wells. The QW emission from the 4nm and 7nm wells is also sufficiently higher in energy than the GaAs substrate emission that it should remain well resolved in the quantum structures. The 10nm well was included to ensure the quality of the upper 2 wells by gettering many of the impurities. This material design was grown by MOCVD.

6.7.2 Quality of MOCVD quantum well material

The three main factors to assess in the starting material are the homogeneity of the well width over the sample area and the linewidth and intensity of the PL signatures from the wells. It is extremely important that the as-grown material has a uniform quantum well thickness over the entire sample area. This is important for three reasons.

- 1) If quantum confinement is achieved one way to measure it is by a systematic blue shift in exciton emission wavelength with decreasing dot size. If there is already a shift in PL peak position due to variations in well thickness across the sample then confinement would be impossible to prove.
- 2) The luminescence efficiency will be different depending on the thickness of the well. For example a small dot with a thicker quantum well has a larger volume of material to be excited than a control mesa where the well is thinner. This could give false results on the luminescence efficiency of the quantum structures as luminescence efficiency is being compared from different volumes of material.
- 3) If shifts in the peak PL position are already present across a sample before regrowth it will be impossible to draw consistent conclusions on the reasons for any shifts which may occur after regrowth.

Figure 6.7 shows the PL spectra obtained from the QWs at 5K. The PL peak emission at 748, 790.5 and 809.5nm (1.66, 1.57 and 1.53eV) corresponds to the quantum confined $n=1$ electron to $n=1$ heavy hole transition in the 4, 7 and 10nm quantum wells respectively and the linewidths of these wells were

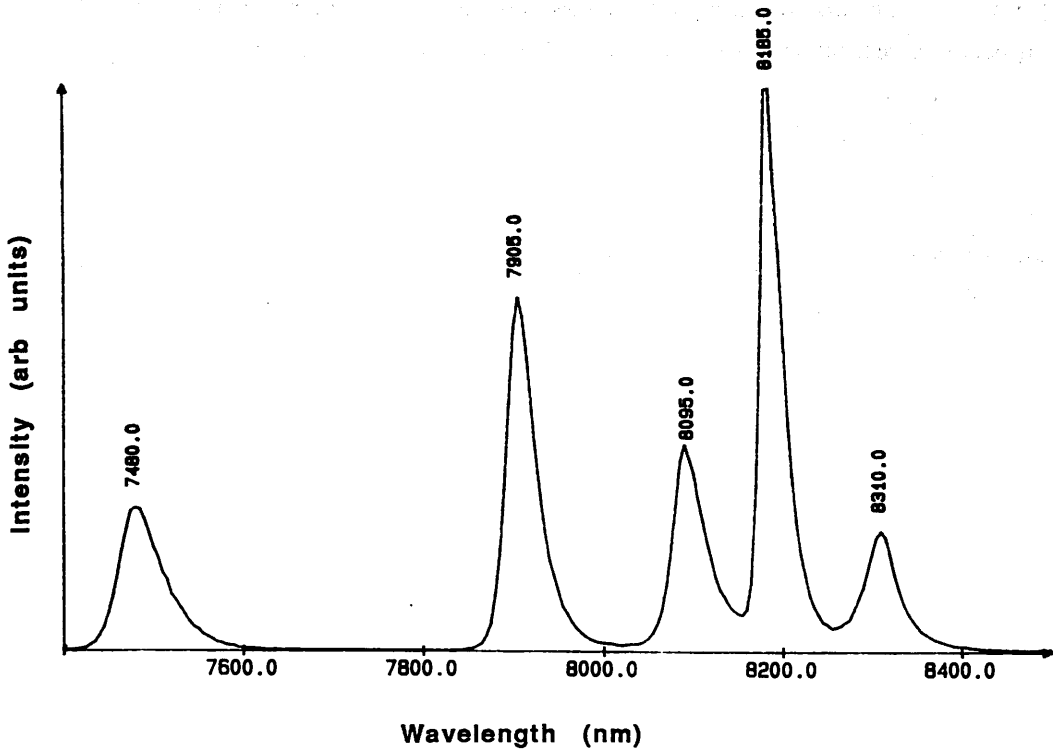


Figure 6.7 PL spectra excited at 2.54eV at 5K from the 4, 7, and 10nm quantum wells. Also shown is the PL from the GaAs substrate and carbon impurity.

found to be 12, 7.5meV and 8meV respectively. The emission at 818.5nm corresponds to the bulk GaAs bound exciton transition and at 831nm to the donor acceptor carbon impurity transition in the bulk GaAs. The homogeneity of the MOCVD sample was excellent. The linewidth of the MOCVD material shows that the interfaces are not as abrupt or smooth as those obtained in the MBE sample described in Chapter 5, Section 5.2. The well thicknesses quoted above are based on the growth rates in the MOCVD chamber and have not been checked by TEM analysis. Ehlers *et al*⁷ have calculated the expected emission for GaAs QWs with Ga_{0.7}Al_{0.3}As barriers at 15K and the results are depicted in Figure 6.8. Comparing the emission obtained from these QWs on this graph gives well thicknesses of 3.8, 8.9 and 18nm respectively. The thinnest well is in excellent agreement with the expected thicknesses from growth times but the two thicker wells are clearly wider than expected from the growth times. There will be a slight difference in emission energy between 5 and 15K but it is worth comparing the values to give an indication as to how close to the desired values the well widths are. Hegarty and Sturge⁸ have also performed this calculation and the results are shown in Figure 6.9. This gives well widths of 3.2, 7.2 and 16nm respectively which are clearly in better agreement with the expected values. However throughout this chapter, the three wells will be referred by their specified widths of 4, 7 and 10nm as no absolute measure of the well width has been made. Also shown in Figure 6.9 is the calculated inhomogeneous linewidth at 5K for a layer fluctuation of one atomic spacing. This gives linewidths of 8, 3.5 and 1.5meV respectively. Tanaka *et al*⁹ have shown that the factors which determine the PL linewidths are broadening by thermal excitation Γ_{th} , interface roughness Γ_{rough} , impurities inside the quantum wells $\Gamma_{well\ imp}$, and impurities at the interface and in the barrier regions $\Gamma_{int. imp}$. In the simple case

$$\Gamma(L_z, T) = \Gamma_{th}(T) + \Gamma_{rough}(L_z) + \Gamma_{well\ imp} + \Gamma_{int. imp}(L_z)$$

where L_z is the thickness of the quantum well, and Γ_{rough} is proportional to $\Delta L_z/L_z^3$ where ΔL_z is the size of the well width fluctuations and $\Gamma_{int. imp}$ also depends on L_z . At low temperatures (<10K) the thermal broadening should be negligible. The broadening due to interface roughness is negligibly small for wide QWs ~15nm in contrast to narrow QWs ~4nm where all factors except thermal broadening are important at 5K. As these linewidths calculated by Hegarty and Sturge⁸ are considerably smaller than the measured values at 5K, this suggests that impurity broadening is significant in all three wells or that well width fluctuations are greater than one monolayer.

While 5K PL measurements give a worthwhile indication of the quality of the sample they are not a reliable method of estimating well width fluctuations as at these temperatures the exciton may be localized at well areas of lower energy thus giving rise to sharper linewidths. As the temperature is raised the excitons become delocalized and the linewidth increases by more than kT as the exciton then samples an average of the well width fluctuations. This localization of the exciton in lower energy sites can also result in the PL emission wavelength changing as the temperature increases as the narrower well regions become populated and hence the wavelength decreases or shifts "blue". This behaviour is showed clearly in Section 6.9 Figures 6.18-6.21.

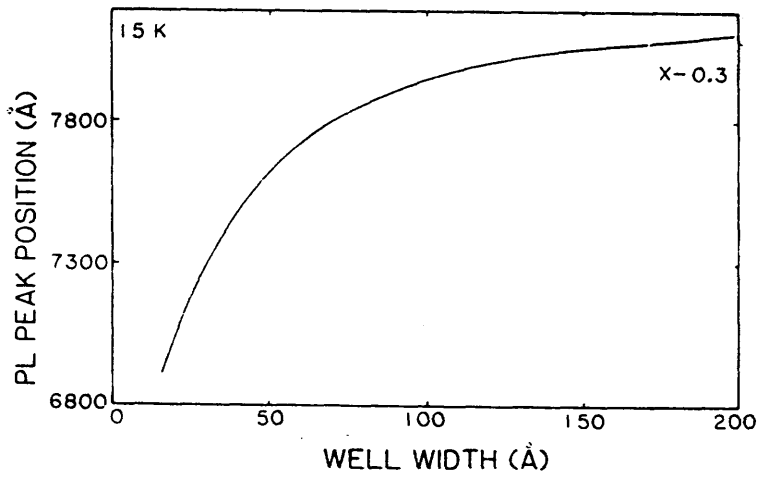


Figure 6.8 15K Photoluminescence peak emission wavelength plotted against well width of the GaAs quantum well $\text{Ga}_{0.7}\text{Al}_{0.3}\text{As}$. (After Ehlers et al⁷)

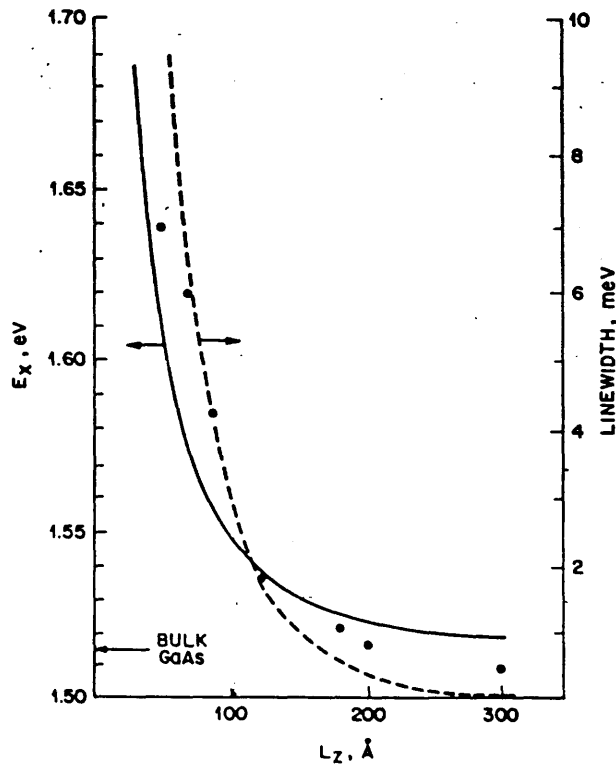


Figure 6.9 Solid line, energy E_x of the heavy-hole exciton in $\text{GaAs}/\text{Al}_x\text{Ga}_{1-x}\text{As}$ quantum wells as a function of GaAs layer width, for $x=0.3$. Dashed line, inhomogeneous linewidth resulting from layer-width fluctuations of a monolayer. (After Hegarty and Sturge⁸)

In summary the material consists of three wells nominally 4, 7 and 10nm thick with linewidths of 12, 7.5 and 8meV respectively. In all three wells impurities in the well and interface and well width fluctuations contribute significantly to PL linewidth broadening. Only the 4nm and 7nm well will be characterized in the quantum dots and wires but the effects of the etching and overgrowth on the whole material structure will also be discussed.

6.8 Sample Design

Three different samples were fabricated to enable the experiments described in Section 6.6 to be carried out. The sample designed to enable the comparison of the behaviour of quantum dots and wires 1) at 5K 2) with increasing temperature both before and after regrowth consists of 16 areas half of which are control mesas. These are exposed the length of the sample to enable direct comparison of the mesa and quantum structure exciton emission peak positions. Wet etched alignment marks (Chapter 2, Section 2.7) are used so they cannot contribute to the overall signal intensity. Four dot sizes, 75, 100 300 and 550nm with pitches approximately 5 times the dot diameter, are exposed in square areas 200x190 μ m on edge. The volume of material remaining in the dot areas is between 3 and 4% compared to the 200 μ m² mesas, exposed beside these dot areas. The dots are deliberately not exposed in order of size. This is necessary because if gradients in well width do exist across the sample systematic shifts in peak position with dot size could occur. This could lead to erroneous conclusions or difficulty in confirming any resulting shifts due to confinement or regrowth. Four wire sizes 80, 150 250 and 500nm are exposed again not in order of size. The wire arrays are 100x76 μ m in size and the filling factor is between 25 and 38%. Mesas 100 μ m on edge are also exposed next to the wire arrays. The dots and wires were exposed using HRN resist and etched to a depth of 0.2 μ m using SiCl₄.

The sample designed to investigate the behaviour of quantum dots etched in MOCVD material using CH₄/H₂ both before and after regrowth consisted of three dot sizes 80, 100 and 250nm in 200x190 μ m arrays with their corresponding 200 μ m² mesas. The dots were etched to a depth of 0.1 μ m.

Finally the sample used to investigate the effects of temperature cycling in an arsenic atmosphere on the PL peak positions of both dots and mesas consisted of 100, 300 and 500nm dots in 200x190 μ m arrays and their corresponding mesas etched using SiCl₄ to a depth of 0.2 μ m. After characterization at 5K the sample was halved, and one half subjected to a longer temperature cycle than the other. When overgrowth is carried out the sample is first gradually warmed up to the growth temperature of 750°C, growth then takes place and the sample is then cooled down. One sample was subjected to the warm up, cool down portion of the cycle (12 min and 47sec) and the other to the whole cycle - warm up, growth period, cool down - (19min 41 sec). In both cases an arsenic overpressure was used to stop out gassing of the arsenic from the sample. To act as a control a piece of completely unprocessed material from the same wafer was also subjected to the temperature cycle in each case. This control material had also been halved to leave a final unprocessed control sample.

6.9 Photoluminescence of SiCl₄ etched dots and wires from 5 to 200K

6.9.1 Experimental Results before regrowth

This sample was characterized using the experimental setup described in Chapter 4 with the continuous flow cryostat that enabled accurate control of temperature and the 90° scattering geometry that enabled accurate focussing of the exciting laser line. The 488nm line of an Argon ion laser was used as the excitation source. The input power was varied using neutral density filters. This value was chosen as this line had a large power range with a maximum of several watts. At this time the only other laser available was a HeNe laser with a maximum output power of 17mW and after filtering using the prism monochromator the maximum power available to pump the quantum structures was only 5.5mW. To enable emission to be obtained from the smallest dots and wires a pump power greater than 5.5mW was needed so the 488nm line was used. This excitation energy of 2.54eV excited both the AlGaAs barriers and the GaAs wells. Therefore excitons created in the AlGaAs dropped into the well before recombining and this would increase the strength of the signal obtained from the dots and wires. However relative values, for example to a mesa or to the 5K emission, are always used to normalize the data.

Figure 6.10 and 6.11 shows representative PL spectra from the 75nm diameter quantum dots and 80nm wide wires respectively measured at 5K. Only the 4nm and 7nm well emission is shown. A representative mesa is included in figure 6.10. Figure 6.12 shows the broadening of the PL spectra measured at 5K for dots and wires in both the 4nm and 7nm QW compared to the corresponding mesa exposed beside the array of wires or dots. A broadening of 0meV therefore shows that the PL linewidth of the quantum structure has not increased over the mesa. The control mesas on the patterned samples showed similar spectra to the starting material, but with exciton peaks typically broadened by ~3-4meV. It is obvious from figure 6.12 that the wires are more sensitive to the effects of processing. In the 4nm QW the broadening is more or less consistent over the whole dot diameter range (1-2meV) with minimum broadening in the largest dot diameter. In the wires however the linewidth variation is much more random. In the 7nm QW the broadening is consistently worse in the wires and is most severe in the smallest 80nm wires but 550nm diameter dots show the severest broadening in the 0D structures. The broadening found in the dots is consistent with the results reported in Chapter 5 although the mesa broadening is more severe compared to as-grown material. After etching, shifts in exciton emission from the 4nm QW are obtained in the dots and wires relative to its corresponding mesa. The 75 and 100nm dots shift red by 2meV, the 250nm dots blue by 2meV and the 550nm dots blue by 13meV. However all the wires consistently shift blue with the smallest shift of 2meV obtained in the smallest wires and the largest shift of 8meV in the 150nm wires. The exciton emission from the 7nm well showed no shifts in either the dots or the wires. These shifts and linewidth broadening are probably due to radiation damage caused by the etching. The fact that the broadening and shifting is worse in the upper well is consistent with this conclusion, as this well is subjected to the effects of the RIE for longer compared to the lower well. The lower well is also protected by another AlGaAs barrier layer and the 4nm well above, whereas the 4nm well is only protected by one AlGaAs barrier and the HRN mask. The broadening in this sample due to etching may be more severe than that reported in Chapter 5

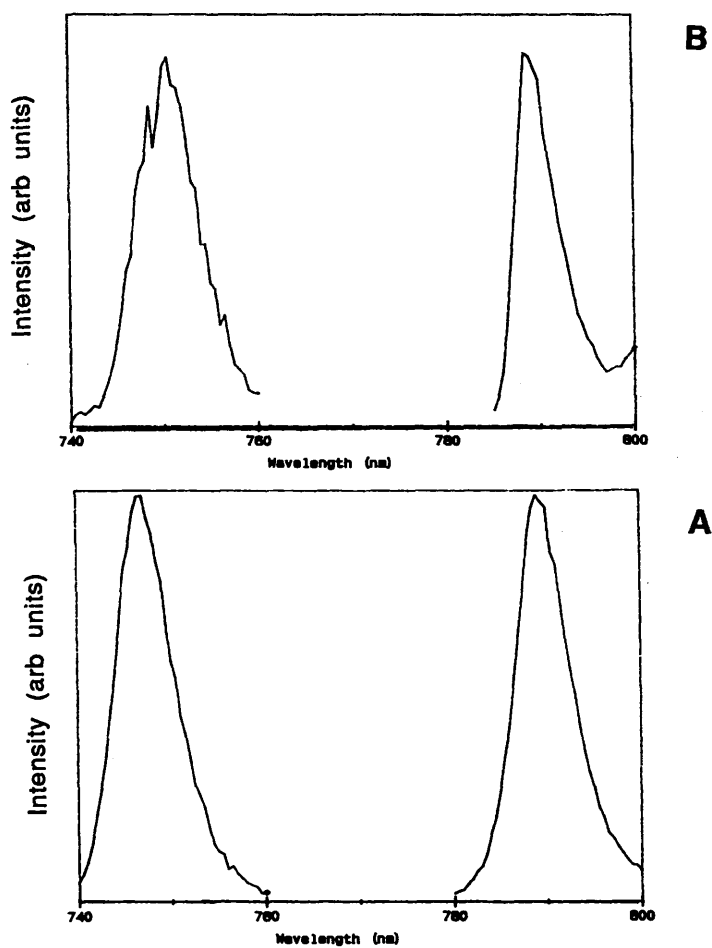


Figure 6.10 Representative PL spectra from a) $200\mu\text{m}^2$ mesa and b) 75nm diameter dots excited at 2.54eV at 5K.

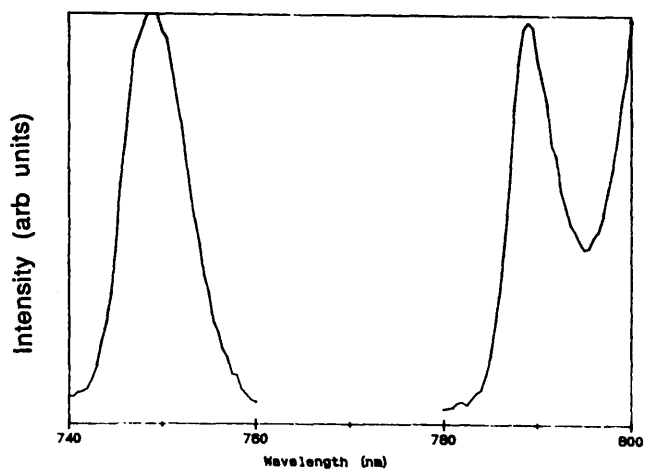


Figure 6.11 Representative PL spectra from 80nm wide wires excited at 2.54eV at 5K.

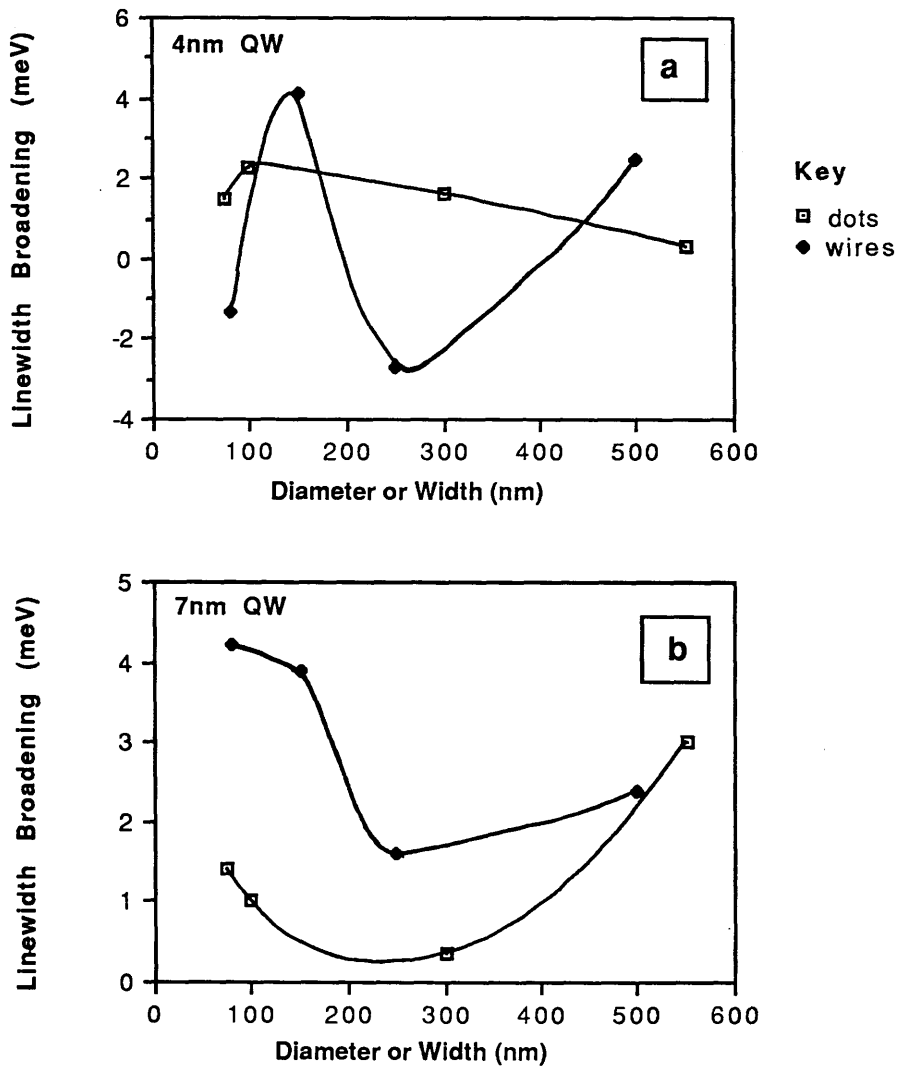


Figure 6.12 Linewidth broadening compared to the corresponding mesa of the PL spectra excited at 2.54eV at 5K from a) 4nm QW and b) 7nm QW both dots and wires

as the 4nm QW is only 20nm from the surface whereas in the material used in Chapter 5 the 5nm QW was 34nm from the surface.

Figure 6.13a and 6.13b shows the relative intensity of luminescence from the 4nm and 7nm quantum wells respectively after patterning into dots and wires. As in Chapter 5 the relative intensity is the ratio of the integrated intensity of the quantum well luminescence from the dot or wire array (divided by the filling factor) to that from an adjacent control mesa. A relative efficiency of 1 therefore indicates a luminescence efficiency which scales with the volume of excited quantum well material. The luminescence efficiency from the dots in both wells scales approximately with the volume of material excited, with the largest reduction of one order of magnitude found in the 75 and 100nm dots in the 4nm well. In the wires however the relative intensities decrease as the wire width is reduced, by 4 orders of magnitude in the smallest structures. This is a surprising result as the behaviour of the dots and wires is quite different. This difference will be discussed in Section 6.9.3.

Figure 6.14 - 6.17 show the variation of the relative intensity of the structures to their own integrated luminescence intensity at 5K (not to the mesa) as the temperature is increased. A relative efficiency of 1 therefore indicates a luminescence efficiency equal to the 5K exciton emission. Figure 6.14 shows the variation in a mesa and the four dot sizes in the 4nm QW. In the 300 and 550nm dots the luminescence efficiency drops to ~0.1 at 100K. In the smaller structures however the luminescence efficiency is much better with the 75nm dots still luminescing (albeit with an efficiency less than 0.1) at 200K. Figure 6.15 shows the variation in a mesa and the four wire sizes in the 4nm QW. Both mesas show a similar variation of PL efficiency with temperature. The larger wires (250 and 500nm) however lose their luminescence at a much lower temperature than the larger dots - the 250nm wires at 30K and the 500nm wires at 50K. In the 75 and 150nm wires the luminescence efficiency is better than the larger wires but not as high as the dots with both wire sizes losing luminescence at 130K. In the 7nm QW the temperature dependence was very similar with the smaller structures luminescing to higher temperatures than the larger as is shown in figures 6.16 and 6.17 respectively. However there was a rising background due to the GaAs which swamped the signal from the quantum structures at ~120K. This background luminescence may have contributed significantly to the luminescence in the lower well with increasing temperature so it is difficult to draw any conclusions from this result above 50K.

Figures 6.18 and 6.19 show the exciton wavelength emission shift with temperature for the 4nm well in the dots and wires respectively as well as a comparison mesa. From figure 6.18 it can be seen that there is a slight blue shift of 1nm in the mesa and the largest dots as the temperature is increased to 50K and the emission energy then follows the GaAs bandedge. In the 75nm and 100nm dots the shift is much larger and the exciton energy follows that of the mesa only from 100K upwards. Figure 6.19 shows the shifts for the wires. Again a slight shift of 1-2nm is seen in the control mesa and an enhanced shift in the smallest wires but the 150nm wires follow the GaAs bandedge. In the 7nm well no shifts were obtained in either the dots or wires. Figure 6.20 shows a comparison of the shifts obtained in the two control mesas (a) and the 75nm dots and the 80nm wires (b). It can be seen that the dots shift blue by ~0.5nm more than the 80nm wires. Overall the shifts are very similar.

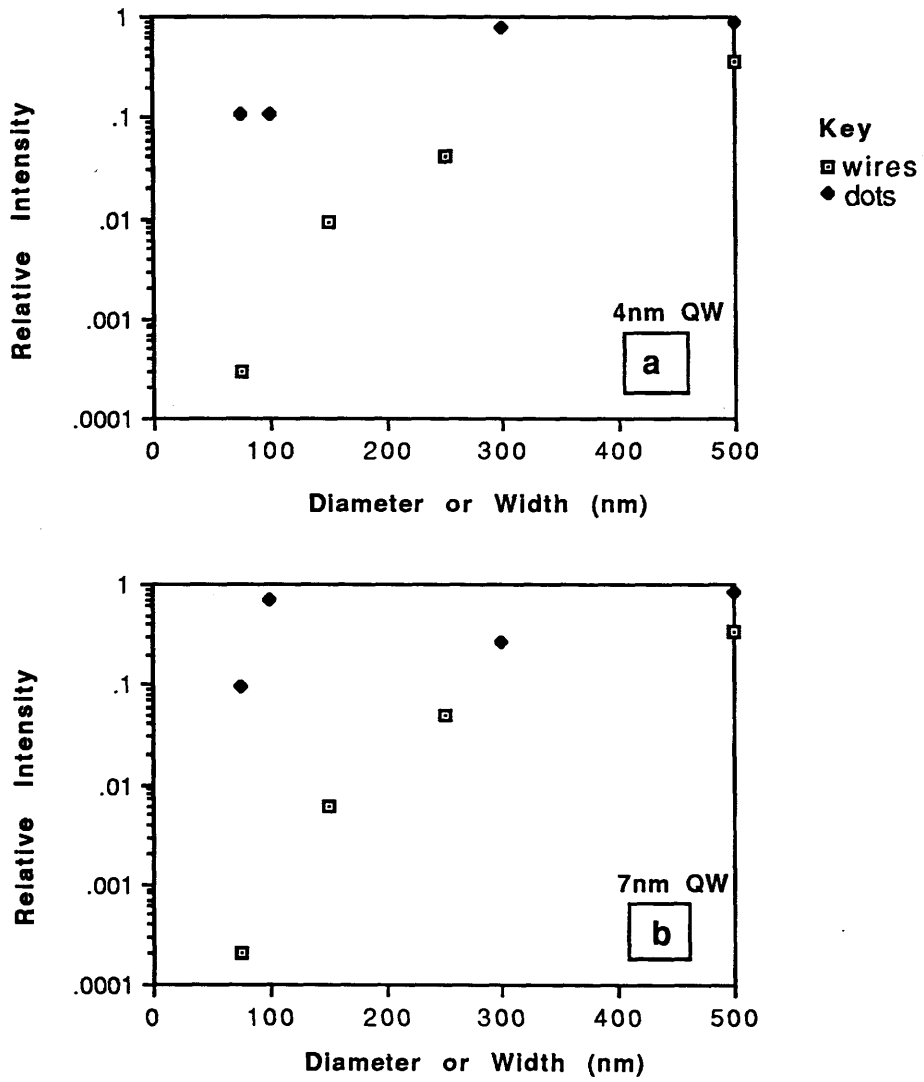


Figure 6.13 Relative integrated luminescence intensity excited at 2.54eV from GaAs/AlGaAs quantum dots and wires etched using SiCl₄ from a) 4nm quantum well and b) 7nm quantum well.

4nm QW dots

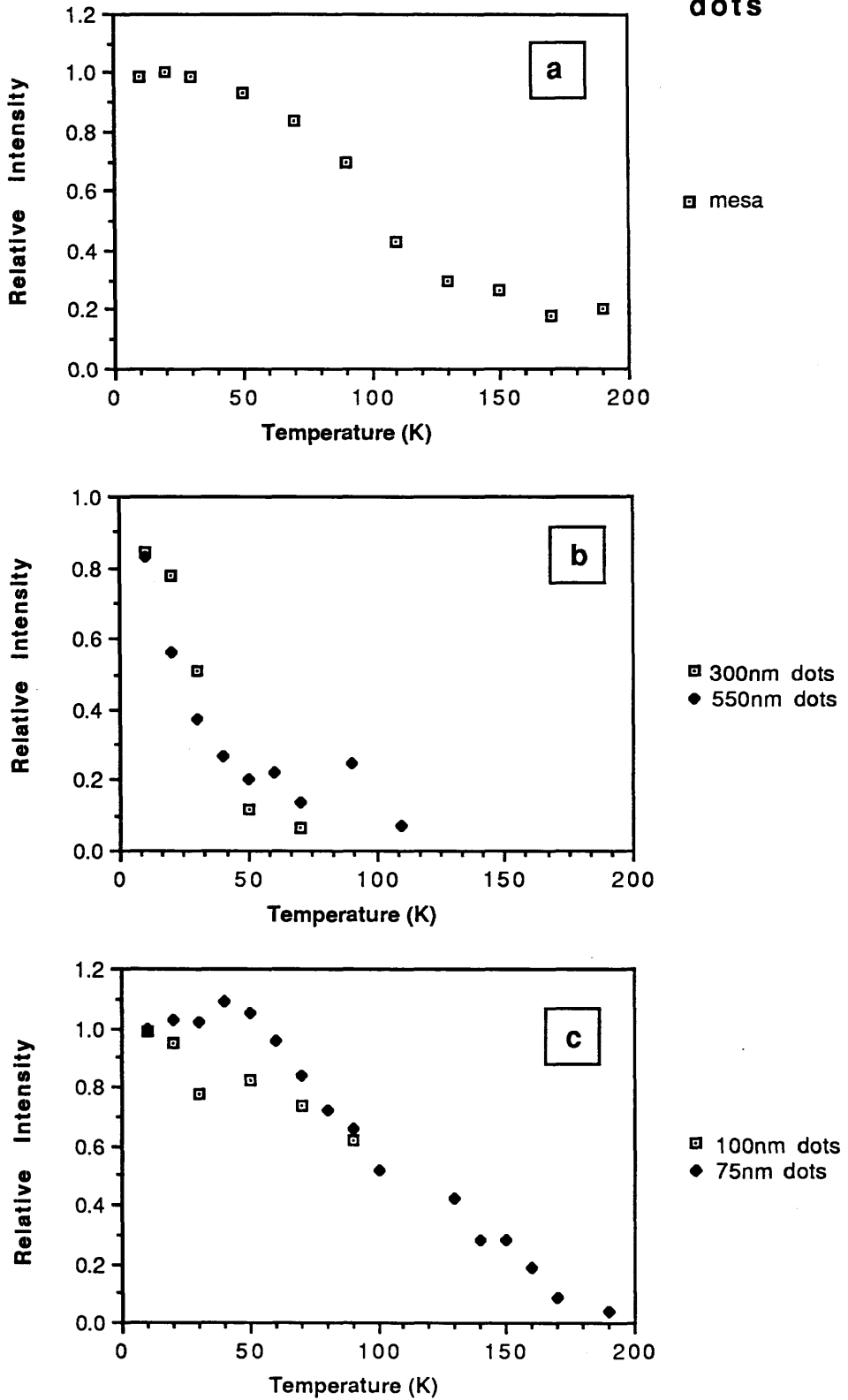


Figure 6.14 Temperature dependence of the integrated luminescence intensity relative to that at 5K from the 4nm QW in a) a 200µm² mesa b) 300 and 550nm diameter dots and c) 75 and 100nm diameter dots.

4nm QW
wires

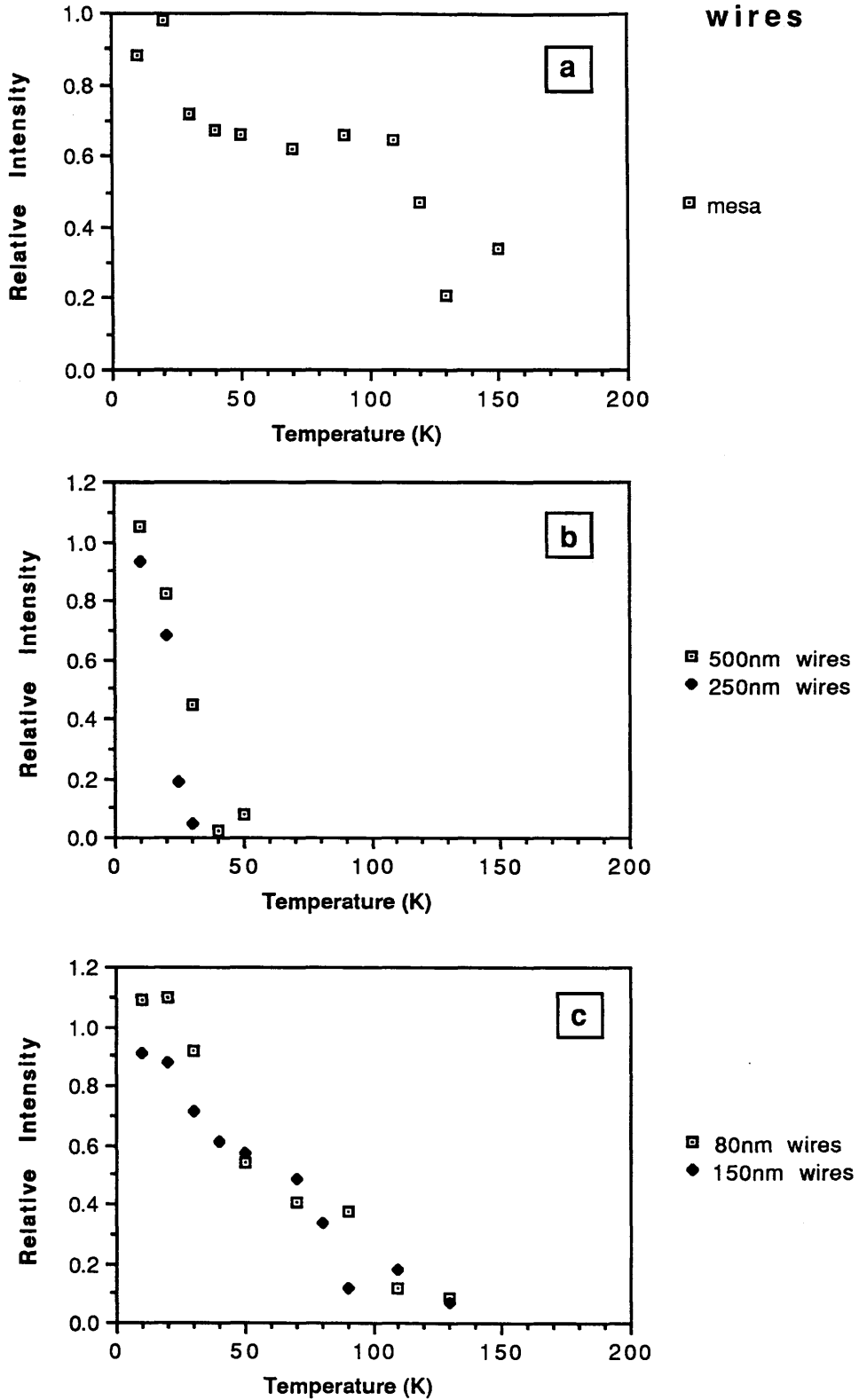


Figure 6.15 Temperature dependence of the integrated luminescence intensity relative to that at 5K from the 4nm QW in a) a 100µm² mesa b) 250 and 500nm and c) 80 and 150nm wide wires.

7nm QW
dots

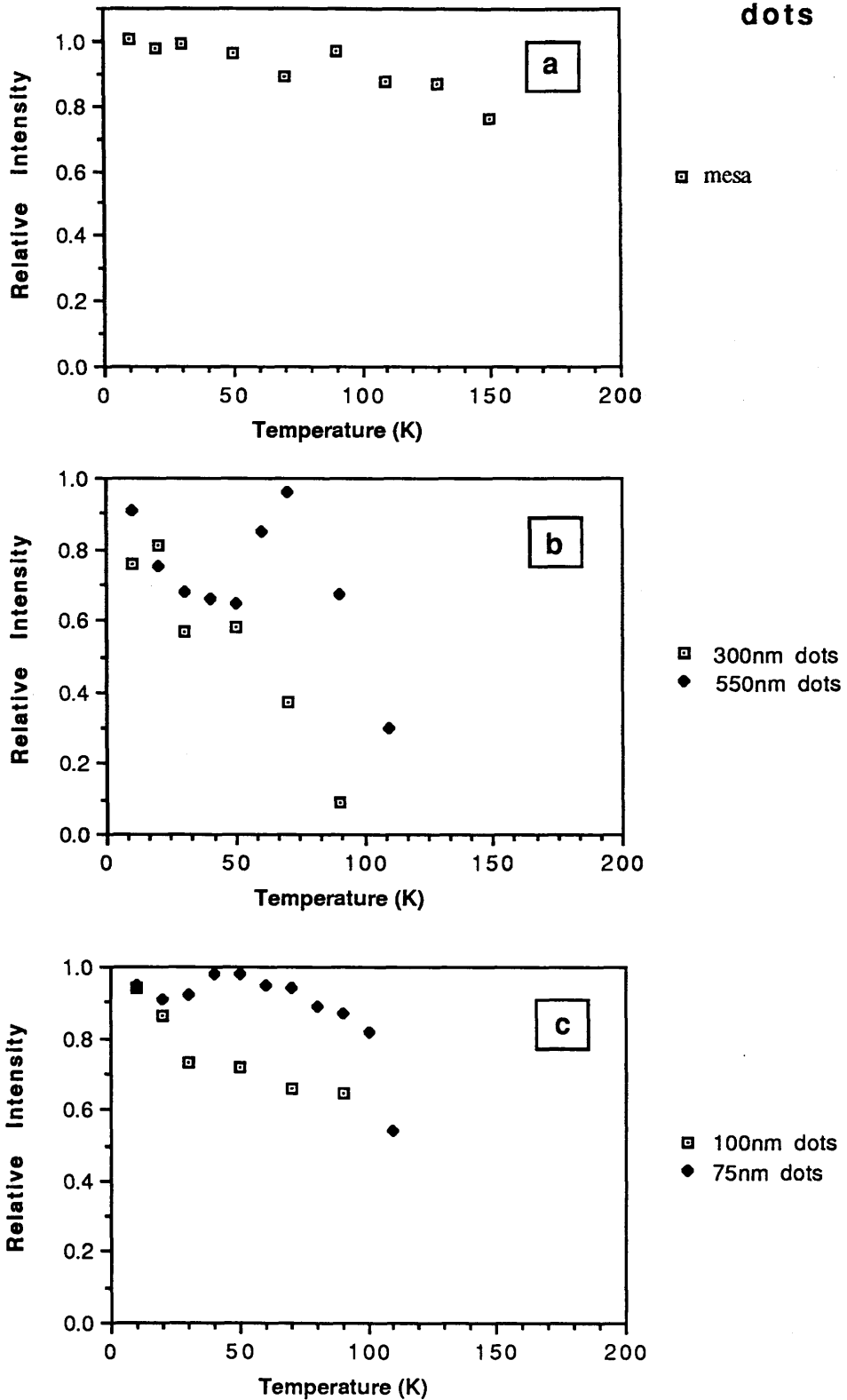
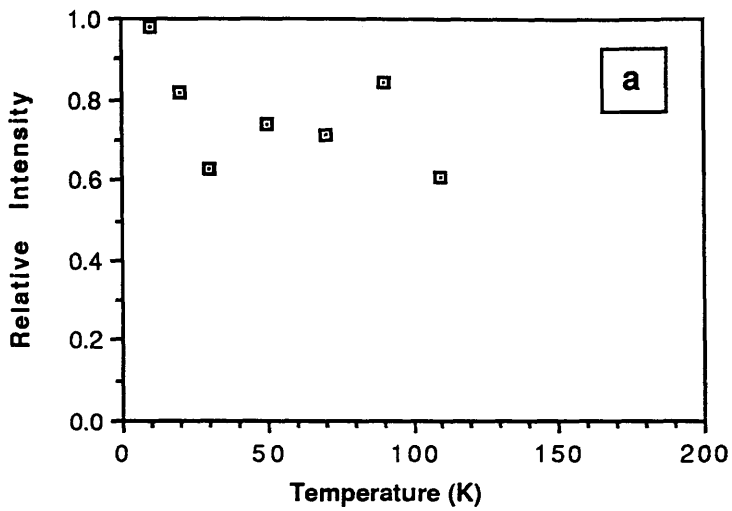
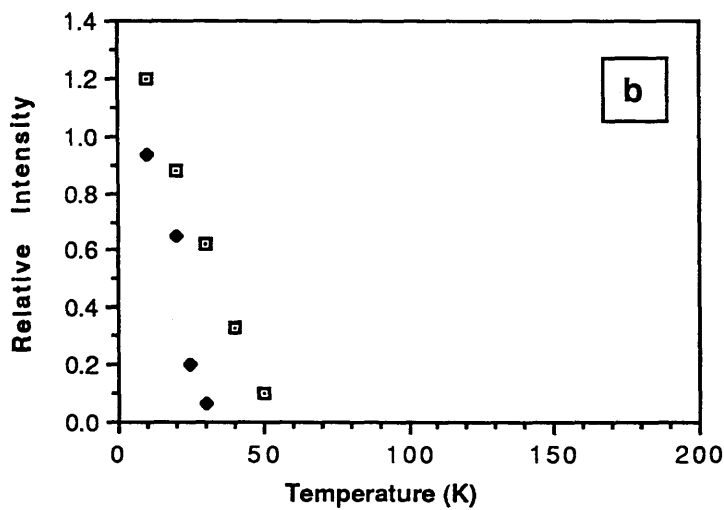


Figure 6.16 Temperature dependence of the integrated luminescence intensity relative to that at 5K from the 7nm QW in a) a $200\mu\text{m}^2$ mesa b) 300 and 550nm and c) 75 and 100nm diameter dots.

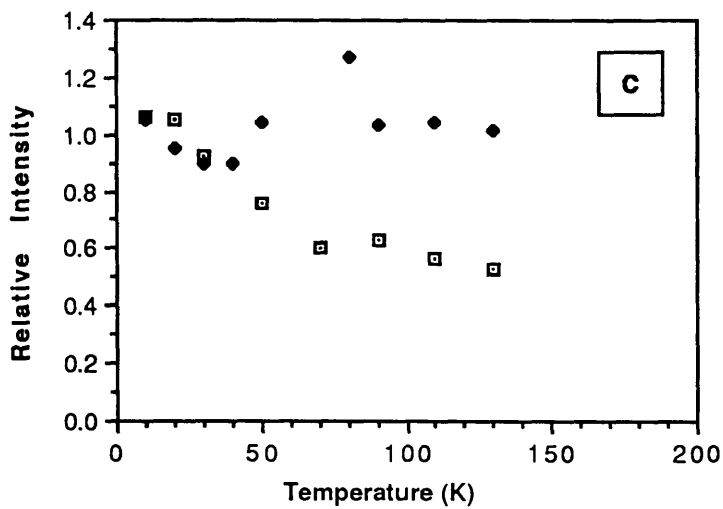
7nm QW dots



□ mesa



□ 550nm wires
◆ 250nm wires



□ 80nm wires
◆ 150nm wires

Figure 6.17 Temperature dependence of the integrated luminescence intensity relative to that at 5K from the 7nm QW in a) a 100µm² mesa b) 250 and 500nm and c) 80 and 150nm wide wires.

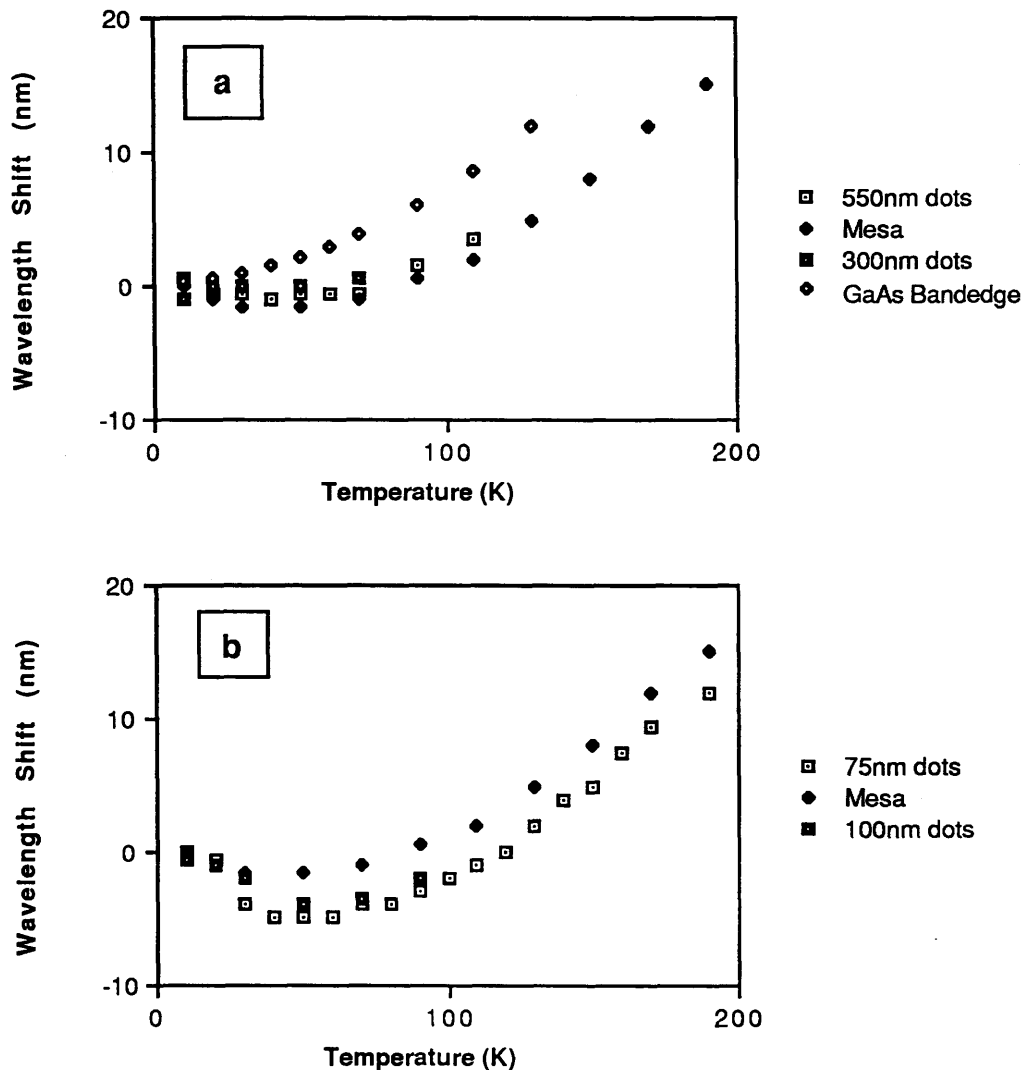


Figure 6.18 Wavelength shift in exciton emission relative to the 5K position in a) 300 and 550nm diameter dots and b) 75 and 100nm diameter dots for the 4nm quantum well. The behaviour of a 200 μ m square mesa is shown for comparison purposes in each case. The peak positions are plotted relative to the 5K exciton emission peak position. A shift to higher energy corresponds to a negative wavelength shift on the graph.

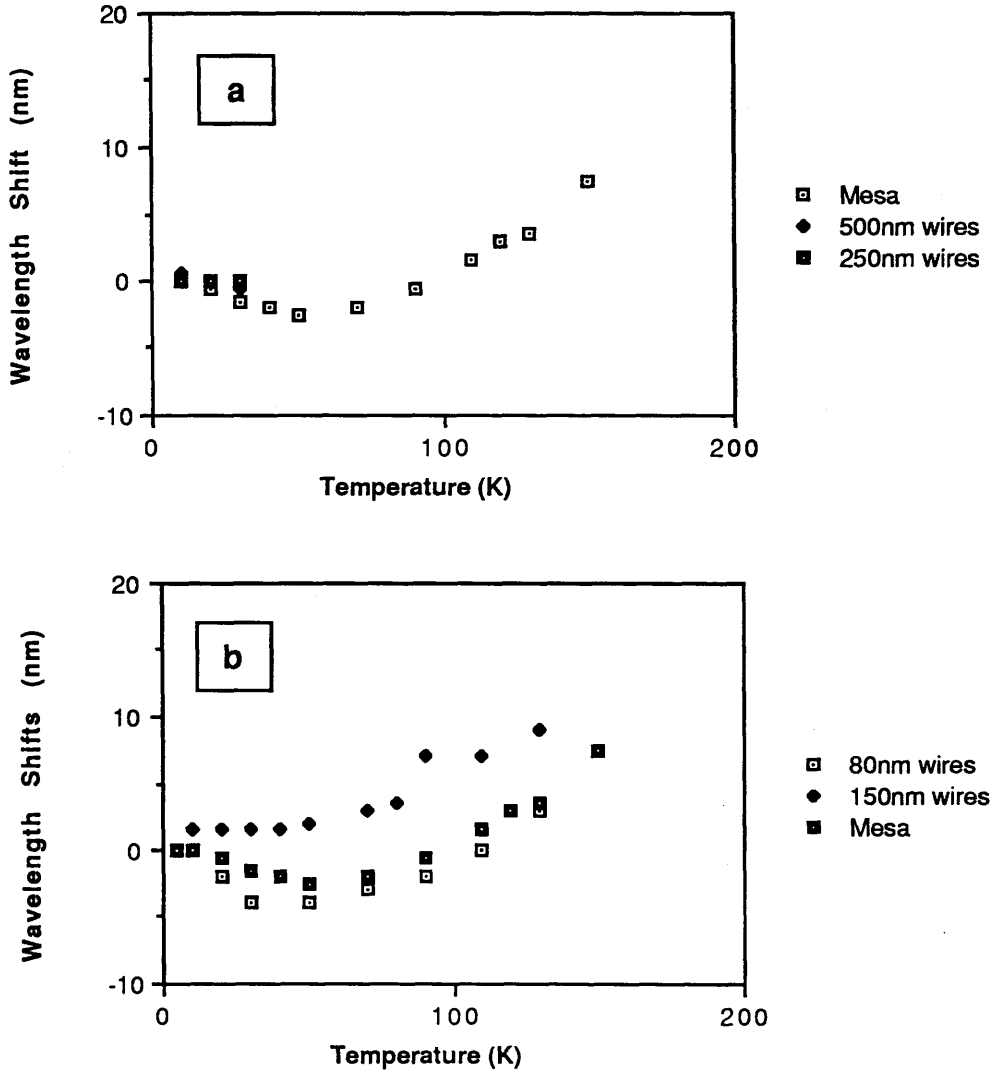


Figure 6.19 Wavelength shift in exciton emission relative to the 5K position in a) 250 and 500nm wide wires and b) 80 and 150nm wide wires for the 4nm quantum well. The behaviour of a 100 μ m square mesa is shown for comparison purposes. The peak positions are plotted relative to the 5K exciton emission peak position. A shift to higher energy corresponds to a negative wavelength shift on the graph.

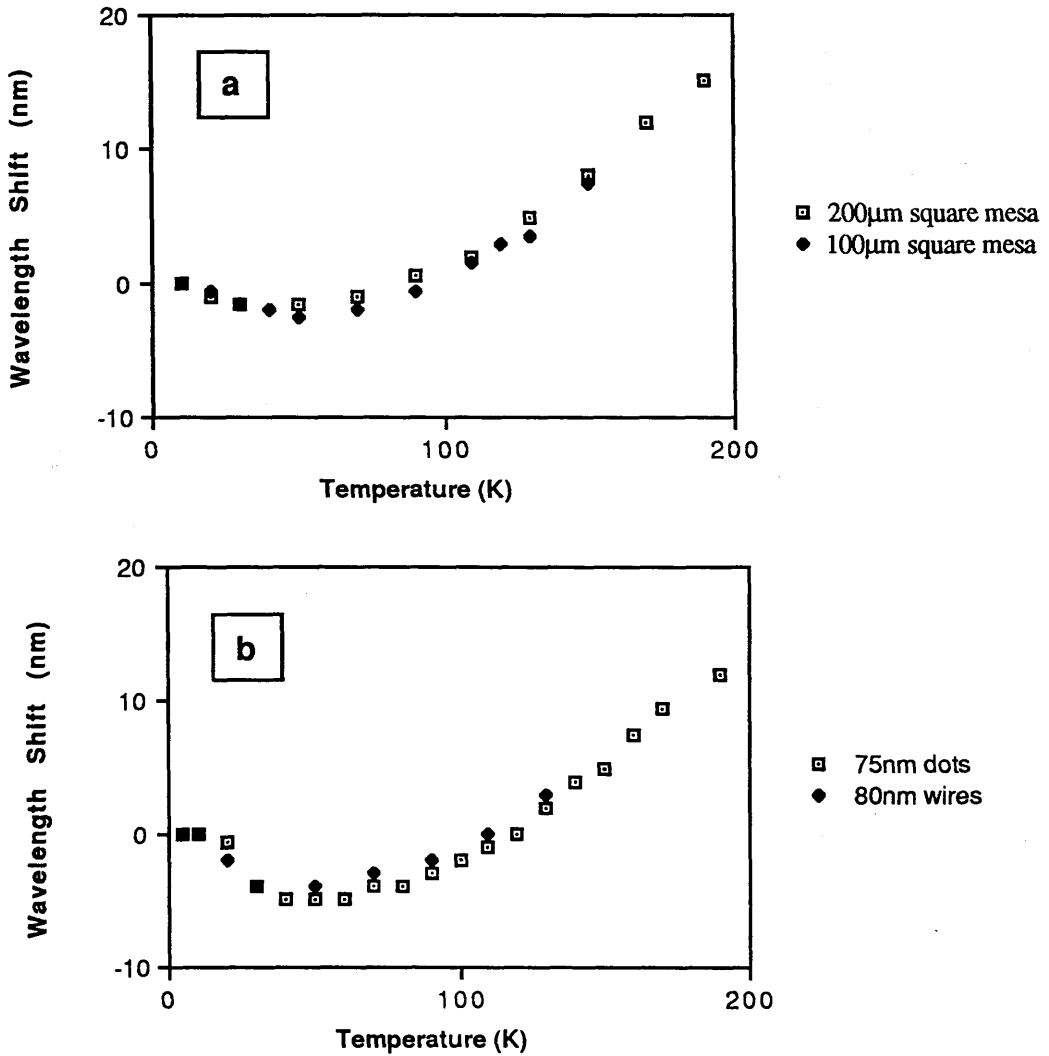


Figure 6.20 Comparison of wavelength shift in exciton emission relative to the 5K position for a) 200 and 100µm square mesas and b) 75nm diameter dots and 80nm wide wires. A shift to higher energy corresponds to a negative wavelength shift on the graph.

Figures 6.21 - 6.23 show the variation of the PL linewidth with temperature. Figure 6.21 shows the variation in a mesa. The most striking feature is an abrupt increase in the 4nm well linewidth at 10K which then decreases as the temperature is increased to 60K then gradually increases. Again in the 7nm well this effect is not seen. The linewidth shows an approximate linear variation with increasing temperature. The additional linewidth over the 5K-temperature value is approximately equal to kT . The broadening of the 4nm well is much less severe than the 7nm with increasing temperature. The two larger dot sizes follow this behaviour whereas in the smaller dot sizes the 4nm QW linewidth broadens abruptly at 20K and then decreases as the temperature increases. The 7nm QW behaviour follows the mesa. In the smallest dots there is virtually no increase in linewidth in the 4nm QW from 50 to 180K. The wires show very similar behaviour to the dots with abrupt linewidth broadening also occurring in the 80nm wires at 20K.

Figure 6.24 shows the variation of output integrated PL intensity with input power variation in a $200\mu\text{m}^2$ mesa and the 75 and 300nm dots in both the 4 and 7nm QW. Figure 6.25 shows the same but this time in a $100\mu\text{m}^2$ mesa and the 80 and 250nm wires. In all cases a linear dependence is found suggesting that over these input power ranges radiative recombination is the dominant recombination mechanism. At very low input powers the emission energy decreases by 7meV in the mesa and 9meV in the 300nm diameter dots but only in the 4nm QW. This suggests that at these input powers impurity bound exciton radiative recombination is the dominant mechanism which is saturated at higher input powers where intrinsic processes dominate. In the dots and wires however much higher input powers are always used to pump the structures so this mechanism should not be dominant.

6.9.2 Experimental Results After Regrowth

The samples were characterized using the same optical set-up as before regrowth and various excitation energies - 2.54, 2.41 and 1.96eV. After regrowth, luminescence was obtained only in the 300 and 550nm diameter dots and in the 150, 250 and 500nm wide wires. It is lost in the 75 and 100nm dots and the 80nm wires. Figure 6.26 shows a) 100nm diameter dots and b) 250nm wide wires before regrowth and (c) and (d) after regrowth with a $0.35\mu\text{m}$ thick layer of $\text{Al}_{0.4}\text{Ga}_{0.6}\text{As}$. The overgrown layer is not as smooth as that obtained in figure 6.2 and 6.5. In the initial experiments a short wet etch with HF was carried out to clean up the surface prior to regrowth. It was thought that this etch might have destroyed the GaAs well and AlGaAs barriers in the smallest structures as HF etches both these materials. It was therefore decided to remove this step to see if the smallest structures would still luminesce. As they did not, another mechanism must be responsible for the loss of emission. It is perhaps the removal of this etch step and the resulting poorer quality of surface onto which the overlayer is grown that caused the poorer quality regrowth. The other major difference is in the relative exciton emission strengths from the 4nm and 7nm QW. After regrowth the efficiency in exciton emission from the 7nm QW is greatly reduced. In a $200\mu\text{m}^2$ mesa the ratio of the intensity of the exciton emission from the 4nm QW to the 7nm QW before regrowth is ~ 0.3 and after regrowth is ~ 10 . It is uncertain why this reduction in luminescence efficiency should occur in the 7nm QW. The most likely reason is enhancement of the nonradiative recombination sites within this well, a mechanism for which is discussed in Section 6.9.3. To try and clarify the cause of this effect the results

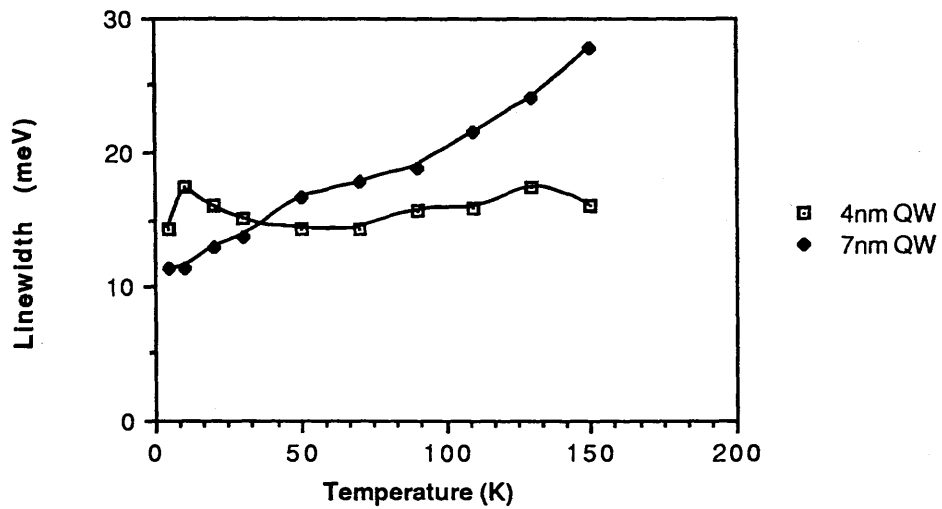


Figure 6.21 Photoluminescence linewidth variation with temperature for the 200 μ m square mesa.

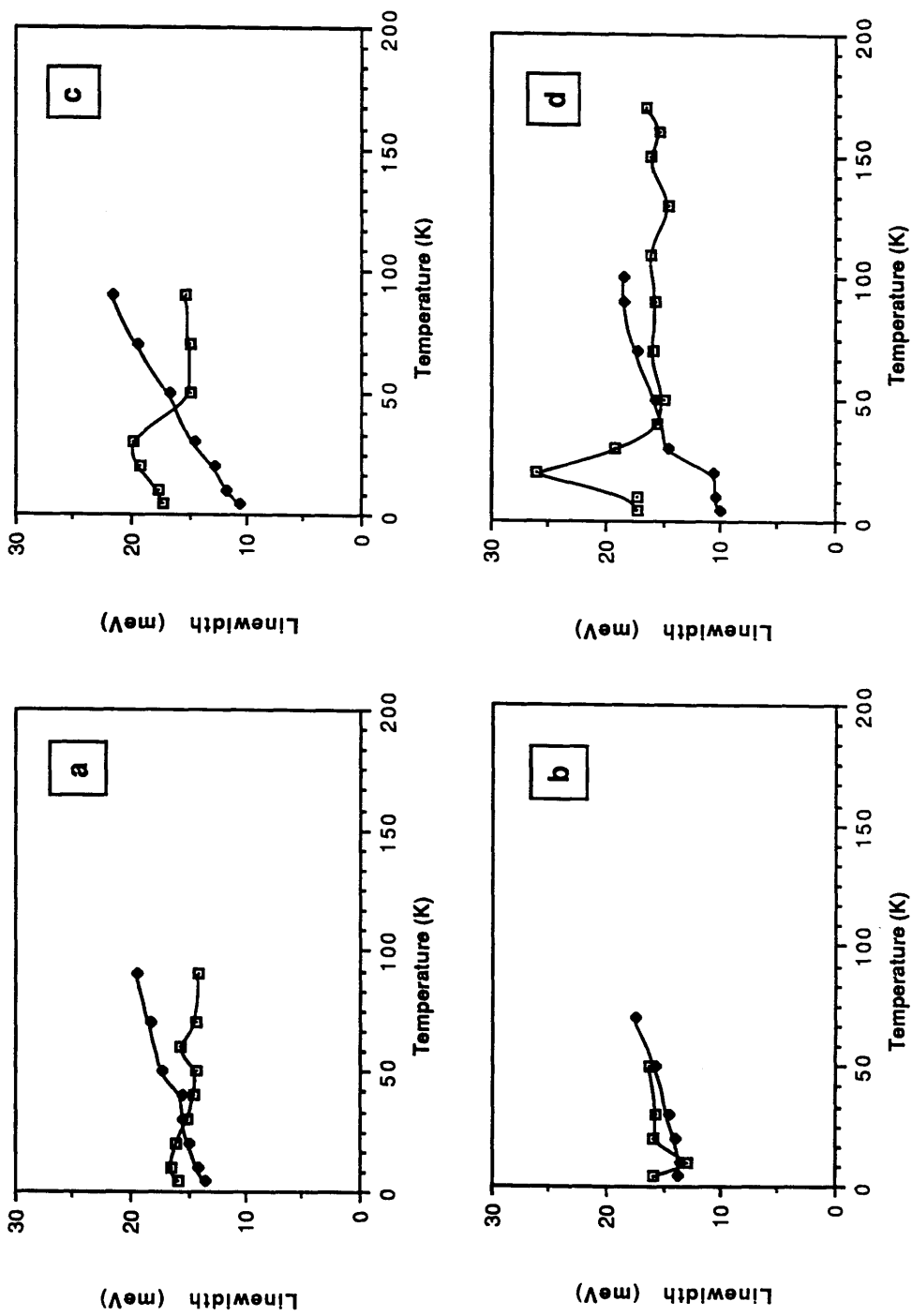


Figure 6.22 Photoluminescence linewidth variation with temperature for a) 550nm b) 300nm c) 100nm and d) 7nm diameter dots excited at 2.54eV. The open squares represent the 4nm QW and the filled diamonds the 7nm QW.

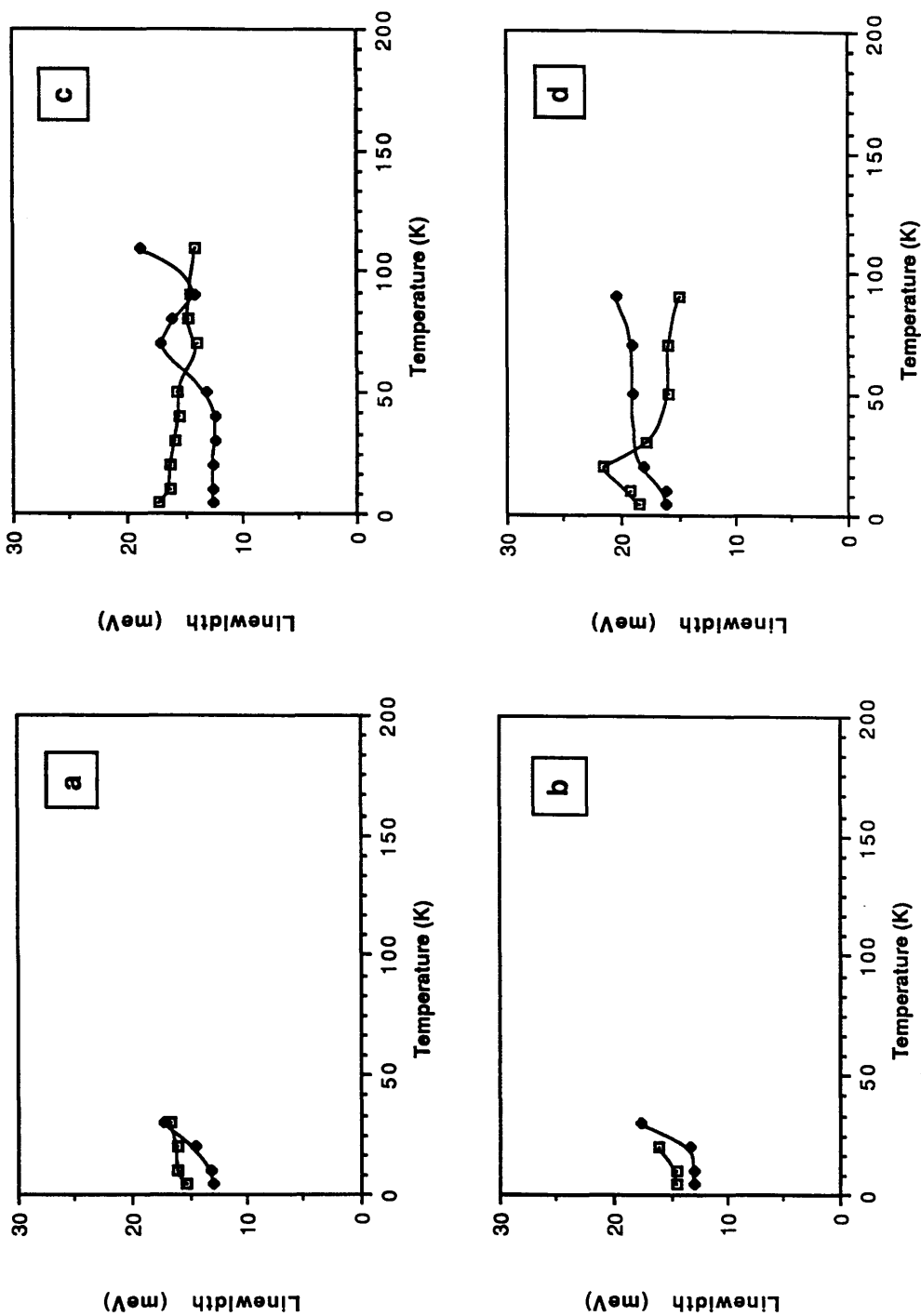


Figure 6.23 Photoluminescence linewidth variation with temperature for a) 500nm b) 250nm c) 150nm and d) 80nm wide wires excited at 2.54eV. The open squares represent the 4nm QW and the filled diamonds the 7nm QW.

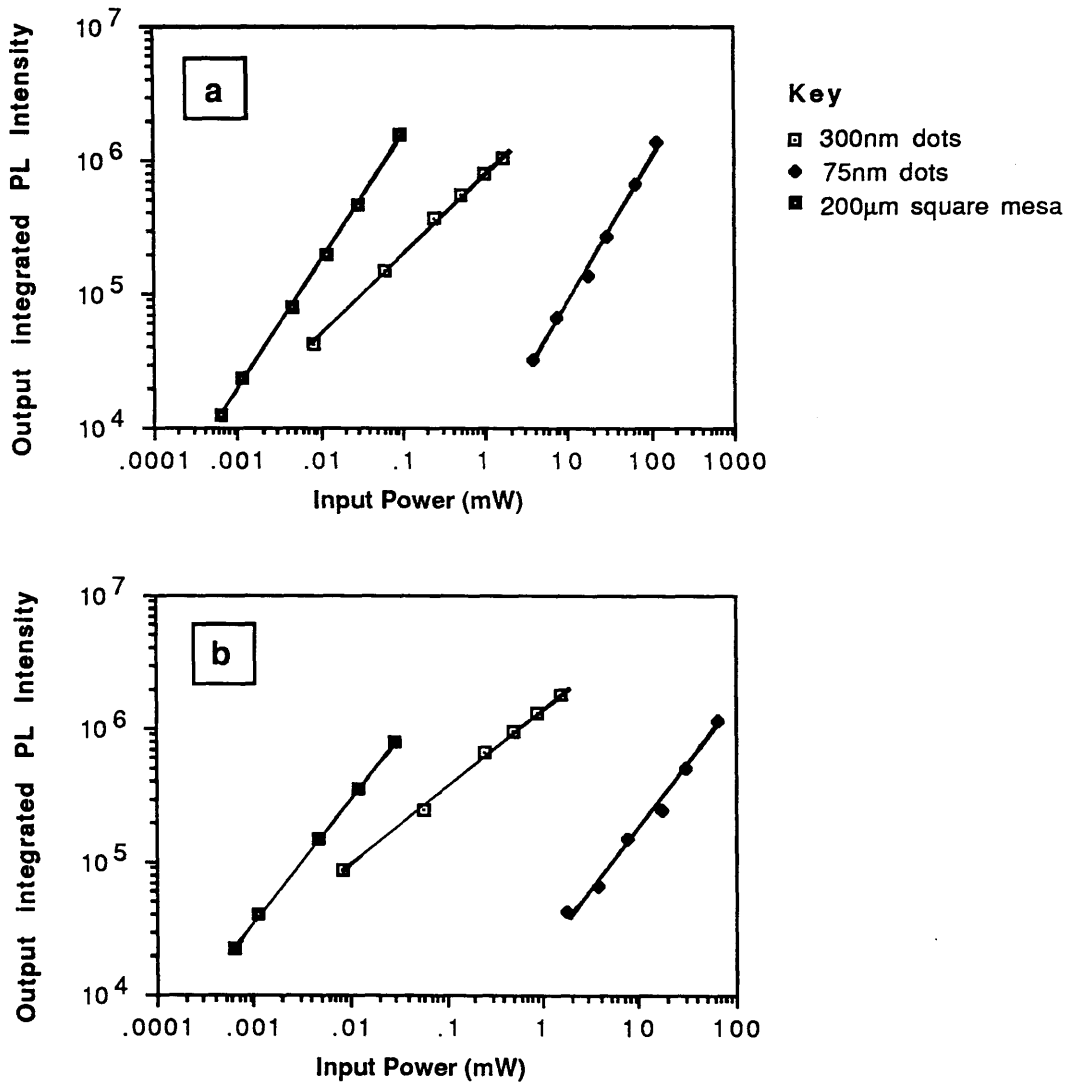


Figure 6.24 Excitation power dependence at 2.54eV of the integrated PL intensity from a) 4nm QW and b) 7nm QW from 75 and 300nm dots and the 200μm square mesa..

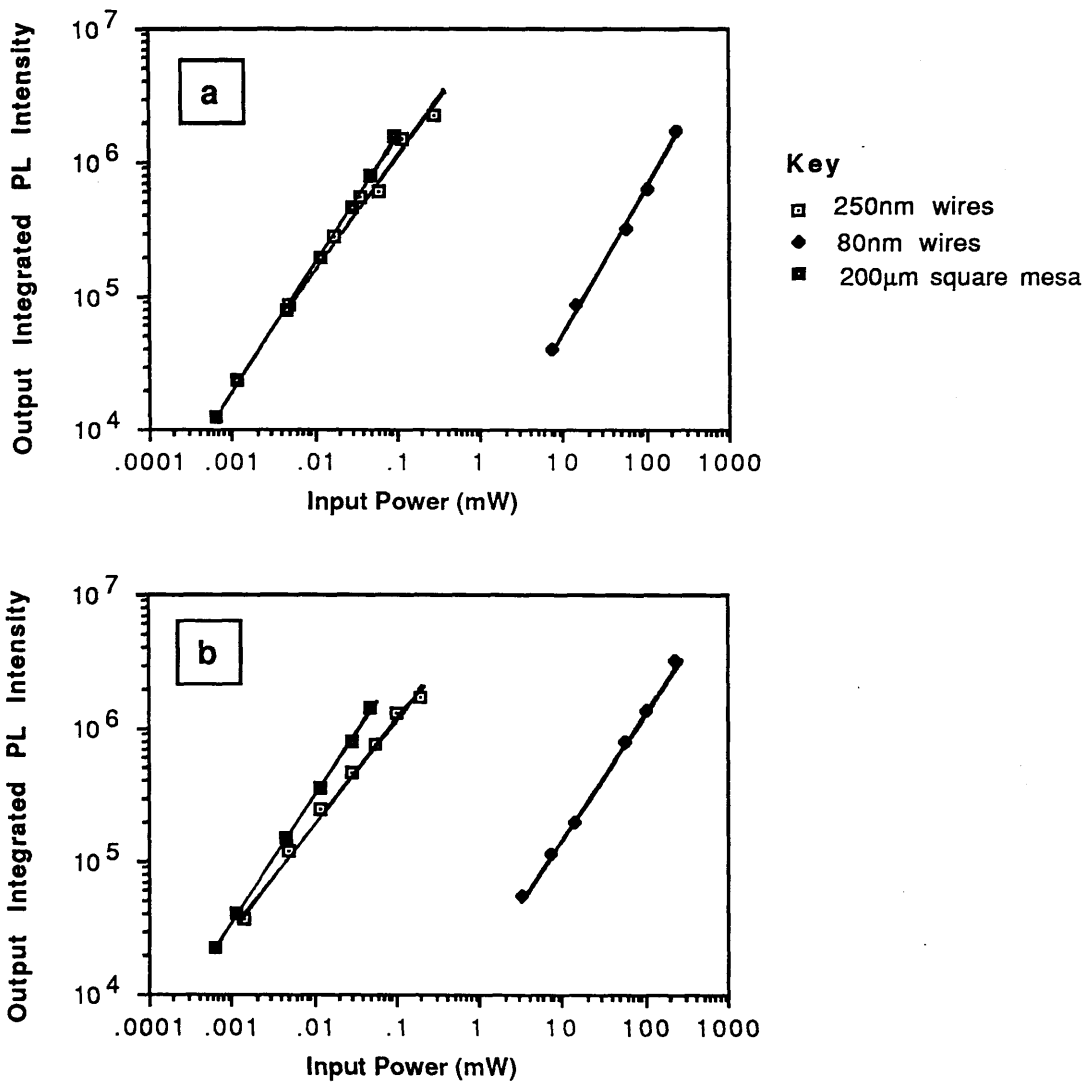
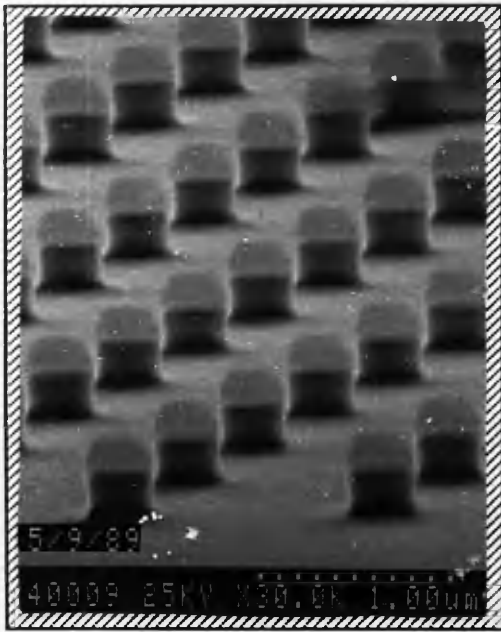
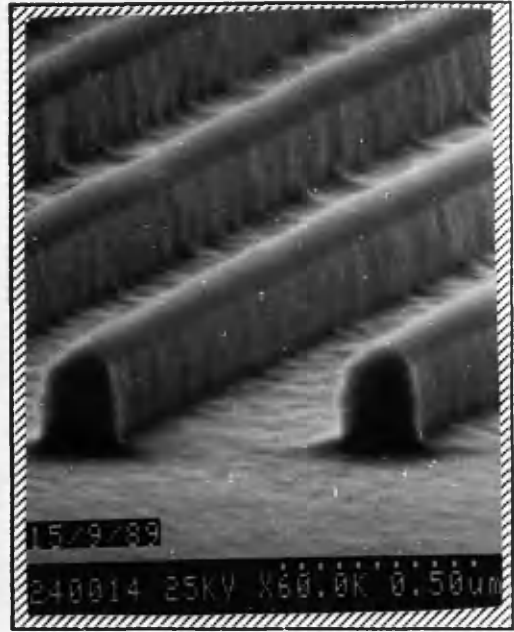


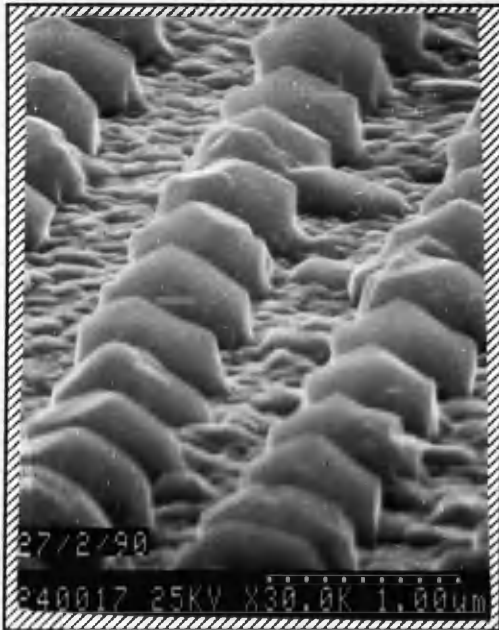
Figure 6.25 Excitation power dependence at 2.54eV of the integrated PL intensity from a) 4nm QW b) 7nm QW from 80 and 250nm wires and the 200μm square mesa.



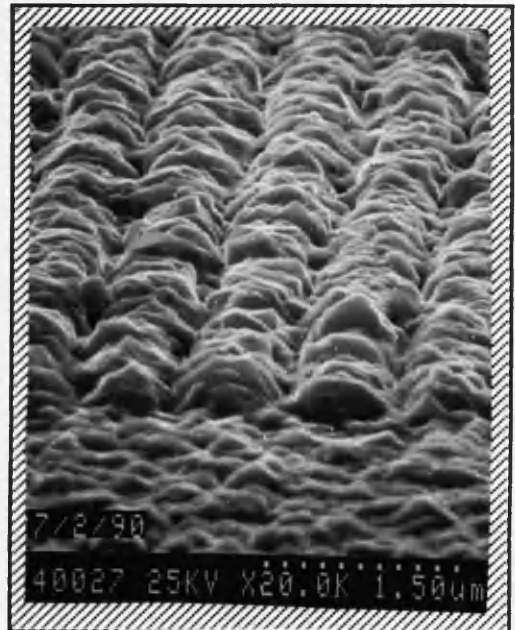
(a)



(b)



(c)



(d)

Figure 6.26 a) 300nm diameter dots and b) 250nm wires etched using SiCl_4 before regrowth and c) and d) after regrowth with a $0.35\mu\text{m}$ thick layer of $\text{Al}_{0.4}\text{Ga}_{0.6}\text{As}$. Notice that before regrowth the HRN mask has not been removed.

of regrowth on CH_4/H_2 etched dots and mesas are presented in Section 6.10. Due to this severe reduction in PL efficiency from the 7nm QW, mainly results for the 4nm QW will be given.

Figures 6.27, 6.29 and 6.30 show a comparison of the relative integrated PL intensity (relative to the 5K integrated luminescence from that structure) versus temperature both before and after regrowth for those structures which still luminescence. In these figures the temperature axis maximum has been reduced from 200K to 120K. Figure 6.27 shows the results obtained from a $200\mu\text{m}^2$ and $100\mu\text{m}^2$ mesa both before and after regrowth. The only noticeable difference is that in the $200\mu\text{m}^2$ mesa the intensity varies almost linearly from 1 at 10K to 0.1 at 150K after regrowth, whereas before regrowth the relative efficiency was 1 up to 50K. In the $100\mu\text{m}^2$ mesa there is little variation before or after regrowth. Figure 6.28 shows the PL spectra obtained from the $200\mu\text{m}^2$ mesa before and after regrowth for both the 4 and 7nm QW as the temperature is varied. This clearly shows the degradation in the luminescence intensity from the 7nm QW after regrowth. Figure 6.29 shows that there is little difference in the relative integrated intensities from the dots before or after regrowth. Figure 6.30 shows however that the relative integrated PL intensities from the wires has been affected by the overgrowth layer. Instead of losing their luminescence at 60K, the 500nm wires continue to luminesce up to 120K and the reduction tends asymptotically to zero without a sharp cutoff as happens prior to regrowth. Figure 6.31 shows the PL spectra obtained from the 500nm wires before and after regrowth from both the 4 and 7nm QW. This clearly shows the improvement in the intensities of the emission after regrowth. The efficiency of the 250nm wires is also improved with emission still being obtained at 60K instead of 40K as before regrowth. The efficiency of the 150nm wires however is reduced after overgrowth, with a relative intensity of 0.15 obtained at 60K after overgrowth whereas before overgrowth luminescence persisted to 110K. Figure 6.32 shows the relative intensity from the three wires and the $100\mu\text{m}^2$ mesa after regrowth. As can be seen the wire luminescence efficiency is now very similar for all wire widths with the 500nm wires only slightly more efficient than the 150 and 80nm wires. The mesa emission is still more efficient than the wires.

Figures 6.33 - 6.35 show how the exciton emission wavelength shifts with temperature. Figure 6.33 compares the results obtained from the 100 and $200\mu\text{m}^2$ mesas. Figure 6.34 compares the results obtained before and after regrowth from the 4nm well in the 300 and 550nm dots. There are marked differences after regrowth. The $200\mu\text{m}^2$ mesa and the 300nm dots more or less still follow the GaAs bandedge after regrowth. The 550nm dots however show a 10nm shift blue between 40 and 70K. In figure 6.35 there is little difference in the behaviour of the 250 and 500nm wires after regrowth but the 150nm wires shows a 10nm red shift between 30 and 60K. Why the 550nm dots and 150nm wires should show such a marked departure from the expected behaviour of decreasing exciton energy with increasing temperature is unclear.

Figure 6.36 shows how the PL linewidth from the 4nm QW varies with temperature after regrowth. In the $200\mu\text{m}^2$ mesa the 5K PL linewidth has broadened considerably from 15meV before regrowth to ~25meV after regrowth (see figure 6.21-6.23 for comparison). As the temperature is increased the broadening follows a similar pattern to the before regrowth behaviour. In the 300 and 550nm dots the 5K linewidth has increased from ~16meV before to 27meV after regrowth. This is consistent with

4nm QW mesas

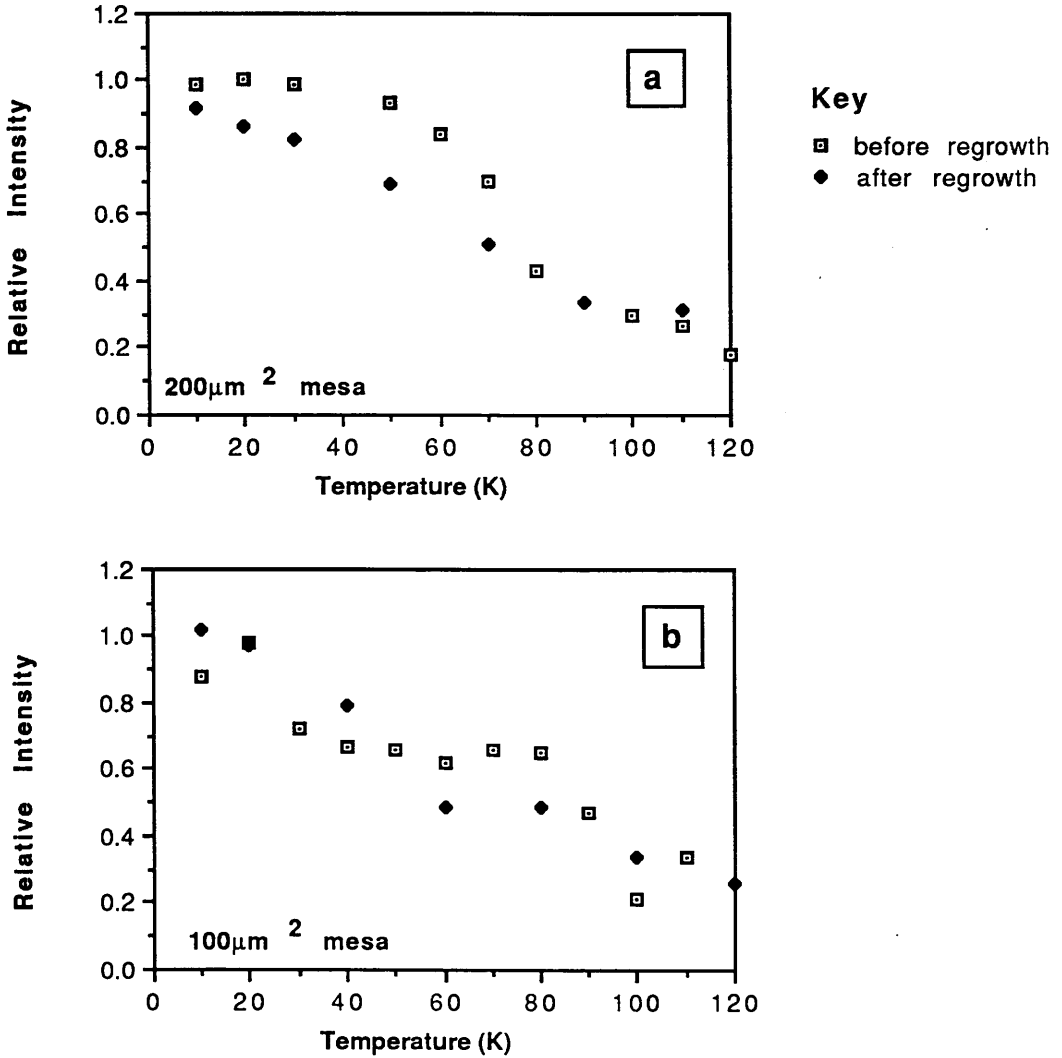


Figure 6.27 Comparison of the relative intensity of PL from the 4nm QW in a) 200µm square mesa and b) 100µm square mesa before regrowth (open squares) and after regrowth (filled diamonds). Before regrowth PL was excited at 2.54eV and after regrowth at 1.96eV. Notice that the temperature axis maximum is now 120K and not 200K.

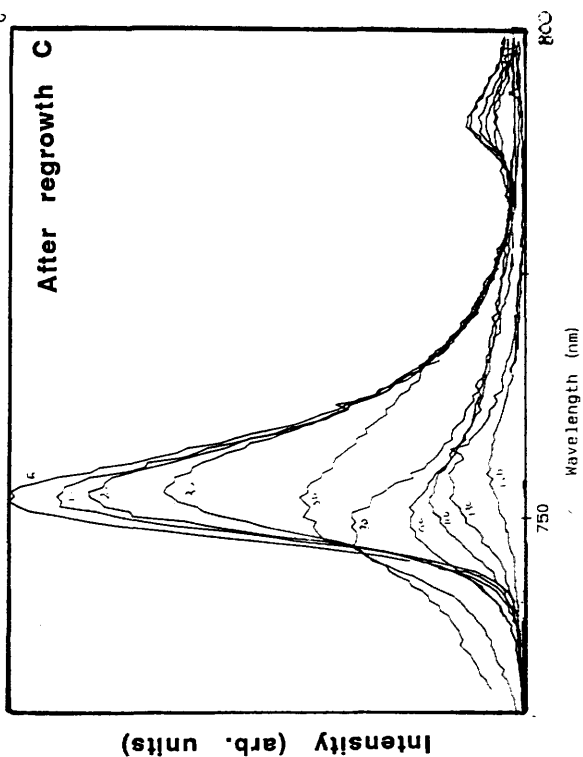
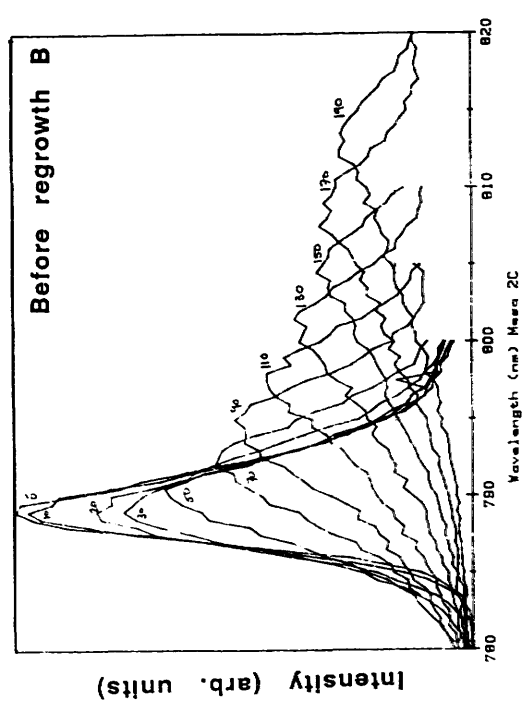
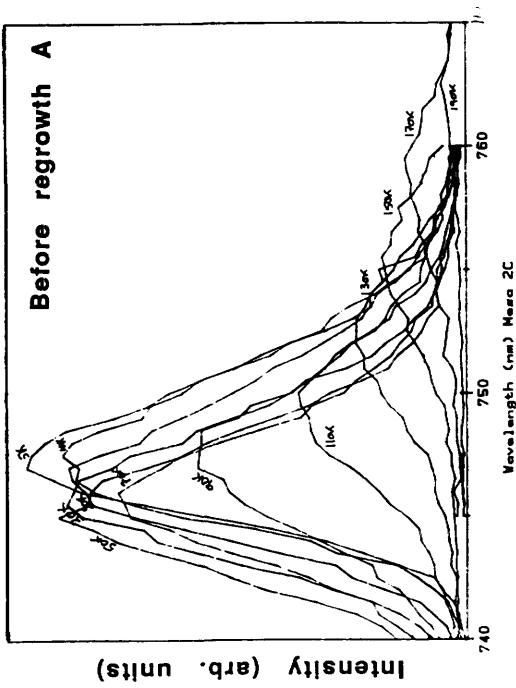


Figure 6.28 Variation in PL spectra from the $200\mu\text{m}^2$ mesa a) before regrowth 4nm QW b) before regrowth 7nm QW and c) after regrowth 4 and 7nm QW. Before regrowth the 7nm QW is twice as bright as the 4nm QW for the same incident pump power. Notice the sharp decrease in emission intensity from the 7nm QW after regrowth.

4nm QW
dots

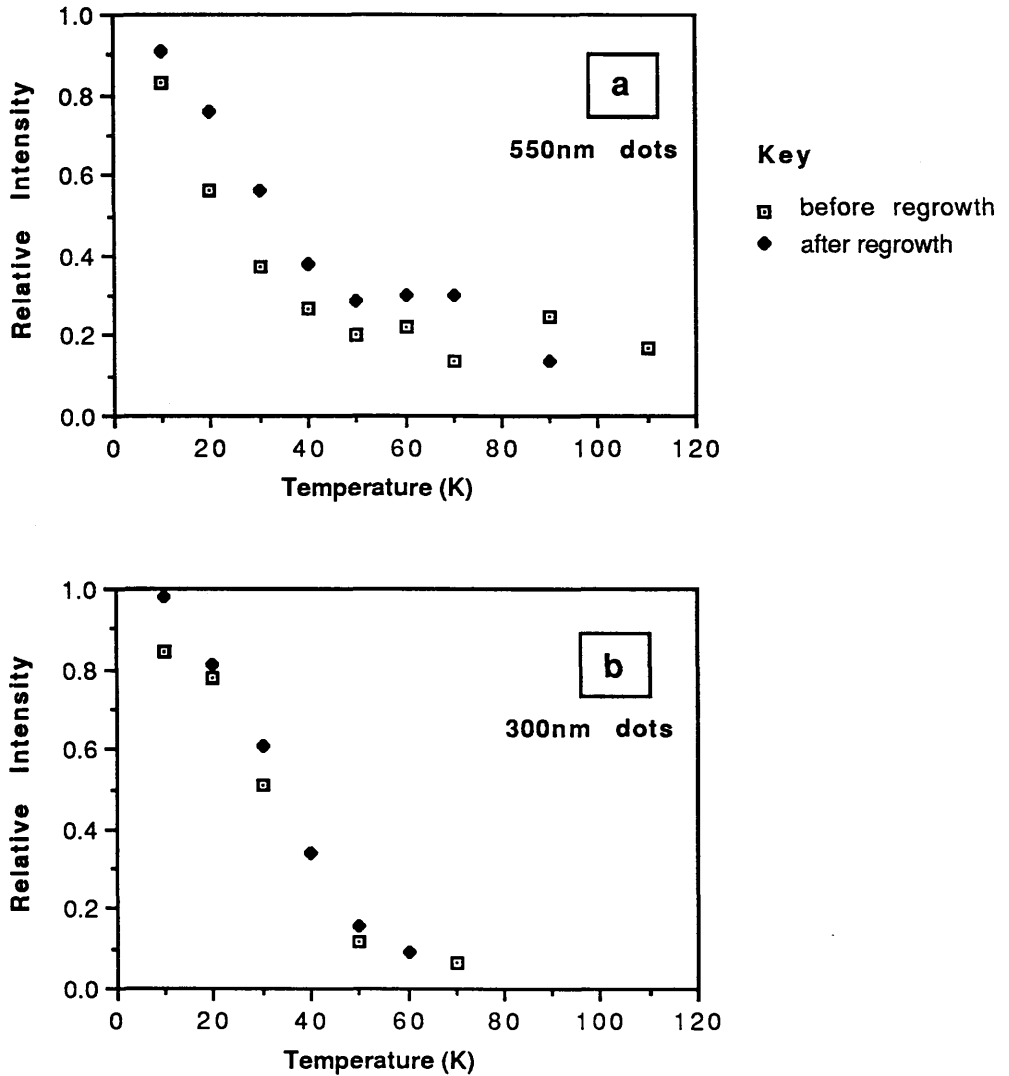


Figure 6.29 Comparison of the variation of the relative integrated PL intensity with temperature from the 4nm QW in a) 550nm dots and b) 300nm dots before regrowth (open square) and after regrowth (filled diamonds). Before regrowth PL excited at 2.54eV and after at 1.96eV.

4nm QW wires

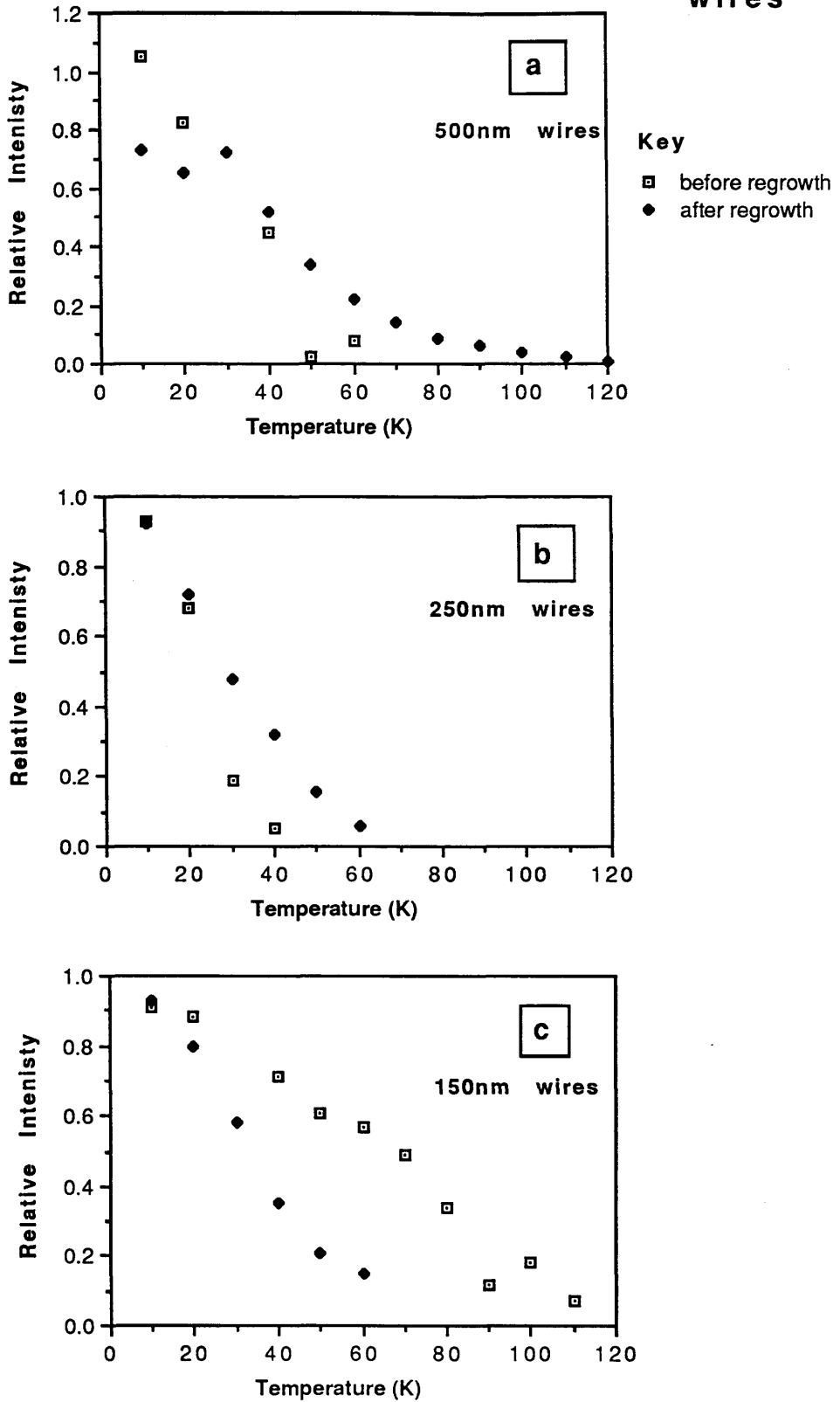


Figure 6.30 Comparison of the relative integrated PL intensity from the 4nm QW in a) 550nm b) 250nm and c) 150nm wide wires before regrowth (open squares) and after regrowth (filled diamonds). Before regrowth PL excited at 2.54eV and after 1.96eV.

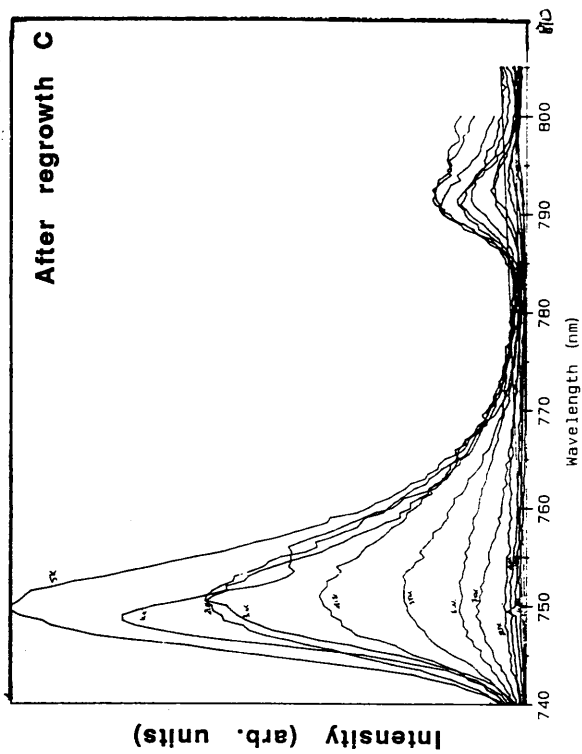
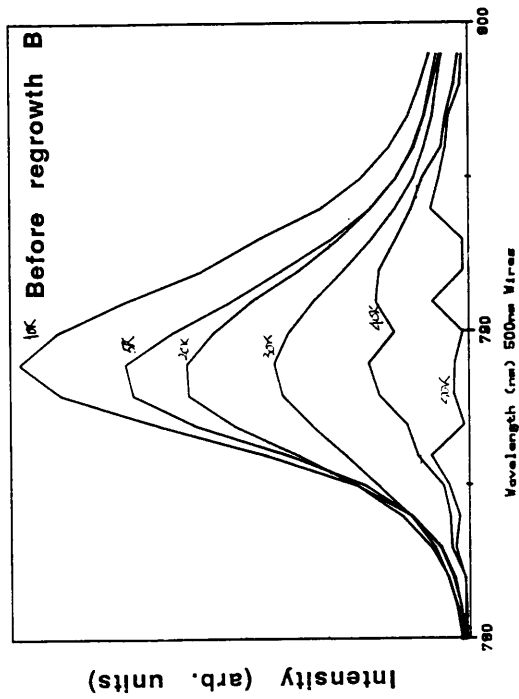
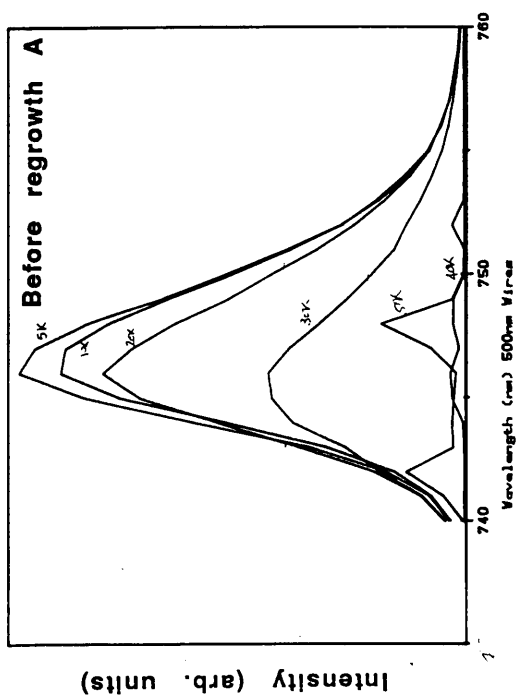


Figure 6.31 Variation in PL spectra from the 500nm wide wires a) before regrowth 4nm QW b) before regrowth 7nm QW and c) after regrowth 4 and 7nm QW. Before regrowth the 4nm QW is 1.5 times brighter than the 7nm QW for the same incident pump power. Notice the sharp decrease in emission intensity from the 7nm QW after regrowth.

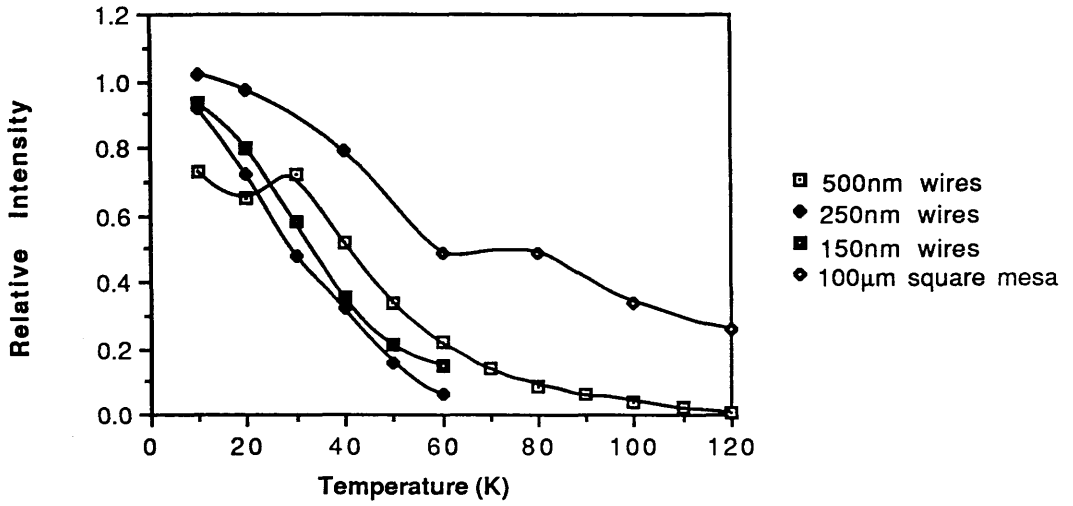


Figure 6.32 Variation of relative integrated PL intensity excited at 1.96eV with temperature from 150, 250 and 500nm wires and the 100µm square mesa after regrowth.

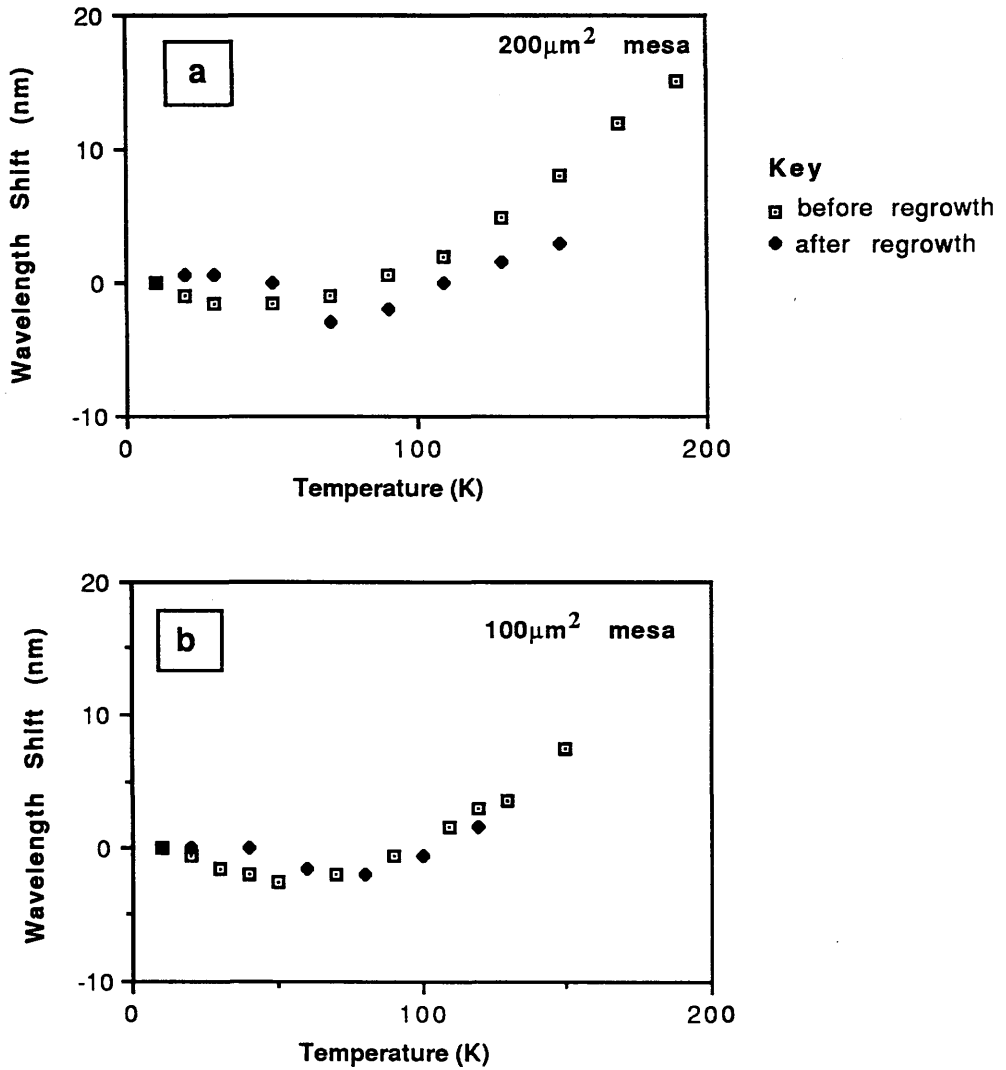


Figure 6.33 Shift in exciton emission wavelength with temperature for a) 200 μm square mesa and b) 100 μm square mesa for the 4nm QW before regrowth (open squares) and after regrowth (filled diamonds). The positions are plotted relative to the 5K exciton emission peak position. A shift to higher energy corresponds to a negative wavelength shift on the graph.

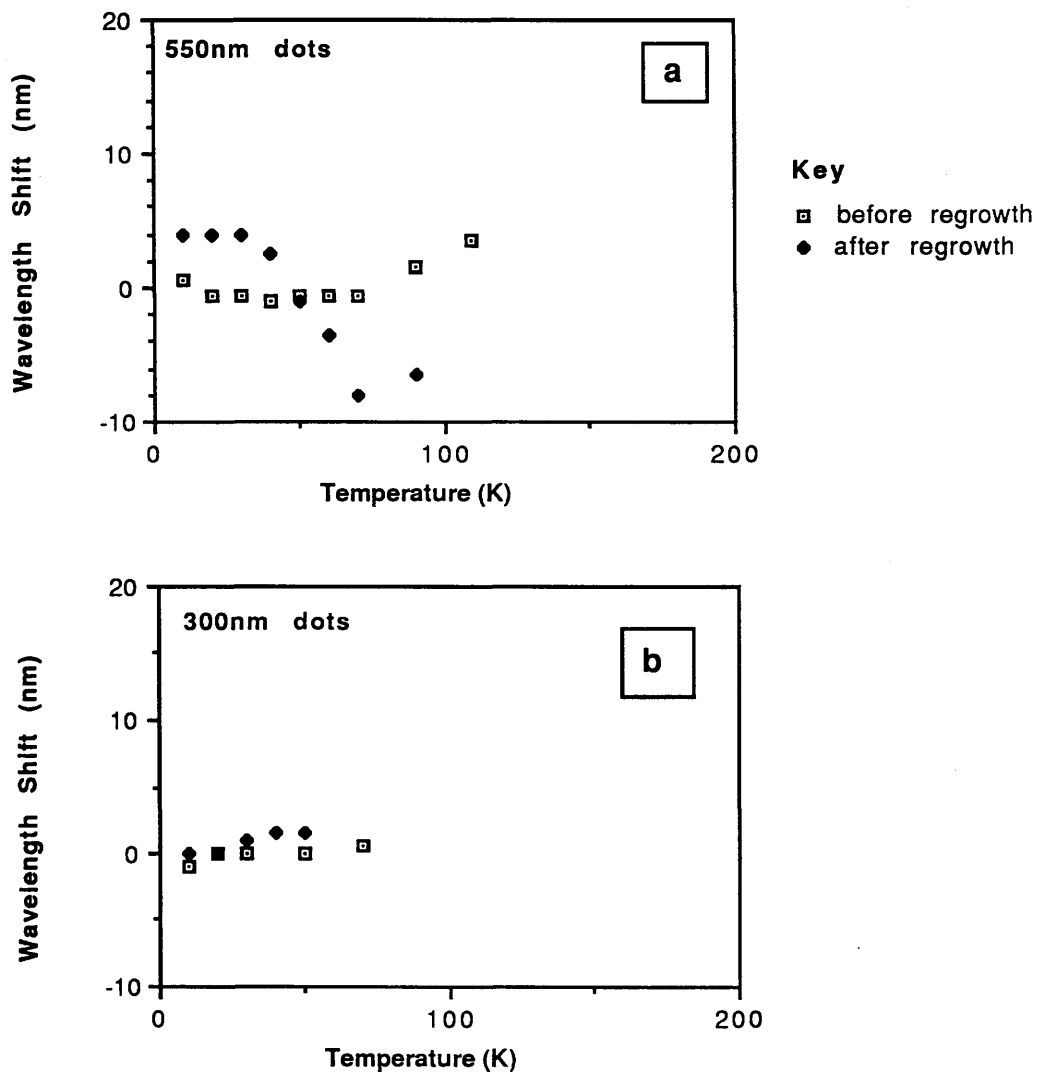


Figure 6.34 Shift in exciton emission wavelength with temperature for a) 550nm dots and b) 300nm dots for the 4nm QW before regrowth (open squares) and after regrowth (filled diamonds). The positions are plotted relative to the 5K exciton emission peak position. A shift to higher energy corresponds to a negative wavelength shift on the graph.

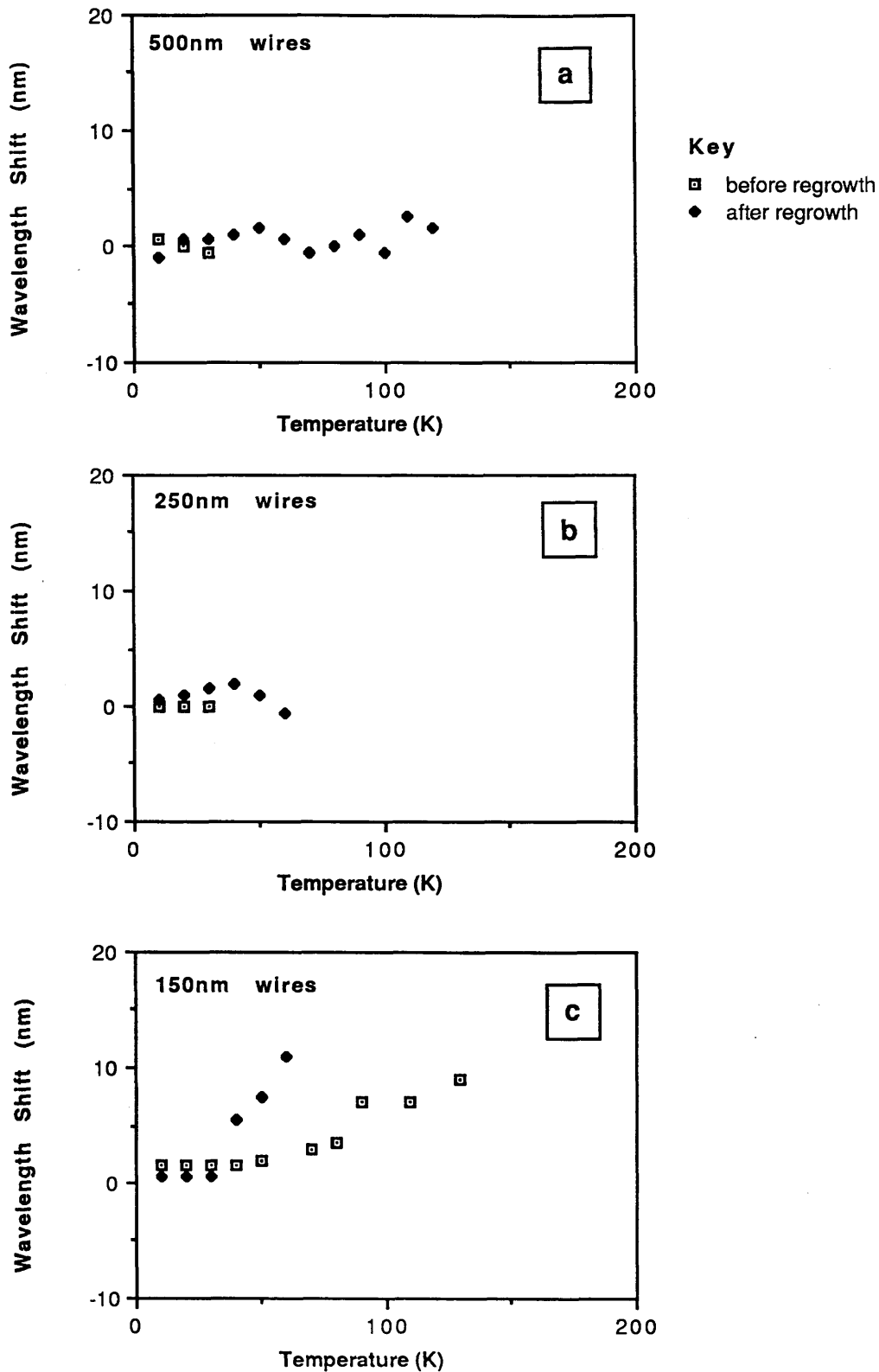


Figure 6.35 Shift in exciton emission wavelength with temperature for a) 500nm b) 250nm c) 150nm wide wires from the 4nm QW before regrowth (open squares) and after regrowth (filled diamonds). The positions are plotted relative to the 5K exciton emission peak position. A shift to higher energy corresponds to a negative shift on the graph.

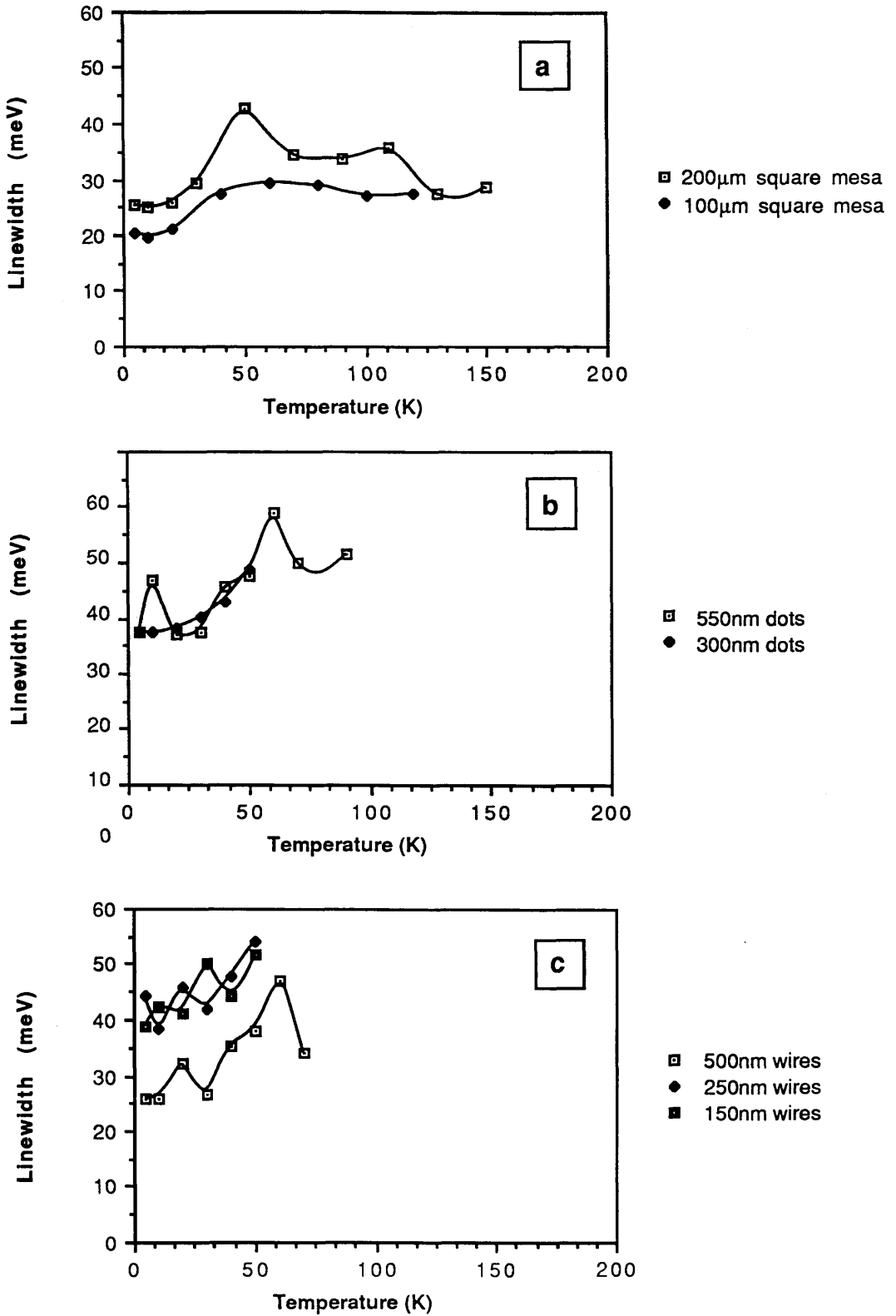


Figure 6.36 Photoluminescence linewidth variation with temperature for the 4nm QW in a) 200 and 100µm square mesas b) 300 and 550nm diameter dots and c) 500, 250 and 150nm wide wires excited at 1.96eV.

the mesa broadening. At 60K the linewidth broadens from 15meV before to 50meV after regrowth. Sensitivity to temperature has increased, as before the 4nm well retained an almost constant linewidth over the whole temperature range. In the wires however the broadening is much more severe than the dots and is increased in severity as the wire width is reduced. The 5K linewidths are 25, 45 and 40meV for the 500, 250 and 150nm wires respectively compared to 15, 15 and 17meV before regrowth. Again as the temperature is increased the linewidth increases to 38, 53 and 50meV respectively at 50K. The linewidth variation with temperature is not consistent with the mesa behaviour as at 50K the linewidth of the $100\mu\text{m}^2$ mesa has broadened from 20meV at 5K to 25meV. Therefore the regrowth on the quantum structures has degraded the PL linewidth more severely than regrowth on the control mesas. Impurity incorporation and increased well width fluctuations are the most likely cause of this and will be discussed in Section 6.9.3.

A further experiment was carried out to try and assess the quality of

- 1) the barriers themselves.
- 2) the interfaces between the quantum structures and the overgrowth layer
- 3) the interfaces between the GaAs well and the AlGaAs barriers

Figure 6.37 shows the PL excited at 2.41eV (514nm line of the Argon ion laser) obtained from a) the $\text{Al}_{0.3}\text{Ga}_{0.7}\text{As}$ barriers before regrowth and b) the $\text{Al}_{0.3}\text{Ga}_{0.7}\text{As}$ barriers after regrowth with a layer of $\text{Al}_{0.4}\text{Ga}_{0.6}\text{As}$ from a control sample that had not been processed in any way prior to regrowth. It is apparent that after regrowth there is little degradation in the quality of the AlGaAs barriers. This however is not the case in the processed samples. Figure 6.38 shows the emission obtained from the AlGaAs barriers in a) the 300nm dots and b) the corresponding $200\mu\text{m}^2$ mesa. It is apparent that the AlGaAs barrier emission has broadened considerably after regrowth and in the 300nm dots has shifted to lower energies by 12meV compared to the mesa emission. This suggests that the Al percentage in the dot barriers is reduced compared to the mesas and both are reduced compared to regrown unprocessed material. This is consistent with the suggestion made in Section 6.3.2 that Al has migrated into the wells. This figure also shows the emission obtained from the regrown AlGaAs layer over c) the mesa and d) the 300nm dots. Notice that the emission from the AlGaAs overlayer has shifted to higher energies in the mesa and was not measurable over the dots. This suggests that the aluminium percentage in the overlayer on the mesa is higher compared to the regrown unprocessed sample as the higher the Al percentage the band gap narrows and the exciton energy increases. It is not clear why no signal was obtained from over the dot area.

The quality of the interfaces can be assessed by changing the wavelength of the excitation source. When the 514nm (2.41eV) line from the Argon ion laser was used as the source the overlayer, barriers and wells are excited. Using the dye laser with Rhodamine 101 and selecting the 622nm (1.99eV) line excited both the barriers and the wells, and selecting the 663nm (1.87eV) line excited only the wells. The AlGaAs overlayer is transparent when using the 622 and 663nm lines. This is obvious when comparing these wavelengths with the AlGaAs emission shown in Figure 6.37. When the excitation energy is decreased from 2.41 to 1.99eV and the incident power remains constant, the signal intensity from the mesas and dots reduces by approximately a factor of 2-3 and from the wires by a factor of 3-5.

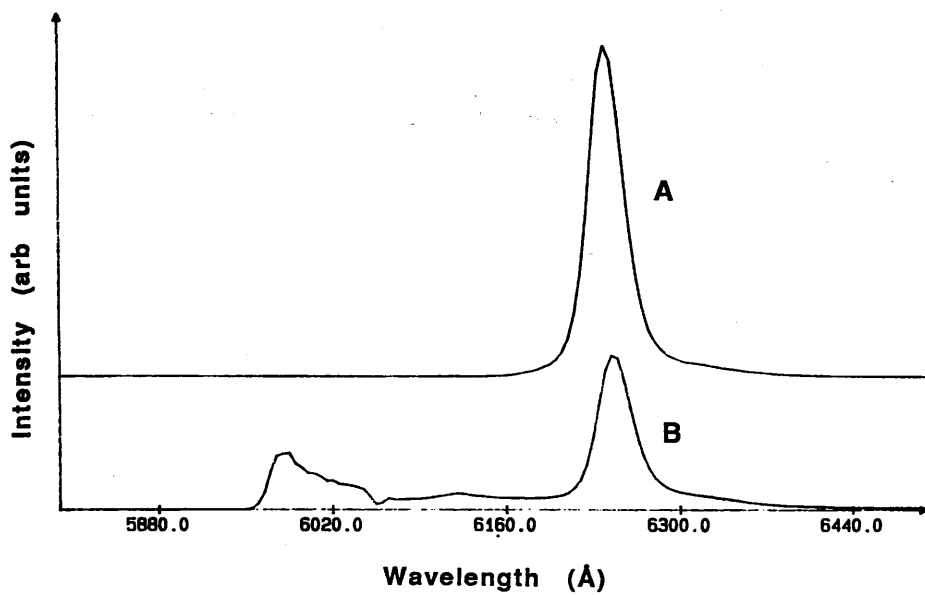


Figure 6.37 PL excited at 2.41eV from a) the Al_{0.3}Ga_{0.7}As barriers before regrowth and b) the Al_{0.3}Ga_{0.7}As barriers after regrowth with a layer of Al_{0.4}Ga_{0.6}As from a control sample that had not been processed in any way prior to regrowth.

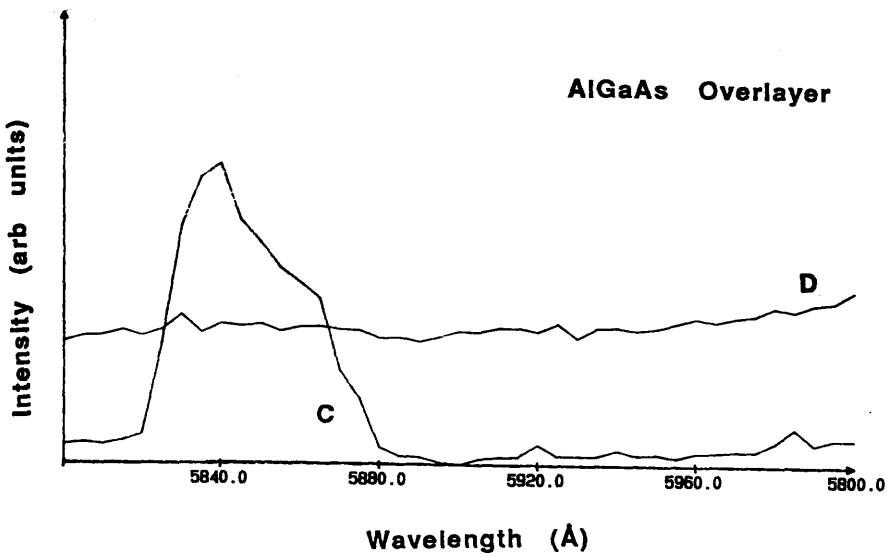
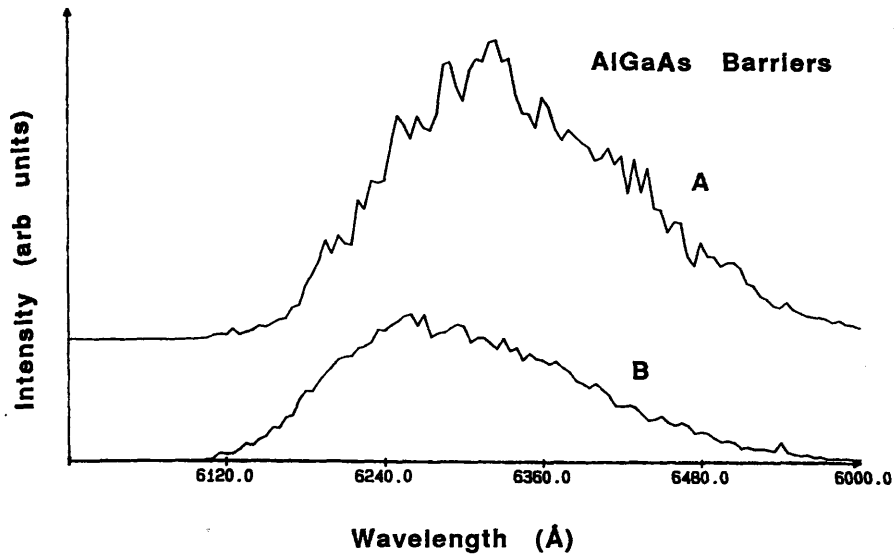


Figure 6.38 PL excited at 2.41eV from the $\text{Al}_{0.3}\text{Ga}_{0.7}\text{As}$ barriers after regrowth in a) 300nm dots and b) the corresponding $200\mu\text{m}^2$ mesa and the $\text{Al}_{0.4}\text{Ga}_{0.6}\text{As}$ overlayer on c) the same $200\mu\text{m}^2$ mesa and d) 300nm dots.

This suggests that excitons created in the AlGaAs overlayer contribute to the overall signal intensity. When the excitation energy is decreased further to 1.87eV and the results compared to the values obtained when exciting with 1.99eV, the signal intensity from the mesas reduces by a factor of ~2 but there is little change (if anything a slight increase) in the signal from the dots and the two larger sizes of wires. There was not enough power to pump the 150nm wide wires. This suggests that in the mesas there is some contribution to the overall signal strength from diffusion of excitons from the barriers across the interface into the wells which does not occur in the dots and wires. This is perhaps due to the degraded interface quality in the quantum structures after regrowth.

The 5K relative integrated PL intensities to a corresponding mesa from the quantum dots and wires are shown in Table VII. The relative efficiencies are increased compared to the before regrowth measurements. The comparison is made with the results obtained using the 622nm line as this corresponds to the situation before regrowth where both the barriers and wells were excited. This increase is most noticeable in the case of the 150nm and 250nm wires where the luminescence efficiency has increased by two and one orders of magnitude respectively. In the 300 and 550nm dots and 500nm wires the increase in efficiency is between 2 and 7 times more efficient. This result suggests that nonradiative recombination centres on the surface of the wires have been reduced by the growth of an overlayer. There is little improvement in the relative efficiencies between the 514 or 622nm line. This suggests that there are few nonradiative traps in the AlGaAs overlayer. When however the 663nm line is used the relative efficiencies increase still further. This suggests that the main region for nonradiative traps in the quantum structures is in the AlGaAs barriers.

The principal observations are therefore:

- 1) The dominant recombination mechanism for photoexcited carriers in sub-micron lattice matched MOCVD grown dots was found to be radiative at 5K for lateral dimensions as small as 75nm. In contrast for wires nonradiative recombination predominates as the wire width is reduced.
- 2) As the temperature is increased the dots and wires show a size dependence in the relative integrated PL intensities. The smaller dots (75 and 100nm in diameter) and the narrower wires (80 and 150nm in width) luminesced to higher temperatures than the larger dots (300 and 550nm in diameter) and larger wires (250 and 500nm in width) respectively and the smaller dots luminesced to higher temperatures than the smallest wires. This is also true when comparing the larger dots to the larger wires.
- 3) The 5K relative integrated PL intensities from the wires increased after regrowth with no change in the dots. The relative intensities from the 4nm QW of the 250 and 150nm wide wires improved from 0.042 and 0.009 before to 0.77 and 0.16 after regrowth.
- 4) The temperature dependence of the luminescence from the two larger wire structures improved after regrowth but there was no change in the dots. The 500nm wires luminesced to 60K before but 110K after regrowth and the 250nm wires 40K before but 60K after regrowth.
- 5) the QW exciton emission shifts predominately to higher energy after regrowth

Table VII

Relative integrated PL intensities from the 4 and 7nm QWs for dots and wires after regrowth using different excitation wavelengths.

4nm QW	Laser excitation wavelength		
	514nm	622nm	663nm
550nm dots	2.71	7.72	15.2
300nm dots	2.66	1.89	5.77
500nm wires	1.76	1.10	12.6
250nm wires	1.24	0.77	1.33
150nm wires	0.24	0.16	*

7nm QW	Laser excitation wavelength		
	514nm	622nm	663nm
550nm dots	2.34	10.5	95
300nm dots	5.13	*	*
500nm wires	0.76	0.61	5.02
250nm wires	1.86	1.48	1.12
150nm wires	*	*	*

* not enough pump power to enable a exciton emission to be measured

6.9.3 Discussion

The first important question to address is why the 5K relative efficiencies from the dots and wires should be so different. To reiterate, at submicron dimensions it is expected that nonradiative surface states will dominate the recombination mechanism due to the increase in the surface to volume ratio. If this were the case, the characteristic behaviour would be decreasing luminescence efficiency with decreasing structure size. This behaviour is seen in the wires but not in the dots. In Chapter 5 it was suggested that the mechanism which enabled the quantum dots to luminesce with relative efficiencies of approximately 1 down to dot sizes of 50nm is the localization of excitons in lower energy sites caused by fluctuations in the well width or lateral localization as a result of relief of the mismatch strain in the AlGaAs barriers due to removing the surrounding material. If well width fluctuations were the mechanism then the wires should also show similar behaviour as areas of lower energy will also exist along the length of the wire. Fluctuations in well width exist in the material used in these experiments as evidenced by the blue shift at about 10K in exciton emission as the temperature is increased. Skolnick *et al*¹⁰ reported seeing blue shifts in InP/InGaAs QWs with increasing temperature. They ascribed these blue shifts to excitons becoming unbound with increasing temperature enabling them to populate higher energy free exciton states. In this case they suggest that excitons could be bound either in well width fluctuations or to inadvertently introduced impurities. If the emission was purely intrinsic then the PL peak energy would follow the band-edge variation to lower energy with increasing temperature. As this blue shift seems to be enhanced in the smallest dots and wires but at small dimensions the wires do not show relative efficiencies of 1 suggests that while localization on well width fluctuations or impurities may be enhanced in the smallest structures, it alone is not the mechanism responsible for the high relative intensities found in quantum dots. It is not clear what difference in strain relaxation would occur in wires compared to dots as in one direction in the wires the strain will be the same as the bulk material.

The variation of the relative PL intensity of the structures (to their own integrated luminescence intensity at 5K) with temperature show differences in dot and wire behaviour dependent on the size and the number of degrees of freedom of the structure. The smaller diameter dots (75 and 150nm) and the narrower wires (80 and 150nm in width) luminesced to higher temperatures than the larger diameter dots (300 and 550nm) and the wider wires (250 and 500nm) respectively and the smaller dots luminesced to higher temperatures than the narrower wires. This was also true when comparing the larger dots to the larger wires. This suggests that it is a) the number of degrees of freedom and b) the size of the structure that are significant. Deveaud *et al*¹¹ measured the diffusion length of an exciton in GaAs to be of the order of 200nm at 15K. Hegarty and Sturge⁸ however reported a minimum diffusion length of ~445nm. Clausen *et al*¹² have shown that the diffusion mechanism of bulk semiconductors is no longer applicable in etched quantum dots and in their model, insensitive to the value of the surface recombination velocity when the size regime is smaller than the diffusion length of an exciton. In the wires however one dimension is always greater than the exciton diffusion length and therefore excitons may always be able to diffuse to nonradiative sites within the exciton lifetime which are probably located on the surface of the wire. If this is the case then there must also be a contribution from the width of the wire as there is an enhancement in luminescence intensities with increasing temperature as the wire width is reduced. This may also be due to the breakdown in the bulk exciton diffusion

model. The diffusion length L_d is equal to $(D\tau)^{1/2}$ where D is the diffusion coefficient in cm^2/sec and τ is the exciton lifetime in sec. The diffusion coefficient is therefore measured over an area. In bulk material there is no restriction on the direction in which an exciton can diffuse whereas in wires as the width is reduced restrictions might occur. This is not taken into account in the bulk measurement and therefore in smaller wires instead of having a contribution from exciton diffusion along the length and across the width of the wire only the diffusion along the wire could be significant. This enhancement in luminescence efficiency in the smaller structures could however be due to quantum confinement effects on the exciton due to the patterning of the quantum well. Bryant^{13,14} has shown that binding energies for free excitons and for impurities located at the centres of the wires are enhanced as one dimension of the wire is reduced. This enhancement of the binding energy constricts the bound state in the z direction (well thickness) and the direction of the wire width. Bryant¹⁵ has also shown that size effects could still contribute to the optical properties of quantum dots for diameters of the order of 50nm. Therefore it is possible that confinement effects on the exciton could also be contributing to the observed behaviour. Although the 75 and 100nm dots and 80 and 150nm wires may be too large to show any shift in exciton emission to higher energies, they may be small enough to still perturb the exciton behaviour. In the 75 and 100nm diameter dots the luminescence intensity falls at the same rate as the mesa. The nonradiative recombination rate is therefore not higher in these structures.

Further information on the possible mechanism causing these effects can be obtained from considering the results obtained after regrowth. Here there was absolutely no difference in the luminescence efficiencies of the dots either before or after regrowth. The two larger widths of wires (500 and 250nm) however showed a marked improvement in the luminescence efficiencies as the temperature was increased. In the 150nm wide wires the relative intensities obtained were reduced, but down to a level similar to the larger wires. Considering the results from the larger wires would suggest that nonradiative surface states had been reduced thereby increasing the intensity of the luminescence obtained from these structures. This result is in agreement with the results reported by Izrael *et al*¹⁶ where GaAs/AlGaAs quantum wires 40nm in width recovered luminescence after regrowth. The fact that in these results no change is seen in the dots suggests that the surface states play little or no role in the recombination mechanism in these 0 degree of freedom structures. The reduction in the PL intensities from the 150nm wires is harder to explain. If the same mechanism was acting as in the larger wires it would be expected that the PL intensities should persist to yet higher temperatures or perhaps not change but certainly not degrade. It may be that a more severe degradation in the quality of the well in small structures compared to the larger structures occurs as a competing mechanism which is evidenced by the complete loss of luminescence from the smallest wires. Perhaps this behaviour could be explained by surface recombination being dominant in the larger structures with a cut-off in the smaller structures when confinement effects start to dominate.

A further point to consider is the coupling of the incident light into the dots and wires. Tsuchiya *et al*¹⁷ found strong optical anisotropy in PLE spectra from quantum wires fabricated by growth on tilted substrates which produced wire widths in the low-nanometer range. They found that the ratio of the electron-light hole exciton peak intensity to the electron-heavy hole peak intensity depended strongly on the polarization orientation of the incident light with respect to the wire direction. In the

measurements detailed in this chapter the wires were excited using unpolarized light (the light loses its linear polarization after passing through the filter monochromator) and therefore would not be affected by the anisotropy found when light polarized parallel to or at right angles to the wires. Kohl *et al*¹⁸ also reported polarization dependence of confined 1D energy levels in wires. The difference in relative intensities from the dots and wires could therefore be due to the different efficiency with which light couples into the structures. Figure 5.5 in Chapter 5 shows how the relative intensity decreases in small diameter (60 and 90nm) dots as the sample angle to incident beam is reduced. This may be a manifestation of the effects of light coupling.

Other data to consider which may add to the overall picture is the linewidth variation before and after regrowth. When comparing the results from the dots the most noticeable feature is the severe broadening of the 75nm dot linewidth at 20K and the subsequent reduction. This increase is seen to a lesser degree in the mesa and the 100nm dots. A mechanism which could be responsible for this broadening is that at 5K the exciton is localized in a well width fluctuations. As the temperature increases towards 20K it thermalises and can become bound to other impurities in the material and above 20K it becomes completely unbound and the emission becomes more intrinsic in nature thus reducing the linewidth. The fact that both the smallest dots and wires show this behaviour most strongly compared to the larger structures suggests that perhaps more impurities are present in these structures or that the probability of the exciton binding to it is higher as the structure is smaller. It is expected that the smallest quantum structures will be most sensitive to the effects of the dry etching and could have a higher defect density than the larger structures therefore increasing the likelihood of an exciton binding to an impurity¹³. At 5K the linewidth variation is much more random and severe in the wires. This is in agreement with the results reported by Bryant¹⁴ that the broadening in the wires will be dependent on the position of the impurity or exciton in the wire relative to the well boundary. This is not the case for dots.

After regrowth the linewidth broadening has increased in severity suggesting a reduction in the quality of the interfaces and probably increased impurity associated transitions. The 300 and 550nm dots and the 250 and 150nm wires show the severest broadening compared to the mesa. This would suggest that as the size of the structure is reduced the effects of overgrowth on the linewidth become more pronounced.

The remaining question is why should the dots fabricated in MOCVD material behave differently to the dots fabricated in MBE material which are described in Chapter 5. The two most likely differences between the material are the interfaces and the impurities introduced at the growth stage (see Chapter 4 Section 4.3). If well width fluctuations contribute to the effects seen then it is possible that they are enhanced in MOCVD material as the interfaces are definitely not as abrupt in this material compared to the MBE material. It is likely that the interfaces are more graded in composition and that fluctuations are greater than one monolayer. The localization potentials could therefore be larger in this material. If excitons bound to impurities contribute to the overall effect a higher defect density as exists in the MOCVD material might be significant.

The final point to consider is what causes the change in material structure - the shifts in exciton emission energy and the change in the 4/7nm QW intensity ratio. By considering the results from CH₄/H₂ etched samples discussed in Section 6.10.3 and the results obtained from temperature cycling SiCl₄ etched dots the mechanisms responsible for this are more apparent and are discussed in Section 6.11.3.

6.10 Photoluminescence of CH₄/H₂ etched dots from 5 to 200K

6.10.1 Experimental Results before regrowth

This sample was characterized using the same experimental set-up described in Section 6.9. The most noticeable difference between dots etched using CH₄/H₂ and SiCl₄ is that in CH₄/H₂ dots the 7nm QW luminescence was so weak as to be unmeasurable and therefore only results for the 4nm QW will be presented. This result is suggestive of increased sensitivity to the etching process. Figure 6.39a shows the relative integrated PL intensity for dots of diameter 80, 100 and 250nm etched using CH₄/H₂. Unlike the results for dots etched using SiCl₄ and shown in Figure 6.13 the relative intensities reduce as the dot diameter is reduced with the 80nm dots having a relative efficiency smaller by 2 orders of magnitude on the 250nm dots. This reduction however, is not as dramatic as the 4 orders of magnitude drop seen in 80nm diameter SiCl₄ etched wires also shown in Figure 6.13. This result is also in disagreement with the results presented in Chapter 5 Figure 5.4 where no reduction in relative efficiencies were obtained with a reduction in dot diameter for CH₄/H₂ etched structures. This result tends to suggest that the MOCVD material is more sensitive to the effects of etching with CH₄/H₂ and it may explain why there was difficulty in finding signals from CH₄/H₂ etched dots in Section 6.3 as the efficiency was reduced relative to dots etched with SiCl₄. Why this should be the case though is unclear as there is no known major difference between MOCVD and MBE material that could account for this difference. There are however differences in sample design. Using CH₄/H₂ the dots are etched to a depth of 0.1μm whereas the SiCl₄ etched dots were 0.2μm in height. If there was some difference in the way light coupled into structures of different heights this would have shown up in the MBE dots in Chapter 5, as there the CH₄/H₂ etch depth was also 0.1μm and the SiCl₄ etched dots at least twice as deep (see Table VI for comparison of etched depths in Chapter 5). In the MOCVD material used here the 4nm QW is closer to the surface than in the MBE material used in Chapter 5 (see Section 6.9.1). By placing the well nearer to the surface the radiation damage introduced by the CH₄/H₂ etching may be increased.

Figure 6.39b shows the variation in the relative integrated PL intensity from each dot as the temperature is increased. As can be seen the dots display similar behaviour to the SiCl₄ etched dots described in Section 6.9. The relative intensity of the luminescence from the 250nm diameter dots drops more quickly than the intensities from the 80 and 100nm dots. Again the mesa luminesces most efficiently. This behaviour will be discussed in Section 6.10.3.

Figure 6.39c shows the shift in exciton emission wavelength with increasing temperature. A negative wavelength shift corresponds to an increase in exciton energy. The 80 and 250nm dots do not show any blue shift but the mesa and the 100nm dots show a shift of 1nm to shorter wavelengths.

Finally figure 6.40 shows the variation in PL linewidth with temperature from all dot sizes and a mesa. The main feature to notice is the increased linewidth of $\sim 17\text{meV}$ of all the dots over the mesa linewidth of 11meV at 5K . As the temperature was increased the linewidth from the dots decreased to 15meV at 30K and followed the mesa linewidth which then remained almost constant at 15meV across the whole temperature range. It is not obvious why the linewidth should be larger at 5K and then reduce as the temperature is increased as the inverse would normally be expected as the excitons thermalise out of lower energy well areas and sample an average of the well width fluctuations. However if impurities are responsible for the linewidth broadening, as the temperature is increased these defect bound excitons thermalise and the emission becomes more intrinsic in nature which could then account for the linewidth reduction. That the mesa linewidth increases with increasing temperature from 11meV at 5K to 15meV at 20K is further evidence that impurity broadening is the dominant mechanism in the dots as the mesa would be less sensitive to the effects of any radiation damage causing impurity incorporation.

6.10.2 Experimental Results after regrowth

Figure 6.41 shows the 100nm CH_4/H_2 etched dots a) before regrowth and b) after regrowth with a $0.2\mu\text{m}$ thick layer of $\text{Al}_{0.4}\text{Ga}_{0.6}\text{As}$. The main findings after regrowth are as follows

- 1) exciton emission is seen from the 4nm well in all three dot sizes though only barely resolved in the 80nm dots (see figure 6.42) at 5K . In the 100nm diameter dots the emission has shifted 31meV to higher energy but in the 80nm dots no shift is seen and in the larger dots no emission is seen from the 7nm QW but in the 80nm dots it is well resolved. The GaAs substrate emission is also shown for different excitation power levels. In figure A, two peaks are clearly seen but in figure C where the incident laser power has been increased by a factor of 50 the bulk GaAs bound exciton transition dominates. The exciton transition bound to a carbon impurity is saturated at higher powers but this is not the case in the SiCl_4 etched samples. The relative intensities of the 80 and 100nm dots have not increased after regrowth but the 250nm dots are improved by an order of magnitude. This again shows that the regrown layer does not significantly affect the luminescence efficiency of quantum dots.
- 2) The second noticeable difference to regrowth on SiCl_4 etched structures is in the material structure in the mesas. There are three well resolved peaks at 733 , 780 and 810nm (figure 6.43). The ratio of the $4/7\text{nm}$ QW has not increased as happened in the SiCl_4 etched samples. The exciton mesa emission has consistently shifted blue by 29.7 and 22.5meV ($\sim 10\text{nm}$) for both the 4 and 7nm QWs respectively.
- 3) Finally the quality of the AlGaAs barriers does not seem to be reduced as much as in the SiCl_4 etched sample.

These results suggest that samples etched with CH_4/H_2 show different effects compared to samples etched with SiCl_4 after regrowth. The most likely cause of this are the different impurities introduced into the material by the two different etch processes and the depth to which the impurities penetrate in the dry etch step. This will be discussed in Section 6.10.3.

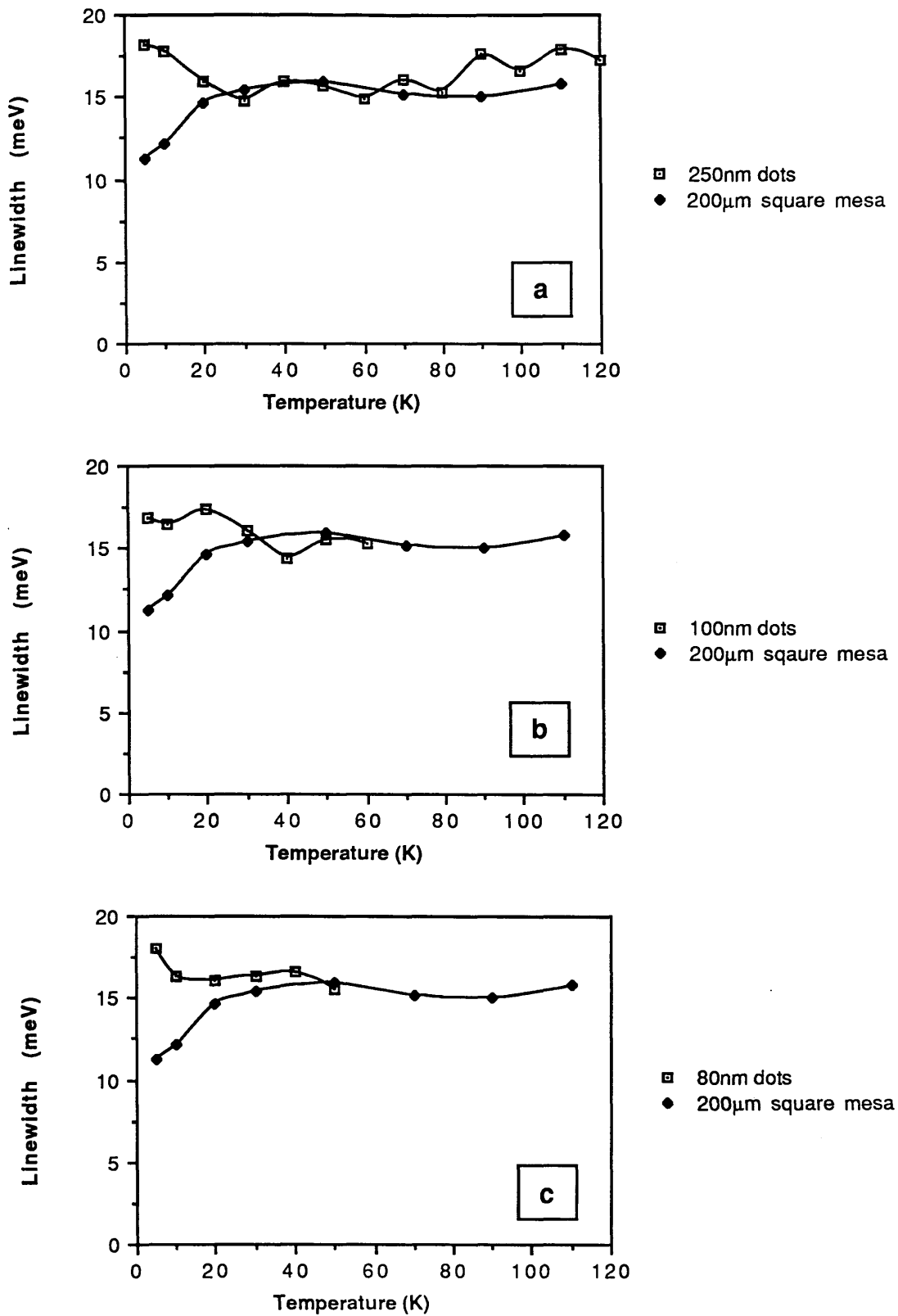
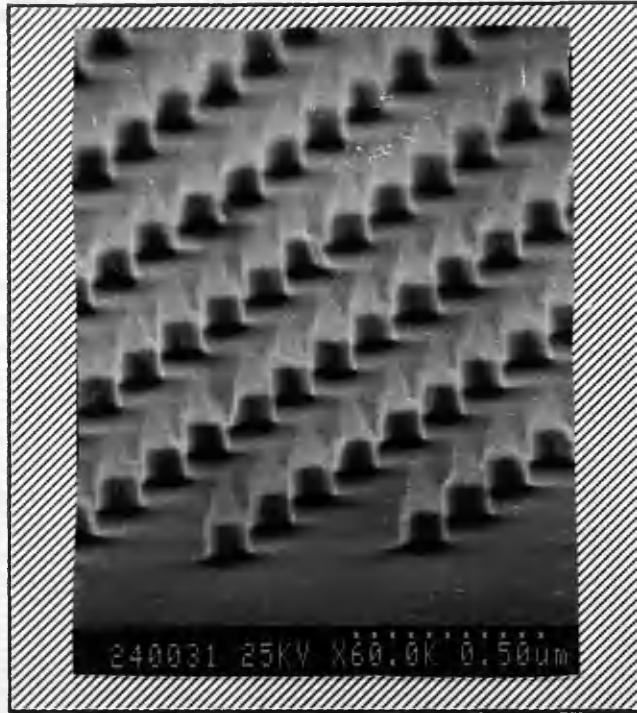
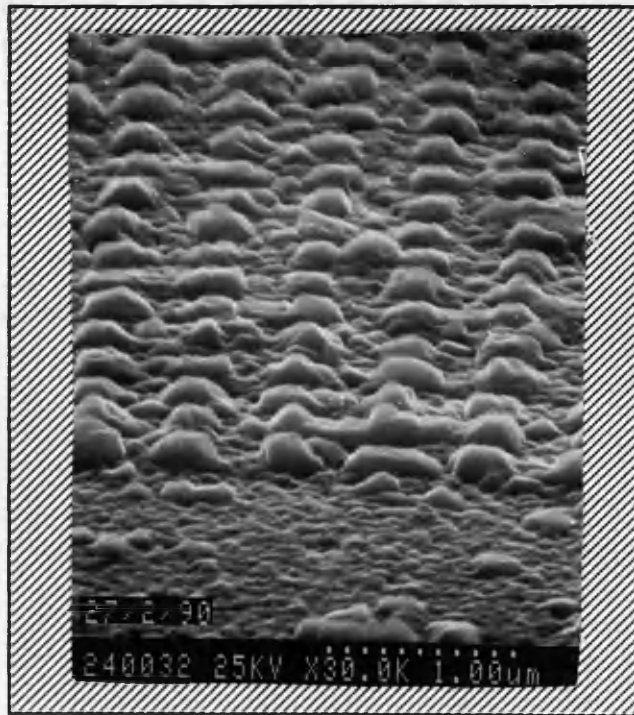


Figure 6.40 Variation of PL linewidth with temperature for a) 250nm b) 100nm and c) 80nm diameter dots etched using CH_4/H_2 . The variation in linewidth for a $200\mu\text{m}$ square mesa is also shown for comparison purposes.



(a)



(b)

Figure 6.41 100nm diameter dots etched using CH_4/H_2 a) before regrowth and b) after regrowth with $0.2\mu\text{m}$ of $\text{Al}_{0.4}\text{Ga}_{0.6}\text{As}$. Notice that before regrowth the HRN mask has not yet been removed.

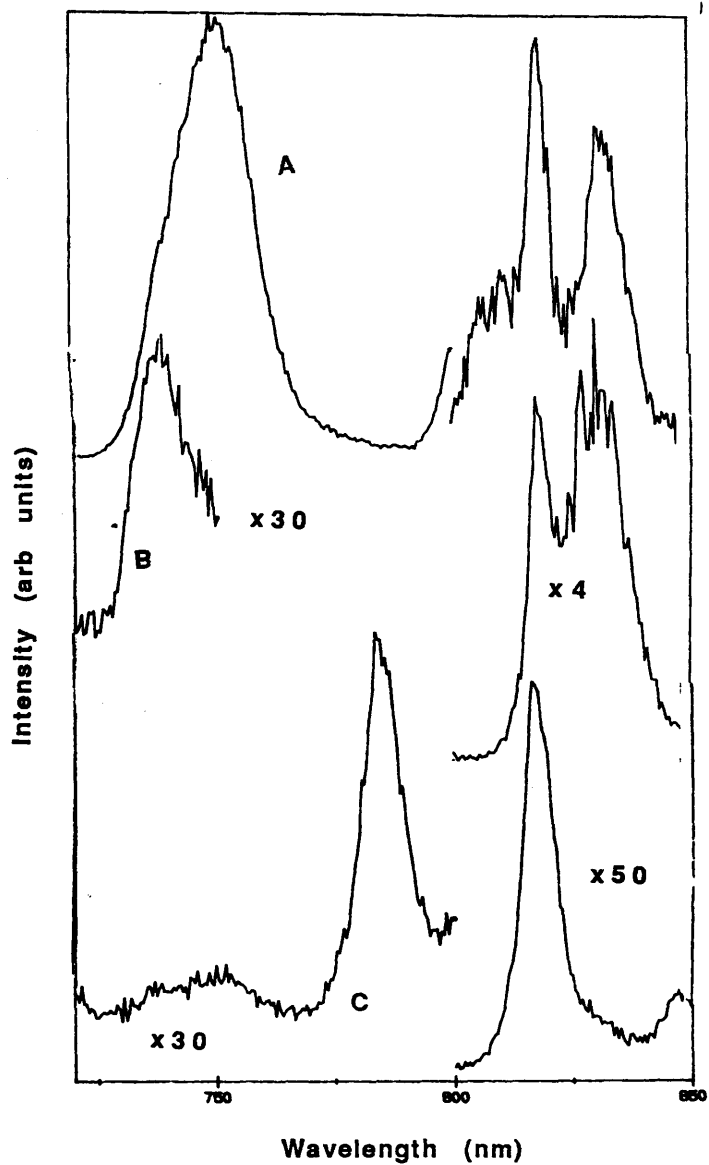


Figure 6.42 PL excited at 2.54eV from a) 250nm b) 100nm and c) 80nm diameter dots etched using CH_4/H_2 after regrowth with a $0.2\mu\text{m}$ thick layer of $\text{Al}_{0.4}\text{Ga}_{0.6}\text{As}$.

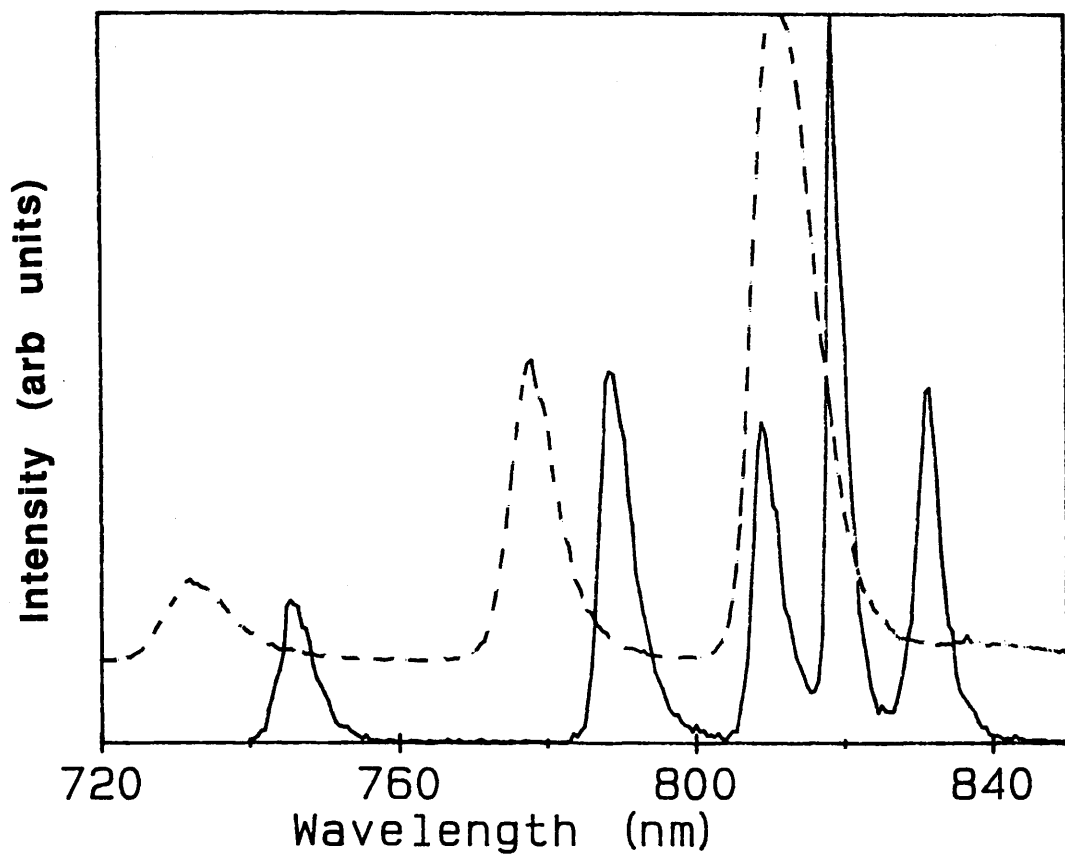


Figure 6.43 Material structure of a $200\mu\text{m}^2$ mesa etched using CH_4/H_2 before regrowth (solid line) and after regrowth (dashed line). PL excited before regrowth using 2.54eV and after using 2.41eV.

6.10.3 Discussion

Two main questions have been raised in this experiment 1) why should the results be different for structures etched using CH_4/H_2 on MOCVD or MBE material and 2) why is the structure of the material different after regrowth compared to SiCl_4 etched structures. After etching luminescence was only obtained from the 4nm QW unlike SiCl_4 etched dots where emission was obtained from both the 4 and 7nm QWs. This suggests that the radiation damage in the CH_4/H_2 etched dots is worse. It is perhaps possible that the hydrogen ions can penetrate deeper into the crystal than the impurities introduced in SiCl_4 etching. This may then cause the degradation in quality of the 7nm QW. It is possible that carbon may also be incorporated as an impurity in the crystal. After regrowth there was no emission from the 7nm QW in the 300 and 100nm dots but in the 80nm dots luminescence seems to have been recovered in this well. Why this happens is unclear.

It has been suggested that the etch mechanism in CH_4/H_2 may in fact be the reverse of the MOCVD growth process and that many of the reactions occurring in the growth process will also occur in the reverse etching process. It may be possible that in both cases the same impurities and defects are generated. H_2 is used as the carrier gas for the arsenic in the growth process and as an etchant and dilutant in the etching process. Perhaps the amount of a certain type of impurity and defect is increased by using a similar process twice. This then may significantly increase the number of efficient nonradiative centres in the material and this may be why MOCVD material is particularly sensitive to the effects of CH_4/H_2 etching. When SiCl_4 is used as the etch gas, different impurities are introduced which may not contribute as many nonradiative traps.

6.11 Temperature Cycling of SiCl_4 etched dots and mesas

To reiterate this experiment was designed to investigate whether the shifts in exciton emission to higher energy after regrowth were due to strain from the regrown AlGaAs overlayer or from the effects of the temperature cycle the samples undergo when overlayer is grown. The experiment is described in detail in Section 6.8.

6.11.1 Experimental Results and Discussion

Figure 6.44 shows the spectra obtained from unovergrown and overgrown material excited at 2.54eV from completely unpatterned material. There are no differences between the spectra. When unprocessed samples were subjected to the two different temperature cycles again no difference was found. This then suggests that in samples where no processing or etching has been done the overgrowth process has no affect on the quality of the material. Figure 6.45 shows the results of the complete growth temperature cycle on a mesa etched using SiCl_4 . It seems that the 10nm QW has disappeared, the 7nm QW has broadened and shifted 2.6meV (1.5nm) to lower energies and the 4nm QW has broadened and shifted 8.8meV (4nm) to higher energies. The ratio of 4/7nm QW has increased after the temperature cycle. Figure 6.46 shows the mesa emission obtained after the short temperature cycle. Again both QWs have shifted - 19meV red in the 7nm QW and 10.2 meV blue in the 4nm QW. The 4/7nm QW ratio is increased even more compared to the uncycled data. These results show that the shifts found in the QW

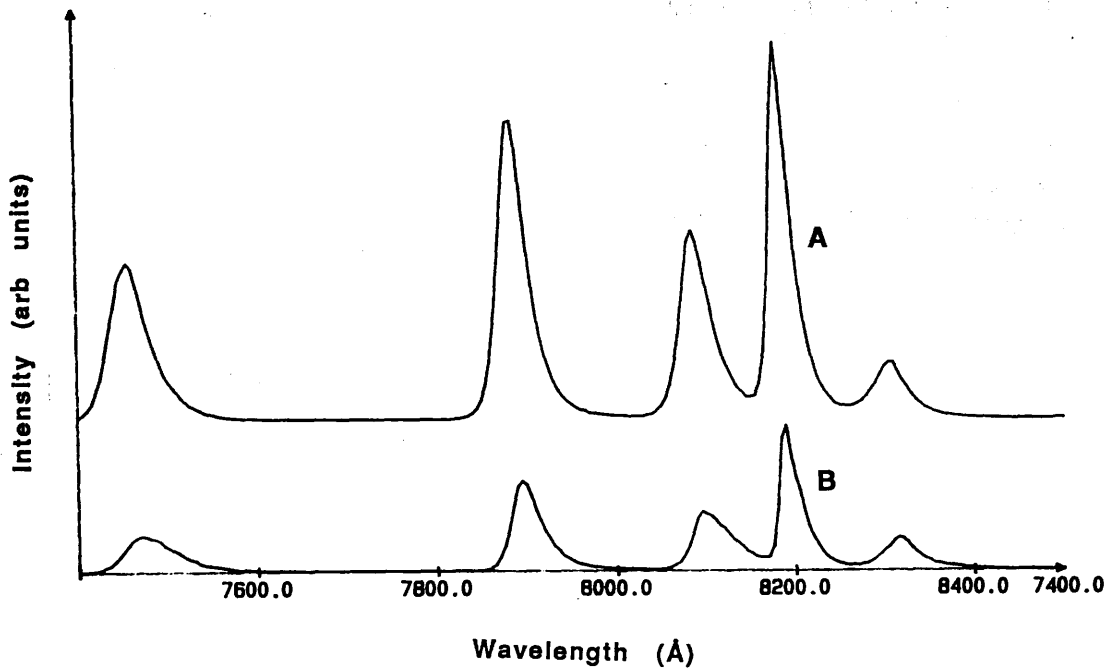


Figure 6.44 Spectra obtained from a) unovergrown and b) overgrown material excited at 2.54eV from completely unprocessed and unpatterned material.

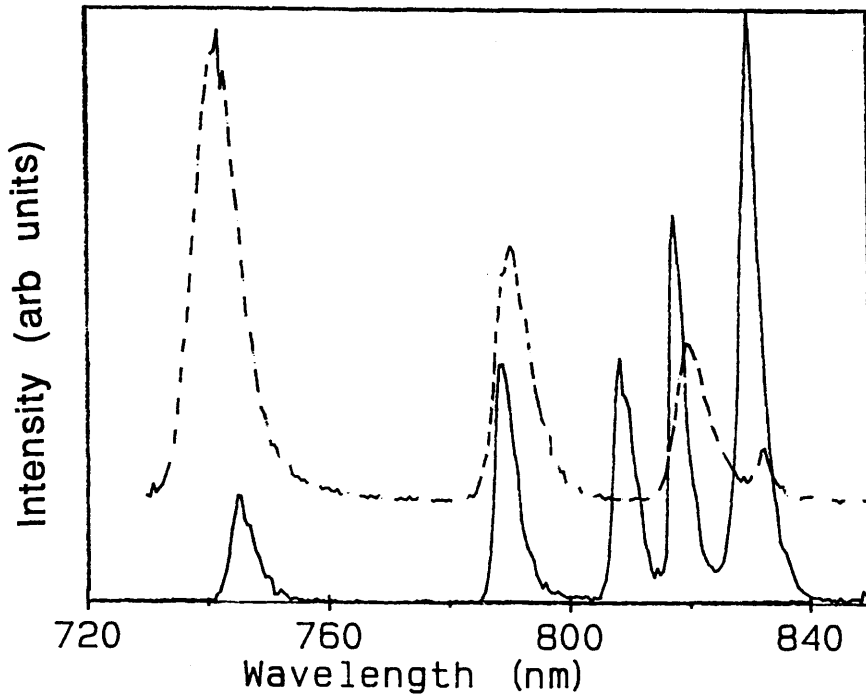


Figure 6.45 PL excited at 2.41eV from a SiCl_4 etched $200\mu\text{m}^2$ mesa before temperature cycling (solid line) and after complete growth (warm up, growth period, cool down) temperature cycle (dotted line).

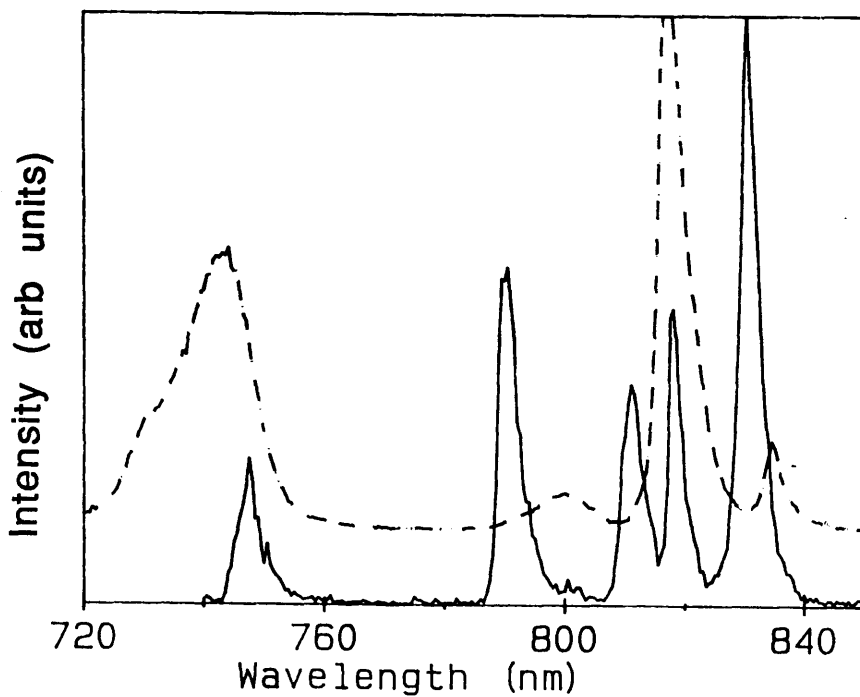


Figure 6.46 PL excited at 2.41eV from a SiCl_4 etched $200\mu\text{m}^2$ mesa before temperature cycling (solid line) and after short (warm up, cool down) temperature cycle (dotted line).

emission after regrowth are due to the temperature cycling and are not due to strain introduced by the overgrown layer as no layer is regrown on the samples. The effects seem to be worse in the sample subjected to the more rapid changes in temperature (warm up, cool down) when there was no constant temperature in the middle of the cycle.

These exciton emission shifts are probably caused by aluminium diffusion into the QWs from the AlGaAs barriers. Thermal annealing has been shown³ to alter the composition profile across the QW through solid state diffusion of Ga and Al. Thermal annealing results in the transition from an initially square well to a compositionally gradually graded profile. The compositional profile will determine the potential energy profile confining the carriers. The diffusion of Al into the well effectively raises the bottom of the well (by increasing the bandgap energy of the well material) and also narrows it. The result is to increase exciton energies. Since exciton energies are most sensitive to well width in narrow wells, it is expected that these wells will show the largest shift in exciton energy²⁰ and this has been found to be the case. Schulman¹⁹ calculated the quantum well energy shift versus the thickness of the compositionally graded region for various well thicknesses. These calculations showed that for a well 15 monolayers thick (~4.2nm) a 30% shift to higher energy would occur in the conduction band energy for grading over six layers and a shift of 10meV to higher energy would indicate a grading over 2 monolayers or 0.566nm. Schlesinger *et al*² concluded that the interdiffusion of Al and Ga is very small at temperatures of 650 - 750°C and found that for temperatures greater than 800°C interdiffusion begins to become significant and then only when samples are annealed for ~6 hours. These results are in perfect agreement with those described above as on unprocessed quantum wells no shift or change is seen after temperature cycling or regrowth. Other authors²¹⁻²³ have shown that thermal annealing results in shifts in laser emission to shorter wavelengths due to this modification of the well structure. However the effects reported here are seen in samples that have been dry etched. Koteles *et al*²⁰ reported that rapid thermal annealing of GaAs/Al_{0.32}Ga_{0.68}As MQWs at 950°C for 15 sec resulted in energy shifts as large as 61meV, but only if the material was capped with SiO₂ (see also reference 23). The mechanism suggested to account for these shifts was that during heat treatment Ga atoms preferentially diffuse in the SiO₂ leaving behind vacancies which quickly diffuse into the structure. These vacancies facilitate the diffusion of Al and Ga atoms producing an intermixing of the GaAs well and the AlGaAs barrier material. Indeed impurity enhanced diffusion using Ga⁺ ions is one of the methods used to fabricate 0 and 1 DOF structures without using dry etching techniques (see Chapter 1, Section 1.4.1.2). It has been proposed that after etching with SiCl₄, As vacancies exist on the surface of the material and that impurities are introduced into the material (Chapter 3, Section 3.4). It is possible therefore that although annealing takes place at comparatively low temperatures ie 750°C the inclusion of impurities and vacancies greatly enhances this mechanism and contributes to the change in well shape that causes the shifts. Both Lee *et al*²⁴ and Ralston *et al*²⁵ measured the Ga, Al interdiffusion in superlattices caused by rapid thermal annealing and concluded that the interdiffusion mechanism is very sensitive to the presence of small amounts of impurities and defects and that different values for diffusion coefficients could result due to differences in the native defect densities between MBE and MOCVD grown materials respectively. The apparent red shift seen in the 7nm QW and the disappearance of the 10nm QW could be due to the smearing out of the wells and barriers of these two wells resulting in the much poorer red shifted exciton emission.

The 100, 300 and 500nm dots luminesce in both wells before and after temperature cycling. This result is significant in that the 100nm dots still luminesce whereas they do not after overgrowth with a layer of AlGaAs. This suggests that in the smallest structures luminescence may be lost after regrowth due to complete lateral migration of Al or complete alloy mixing of the wells. It may be that in quantum structures temperature gradients across the dot are higher than on flat uniform samples causing enhanced Al and Ga diffusion. Both the 100 and 500nm dots were subjected to the longer warm up, growth period, cool down temperature cycle (19 min 47 sec). In both cases the 10nm QW disappears and two peaks are left both of which are blue shifted by 7meV in the 100nm dots and 58meV in 500nm dots. In the 300nm dots subjected to the shorter warm up cool down cycle (12 min 41 sec) the 7nm and 10nm QW have all but disappeared and the 4nm has broadened and shifted blue. Temperature cycling has therefore been shown to cause exciton emission shifts to higher energies in the dot spectra and it causes a general smearing out of the material structure.

6.12 Summary

The dominant recombination mechanism for photoexcited carriers in sub-micron lattice matched MOCVD grown GaAs/AlGaAs quantum dots was found to be radiative at temperatures of 20K and below for lateral dimensions as small as 75nm. For GaAs/AlGaAs quantum wires fabricated on the same sample nonradiative recombination predominates as the wire width is reduced. As the temperature at which the structures were characterized was increased a size dependence was found in the relative integrated PL intensities from the dots and wires. Emission was still obtained from the smallest diameter dots (75nm) at 200K and from the smallest wires (80nm) at 130K. The smaller dots (75 and 150nm in diameter) and the smaller wires (80 and 150nm in width) luminesced to higher temperatures than the larger dots (300 and 550nm in diameter) and the larger wires (250 and 500nm in width) respectively and the smaller dots luminesced to higher temperatures than the smallest wires. This was also true when comparing the larger dots to the larger wires. This temperature dependence may be due to confinement dependent on the dot diameter or wire width. This conclusion is supported by the enhanced blue shift seen in the exciton emission from the smallest dots and wires as the temperature is increased. Restrictions on the diffusion lengths of excitons to nonradiative sites due to the patterning of the QW into dots and wires could be the mechanism responsible for the effects seen at 5K. In wires the extra degree of freedom of the exciton contributes to the loss of luminescence at 5K as it is still possible for the excitons to diffuse to nonradiative sites within the exciton lifetime. This does not happen in the dots. This conclusion is supported by the results obtained after regrowth.

Regrowth on SiCl_4 etched quantum structures with a layer of $\text{Al}_{0.4}\text{Ga}_{0.6}\text{As}$ increases the luminescence efficiency of the 250 and 500nm wires but reduces the efficiency of the 150nm wires. The 550 and 300nm dots show no change in efficiency either before or after regrowth. Luminescence is completely lost in the 75 and 150nm diameter dots and 80nm wide wires. This suggests that in the wires surface states contribute significantly at 5K to the nonradiative recombination rate whereas in dots they do not. The overgrown AlGaAs layer passivates the nonradiative surface states thereby increasing the luminescence efficiency of these structures. Regrowth causes predominately blue shifts to higher energy in the exciton emission but only in samples subjected to RIE with either SiCl_4 or CH_4/H_2 . This is most likely due to enhanced diffusion of Al into the quantum well caused by

impurities introduced during the dry etch process. This changes the profile of the well from a square potential profile to a compositionally graded well and this causes the shift to higher emission energies. Structures etched using SiCl₄ show a degradation in luminescence efficiency from the lower well after regrowth and in the upper well the PL linewidth has increased by a factor of 1.4 in the dots and 2 in the 150 and 250nm wide wires with little change in the 500nm wires.

MOCVD material is more sensitive to the effects of CH₄/H₂ RIE compared to SiCl₄ etching as the PL intensities from the dots reduce with dot size and in the lower well. After regrowth blue shifts are seen in the PL emission from the wells as in SiCl₄ etching. These results and those for SiCl₄ etched and regrown quantum structures suggest that different impurities are introduced into the material by the different etch gases. It is these impurities which contribute to the differences in material structure before and after regrowth and which enhance the layer mixing at the interface between the barriers and the wells thus causing shifts to higher energy in the PL emission from the wells.

Shifts induced by strain from the regrown layer can be discounted as temperature cycling (following the regrowth temperature cycle) on SiCl₄ etched dots also showed shifts in exciton emission to higher energy.

References

- 1 R Cheung, S Thoms, S P Beaumont, G Doughty, V Law and C D W Wilkinson: Elec. Letts, Vol. 23 No. 16 1987 pp. 857.
- 2 T E Schlesinger and T Kuech: Appl. Phys. Lett. (49) 9 1986 pp. 519.
- 3 S R Andrews, H Arnot, P K Rees, T M Kerr and S P Beaumont: J. Appl. Phys. 67 (7) 1990 pp.3472
- 4 H E G Arnot, R Glew and S P Beaumont: to be published.
- 5 R Glew, H E G Arnot, S P Beaumont, J Lambkin and D Dunstan: presented at the 4th Int Conf on MOVPE, Hakone, Japan, May 1988.
- 6 H E G Arnot, M Watt, C M Sotomayor-Torres, R Glew, R Cusco, J Bates and S P Beaumont: Superlattices and Microstructures, Vol. 5, No. 3, 1989.
- 7 H L Ehlers, A W R Leitch and J S Vermaak: J. Crystal Growth 96 1989 pp.101
- 8 J Hegarty and M D Sturge: J. Opt. Soc. Am. B Vol. 2, No. 7 1985 pp. 1143.
- 9 M Tanaka, H Sakaki, J Yoshino and T Furuta: Surf. Sci. 174 1986 pp. 65.
- 10 M S Skolnick, P R Tapster, S J Bass, A D Pitt, N Apsley and S P Aldred: Semicond. Sci. Technol. 1 1986 pp. 29.
- 11 B Deveaud, T C Damen, J Shah and C W Tu: Appl. Phys. Lett. 51 (11) 1987 pp. 828.
- 12 E M Clausen Jr, H G Craighead, J M Worlock, J P Harbison, L M Schiavone, L Florez and B Van der Gaag. Appl. Phys. Lett. (14) 2 1989 pp. 1427.
- 13 G W Bryant: Phys. Rev. B Vol. 29, No. 12 1984 pp. 6632
- 14 G W Bryant: Phys. Rev. B Vol. 31, No. 12 1985 pp. 7812
- 15 G W Bryant: Phys. Rev. B Vol. 37, No. 15 1988 pp. 8763

- 16 A Izrael, B Sermage, J Y Marzin, A Ougazzaden, R Azouley and J Etrillard: *Appl. Phys. Lett.* 56(9) 1990 pp.830.
- 17 M Tsuchiya, J M Gaines, R H Yan, R J Simes, P O Holtz, L A Coldren and P M Petroff: *Phys. Rev. Lett.* Vol. 62, No. 4 1989 pp. 466.
- 18 M Kohl, D Heitmann P Grambow and K Ploog: *Phys. Rev. Lett.* Vol. 63, No. 19 1989 pp. 2124.
- 19 J N Schulman: *J. Vac. Sci. Technol.* B1 (3) 1983 pp. 644
- 20 E S Koteles, B Elman, R P Holmstrom, P Melman, J Y Chi, X Wen, J Powers, D Owens, S Charbonneau and M L W Thewalt: *Proceedings of the 4th International Conference on Superlattices, Microstructures and Microdevices, Trieste, Italy 1988.*
- 21 M D Camras and N Holonyak, R D Burnham, W Streifer, D R Scifres, T L Paoli and C Lindström: *J. Appl. Phys.* 54 (10) 1983 pp. 5637.
- 22 K Meehan, J M Brown, P Gavrilovic and N Holonyak, R D Burnham, T L Paoli and W Streifer: *J. Appl. Phys.* 55 (7) 1984 pp. 2672.
- 23 D G Deppe, L J Guido, N Holonyak and K C Hsieh, R D Burnham, R L Thorton and T L Paoli: *Appl. Phys. Lett.* 49 (9) 1986 pp. 510.
- 24 J C Lee, T E Schlesinger, and T F Kuech: *J. Vac. Sci. Technol.* B5 (4) 1987 pp. 1187.
- 25 J D Ralston, S O'Brien, G W Wicks and L F Eastman: *Appl. Phys. Lett.* 52 (18) 1988 pp. 1511.

Chapter 7

Conclusions and Future Work

Quantum dots and wires have been successfully fabricated on a variety of semiconductor material systems - GaAs/AlGaAs, InP/InGaAs and GaAs/InGaAs. Metal quantum dot masks 40 to 250nm in diameter with pitches of two and four times the dot diameter can be routinely fabricated using a two layer positive PMMA resist scheme and Nichrome or Titanium as the evaporated metal. A negative resist (HRN) has been used successfully to fabricate quantum dots masks 60 to 500nm in diameter with pitches three and five times the dot diameter. This mask has the advantage that it could be completely removed using an oxygen plasma etch. HRN has also been used to fabricate quantum wires 75 to 500nm in width and 100 μ m in length with either a constant pitch of 1000nm or a constant filling factor of 25%. PMMA has been used to fabricate wires 100 to 400nm in width with a filling factor of 50%. A higher filling factor is possible using PMMA due to the better contrast of this resist over HRN.

The main limitation in fabricating the etch masks is the time taken to expose the patterns on the Philips electron beam system and the resolution of this system due to the 50kV beam voltage and smallest spot size of 8nm. By using the JEOL electron beam writer the patterns can be scanned much more quickly enabling larger areas to be covered. The resolution of this system is much higher due to the increased beam voltage of 100kV and dots 20nm in diameter have been fabricated successfully. There are other masking materials which could be investigated - for example strontium fluoride which dissolves in water and has been shown to be resistant to reactive ion etching¹ and nickel instead of nichrome which can be removed by using dilute nitric acid². By using a metal mask which can then be removed (a necessity when regrowth is to be carried out) the radiation damage to the underlying wells may be reduced.

Laser Holography combined with oxygen plasma etching has been shown to be a viable method for fabricating quantum dots as small as 40nm in diameter over areas as large as 20mm². The main drawback of this system is that dots and wires of different sizes cannot be fabricated together on the one sample to enable direct comparisons. However the throughput of this system is much faster than an electron beam system and it enables quantum structures to be fabricated without the need for an e-beam writer. Further work in this area should investigate the smallest sizes of wires that could be fabricated using this process.

These etch masks have been successfully transferred to the semiconductor material using a variety of etching techniques. Reactive ion etching with SiCl_4 , CH_4/H_2 and SiCl_4/H_2 and Argon ion milling can be used to fabricate GaAs/AlGaAs quantum dots or wires less than 100nm in diameter or width. Indeed the fact that SiCl_4 etched GaAs/AlGaAs dots as small as 40nm luminesce as efficiently as the bulk material suggests that without any subsequent processing the effects of radiation damage are minimal. Regrowth with a layer of AlGaAs or thermal annealing has shown however that the impurities introduced by the dry etching are important as they can cause a degradation in the quality of emission obtained from the wells. InP/InGaAs dots have been etched using CH_4/H_2 and GaAs/InGaAs dots using SiCl_4 . The smallest structures made were 20nm diameter dots etched using SiCl_4 .

There is much work however still to be done on understanding the effect reactive ion etching with different gases has on the optical properties of different semiconductor systems grown by either MBE or MOCVD. It would be interesting to grow several different wafers with the same 4, 7 and 10nm well structure as used in Chapter 6, but with varying AlGaAs barrier widths to investigate the penetration depth of impurities into the material before and after regrowth. Photoluminescence on flat samples subjected to dry etching and on dots and wires on this material could clarify the importance and if necessary the minimum width of the top AlGaAs barrier layer if the underlying wells are to be sufficiently protected from the effects of radiation damage. Further work with SiCl_4/H_2 etching to exploit the vertical undercut effect could be used to reduce the overall sizes of structures and reduce the need for ultrahigh resolution lithography. It would also be worthwhile to use this gas to fabricate regrown dots and wires as it may help to clarify the role of H_2 impurities in degrading material quality both before and after regrowth.

The dominant recombination mechanism for photoexcited carriers in sub-micron lattice matched MBE and MOCVD grown GaAs/AlGaAs quantum dots was found to be radiative at temperatures below 20K for lateral dimensions as small as 40nm and 75nm respectively. In contrast, for MOCVD GaAs/AlGaAs quantum wires fabricated on the same sample as the MOCVD dots nonradiative recombination predominates as the wire width is reduced. The dominant recombination mechanism in the sub-micron strained layer InGaAs/GaAs quantum dot system at low temperatures was also found to be non-radiative.

From the results on quantum dots alone presented in Chapter 5 it was suggested that non-radiative surface recombination was inhibited by the existence of lateral potential barriers in the GaAs/AlGaAs dots but not in the InGaAs/GaAs dots. Two possibilities were suggested: disorder in the plane of the well (with surface disordering as an extreme case) and strain. The first suggestion was disproved by the results from the MOCVD wires. If well width fluctuation were responsible for exciton localization, the wires should show similar behaviour to the dots, with high relative efficiencies persisting in the narrowest wires. The fact that nonradiative recombination dominates in wires of less than 500nm in width but not in dots and well width fluctuations do exist in the material shows that this mechanism alone cannot be responsible. The effects of strain relief after patterning are still unclear.

Temperature variation experiments on the MOCVD dots and wires showed a size dependence in the relative integrated PL intensities. The smaller dots (75 and 100nm in diameter) and the smaller wires (80 and 150nm in width) luminesced to higher temperatures than the larger dots (300 and 550nm in diameter) and the larger wires (250 and 500nm in width) respectively and the smaller dots luminesced to higher temperatures than the smallest wires. This was also true when comparing the larger dots to the larger wires. It was suggested that this temperature dependence may be due to confinement dependent on the dot diameter or wire width. This conclusion was supported by the enhanced blue shift seen in the exciton emission from the smallest dots and wires as the temperature was increased. Restrictions on the diffusion lengths of excitons to nonradiative sites due to the patterning of the QW into dots and wires could be the mechanism responsible for the effects seen at 5K. In wires the extra degree of freedom of the exciton contributes to the loss of luminescence at 5K as it is still possible for the excitons to diffuse to nonradiative sites within the exciton lifetime. This does not happen in the dots. This conclusion is supported by the results obtained after regrowth.

Regrowth with a layer of $\text{Al}_{0.4}\text{Ga}_{0.6}\text{As}$ on SiCl_4 etched quantum structures increased the luminescence efficiency of the 250 and 500nm wires but reduced the efficiency of the 150nm wires. The 550 and 300nm dots showed no change in efficiency either before or after regrowth. Luminescence was completely lost in the 75 and 150nm diameter dots and 80nm wide wires. This suggests that in the wires surface states contribute significantly at 5K to the nonradiative recombination rate whereas in dots they do not. The overgrown AlGaAs layer passivates the nonradiative surface states thereby increasing the luminescence efficiency of these structures.

To prove that exciton diffusion is affected by patterning and that there is a fundamental difference between dots and wires a series of structures could be patterned where the dot is stretched into a wire. One dimension would be kept constant. For example a 100nm diameter dot could be stretched into a rectangle 100x1000nm, 100nmx10 μm and 100nmx100 μm . Arrays of these structures could be exposed on the same sample and the low temperature (5K) Photoluminescence compared. If a cut-off in luminescence behaviour from wire like to dot like was found between the different rectangle sizes this would show that the diffusion mechanism was indeed being affected by the patterning.

It was found that MOCVD material was more sensitive to the effects of CH_4/H_2 RIE compared to SiCl_4 etching as the PL intensities from the dots reduce with dot size and in the lower well. Further work could be done to compare identical designs of MOCVD and MBE grown material, and if possible similar quality in terms of signal intensity and linewidth, to ascertain if the differences in luminescence efficiencies still result. By using material of identical design differences due to barrier thickness could be removed.

It has been shown that shifts in exciton emission to higher energy after regrowth on samples subjected to RIE with either SiCl_4 or CH_4/H_2 are most likely due to enhanced diffusion of Al into the quantum well caused by impurities introduced during the dry etch process. This changes the profile of the well from a square potential profile to a compositionally graded well causing the shift to higher emission energies. Structures etched using SiCl_4 show a degradation in luminescence efficiency from the lower well after regrowth and in the upper well the PL linewidth broadens. In CH_4/H_2 etched dots

luminescence is not obtained from the lower well after etching but QW exciton emission is obtained from all the wells in the mesas. After regrowth the exciton emission from the dots and mesas has shifted blue and in the mesas the emission from the lower QW has not degraded as in the SiCl_4 etched samples. These results suggest that different impurities are introduced into the material by the different etch gases. It is these impurities which contribute to the differences in material structure before and after regrowth and which enhance the layer mixing at the interface between the barriers and the wells thus causing shifts to higher energy in the PL emission from the wells. Shifts induced by strain from the regrown layer can be discounted as temperature cycling (following the regrowth temperature cycle) on SiCl_4 etched dots also showed shifts in exciton emission to higher energy.

Quantum confinement has still not been reported in GaAs/AlGaAs quantum dots. The 20nm dots fabricated using the JEOL should be small enough to exhibit quantum confinement and hence the desired blue shift. It is therefore obvious that this experiment should be carried out. However the material used must be of the utmost quality - extremely bright, narrow linewidth and excellent homogeneity. Low temperature Photoluminescence alone is not sufficient to prove that quantum confinement has been achieved as shifts can occur due to localization in monolayer fluctuations in well width, band filling effects and impurity inclusion at the dry etching step. Photoluminescence excitation spectroscopy must therefore be used to prove conclusively that confinement has been achieved as this technique measures intrinsic free exciton effects and shows structure other than the e1-h1 transition which is measured in Photoluminescence. The PLE system must therefore be set-up. A range of dot sizes and control mesas must also be included on the sample to prove that at a specific dot diameter quantum effects start to dominate so process induced effects can be discounted.

The experiments outlined in Chapter 6 Section 6.7 should be repeated on MBE grown material to try and ascertain if the effects seen were purely material dependent or were indeed due to the effects of patterning. The original impetus behind this work was to try and fabricate a quantum dot or wire laser. In all the overgrowth experiments luminescence was lost in the smallest structures. In order for enhanced laser performance to be obtained quantum GaAs/AlGaAs structures even smaller than those used in these experiments must be fabricated and it therefore doubtful that this method will ultimately achieve working quantum dot or wire lasers without much greater control of the regrowth step.

Regrowth on CH_4/H_2 etched InP/InGaAs dots and wires for applications in quantum dot and wire lasers is more likely to succeed as in this material system the exciton Bohr radius is larger than in GaAs/AlGaAs so the dots and wires need not be as small to achieve quantum confinement. This may reduce problems associated with the loss of luminescence in the smallest dots and wires on regrowth. The affect of well mixing enhanced by impurity diffusion is unknown in this system.

References

- 1 I MacIntyre: Thesis, Glasgow 1990 to be published.
- 2 A Izrael, B Sermage, J Y Marzin, A Ougazzaden, R Azoulay and J Etrillard, V Thierry-Mieg and L Henry: Appl. Phys. Lett. 56 (9) 1990 pp. 830.